Doctoral Thesis

North Atlantic anthropogenic carbon: methods, trends, budgets, variabilities, and uncertainties

Submitted by Tobia Tudino to the University of Exeter as a thesis for the degree of Doctor of Philosophy in Geography in July 2018

Supervisors:
Dr Marie-Jose Messias
Dr Ute Schuster
Dr Andrew J. Watson
Internal examiner:
Dr Katy Sheen
External examiner:
Dr Samar Khatiwala
Independent Chair:
Dr Pierre Friedlingstein

Author:
Tobia Tudino

Exploring the unknown requires tolerating uncertainty.

B. Greene

Acknowledgements

Working on a doctoral research has been the most challenging experience of my life. Luckily, I have not tackled each step on my own, but I have received a tremendous support from several people that I would like to thank deeply hereafter.

To M.-J. Messias, thanks for having supported my scientific and personal growths.

To U. Schuster, thanks for the enjoyable discussions and priceless hints.

To Prof. A.J. Watson, thanks for the patience and brilliant comments.

To P.R. Halloran, thanks for the modelling supports and occasional beers.

To Prof. R.G. Williams, thanks for unveiling me the ocean carbon framework.

To R. Wanninkhof, thanks for the suggestions on the ocean acidification and beyond.

To J. Palmieri, thanks for helping me setting a work in progress with the UKESM.

To J. Lauderdale, thanks for not giving up on supporting my MITgcm exploration.

To B. King, thanks for having organised two wonderful oceanographic cruises.

To A. Yool, thanks for letting me play with the OCCAM outputs.

To P.J. Brown, thanks for having supported the kick-off of this doctoral research.

To S. Torres-Valdes, thanks for showing me that nutrients and oxygen can be cool.

To R. Bernardello, thanks for having built with me the core of my CM2Mc study.

To G. Bortoluzzi, thanks for everything you taught me on the operational science.

To B.J.W. Mills, thanks for sharing coffees, cokes, beers, and sometimes science.

To M. Couldrey, thanks for having shared 'Middle Earth' adventures at sea.

To J. Baker, thanks for the time shared at sea, in the office, in the lab, and at home.

To N. Davies, thanks for occasional dinners, TV programmes, jokes and laughs.

To G. Murphy, thanks for having explained the meaning of the 'Murphy's law.

To S. Durante, thanks for remind me the reasons why we even started.

To G. Calogero, thanks for remind me that there is a word of TV series out there.

To A. Tudino, thanks for being there and supporting me with your 'superpower'.

To B. Tudino, thanks for taught me that one could always do more.

To M. Koch, thanks for being always there for me, even if in a different nation.

To L. Giacometti, thanks for much more than a written line could ever contains.

And thanks to you that I surely forgot to mention.

Abstract

Since the advent of the industrial revolution, atmospheric CO_2 has increased from 275 ppm to over 400 ppm, enhancing the associated Greenhouse effect and being suggested as the main cause of recent climate change. The global ocean sequesters around a third of the CO_2 emitted by human activity, mitigating climate impacts, with the highest anthropogenic CO_2 (C_{ant}) storage per unit area occurring in the North Atlantic. However, ocean C_{ant} cannot be measured directly, but it is calculated with published uncertainties that range between ±10 % and ±20 %. Here, we assess five methods used to estimate C_{ant}, named ΔC^*, $\Phi C_T{}^0$, TrOCA, TTD, and eMLR, by using the outputs of four climate models (CCSM, CM2Mc, OCCAM, and GFDL-ESM2M) between 1860 and 2100, the most recent observation database (e.g. GLODAPv2) between 1980 and 2013, and the repeated time series collected along the 24.5°N Atlantic transect between 1992 and 2016. We focus on the North Atlantic upper 1000 m, where the Mode waters store the largest C_{ant} amount. In this layer, the TTD and ΔC^* estimates confine the probable range of C_{ant} concentrations, therefore we focus on these two methods. For both, we quantify a total (analytical precisions + methodological assumptions) uncertainty of ±34 %, which is higher than previously suggested. However, the C_{ant} uncertainties depend on timeframes and regions: between 1992 and 2010, observations enable us to reliably decrease these uncertainties to ±13 % (TTD) and ±14 % (ΔC^*) in the upper 1000 m of the subtropical North Atlantic (20-30°N). Here, we estimate with a quasi Monte Carlo approach that the Mode waters C_{ant} pool increases by 0.5 (TTD) and 0.8 (ΔC^*) ± 0.2 μmol kg^{-1} yr^{-1}, thus the estimates diverge over time. We associate the divergence to unsteady CO_2 disequilibrium between the atmosphere and ocean (0.3 (ΔC^*) and 0.5 (TTD) ± 0.3 μmol kg^{-1} yr^{-1}), and biogeochemical changes, as suggested by the increasing (0.3 ± 0.1 μmol kg^{-1} yr^{-1}) dissolved inorganic carbon from remineralised soft tissue: these alterations are unequally captured by the TTD and ΔC^* techniques. Changes in ocean biogeochemistry are further explored using the output of a CM2Mc pre-industrial 'control' simulation over two millennia. Here, the statistically significant drivers of the enhancement in remineralised soft-tissue carbon are increasing mean residence time ($R^2 = 0.86$) and acidification ($R^2 = 0.68$). Feedback mechanisms have the potential to shift the oceanic carbon cycle towards new equilibria, significantly influencing the future North Atlantic carbon uptake.

Contents

List of Figures

List of Tables

Declaration of Authorship

This thesis is available for Library use on the understanding that it is copyright material and that no quotation from the thesis may be published without proper acknowledgement.

I certify that all material in this thesis which is not my own work has been identified and that no material has previously been submitted and approved for the award of a degree by this or any other university.

Signed: _____

Date: _____

Abbreviations

AABW = Antarctic bottom water

AAIW = Antarctic intermediate water

Alk = alkalinity

AMOC = Atlantic meridional overturning circulation

Ca^{2+} = calcium ion

$CaCO_3$ = calcium carbonate

C_{ant} = anthropogenic carbon partition

C_{carb} = carbonate carbon partition

C_{dis} = disequilibrium carbon partition

CFC = chlorofluorocarbon

CO_2 = carbon dioxide

$CO_3{}^{2-}$ = carbonate

C_{res} = residual carbon partition

C_{sat} = saturated carbon partition

C_{soft} = soft-tissue carbon partition

C_{tot} = total carbon partition

DIC = dissolved inorganic carbon

E = eastern basin

eMLR = extended multi linear regression

FS = Florida strait

GH = greenhouse

GS = Gulf Stream

H_2CO_3 = carbonic acid

HCO_3^- = bicarbonate

lNADW = lower North Atlantic deep water

MC = Monte Carlo

ME = main effect

MEM = maximum entropy method

MLD = mixed layer depth

MMoW = Madeira mode water

MOD = model

MoW = Mode water

NAO = North Atlantic oscillation

NO_3 = nitrate

OFAT = one factor at a time

pCO_2 = carbon dioxide partial pressure

PO_4 = phosphate

RR = Redfield ratio

SF_6 = sulphur hexafluoride

$Si(OH)_4$ = silicate

SPMoW = subpolar mode water

STMoW = subtropical mode water

TE = total effect

TMM = transport matrix method

TrOCA = tracer combining oxygen, total carbon and total alkalinity

TTD = transit-time distribution

uNADW = upper North Atlantic deep water

VBSA = variance-based sensitivity analysis

W = western basin

Symbols

α = CO_2 solubility coefficient

γ = neutral density

Δ = variation between estimates

δ_t = variation over time

Θ = potential temperature

μ = average

σ = standard deviation

σ_0 = density referred to ocean surface

σ_2 = density referred to 2000 dB

σ_4 = density referred to 4000 dB

H^+ = free hydrogen ion

k = CO_2 transfer velocity

O_2 = dissolved oxygen

P = pressure

T = temperature

Thesis outline

- **Chapter 1** states the work rationale. Anthropogenic influences on the carbon cycle are explored with respect to past reconstructions, present measurements and future projections. Predictability is investigated, being of key relevance to shed light on the imminent scenarios, reducing the overall uncertainty, and thus allowing for feasible mitigations.

- **Chapter 2** summarises the methods and the models adopted in this work. Total oceanic carbon estimates are detailed within the seawater carbon system suite of programs. Anthropogenic carbon estimates are discussed exploring the caveats, challenges, and advantages of each method. Resolutions, components, and available outputs are also explored for the climate models used.

- **Chapter 3** assesses the uncertainty of the anthropogenic carbon estimates for five different methodologies. We use sensitivity analyses over twenty years of observations and model outputs.

- **Chapter 4** presents the oceanic carbon partitions, data collection, trends, and variability. Model outputs are discussed with respect to observations.

- **Chapter 5** integrates the analyses of chapter 3 within the oceanic carbon cycle (chapter 4). The results suggest unexpected mechanisms and the emerging hypotheses are tested using other observations and climate model outputs.

- **Chapter 6** provides a summary of all of the key findings and recommendations for future works.

Chapter 1

Introduction

1.1 Literature review and research aim

Since 1860, anthropogenic emissions have increased the atmospheric carbon dioxide (CO_2) to a current mean mole fraction (xCO_2) that is approximately 1.5 times higher than the pre-industrial value. This increase in atmospheric xCO_2 has caused severe environmental impacts, such as the strengthening of the CO_2 absorption of the long-wave radiations emitted by the Earth surface (Greenhouse (GH) effect). The increase in CO_2 absorption was suggested as the main driver of the recent rise in the Earth mean Temperature (T; Solomon et al. (2007)), which is named 'global warming', with the CO_2 being the most influential of the permanent GH gases (section 1.2).
To better understand the CO_2 impact on the mean temperature of the Earth and the other effects due to changes in the mole fraction of this Greenhouse gas (e.g. ocean acidification; Garcia-Ibánez et al. (2016); Guallart et al. (2015a)), researchers have enlarged fieldworks and developed climate models, therefore assessing past, present, and future responses of natural environments to different economic scenarios (IPCC, 2014; UNFCCC, 2016).
Under this perspective, ocean studies are of key relevance, as the global ocean has mitigated the GH effect by sequestering approximately a third of the total emitted CO_2 (Ciais et al., 2013; Sabine et al., 2004). We define this anthropogenic Carbon (C_{ant}) as the increase in Dissolved Inorganic Carbon (DIC) that is caused by rises in

atmospheric xCO_2 when compared to pre-industrial times and a physically driven ocean CO_2 uptake (Friis, 2006; Khatiwala et al., 2013; McNeil and Matear, 2013). However, accurate C_{ant} estimates are challenging to obtain owing to three aspects. (1) C_{ant} is a small DIC fraction. (2) The oceanic anthropogenic and natural carbon pools are involved in complex biological cycles. (3) The ocean circulation leads to a highly heterogeneous distribution of the anthropogenic carbon. These aspects propagate analytical and methodological uncertainties combinedly estimated as ±10-20 % (Matsumoto and Gruber, 2005; Vázquez-Rodríguez et al., 2009b; Waugh et al., 2006).

Vázquez-Rodríguez et al. (2009b) started the assessment of the C_{ant} uncertainty by comparing some of the most adopted methods (ΔC^*, $\Phi C_T{}^0$, and the Transit-Time Distribution (TTD)) by using the Global Ocean Data Analysis Project (GLODAP; Key et al. (2004)) data in the eastern Atlantic. Those authors found increasing divergences in the C_{ant} estimates obtained using different methods from the tropics to the poles. They recommended additional comparisons between C_{ant} estimates in observations and model outputs.

More recently, Guallart et al. (2015b) compared the C_{ant} estimates obtained with the TrOCA (Tracer combining dissolved Oxygen, Carbon, and Alkalinity), TTD, ΔC^*, and $\Phi C_T{}^0$ methods in the subtropical North Atlantic. Here, those authors focused on observations, quantifying C_{ant} increases everywhere over time, with the highest range of temporal trends estimated in the Mode water. Method agreements were found in areas of low variability, while C_{ant} differences were estimated in more dynamical areas, such as the deep western boundary current.

Enlarging the study to an Earth System Model (ESM), Matsumoto and Gruber (2005) assessed the ΔC^* technique comparing observations and outputs from the PRINCE ESM. Those authors quantified a ΔC^* C_{ant} overestimate with respect to the simulated field and an uncertainty of ±20 % at the scale of a basin. As future recommendations, Matsumoto and Gruber (2005) suggested the use of repeated datasets to quantify changes in the measured DIC, rather than extrapolate C_{ant}.

Under a similar approach, Waugh et al. (2006) assessed the TTD method use by comparing the C_{ant} obtained with this method and a synthetic field. Overall, the

first matches the second everywhere in the global ocean. The greatest differences are found in areas of highly variable CO_2 disequilibrium (e.g. Southern Ocean), where Waugh et al. (2006) highlighted discrepancies of ±20 %. As an additional assessment, the authors compared the TTD and the ΔC^* C_{ant} estimates, finding consistency at global scale, but increasing divergences with depth owing to the unique time of ventilation (age) assumed by the ΔC^* method.

Similarly, Yool et al. (2010) assessed TrOCA by comparing the C_{ant} obtained with this technique and the ΔC^* estimate within GLODAP observations and outputs of the OCCAM model (Marsh et al., 2005). Their results showed that the definition of a global TrOCA index is not an achievable goal, propagating a bias of 50 %.

Our work evolves from the results of the papers discussed above. We assess the five most-adopted C_{ant} techniques (ΔC^*, $\Phi C_T{}^0$, TrOCA, TTD, extended Multi-Linear Regression (eMLR)), comparing them as appropriated within each thesis section, and we explore the ΔC^* and TTD C_{ant} estimates in respect to the different pools of inorganic carbon using the partitioning defined by Williams and Follows (2011). Over space, we focus mostly on the subtropical North Atlantic, where an on-going monitoring of the Atlantic Meridional Overturning Circulation (AMOC) and other key oceanic properties allow us to investigate the North Atlantic circulation and the total CO_2 storage variabilities over two decades. We use the measurements collected during repeated oceanographic cruises conducted at 24.5°N, which provide data for the years 1992 (Millero et al., 2000), 1998 (Peltola et al., 2001), 2004 (Cunningham et al., 2005), and 2010 (King et al., 2012). For the first time, we add measurements collected on 2016 to this set of data (section 1.4.5 and appendix A). Over depth, we focus on the North Atlantic Mode Waters (MoW) as they store the highest C_{ant} in the North Atlantic subtropics, influencing the CO_2 uptake with percentages included between 3 % and 10 % (Bates et al., 2002). Comparative assessments are done in the Antarctic Intermediate Water (AAIW) mass that stores the highest remineralised carbon pool in the North Atlantic subtropical upper 1000 m (section 1.4.3). To extend our study over time and test the mechanisms that influence the CO_2 storage variations, we use the most recent observations from the second version of the GLODAP database (GLODAPv2;

Lauvset et al. (2016)) between 1980 and 2013, and the outputs of the CM2Mc, OCCAM, GFDL-ESM2M, and CCSM models between 1860 and 2100.

We assess the uncertainty on each C_{ant} method estimate separating analytical (e.g. nitrate measurement precision) and methodological (e.g. circulation steady state) sources (Matsumoto and Gruber, 2005; Vázquez-Rodríguez et al., 2009b; Waugh et al., 2006). These sources of C_{ant} uncertainty are studied by combining one factor at a time and variance based sensitivity analyses. We evidence that the use of a single technique is not sufficient to reliably account for C_{ant} estimates, requiring at least two methods to constrain those values in the probable concentration range. We suggest that the C_{ant} uncertainty may increase over time as different methods provide increasingly diverging estimates, such as the TTD and ΔC^* at 24.5°N in the Atlantic from 1992 to 2010. We underline that the C_{ant} uncertainty depends on locations and available datasets.

We highlight that the C_{ant} uptake is the most influential driver of ocean DIC rises, but other components of the inorganic carbon cycle (e.g. soft-tissue Carbon (C_{soft}); Williams and Follows (2011)) also affect the sequestration of the total CO_2 with percentages of influence that vary between locations and time intervals. Potential interactions between carbon components may be significant, with pre-industrial saturated Carbon (C^0_{sat}) and disequilibrium Carbon (C_{dis}) influencing the strength of the air-to-sea fluxes and C_{ant} modifying the remineralisable soft and hard tissues by changing the pH in addition to variations in the ocean circulation.

Interestingly, we evidence a significant increase in the total pool of North Atlantic subtropical C_{soft} from 1992 to 2010, which may influence the divergence between the TTD and ΔC^* C_{ant}. So, we investigate the mechanisms that could have caused it, exploring changes in meridional and barotropic stream functions, wind stress curl, mean age, Mixed Layer Depth (MLD), phosphate remineralisation, and pH.

We start our study by highlighting the importance of quantifying reliable C_{ant} and other ocean carbon pools to deepen the anthropogenic effect on the Earth climate. We present the Greenhouse effect and the ocean carbon cycle in the next sections.

1.2 The Greenhouse effect

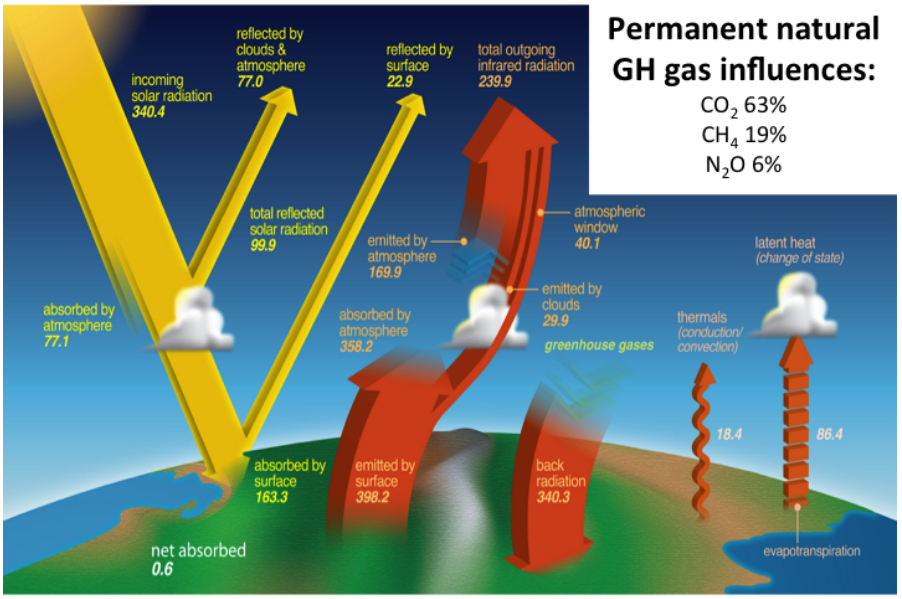

FIGURE 1.1: *Earth energy balance: fluxes averaged over ten years of observations and quantified as W m^{-2}. Shortwave and long-wave radiations are reported in yellow and red, respectively, while the Greenhouse (GH) influence is quantified as percentage at the top right corner for the carbon dioxide (CO_2), methane (CH_4), and nitrous oxide (N_2O), using the atmospheric abundances and radiative efficiencies (adapted from the NASA Earth energy budget poster, https://science-edu.larc.nasa.gov/energy_budget/).*

Earth climate changes through time. In the last 800,000 yr, eight cycles of glacial and interglacial turnover have been detected (Luthi et al., 2008). This change in the overall climate was mainly due to variations in the Earth orbit and resulting distribution of solar radiation. However, in the industrial era, an averaged global T increase, unprecedented in the ice core records, was detected, under the highly probable influence of anthropogenic activities (Field et al., 2014; Hegerl et al., 1996; Santer et al., 1996). Accompanying impacts could be significant in the Earth energy balance (Kiehl and Trenberth, 1997).

In the energetic summary of Kiehl and Trenberth (1997), on average, an incoming solar shortwave radiation of 340 W m^{-2} reaches the top of the Earth atmosphere, being here partially reflected by clouds back to the space, partially absorbed by the

atmosphere, while 186 W m^{-2} penetrates to the Earth surface, being here partially reflected and partially absorbed. The Earth itself emits long-wave radiations of which 85 % are absorbed by an ensemble of atmospheric gases (mostly water vapour and CO_2) and trapped in the lower atmosphere, originating the GH effect (Fig 1.1). The comparative influences of the GH gases depend on their radiative efficiencies and atmospheric abundances, with the CO_2 ones discussed in the next paragraph.

CO_2 relevance. Among the permanent natural GH gases (CO_2, methane (CH_4), and nitrous oxide (N_2O)), CO_2 is the most abundant, the most rapidly increasing, and hence the most important for changes to the GH effect. So, the study of its trend and accompanying anthropogenic influences are critical to our understanding of the current climate change. CO_2 rise has forced the increase in ocean inorganic carbon named C_{ant} (Friis, 2006; Khatiwala et al., 2013; McNeil and Matear, 2013).

1.2.1 Natural and anthropogenic carbon dioxide

Antarctic ice core data show that atmospheric xCO_2 oscillated between 172 ppm and 300 ppm for approximately 450.000 years (Fig 1.2a; Luthi et al. (2008)), hence characterising a steady state global carbon cycle (Sarmiento, 2000).

In this steady state, the atmospheric xCO_2 fluctuated between glacial (minimum) and interglacial (maximum) periods, in synchrony with the ocean ice volume and mean Southern Ocean T variations, suggesting a potential control by this basin on the long-term natural carbon cycle (Watson et al., 2015).

With the industrial revolution advent in the year 1860, anthropogenic activities (mainly fossil fuel burning and deforestation) have emitted a rising CO_2 amount to the atmosphere. As a result, this GH gas has increased from an averaged value of 280 ppm in 1860 to over 400 ppm currently (Fig 1.2b), with an observed mean seasonal oscillation of 5 ppm between May (maximum) and September (minimum, Fig 1.2c), quantified from the measurements collected at the observatories of the National Oceanic and Atmospheric Administration (NOAA; Dlugokencky et al. (2017)). As a consequence, the mean global temperature has also increased by approximately 1°C with potentially severe impacts on the natural environment.

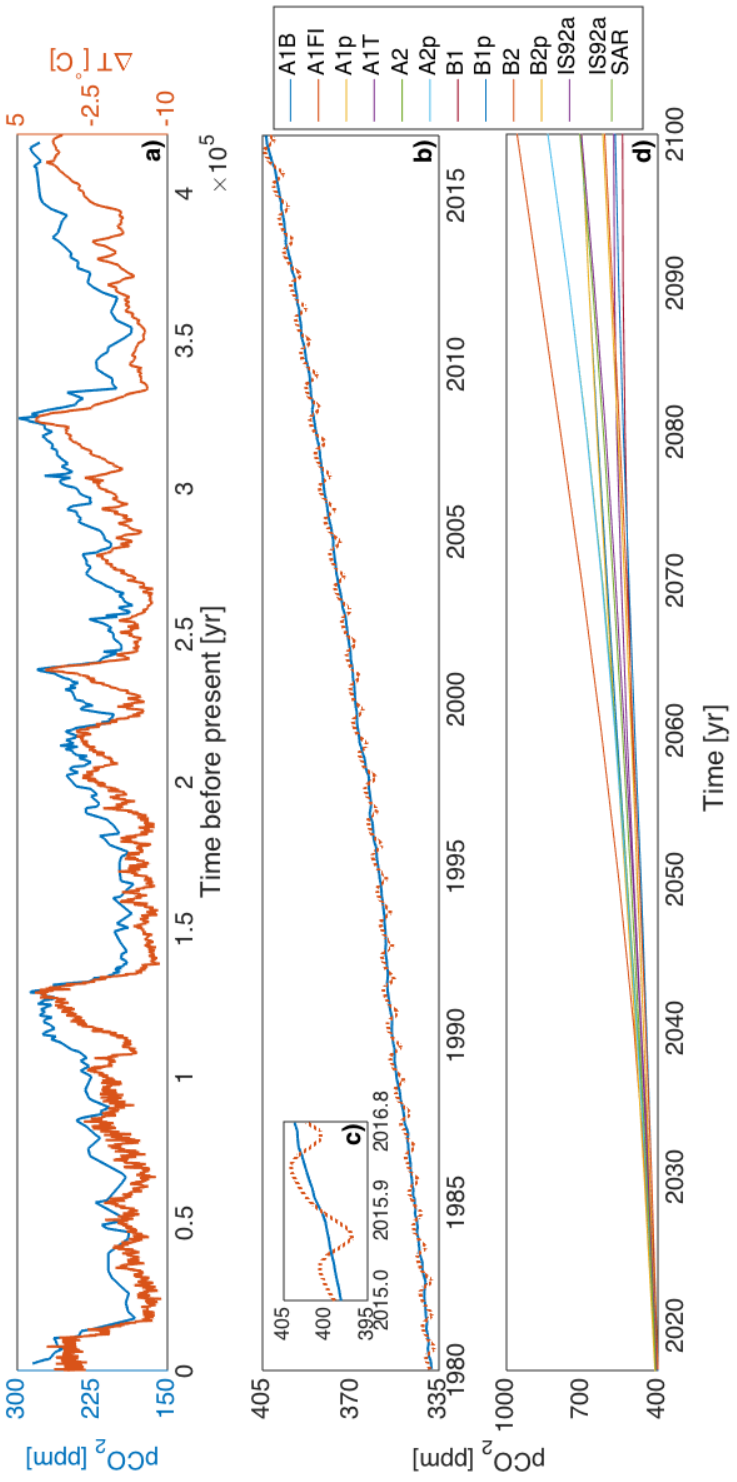

FIGURE 1.2: *a) Evolution of atmospheric Temperature variations (ΔT) and carbon dioxide (CO_2) partial pressures (pCO_2) estimated from the Antarctic ice cores. b,c) Atmospheric pCO_2 measurements (orange dots), trend (blue line), and seasonality highlighted between January 2015 (2015.0) and October 2016 (2016.8). d) Predicted atmospheric pCO_2 using several scenarios of the BERN carbon model (Barnola et al., 1987; Dlugokencky et al., 2017; Field et al., 2014; IPCC, 2014; Joos et al., 1996; Jouzel et al., 1987, 1996; NOAA, 2016; Petit et al., 1999; Siegenthaler and Joos, 1992).*

In the future (2005-2100), the most scenarios predict that the current trend of rising atmospheric CO_2 will continue due to human activities (England et al., 2015; Field et al., 2014). This rise will worsen the resulting impacts on the natural environments, but exact climate change estimates are challenging. In Fig 1.2d, future variations of atmospheric pCO_2 are plotted by using the BERN carbon model (Joos et al., 1996; Siegenthaler and Joos, 1992) under several socio-economic scenarios (Field et al., 2014). They differ with respect to the economic growth, technological developments, and so carbon emissions. All of the projections highlight an atmospheric pCO_2 rise, at various rates, leading to discrepancies of ∼400 ppm in 2100. A quantification of their reliability is of key importance: projections are studied with model ensembles under different scenarios, rather than focusing on a single case (Taylor et al., 2012).

1.2.2 Global carbon cycle

The study of the atmospheric CO_2 trend and variability needs to be combined with terrestrial, oceanic and atmospheric processes to better understand the influence of increasing CO_2 on the global carbon cycle. Fig 1.3 summarises the major fluxes and reservoirs for the anthropogenic (red) and natural (black) carbon cycles.
The atmosphere is a dilute reservoir of natural (589 PgC) and anthropogenic (240 ± 10 PgC) CO_2, exchanging them with the land and the ocean at variable scales. On land, human activities emit C_{ant} while photosynthesis and respiration by vegetation exchange the main natural carbon fraction. The largest terrestrial carbon reservoirs are soil and permafrost. In the ocean, most of the natural and anthropogenic carbon fractions are stored in the intermediate and deep layers (37 x 10^3 PgC and 155 ± 30 PgC, respectively). This CO_2 amount is 63 and 18 times higher than the atmospheric and terrestrial counterparts, leading to an expectation that in the long term the oceans will dominate CO_2 removal (Sarmiento and Gruber, 2006; Watson et al., 2015). To date, the oceanic uptake has mitigated global warming, having removed about a third of the emitted C_{ant} (Ciais et al., 2013; Sabine et al., 2004), particularly in the North Atlantic and Southern Ocean, which are key areas for the global circulation.

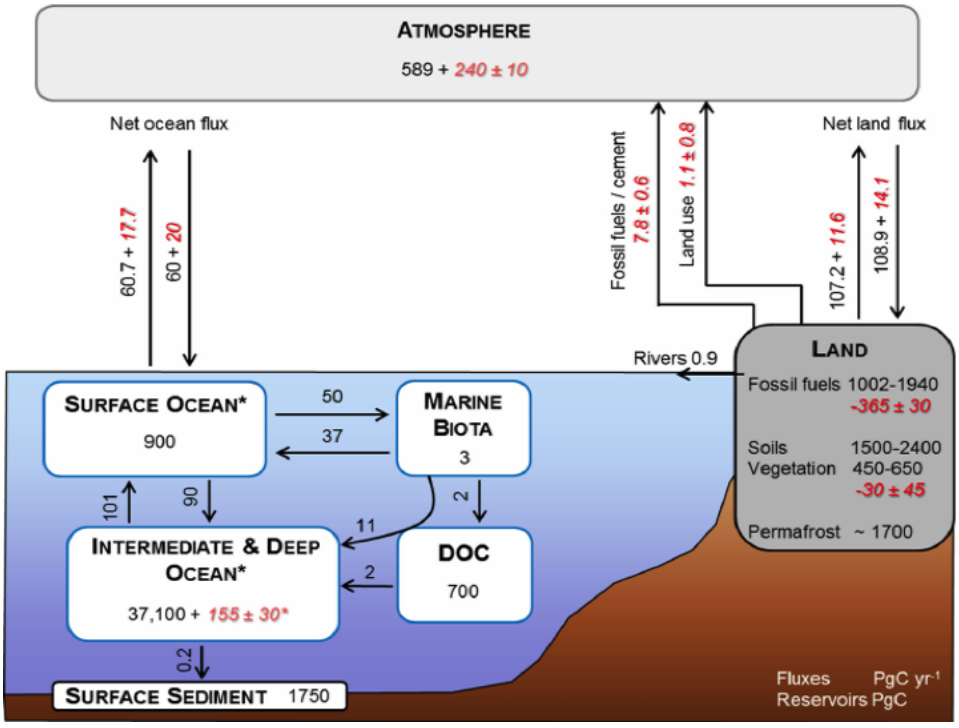

FIGURE 1.3: *Earth carbon cycle adapted from Ciais et al. (2013) and Heinze et al. (2015). Averaged fluxes (arrows) and reservoirs (boxes) are reported for the natural (black) and anthropogenic (red) components.*

1.3 Ocean carbon cycle

The ocean total CO_2 uptake is important in mitigating the current climate change rate. This uptake occurs by carbon cycle key processes: air-sea exchange, biological fixation, water upwelling and down welling, which we now briefly introduce.

Air-sea exchange. At the ocean surface, differences between the atmosphere and ocean CO_2 contents drive fluxes of this gas (Wanninkhof, 1992, 2014). These fluxes tend to equilibrate lower atmosphere and upper-ocean CO_2 concentrations, but the process is not instantaneous, requiring instead annual timescales (Jones et al., 2014). Within this timeframe, variations in the gas exchange velocity, MLD, circulation, primary production, and chemistry of the ocean modify the DIC concentration, contributing to the maintenance of a disequilibrium at the ocean surface that vary with longitude. Greatest CO_2 sequestrations are found at the poles and there is a tropical degassing (Takahashi et al., 2009). CO_2 fluxes are calculated using the gas

exchange equation (Eq 1.1).

$$FCO_2 = k\,\alpha\,\Delta pCO_2 \tag{1.1}$$

where α is the solubility coefficient, k is the transfer velocity and ΔpCO_2 is the difference between oceanic and atmospheric CO_2 partial pressures.

Excluding the Arctic Ocean and the coastal regions, a mean net flux of total CO_2 towards the ocean was recently estimated as 1.4 ± 0.5 PgC yr^{-1} (Landschützer et al., 2014), quantifying a carbon uptake between 1998 and 2011 of approximately 1 % and 0.004 % of the anthropogenic and the natural inventories respectively (Fig 1.3). However, the total CO_2 flux estimates vary when using different approaches, increasing the uncertainty (Couldrey et al., 2016; Le Quéré et al., 2000; Rödenbeck et al., 2014). On the global ocean scale, this uncertainty may be relatively small, but on a smaller area of study, such as a basin, its influence increases substantially. Furthermore, the total CO_2 net flux has varied over time, reaching 0.8 ± 0.5 PgC yr^{-1} in the 1990s and 2.0 ± 0.5 PgC yr^{-1} in the 2000s (Landschützer et al., 2016). A concurrent C_{ant} flux of 2.3 ± 0.6 PgC yr^{-1} (Khatiwala et al., 2009), estimated using observations in a comparable interval of time, suggests this partition as the main driver of the total CO_2 uptake.

Inorganic chemistry. In the global ocean, most (98 %) of the carbon exists as DIC, with a small organic fraction (2 %; Sarmiento and Gruber (2006)). The DIC can be further divided into free aqueous CO_2 (1 %), carbonic acid (H_2CO_3, 0.3 %), bicarbonate (HCO_3^-, 86.7 %), and carbonate (CO_3^{2-}, 10 %) ions (Fig 1.5), with comparative equilibria dependent on pH and T (Zeebe and Wolf-Gladrow, 2000).

The thermodynamic equilibrium constants for the dissociation of carbonic acid to bicarbonate ions, and bicarbonate to carbonate are well documented, such that determination of any two variables among the observed pH, pCO_2, DIC, and Alkalinity (Alk) is sufficient to define the concentrations of all the constituents.

Hard-tissue pump. Carbonate is precipitated by some marine organisms with the formation of calcium carbonate ($CaCO_3$) compounds (mainly calcite and aragonite (hard tissue)) that sink under the effect of ventilation and gravity. While sinking, the

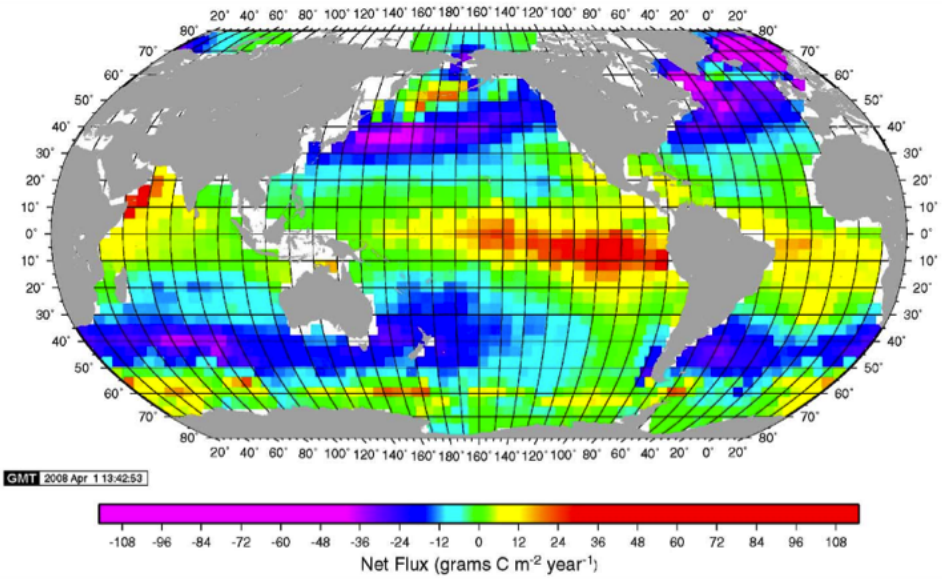

FIGURE 1.4: *Contour plot of carbon dioxide (CO_2) fluxes at the ocean surface taken from Takahashi et al. (2009). Values quantified as differences between the atmospheric and oceanic pCO_2 and averaged annually as described by Takahashi et al. (1993, 2002).*

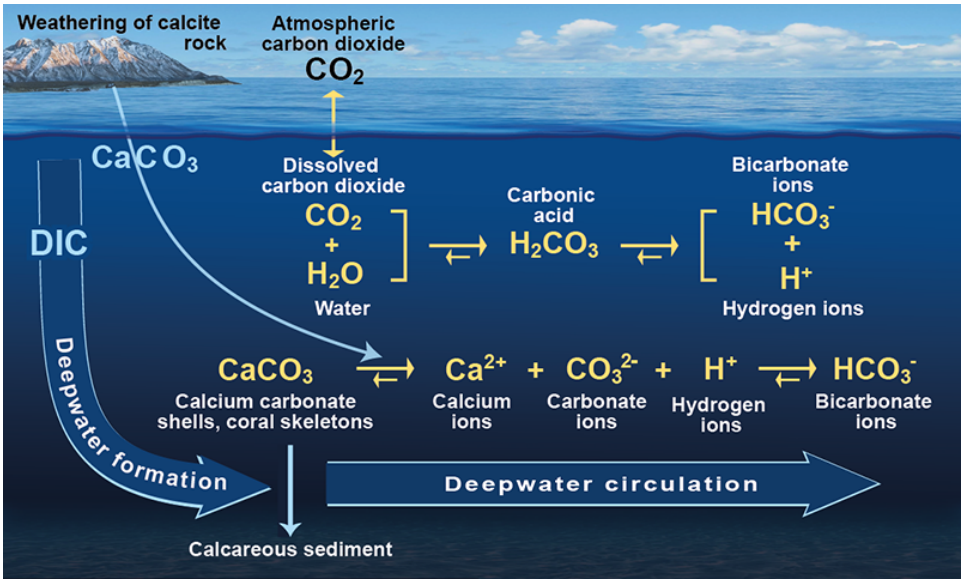

FIGURE 1.5: *Schematic representation of the air-to-sea CO_2 exchange and solubility pump. The overturning includes only the deep-water formation for simplicity. Credit: V. Byfield, www.rapid.ac.uk/abc/.*

solubility increase enhances the $CaCO_3$ dissolution, particularly below the lysocline, representing a source of DIC in the ocean interior.

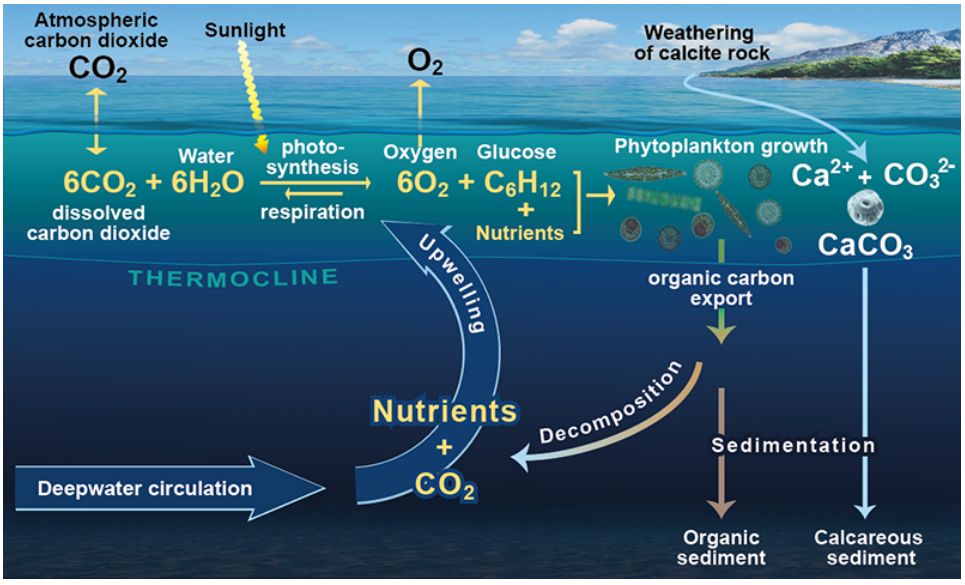

FIGURE 1.6: *Schematic representation of the ocean hard-tissue and soft-tissue pumps. Living organisms influence the ocean CO_2 uptake driving the formation of compounds that sink under the effect of gravity and ventilation, originating organic and calcareous sediments or being remineralised along the water column. Credit: V. Byfield, www.rapid.ac.uk/abc/.*

Soft-tissue pump. Living organisms influence further the oceanic carbon uptake within the so-called soft-tissue pump. This pump is separable in three sequential steps: photosynthesis, export, and remineralisation.

As with land vegetation, marine primary producers photosynthesise, taking up CO_2 from the surrounding seawater, thus reducing the ocean surface pCO_2, and so enhancing air-to-sea fluxes. These organisms fix the CO_2 with inorganic nutrients and water, forming soft tissue with dissolved oxygen (O_2) as waste product. Once fixed, the soft tissue starts sinking driven by gravity, ventilation, or living organism migrations. Approximately 2 % of these sinking materials reach the ocean bottom where they may be stored for millennia, representing a significant fraction of the global ocean organic sediments. However, the sinking compound majority (98 %) is remineralised, along the water column, by heterotrophic organisms and converted back to DIC (Fig 1.6).

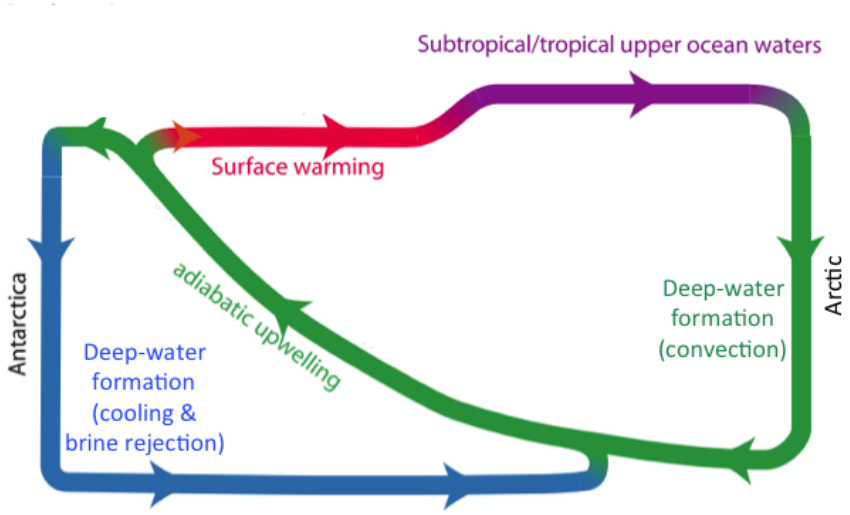

FIGURE 1.7: *Schematic of the Meridional Overturning Circulation (MOC), modified from Talley (2013). Colours indicate water mass features and processes of deep-water formations.*

Solubility pump. The carbon cycle is also influenced by a system of surface and deep currents that encircle the global ocean, linking the basins and the surface to the ocean interior, termed the Meridional Overturning Circulation (MOC).

In a simplified description (Fig 1.7), this system consists of two meridional cells, describing the Northern Atlantic deep-water convection and Southern Ocean deep-water formation (Broecker, 1991; Gordon, 1986; Talley, 2013).

Starting from the upper North Atlantic cell, warm and shallow seawater moves from the tropics northwards. On its way, this seawater exchanges with the atmosphere and mixes with the surrounding seawater, losing heat, reducing pCO_2 and taking up atmospheric CO_2 while increasing density (Takahashi et al., 2009; Talley, 2013). As a result, the seawater subducts, carrying DIC to the ocean interior where it can be stored for decades. An adiabatic upwelling that drives seawater back to the surface in the Southern Ocean closes the cell. Here, similar processes modify seawater, forming a second area of deep-water formation with comparable effects on the carbon cycle.

1.3.1 Seawater anthropogenic carbon

C_{ant} is an estimate of key relevance as it quantifies the anthropogenic footprint on the Earth climate. By definition, C_{ant} is influenced only by oceanic circulation and CO_2 disequilibrium (Friis, 2006; McNeil and Matear, 2013). These drivers confine the C_{ant} highest pools to the North Atlantic and Southern Ocean (Fig 1.8; Khatiwala et al. (2009); Sabine et al. (2004)). Accompanying estimates rely on indirect methods (based on DIC or oceanic transient tracers), as C_{ant} direct quantifications are not obtainable in the ocean (Chen and Millero, 1979; Poisson and Chen, 1987): C_{ant} is a small component of the DIC reservoir and it is influenced by complex biogeochemical cycles and ocean circulation changes, which increase the uncertainty associated to the indirect method estimates.

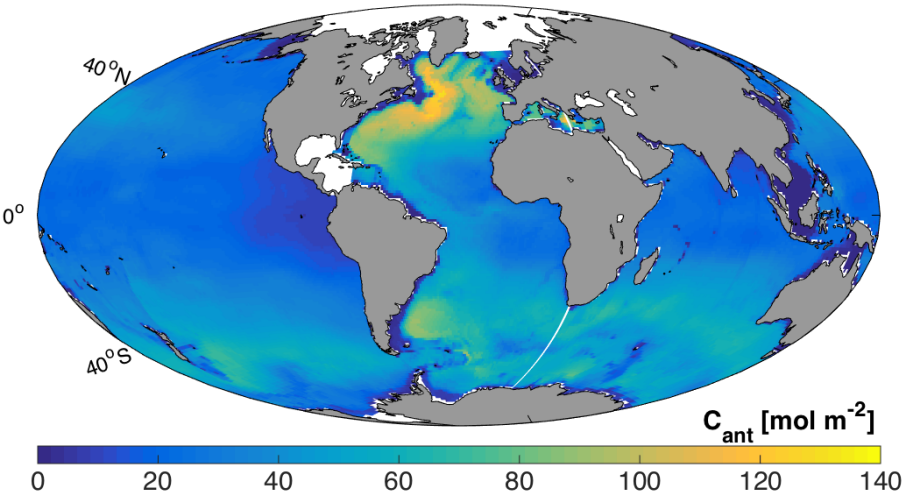

FIGURE 1.8: *Global ocean anthropogenic carbon (C_{ant}) column inventory. Data taken from the GLODAPv2 climatology (Lauvset et al., 2016), where they were estimated using the TTD method based on CFC-12 observations.*

The C_{ant} methods are based on carbon-related observations (e.g. Alk) or transient tracers, such as Chlorofluorocarbons (CFCs: trichlorofluoromethane (CFC-11), dichlorodifluoromethane (CFC-12), trichlorotrifluoroethane (CFC-113)), carbon tetrachloride (CCl_4), and sulphur hexafluoride (SF_6, Fig 1.9).

Among these indirect methods, the so-called back-calculations (ΔC^*, $\Phi C_T{}^0$, and TrOCA) estimate C_{ant} by removing from the DIC a quantification of the surface

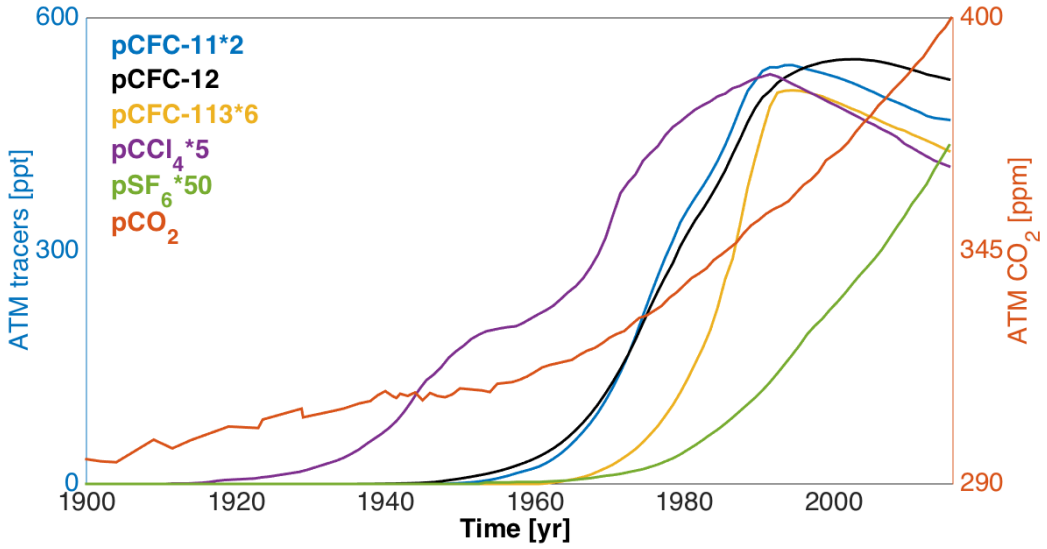

FIGURE 1.9: *Evolution over time of anthropogenic transient tracer (pCFC-11, pCFC-12, pCFC-113, $pCCl_4$, pSF_6) and carbon dioxide (pCO_2) partial pressures in the atmosphere. Data taken from the carbon dioxide information analysis centre (cdiac.ornl.gov/oceans/; Battle et al. (1996); Bullister and Wisegarver (2008)).*

disequilibrium, biological and preformed carbon fractions (Gruber et al., 1996; Touratier and Goyet, 2004; Vázquez-Rodríguez et al., 2009a). The TTD treats C_{ant} as a transient tracer, inferring it by using other anthropogenic tracers (e.g. CFCs; Hall et al. (2002); Waugh et al. (2004)). The eMLR quantifies C_{ant} changes over time as differences between regressed DICs over successive observations separated in time (Friis et al., 2005): the eMLR method can be used as an independent test for other C_{ant} techniques reliability over time (chapter 2).

The resulting C_{ant} estimates are comparable over large temporal and spatial scales, but the combined effect of method assumptions and analytical precisions leads to a nominal uncertainty range estimated between ±10 % and ±20 % (Matsumoto and Gruber, 2005; Vázquez-Rodríguez et al., 2009b; Waugh et al., 2006). Differences among C_{ant} values were assessed comparing observations and Earth System Models (ESMs), hence identifying the North Atlantic (0-65°N) and regions south of 40°S as the areas of greatest C_{ant} disagreements (Khatiwala et al., 2009). Several reasons lead to this confinement with causes and effects detailed in chapters 4 and 5.

1.4 North Atlantic basin

The work presented hereafter is based on analyses conducted in the North Atlantic: the basin is ideal to assess the C_{ant} estimates, caveats, and advantages. Here, international databases report the highest abundance of observations, the overturning circulation stores the highest C_{ant} per unit area, and there are several previous studies (Brown et al., 2010; Guallart et al., 2015b).

1.4.1 North Atlantic bathymetry

The North Atlantic extends from the equator to approximately 65°N, covering around a sixth of the global ocean surface (60 x 10^6 km^2) and a tenth of its water volume (133 x 10^6 km^3).

Clockwise, the North American, West European, and North African coasts confine the basin, while the mid Atlantic ridge dominates the bathymetry, traversing in a north-south direction the entire North Atlantic and dividing it into eastern and western sub basins (Fig 1.10). This ridge constrains the intermediate and deep circulations to its sides with the exception of natural fracture zones, such as the Charlie-Gibbs at approximately 52°N.

1.4.2 North Atlantic circulation

The North Atlantic meridional overturning circulation separates into buoyancy and wind driven circulations. The former drives subduction mainly in the Labrador Sea and Nordic Seas (Schmitz, 1996). The latter moves seawater horizontally, defining a convergent subtropical gyre between 10°N and 40°N, and a divergent subpolar gyre between 40°N and 65°N (Hakkinen and Rhines, 2004).

In the North Atlantic upper layer, seawater is transported northwards by the warm western boundary GS (Fig 1.11). In the subtropical gyre, several branches diverge from this flow, carrying seawater southwards. At the subpolar edge, the GS separates into two branches, which carry Atlantic seawater to the Nordic Seas, through the Norwegian (eastern branch) and Irminger (western branch) currents. In the Nordic

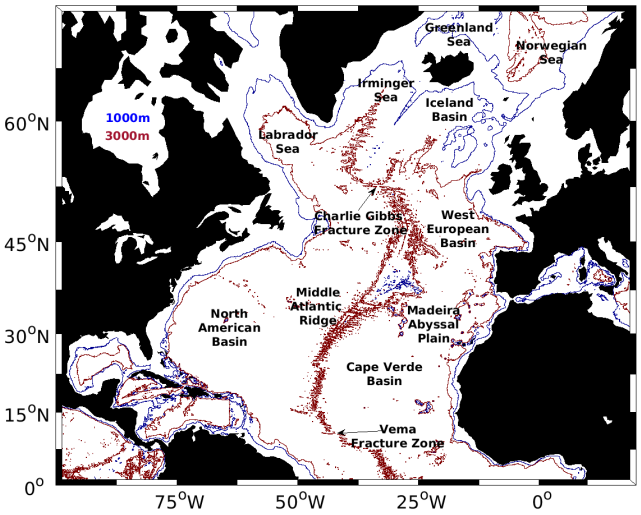

FIGURE 1.10: *North Atlantic bathymetry derived from the ETOPO1 dataset (Amante and Eakins, 2009). Major topographic features are highlighted with the reference depth contour lines at 1000 m (blue) and 3000 m (red).*

Seas, seawater subducts owing to a reduction in the buoyancy (mainly due to a decrease in T) and circulates back to the North Atlantic, originating the Denmark Strait Overflow Water, between Greenland and Iceland, and the Iceland Scotland Overflow Water, between Iceland and the UK.

These water masses circulate to the Labrador Sea, mixing here with the Labrador Sea Water of similar density, locally generated by similar processes, forming proto North Atlantic Deep Water (NADW) that flows southwards in the deep western boundary current (Schmitz and McCartney, 1993; Stanford et al., 2011). Beneath this layer, in both eastern and western basins, Antarctic Bottom Water (AABW) moves northwards (Fig 1.12).

1.4.3 North Atlantic water masses

Seawater properties (e.g. potential temperature (Θ[1])) modify after exchanges with the atmosphere or confining water parcels. Assuming these tracers are conservative in the ocean interior, one can track their paths using the T and Salinity (S) ranges

[1]The potential temperature is the hypothetical seawater temperature after an adiabatic motion of the studied parcel to a pressure of 10 dB.

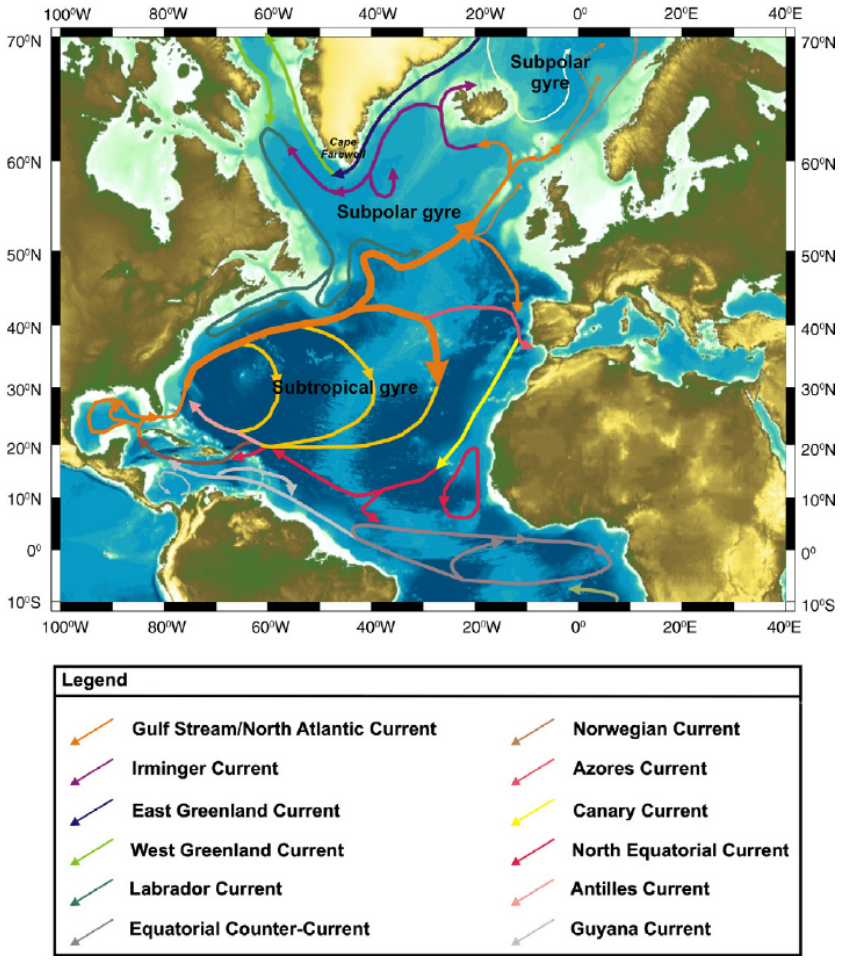

FIGURE 1.11: *Schematic representation of the North Atlantic surface circulation taken from Stanford et al. (2011). Major currents highlighted as coloured arrows.*

measured in the formation areas, characterising fixed property parcels called water masses. The main North Atlantic water masses are summarised in Tab 1.1 and represented graphically using a trans Atlantic salinity distribution in Fig 1.13. Their density intervals are calculated with the Gibbs seawater toolbox (McDougall et al., 2010) and superimposed as isopycnal contour lines.

At the surface, the MoW are water masses characterised by nearly homogenous vertical features due to the deep winter convection (Hanawa and Talley, 2001). Depending on their neutral density range (γ; Jackett and McDougall (1997)), the MoW are separated into Subtropical (ST), Madeira (M), and Subpolar (SP) MoW (Tab 1.1). The STMoW is the most recently ventilated, subducting approximately offshore of New York after heat loss. In this thesis, we identify the STMoW as the

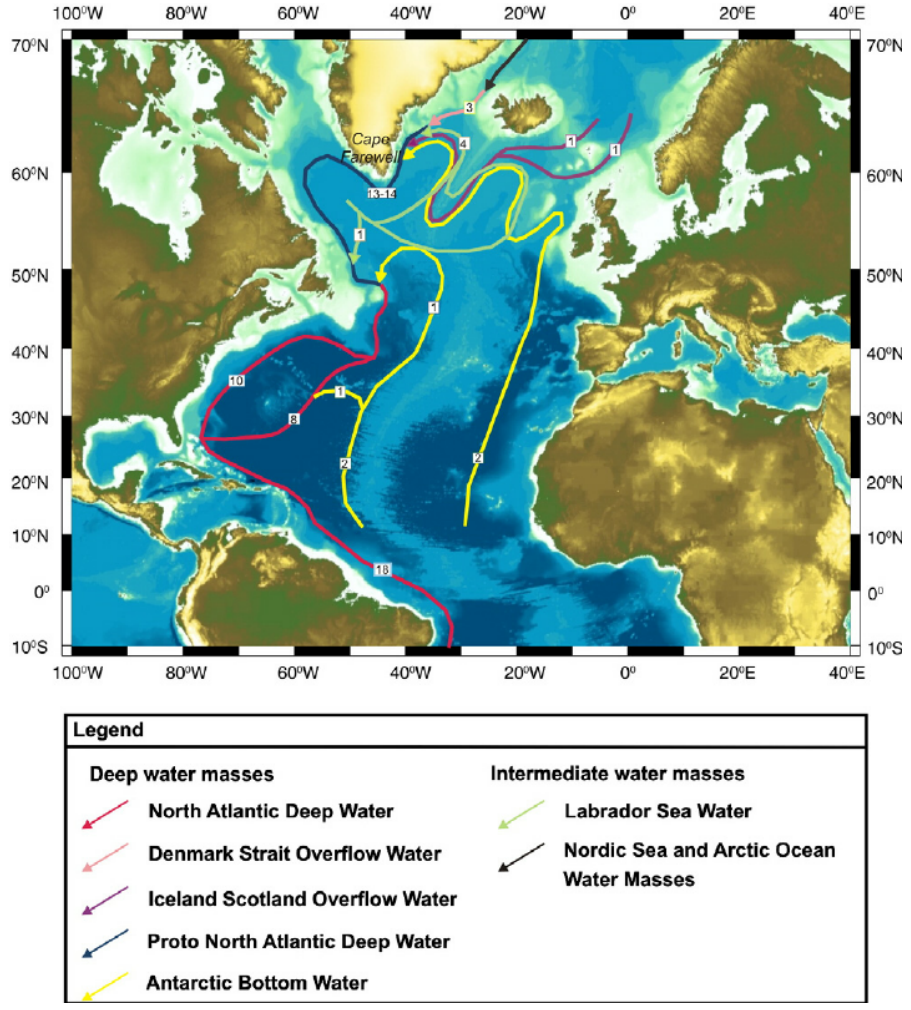

FIGURE 1.12: *Same as in Fig 1.11, but for the intermediate and deep circulations. Arrows and boxes indicate water masses and fluxes in Sverdrup (Sv = 10^6 m^3 s^{-1}).*

layer between 0 m and 200 m, thus comprising temperatures higher than 18°C, and so not identical to the commonly used definition (McCartney, 1982). Nevertheless, we refer to the ocean top layer that comprises STMoW and other surface water masses as STMoW for simplicity. The MMoW subducts in the Madeira Plain (Fig 1.10) due to changes in the MLD. The SPMoW area of formation is confined to the eastern North Atlantic at approximately 58°N. Overall, the Mode waters are of key relevance for our work as changes in their properties are considered good indicators of AMOC (Joyce et al., 2000) and North Atlantic primary production (Krémur et al., 2009) variabilities.

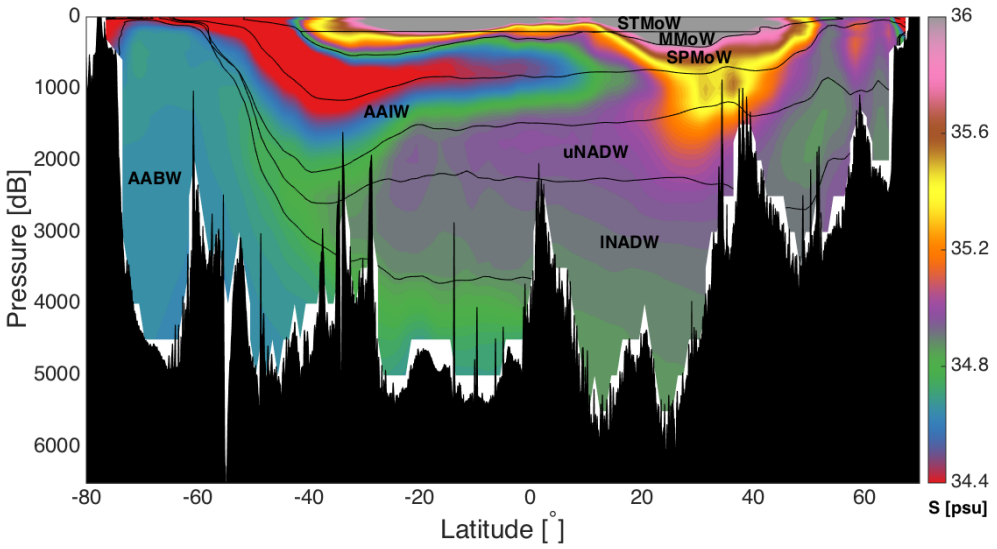

FIGURE 1.13: *Distribution of oceanic Salinity (S) at the 30.5° W Atlantic transect. Major water masses (Subtropical Mode Water (STMoW), Madeira MoW (MMoW), Subpolar MoW (SPMoW), Antarctic Intermediate Water (AAIW), upper North Atlantic Deep Water (uNADW), lower NADW (lNADW), and Antarctic Bottom Water (AABW)) are highlighted with isopycnal contours based on Tab 1.1. Data taken from the GLODAPv2 climatology (Lauvset et al., 2016).*

TABLE 1.1: *Table summarising the boundaries (potential temperature (Θ), Salinity (S), and neutral density (γ)) of the Atlantic major water masses (Guallart et al. (2015b)[1]; Rhein et al. (2015)[2]; Dickson and Brown (1994)[3]; Hanawa and Talley (2001)[4]; Emery (2001)[5]).*

Water mass	Θ [°C]	S [psu]	γ [kg m^{-3}]
STMoW[4]	18.7 to 22.0	36.5 to 36.6	< 24.1
MMoW[4]	15.0 to 18.7	36.6 to 36.7	24.1 to 26.7
SPMoW[4]	9.0 to 15.0	35.9 to 36.5	26.7 to 27.2
AAIW[1,5]	4.0 to 9.0	33.8 to 34.8	27.2 to 27.6
uNADW[1,2,3,5]	2.3 to 4.0	34.9 to 35.0	27.6 to 27.9
lNADW[1,2,3,5]	2.0 to 2.3	34.8 to 34.9	27.9 to 28.0
AABW[1,5]	-1.8 to 2.0	34.9 to 35.0	>28.0

Below the MoW, the Antarctic intermediate water originates in the Southern Ocean. From there, this water mass follows a depth-varying path, being influenced by mixing, and so reaching the North Atlantic with modified features.
At greater depth, the NADW originates in the Nordic Seas and flows southwards, modifying its features by e.g. mixing with the Mediterranean inflow at ∼38°N. The NADW is further separable into an upper (uNADW) and lower (lNADW) layers.
Finally, the AABW originates in the Southern Ocean and rapidly drops to the North Atlantic floor. From there, the AABW flows northwards, being influenced by mixing and rapidly changing its features.

1.4.4 North Atlantic subtropics

The subtropical North Atlantic is of key relevance for the monitoring of the AMOC and associated CO_2 uptake (Bryden et al., 2014; DeVries et al., 2017; Racapé et al., 2018). As a result, an hydrographical section at 24.5°N has been sampled in 1992 (Millero et al., 2000), 1998 (Peltola et al., 2001), 2004 (Cunningham et al., 2005), 2010 (King et al., 2012), and 2016 (section 1.4.5 and appendix A).
Measurements of T, S, Alk, DIC, dichlorodifluoromethane (CFC-12), O_2, inorganic nitrate (NO_3), silicate ($Si(OH)_4$), and phosphate (PO_4) were collected at a high frequency during these 24.5°N cruises, with the sulphur hexafluoride (SF_6) also measured in 2010 and 2016. The measurements averages (μ), standard deviations (σ), Precisions (Pre) and amounts (n) are summarised in Tab 1.2.
Overall, the amount of observations increases over time, allowing for more robust analyses and improving the study of inferred estimates (e.g. C_{ant}). The analytical precisions remain constant for T and S, whereas improvements are quantifiable for CFC-12, $Si(OH)_4$, NO_3, O_2, DIC, and Alk measurements. DIC and Alk for the year 2016 are not yet fully quality controlled, hence not included in this thesis.

1.4.5 North Atlantic transient tracer observations

During my doctoral project, I was involved in a trans Atlantic hydrographic cruise conducted from Nassau to Las Palmas between December 2015 and January 2016.

TABLE 1.2: *Table summarising the statistics of the measurements collected at the 24.5°N Atlantic transect. The main C_{ant}-related parameters are summarised as transect average (μ), standard deviation (σ), measurement Precision (Pre), and data amount (n). 'NA' identifies data that were not available either because they were not yet fully quality controlled (e.g. DIC) or because they were not measured during the cruise (e.g. SF_6).*

		DIC	Alk	Θ	S	O_2	NO_3	$Si(OH)_4$	PO_4	CFC-12	SF_6
unit	yr	μmol kg^{-1}	μmol kg^{-1}	°C	psu	μmol kg^{-1}	μmol kg^{-1}	μmol kg^{-1}	μmol kg^{-1}	pmol kg^{-1}	fmol kg^{-1}
μ	92	2136.4	2365.3	12.7	35.9	209.9	12.0	13.4	0.7	0.5	NA
	98	2144.4	2360.8	11.9	35.8	206.6	13.3	12.9	0.8	0.6	NA
	04	2155.6	2350.4	10.3	35.6	211.6	15.9	17.8	1.0	0.5	NA
	10	2164.6	2350.3	11.6	35.6	206.4	16.4	19.3	1.0	0.5	0.3
	16	NA	NA	10.3	35.6	211.6	15.9	17.8	1.0	0.6	0.4
σ	92	±54.9	±41.2	±8.5	±0.9	±35.7	±10.0	±15.3	±0.6	±0.5	NA
	98	±47.2	±37.8	±7.5	±0.8	±37.3	±9.1	±13.9	±0.6	±0.5	NA
	04	±47.1	±36.8	±8.6	±0.8	±40.4	±9.3	±16.2	±0.6	±0.5	NA
	10	±43.9	±35.7	±8.2	±0.8	±40.2	±9.4	±16.7	±0.6	±0.5	±0.4
	16	NA	NA	±8.6	±0.8	±40.4	±9.3	±16.2	±0.6	±0.5	±0.5
Pre	92	±3.0	±4.0	$\pm 0.1 \times 10^{-2}$	$\pm 0.1 \times 10^{-2}$	±2.2	±0.5	±0.9	±0.1	$\pm 2.4 \times 10^{-2}$	NA
	98	±2.4	±2.0	$\pm 0.1 \times 10^{-2}$	$\pm 0.1 \times 10^{-2}$	±1.9	±0.5	±0.4	$\pm 0.4 \times 10^{-1}$	$\pm 2.2 \times 10^{-2}$	NA
	04	±2.3	±1.1	$\pm 0.1 \times 10^{-2}$	$\pm 0.1 \times 10^{-2}$	±1.5	±0.4	±0.2	$\pm 0.4 \times 10^{-1}$	$\pm 1.5 \times 10^{-2}$	NA
	10	±2.1	±1.3	$\pm 0.1 \times 10^{-2}$	$\pm 0.1 \times 10^{-2}$	±1.0	±0.2	±0.3	$\pm 0.8 \times 10^{-1}$	$\pm 9.8 \times 10^{-3}$	$\pm 0.7 \times 10^{-2}$
	16	NA	NA	$\pm 0.1 \times 10^{-2}$	$\pm 0.1 \times 10^{-2}$	±1.0	±0.2	±0.2	$\pm 0.8 \times 10^{-1}$	$\pm 2.0 \times 10^{-3}$	$\pm 1.1 \times 10^{-2}$
n	92	651	601	584	584	473	588	601	588	282	NA
	98	1220	1207	1235	1231	1234	1200	1179	855	1751	NA
	04	1924	1911	3034	3034	2847	2863	2830	2860	2606	NA
	10	1305	1286	3323	2785	2779	2285	2273	2242	1860	1832
	16	NA	NA	3034	3034	2847	2863	2830	2860	2107	2041

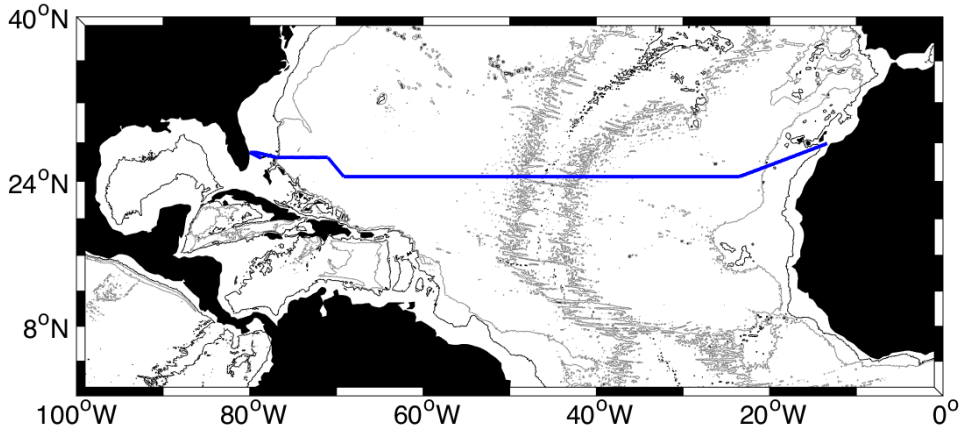

FIGURE 1.14: *Averaged route of the five cruises conducted at the 24.5°N Atlantic transect in 1992, 1998, 2004, 2010, and 2016.*

The resulting dataset is briefly presented here and assessed in appendix A.

Five transient tracers (CFC-11, CFC-12, CFC-113, CCl_4, and SF_6) were measured using a purge-and-trap gas chromatographic instrument mounted in a T-controlled container. This approach merged the Lamont Doherty Earth observatory CFC and Plymouth marine laboratory SF_6 methods (Law et al., 1994; Smethie et al., 2000). The sampling procedure resulted from the international guidelines of the Global Ocean Ship-based Hydrographic Investigations Program (GO-SHIP; Hood et al. (2010)) that identify the CFCs, CCl_4, and SF_6 as the first to be sampled from the rosette owing to high volatility and T dependency (Bullister and Tanhua, 2010). In this procedure, potential air contamination was avoided by overflowing the sample container with at least three times its volume. Then, all of the samples were stored in cool boxes, with the surface ones maintained at ambient temperature, while the deep ones were stored at a constant ∼5°C to avoid further degassing.

Prioritising the most relevant samples, the analyses were conducted within hours after the sampling. Seawater was introduced in the purge-and-trap system forcing a nitrogen pressure at the sample top, filling calibrated volumes of 27 cm^3 and 300 cm^3 for the CFCs and SF_6. The purge gas was then conveyed through perchlorate magnesium dryers to remove water vapour and, finally, captured at -100°C on a

Unibeads 3S trap for the CFCs, and at -80°C on a Porapak Q trap for the SF_6. Both traps were submerged into liquid nitrogen vapours.
The traps were then raised and the respective Ts increased to 110°C and 65°C for the CFCs and SF_6. A 2 m molecular sieve packed column and a 1 m buffer column were used to isolate SF_6, while the CFCs were treated with a 1 m Porasil B packed and a 1.5 m Carbograph AC columns. From there, the tracers were carried to two Agilent 6890N gas chromatographs with electron capture detectors for the quantifications. Calibrations were based on NOAA gaseous standards.
The final tracer precisions were estimated as ±1.1 %, ±0.7 %, ±0.9 %, ±2.6 %, and ±3.5 % for the SF_6, CFC-12, CFC-11, CFC-113, and CCl_4 surface samples. Below, we quantify ±0.011 fmol kg^{-1}, ±0.002 pmol kg^{-1}, ±0.002 pmol kg^{-1}, ±0.001 pmol kg^{-1}, and ±0.020 pmol kg^{-1} for the same tracers.

1.5 Synthesis and discussion

The CO_2 atmospheric mole fraction has increased by approximately half of its pre-industrial value since 1860. This pattern is likely to be caused by anthropogenic activities and it has strengthened the existing Greenhouse effect, being suggested as the main cause of the recent global warming (increase in the Earth temperature).
Luckily, the increase in atmospheric CO_2 has been mitigated by the global ocean, which has sequestered around a third of the mentioned increment. This sequestration however has caused the ocean pH to decrease and has altered the carbon chemistry with consequences on the dissolved inorganic carbon system. As a result, a deeper understanding of the C_{ant} cycle is essential to evaluate future responses of the natural environment to anthropogenic activities. In the next chapter, we will investigate the uncertainty on the ocean C_{ant} estimates and discuss potential influences of changes in biogenic (e.g. nitrates) or physical (e.g. temperature) factors on the estimates of this carbon partition. We will also summarise the methods used in this thesis.

Chapter 2

Methods

2.1 Introduction

In the previous chapter, we summarised the thesis general context and aims of our research, describing the relevant studies done in the literature. Here, we provide an overview of the methods used in our work. We start describing the techniques used to infer the C_{ant} in the ocean from the biogeochemical observations, anthropogenic transient tracers, and regression analyses (section 2.3). The associated uncertainty was estimated, nominally, between ±10 % and ±20 %, with comparable influences of analytical precisions and methodological assumptions (Matsumoto and Gruber, 2005; Vázquez-Rodríguez et al., 2009b; Waugh et al., 2006). However, the specific influence of each source of uncertainty is still under discussion. We investigate the caveats, advantages and errors linked to the sources of intra method uncertainty by using the time series of measurements collected at the 24.5°N Atlantic transect between 1992 and 2010 (section 1.4.4). We also present the use of climate models (CCSM, GFDL-ESM2M, CM2Mc, OCCAM, section 2.4) and statistical approaches (e.g. variance based sensitivity analysis, section 2.5) as tools for the assessment and improvement of these uncertainties, which will be applied in chapter 3.

2.2 The seawater CO_2 system calculation

The oceanic inorganic carbon constituents (H_2CO_3, HCO_3^-, CO_3^{2-}, and CO_2) can be inferred indirectly using a seawater carbon system calculation. For this purpose, we adopt the 'co2sys' suite of programs based on the observations of carbon dioxide partial pressure (pCO_2), pH, Dissolved Inorganic Carbon (DIC), and total Alkalinity (Alk; Lewis and Wallace (1998); Van Heuven et al. (2011)). Only two of these four measurements are needed to describe the speciation of inorganic carbon, with their choice left to researchers, depending on expertise and data availability. To maintain the overall quality of the measurements, Dickson et al. (2007) summarised the best practice for oceanic carbon observations, assessing respective techniques and caveats, with the accompanying uncertainties summarised hereafter. Measurements of pCO_2 are used to calculate surface CO_2 fluxes (Eq 1.1) and are influenced by Temperature (T) and Salinity (S) precisions[1] with an uncertainty of ± 2.0 μatm (approximately ± 0.7 % of the background value). The pH measures the seawater amount of free hydrogen ions (H^+), with four potential scales that propagate an overall difference of ± 0.1 pH units (± 1.3 %) when compared to the reference free scale (Brown, 2008). The DIC quantifies the sum of aqueous CO_2, H_2CO_3, HCO_3^-, and CO_3^{2-}. Sampling precision and instrumental accuracy introduce an uncertainty in this measurement of ± 1.5 μmol kg^{-1} (± 0.1 %), when considering single cruises, and ± 4.0 μmol kg^{-1} (± 0.1 %), when comparing cruises and laboratories (Dickson et al., 2007). The Alk estimates the seawater potential to counterbalance additions of H^+, maintaining the overall pH. A formal calculation in terms of seawater composition involves many ions but the major contributors are HCO_3^-, CO_3^{2-}, and $B(OH)_4^-$. Dickson et al. (2007) suggested an Alk uncertainty of ± 4.0 μmol kg^{-1} (± 0.2 %) on single cruises and ± 6.0 μmol kg^{-1} (± 0.3 %) between laboratories and cruises.

Changes in the co2sys constants and coefficients propagate uncertainty in the carbon estimates, and so stating their values is important (Millero, 1995). We use the pH

[1] Accuracy and precision are terms often confused. Accuracy quantifies the distance between the measured and theoretical values, being influenced mainly by systematic errors. Precision estimates measurement repeatability, being affected and quantifying random errors.

seawater scale, the CO_3^{2-} dissociation constants from Mehrbach et al. (1973) and refitted by Dickson and Millero (1987), and the silicate constant from Dickson (1990).

2.3 Methods to infer ocean anthropogenic carbon

The global ocean conveys around a third of the anthropogenic CO_2 (C_{ant}) to the intermediate and deep oceans, but a direct quantification of this quantity is not possible (section 1.3.1). Estimates are instead inferred using indirect methods based on biogeochemical observations, statistical analyses, and/or anthropogenic transient tracers (Chen and Millero, 1979; Gruber et al., 1996; Hall et al., 2002; Poisson and Chen, 1987; Vázquez-Rodríguez et al., 2009a; Waugh et al., 2004). Their parameters and main assumptions are summarised in Tabs 2.1 and 2.2. In these tables, we also summarise the influence of the main sources of method-specific uncertainty (e.g. ΔC^* estimate of the equilibrium carbon), with the accompanying analyses detailed in the thesis sections 2.3.1 to 2.3.3. The wider inter-method influence of the assumed ocean steady state, the constancy in the biogeochemical influence on C_{ant} and in the surface CO_2 disequilibrium over time will be discussed in chapters 3, 4, and 5.

2.3.1 The back-calculations (ΔC^*, ΦC_T^0, and TrOCA)

The back-calculations (ΔC^*, ΦC_T^0, and TrOCA) infer C_{ant} in the ocean from DIC, Alk, inorganic silicate ($Si(OH)_4$), nitrate (NO_3), phosphate (PO_4), and dissolved O_2 measurements (Gruber et al., 1996; Touratier and Goyet, 2004; Vázquez-Rodríguez et al., 2009a). These methods assume the oceanic ventilation in steady state with a 'weak' mixing influence (Khatiwala, 2009), and constancy in the surface carbon fluxes and Redfield ratios (RRs; Redfield (1934)).

ΔC^* method. ΔC^* quantifies C_{ant} (Eq 2.1) by subtracting from the measured total carbon (C_{tot} or DIC) an estimate of the carbon due to the biological activity (C_{bio}), the carbon that the ocean would have in CO_2 equilibrium with the atmosphere (C_{eq}), and the current surface disequilibrium carbon partition (C_{dis}).

$$C_{ant}^{\Delta C^\star} = C_{tot} - C_{bio} - C_{eq} - C_{dis} \tag{2.1}$$

TABLE 2.1: *Table summary of the five methodologies (ΔC^*, ΦC_T^0, TrOCA, eMLR, and TTD) used here for C_{ant} estimates.*

Name	Methodology	Main parameters	Assumptions
ΔC^*	C_{ant} estimated by correcting the measured DIC with respect to C_{bio}, C_{eq}, and C_{dis}	DIC, Alk, S, Θ, O_2, NO_3, $Si(OH)_4$, PO_4	Oceanic steady state, constant surface CO_2 disequilibrium and Redfield ratios, ventilation assumed as mostly advective.
ΦC_T^0	C_{ant} estimated as for the ΔC^*, but ventilation corrected by using an optimum multi parameter analysis (OMP[a]), upper 100 m removed.	DIC, Alk, S, Θ,O_2, NO_3, $Si(OH)_4$, PO_4	Oceanic steady state, constant surface CO_2 disequilibrium and Redfield ratios, ventilation assumed as mostly advective.
TrOCA	C_{ant} quantified as difference between two indices estimated in the sample and in a reference water mass with known C_{ant}.	DIC, Alk, Θ, O_2	Oceanic steady state, constant surface CO_2 disequilibrium and Redfield ratios, ventilation assumed as mostly advective.
eMLR	C_{ant} estimated as difference between regressed DIC over time.	DIC, Alk, S, Θ, O_2, NO_3	Natural variability included in the predictors. Correlations between DIC and predictors stable over time.
TTD	C_{ant} assumed as a transient tracer and inferred through a convolution equation that provides the age distribution.	CFC-12, SF_6, Θ, Γ, Δ[b]	Oceanic steady state, constant surface CO_2 disequilibrium, advection and mixing included in the ventilation.

[a]The OMP allows for the definition of the oceanic mixing rates using T and S observations. Each water mass is described by using an ensemble of conservative parameters, measured both at the basin inflows and at the point of interest. From these estimates, the accompanying mixing is defined as a system of linear equations, accounting for parameter changes along water mass trajectories.

[b]As it will be detailed in section 2.3.3, Γ estimates the mean ventilation time and Δ the associated spread on which we build the inverse Gaussian that approximates the Green's function in the Transit-Time Distribution (TTD) method.

TABLE 2.2: *Summary of the main sources of uncertainty that influence the oceanic C_{ant} estimates. 'Effect' refers to the direction of C_{ant} change for a unit increase in the source and a subsequent adjustment to the factor range of variation: when C_{ant} increases this is direct, when it decreases, the effect is inverse.*

Methodology	Uncertainty	Influence	Effect	Reference
ΔC^*	$RR_{N:P}$ constancy	±3 %	Inverse	This work
	$RR_{O:P}$ constancy	±6 %	Direct	This work
	Alk^{pre} estimate	±3 %	Inverse	This work
	C_{eq} estimate	±8 %	Inverse	This work
	C_{dis} constancy	±2 %	Inverse	Matsumoto and Gruber (2005)
ΦC_T^0	Φ estimate	±0.4 %	Direct	This work
TrOCA	a, b coefficients	±0.2 %	Direct	This work
	Θ precision	±0.02 %	Direct	This work
	O_2 precision	±3 %	Direct	This work
	DIC precision	±4 %	Direct	This work
	Alk precision	±2 %	Inverse	This work
eMLR	Θ precision	±0.002 %	Direct	This work
	S precision	±0.005 %	Inverse	This work
	Alk precision	±0.1 %	Inverse	This work
	NO_3 precision	±1 %	Direct	This work
	O_2 precision	±0.1 %	Inverse	This work
	regression residual	±10 %	Direct	This work
TTD	Saturation	±2 %	Inverse	This work
	Γ/Δ estimate	±20 %, $0.2 < \Gamma/\Delta < 0.8$	Inverse	Waugh et al. (2006)
	Γ/Δ estimate	±1 %, $\Gamma/\Delta < 0.2$ or > 0.8	Inverse	Waugh et al. (2006)
	C_{dis} constancy	±20 %	Inverse	Waugh et al. (2006)
	Negligible eddies	±4 %	Variable[a]	Fine et al. (2017)

[a]The influence of the ocean eddies on the TTD anthropogenic carbon estimates depends on the tracer concentration in the water masses of origin and the resulting age estimate. For instance, if a water mass mixes with a younger seawater parcel, the initial tracer concentration increases, the water mass age decreases, and the effect is direct. Conversely, the effect of the ocean eddies on the TTD anthropogenic carbon is inverse.

C_{bio} (Eq 2.2) is quantified as a function of the Apparent Oxygen Utilisation (AOU; Pytkowicz (1971)) and a preformed Alk (Alk^{pre}) estimate that we base on regression models (Eq 4.7). For its quantification, we fix the $RR_{C:P}$ as 117, the $RR_{O:P}$ as -170, and the $RR_{N:P}$ as 16 (Redfield, 1934).

$$C_{bio} = \frac{RR_{C:P}}{RR_{O:P}}(-AOU) + 0.5\left(Alk - Alk^{pre} + \frac{RR_{N:P}}{RR_{O:P}}(-AOU)\right) \quad (2.2)$$

C_{eq} (Eq 2.3) is regressed on observations of S, potential temperature (Θ), and the previously regressed Alk^{pre}.

$$C_{eq} = 2076.7 - 8.8(\Theta - 9) - 4.5(S - 35) + 0.8(Alk^{pre} - 2320) \quad (2.3)$$

C_{dis} is calculated as a function of T and S measurements in the upper 100 m of the Atlantic Ocean using GLODAP data, following the same approach of Gruber et al. (1996). Below this depth, we assume C_{dis} to be constant along isopycnal lines, hence treating it as a water mass property (Gruber et al., 1996).

ΔC* uncertainty. The uncertainty in the ΔC* C_{ant} estimates is quantifiable as $\pm$10.0 μmol kg^{-1} ($\pm$20 %), of which $\pm$5.0 μmol kg^{-1} ($\pm$10 %) is due to analytical precisions and $\pm$5.0 μmol kg^{-1} to methodological assumptions (Gruber et al., 1996; Matsumoto and Gruber, 2005). This uncertainty is due to several sources, of which some are method-specific (e.g. C_{eq} estimate) and others influence more than a C_{ant} method (e.g. assumed ocean steady state). In this section, we explore the method-specific uncertainties, focusing on the effect of the assumed constancy in C_{dis} and RRs, and the use of regression models to estimate Alk^{pre} and C_{eq}.

The assumed temporal constancy in the disequilibrium between the oceanic and atmospheric CO_2 influences the ΔC* C_{ant}. Matsumoto and Gruber (2005) assessed the influence of this assumption, quantifying an uncertainty of $\pm$1.0 μmol kg^{-1} ($\pm$2 %) on the ΔC* C_{ant} estimates in the global ocean (section 3.3).

Like the other back-calculations, the ΔC* technique assumes constancy in the RRs over space and time. This RRs assumption adds an uncertainty to the ΔC* C_{ant} that is difficult to quantify. An estimate can be obtained as difference in the ΔC* C_{ant}

estimates after varying the reference values ($RR_{N:P}$ = 16 and $RR_{O:P}$ = -170; Redfield (1934)). For this purpose, we select comparative estimates ($RR_{N:P}$ = 22 and $RR_{O:P}$ = -163) defined globally by Martiny et al. (2014) with observations over forty years of analysis (1970-2010). Using the Redfield (1934) and Martiny et al. (2014) ratios with the data collected at the 24.5°N Atlantic transect (section 1.4.4), we quantify a systematic bias in the ΔC^* C_{ant} of 1.8 μmol kg^{-1} ($\pm$3.6 %). This bias lies within the method uncertainty ($\pm$10.0 μmol kg^{-1}; Gruber et al. (1996); Matsumoto and Gruber (2005)), thus reducing the influence on the C_{ant} estimates of potential biogeochemical changes (Bates, 2001; Bates et al., 2002; Gruber et al., 2002). However, it highlights the necessity of reliable RRs for the ΔC^* C_{ant} estimates.

More generally, the influence of the assumed RRs constancy on the ΔC^* C_{ant} can be estimated by using a One Factor At a Time (OFAT) approach (Morris, 1991). Under the OFAT assumptions (e.g. absence of factor interactions), we alter the $RR_{N:P}$ and $RR_{O:P}$ by 1 unit each, using the resulting change in C_{ant} as an estimate of the RR influence (see section 2.5 for details). By doing so, we determine C_{ant} rises of 0.2 μmol kg^{-1} and 0.3 μmol kg^{-1} by increasing the $RR_{N:P}$ and $RR_{O:P}$. However, the studies of Redfield (1934) and Martiny et al. (2014) suggest that the RR variabilities exceed the unit. Instead, they lie between 15-25 ($RR_{N:P}$) and 160-170 ($RR_{O:P}$), leading to C_{ant} uncertainties of $\pm$1.5 μmol kg^{-1} ($\pm$3 %) and $\pm$3.0 μmol kg^{-1} ($\pm$6 %).

Additional sources of ΔC^* C_{ant} uncertainty are the Alk^{pre} and the C_{eq} regressions. Their reliability was originally quantified by comparing these estimates with the Alk and DIC measurements in the Atlantic upper 100 m to avoid anthropogenic influences on Alk (Gruber et al., 1996). While the Alk comparison is a standardised regression model evaluation, the estimated C_{eq} and measured DIC unavoidably differ, as the last is not in CO_2 equilibrium. Nevertheless, we follow the approach of Gruber et al. (1996), treating separately the water column upper 100 m as this layer accounts for the definition of the Alk^{pre} and C_{eq} regression models. The remaining analyses are conducted in the STMoW, MMoW, and SPMoW, as these water masses carry the highest C_{ant} amount at 24.5°N in the Atlantic (Tab 4.2; Guallart et al. (2015b)). Fig 2.1 shows a comparison between the Alk^{pre} and Alk estimated for repeated occupations of the 24.5°N Atlantic section.

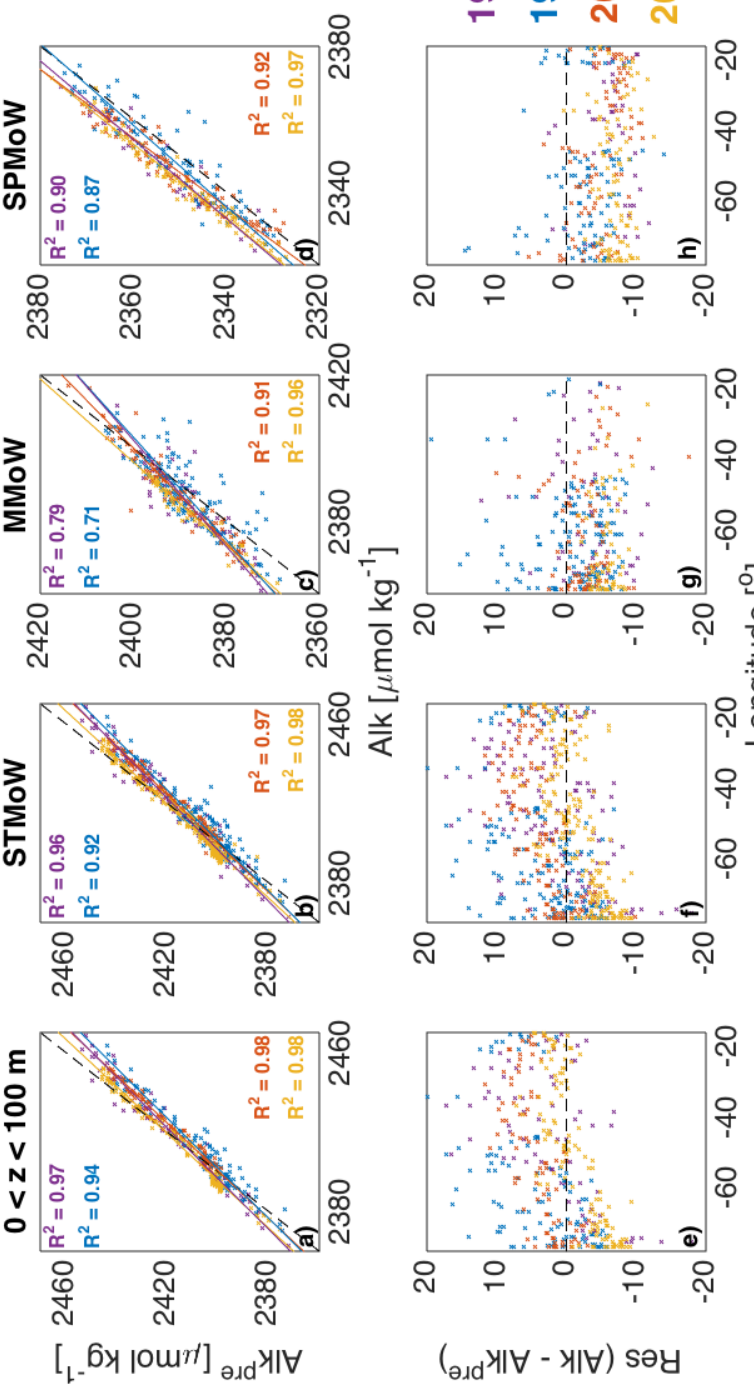

FIGURE 2.1: *Upper) Scatter plots of preformed (Alk^{pre}) versus measured Alk, with the colours indicating the years of observation and the R^2 quantifying the regression reliability. Data collected at the 24.5°N Atlantic transect in the upper 100 m (a), STMoW (b), MMoW (c), and SPMoW (d). Lower) Regression residuals ($Res = Alk - Alk^{pre}$) versus transect longitude over the same categories of water masses as for the upper graphs (e, f, g, h).*

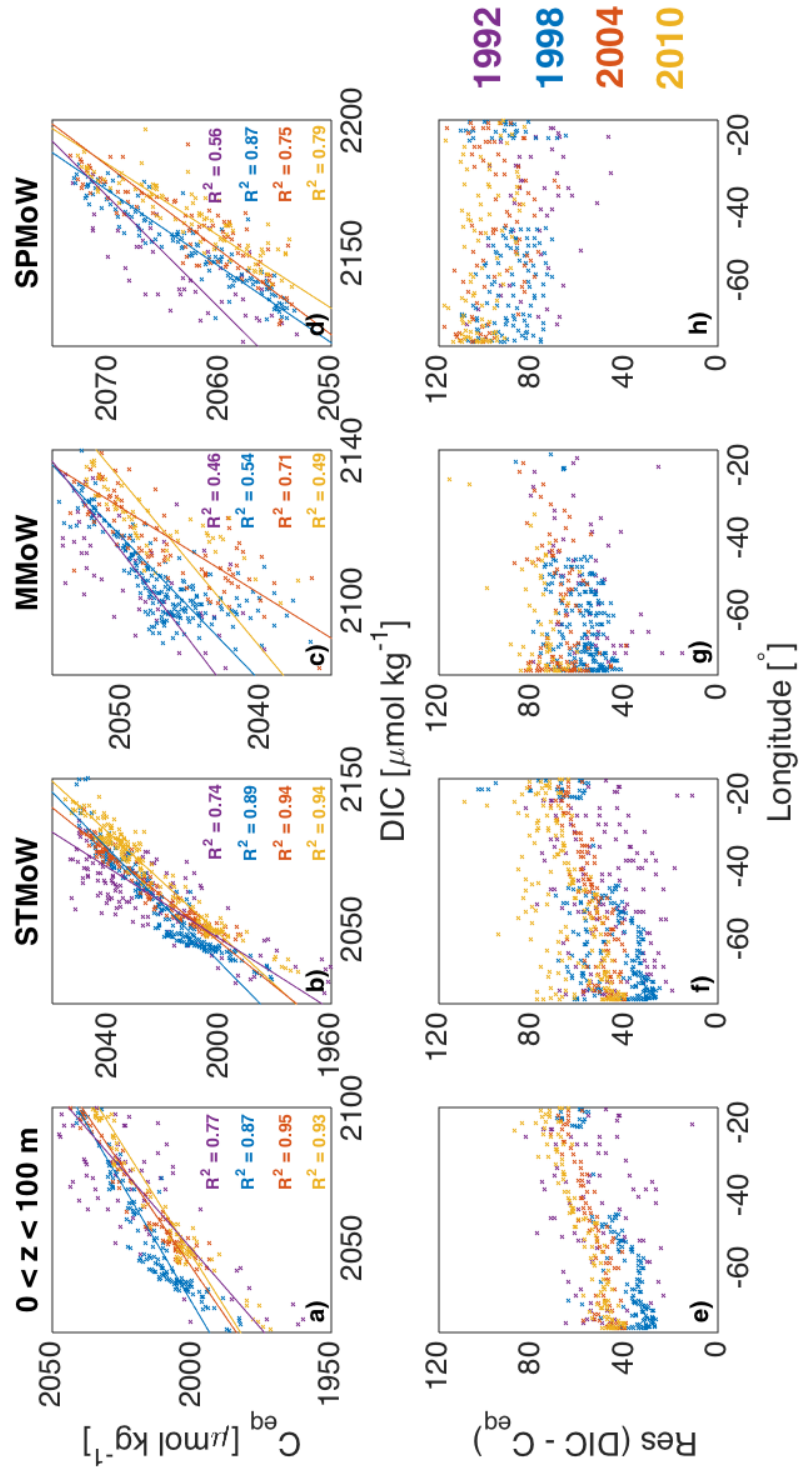

FIGURE 2.2: *Same as in Fig 2.1, but for the regressed equilibrium carbon (C_{eq}) versus the measured DIC.*

There is an overall consistency, with the greatest R^2 estimated above 100 m. Residuals lie within ± 20.0 μmol kg^{-1}, varying between an Alk^{pre} underestimate above 200 m and an overestimate below this depth.

Similarly, the reliability of the regression models used to infer the C_{eq} is assessed versus the measured DIC (Fig 2.2a-d). Residuals (Fig 2.2e-h) show variations over time (± 25.0 μmol kg^{-1}) and depth (± 40.0 μmol kg^{-1}), with the highest reliability quantified above 100 m and the strongest variation estimated in 2010, suggesting reductions over space and time in the regression model applicability.

As for the RRs, we estimate the Alk^{pre} and C_{eq} influences on the ΔC^* C_{ant} uncertainty as ± 0.2 μmol kg^{-1} and ± 1.0 μmol kg^{-1} by increasing each factor at a time by 1.0 μmol kg^{-1}. Then, we combine these influences with the associated variances quantified by using the standard error of each regression, as comparably done by Gruber et al. (1996). In the whole 24.5°N section, changes in the Alk^{pre} and C_{eq} lead to ΔC^* C_{ant} uncertainties of ± 1.3 μmol kg^{-1} (± 3 %) and ± 4.3 μmol kg^{-1} (± 8 %). The values reduce in the upper 1000 m, where the regressions are more reliable. Overall, the uncertainty due to the Alk^{pre} and C_{eq} lie within the ΔC^* nominal value of ± 20 %, but the influences vary with location and in time.

ΦC_T^0 method. The ΦC_T^0 technique (Eq 2.4) improves on the ΔC^*, introducing a correction term (Φ) that accounts for C_{dis} increases over time (Vázquez-Rodríguez et al., 2009a). This Φ term is equal to the ratio between the C_{dis} rate of variation and concentration and it is estimated in the ocean subsurface (100 - 200 m) given that the air-sea CO_2 disequilibrium is settled in the column upper layer (0-100 m). For this reason and to reduce the variability of the estimated C_{ant}, the ΦC_T^0 method removes the water column upper 100 m and uses an Optimum Multi Parameter (OMP; Tomczak (1981)) analysis to correct the ventilation in water masses with Θ lower than 5°C.

$$C_{ant}^{\Phi C_T^0} = \frac{C_{ant}^{\Delta C^\star} \left(0.03\, S \left(0.85\, \Theta + 46\right)\right)}{1 + \Phi \left|C_{dis}\right|} \tag{2.4}$$

ΦC_T^0 uncertainty. The reliability of the ΦC_T^0 C_{ant} estimates depends, mainly, on assumptions similar to the ΔC^* C_{ant}, although the ΦC_T^0 better constrains them by

using the factor Φ. Vázquez-Rodríguez et al. (2009a) assumed this term constant away from the equator, which is an upwelling region, and estimated it as 0.6 ± 0.1 by using Eq 2.5. Here, $\delta_t C_{dis}$ estimates the variation in C_{dis} over time, C_{ant}^{sat} identifies the saturated C_{ant}, a correction factor that refers to an atmospheric mole fraction (xCO_2) of 375 ppm, and C_{ant}^{DEC} is the Decomposition C_{ant} (Eq 4.13).

$$\Phi = -\frac{\delta_t C_{dis}\, C_{ant}^{sat}}{|C_{dis}|\; C_{ant}^{DEC}} \tag{2.5}$$

Following the same procedure, we estimate Φ as 0.2 ± 0.1 by using the observations collected at the 24.5°N Atlantic transect. This estimate propagates an uncertainty to the ΦC_T^0 C_{ant} values of ±0.2 μmol kg^{-1} (±0.4 %) for changes in Φ of ±0.01.

TrOCA method. The TrOCA method (Eqs 2.6-2.8) was developed by Touratier and Goyet (2004) and revisited by Touratier et al. (2007). This approach quantifies an index, named TrOCA, which combines measurements of O_2, DIC and Alk. The index value is determined in the seawater sample and, then, compared to a pre-industrial reference ($TrOCA^0$), with the difference used as the C_{ant} estimate.

$$TrOCA = O_2 \,+\, 1.3\, DIC \,-\, 0.7\, Alk \tag{2.6}$$

$$TrOCA^0 = a\, e^{\frac{-\Theta}{b}} \tag{2.7}$$

where a and b are coefficients dependent on the method used to estimate $TrOCA^0$ and propagate an uncertainty in the C_{ant} estimate of ±0.1 μmol kg^{-1} (±0.2 %).

$$C_{ant}^{TRO} = TrOCA - TrOCA^0 \tag{2.8}$$

TrOCA uncertainty. The definition of the TrOCA index evolves from the Redfield stoichiometric relationships between nutrients, carbon, and dissolved oxygen. Under the assumption that anthropogenically-driven increases in the atmospheric CO_2 have negligible effects on the ocean alkalinity and dissolved oxygen, the TrOCA index can

be considered as an approximately conservative tracer and differences from its pre-industrial value used to estimate C_{ant}. Although the assumption was disproved by Manning and Keeling (2006), one can apply the TrOCA approach and estimate the tracer pre-industrial value as a function of the potential temperature (Eq 2.7). This approach relies on the use of transient tracers, such as CFCs, to estimate the time since the water mass was last ventilated at the ocean surface and therefore to build a background of water masses with known C_{ant} where one can regress the $TrOCA^0$ function on Θ measurements. By doing so, however, we introduce additional sources of uncertainty, such that a water mass has no C_{ant} where no CFCs are detectable (see section 2.3.3 for details).

Yool et al. (2010) started the assessment of the TrOCA C_{ant}, quantifying biases of up to 50 % when comparing it with the ΔC^* estimate. As a result, we consider TrOCA only for comparison with previous studies (Guallart et al., 2015b). We explore the influence on the TrOCA C_{ant} estimates of unit changes in Θ, O_2, DIC, and Alk under the OFAT assumptions (Tab 2.2). Overall, the DIC is the most influential factor in the TrOCA technique, with the associated precision propagating an uncertainty of ± 2.1 μmol kg^{-1} (± 4 %). O_2 (± 3 %) and Alk (± 2 %) also contribute, while the Θ effect is negligible due to the high precision achieved in this measurement.

2.3.2 The extended multi linear regression technique

eMLR method. The extended Multi Linear Regression (eMLR) method quantifies temporal changes in C_{ant} ($\delta_t C_{ant}$) by regressing two DIC distributions over successive times of analyses and subtracting these regressions as in Eq 2.9. Under this approach, the predictive parameter choice is of key relevance: they need to account for the total carbon variability and their correlation with the DIC should be time independent. We use observations of Θ, S, Alk, NO_3 and O_2, as also done by Brown et al. (2010).

$$\delta_t C_{ant}^{eMLR} = (a_2 - a_1)\,\Theta + (b_2 - b_1)\,S + (c_2 - c_1)\,Alk + (d_2 - d_1)\,NO_3 + (e_2 - e_1)\,O_2 + (f_2 - f_1) \quad (2.9)$$

TABLE 2.3: *Table summarising the coefficients of the regression models used for the eMLR $\delta_t C_{ant}$ estimates (Eq 2.9).*

Year	a	b	c	d	e	f	R^2
1992	-8.144	14.610	0.461	1.739	-0.421	690.0	0.97
1998	-11.670	45.950	0.249	0.967	-0.624	163.8	0.99
2004	-11.142	41.635	0.292	0.804	-0.623	215.7	0.98
2010	-11.477	38.917	0.284	-0.001	-0.694	366.1	0.98

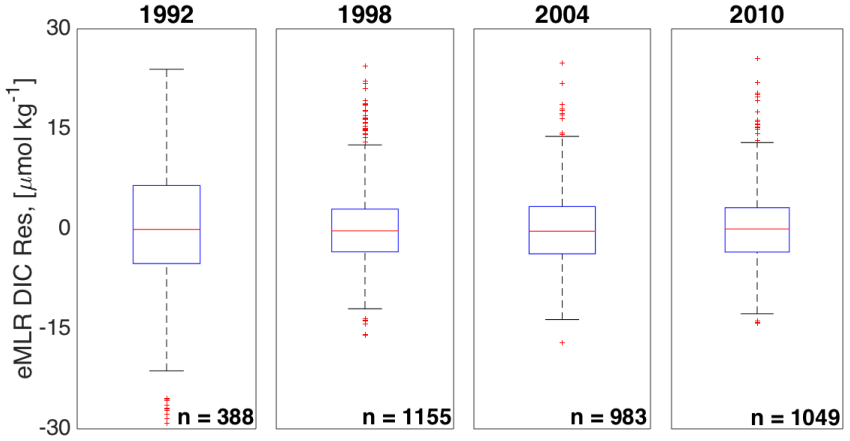

FIGURE 2.3: *Box plots of eMLR residuals (Res = DIC - DIC^{eMLR}) over the four repeats collected at the 24.5°N Atlantic transect in 1992, 1998, 2004, and 2010. Respective data amounts (n) are reported at the bottom right edge of each graph.*

where 1 and 2 denote two consequent times and coefficients a to f are shown in Tab 2.3. Residuals are predominantly (between the 25th and 75th percentiles[2]) included between ±5.0 μmol kg^{-1} (±10 % of the C_{ant} maximum), with 98 % of the outliers confined to the upper 200 m (STMoW) of the water column (Fig 2.3).

eMLR uncertainty. The eMLR $\delta_t C_{ant}$ uncertainty was estimated as ±3.0 μmol kg^{-1} by Woosley et al. (2016). This value is lower than the uncertainties on C_{ant} estimated by using other techniques (e.g. ΔC^*), being the eMLR based on a reduced number of assumptions (Friis et al., 2005).

The eMLR $\delta_t C_{ant}$ uncertainty is mostly due to the use of regression models that smooth the overall variability, introducing biases specific to the region and amount

[2]Box plots are graphical representations of normally distributed functions. All values included between the 25th and 75th percentiles are schematised as a box with a vertical line identifying the median. The remainders are reported as lateral bars, with the outliers identified by single cross.

of observations. An additional source of uncertainty occurs if there are changes in the sample locations over successive times of analysis. Therefore, statistical techniques or water mass averages are used before comparing the data. Notwithstanding that, the eMLR uncertainty increases over time, thus invalidating the use of regression models for period longer than 20 years from their definition (Goodkin et al., 2011). Nevertheless, the eMLR is an independent way of measuring $\delta_{\mathrm{t}}\mathrm{C}_{\mathrm{ant}}$ to which other techniques (e.g. ΔC*) can be compared (section 5.2).

2.3.3 The transit-time distribution technique

TTD method. The Transit-Time Distribution (TTD) technique treats $\mathrm{C}_{\mathrm{ant}}$ as an anthropogenic transient tracer (Eq 2.10; Hall et al. (2002); Waugh et al. (2004)). This method relies on some assumptions in common with the back-calculations (e.g. steady state of ocean circulation), but takes into account comparable influences of mixing and advection in the ocean ventilation by using a convolution equation based on Green's function (G, Eq 2.11; Khatiwala et al. (2009, 2013)).

$$C_{ant}^{TTD}(x,t) = \int dx^{'} \int_{1765}^{t} C_{ant}^{S}(x^{'},t^{'})\ G(x,t|x^{'},t^{'})\ dt^{'} \tag{2.10}$$

where $\mathrm{C}_{\mathrm{ant}}^{\mathrm{S}}$ quantifies the anthropogenic carbon concentration when the water mass was last in contact with the Surface, as it is outlined in step 2 below.
G allows for a probabilistic description of the path followed by a water mass from the surface (at location x' and time t') to the ocean interior (at location x and time t). In the implementation used here, which is based on the work of Waugh et al. (2004), G is approximated as an inverse Gaussian (Eq 2.11) based on the mean ventilation time (Γ) and spread (Δ). This is a solution to the one-dimensional advection-diffusion equation within which Γ and Δ quantifies the first and second temporal moments of G. Changes in these parameters modify the inverse Gaussian structure (Fig 2.4) while Γ/Δ quantifies the ratio of mixing to advection influence included. We use an initial value of one for this ratio, which identifies an identical influence of mixing and advection, and then we adjust it by comparing the TTD performance for two tracers (mostly CFC-12 and SF_6).

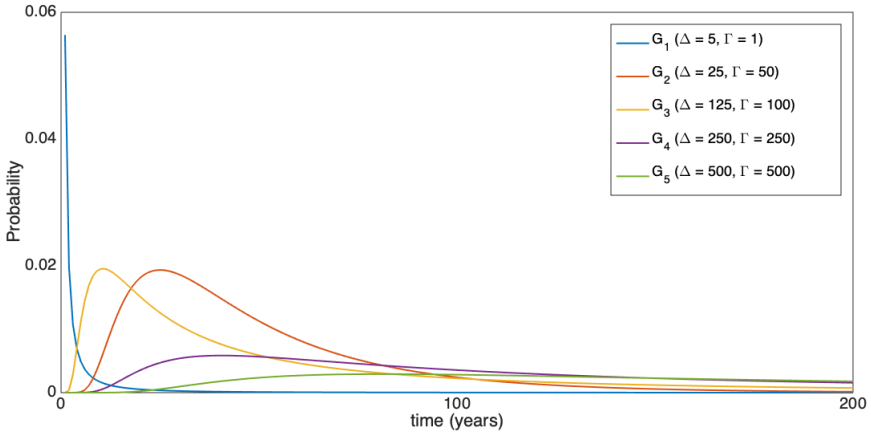

FIGURE 2.4: *Green's function (G) for different spread (Δ) and ventilation (Γ) combinations (Eq 2.11). The ratio between these parameters quantifies the fraction of mixing to advection influence included in the equation. If the ratio is set to zero, no mixing is included, whereas a ratio of one would identify a case where identical influences are attributed to mixing and advection on the ocean circulation.*

$$G(t) = \sqrt{\frac{\Gamma}{4\,\pi\,\Delta^2\,t^3}}\; e^{\frac{-\Gamma\,(t\,-\,\Gamma)^2}{4\,\Delta^2\,t}} \tag{2.11}$$

The TTD method is implemented in two steps. **In step 1**, the water mass path is traced back in time to the formation area, with the associated time interval named mean ventilation time (Γ). The estimate relies on G, measurements of atmospheric CO_2 mole fractions, and ocean surface transient tracer concentrations in the area of formation. These concentrations are not at equilibrium, but they are generally corrected estimating atmospheric to oceanic transient tracer ratios (saturations). From these values and an assumed C_{dis} constancy, it is possible to quantify the seawater pCO_2 at the moment of water mass last contact with the atmosphere, and so its anthropogenic component (pCO_{2ant}) as a difference between it and 278 ppm of pre-industrial carbon background (Eq 3.5). **In step 2**, C^S_{ant} is estimated using the co2sys suite of programs (Lewis and Wallace, 1998; Van Heuven et al., 2011) based on the pCO_2 and on another descriptor of the carbonate system (e.g. Alk), following an approach comparable to the one of section 3.3.1. The first and second TTD steps assume that (1) the transient tracer saturations and associated changes

over time are quantifiable at the ocean surface; (2) the disequilibrium between the lower atmosphere and upper-ocean CO_2 is equal to zero; (3) the ratio between Γ and Δ is known and constant over time (circulation in steady sate).

TTD uncertainty. As for other methods of C_{ant} estimates, the TTD uncertainty is quantifiable as ± 10.0 μmol kg^{-1} (± 20 %; Waugh et al. (2006)). This uncertainty is due to several sources, such as the estimate of tracer saturations, the implicit assumption of C_{ant} absence where tracers are undetectable, the use of a specific G function that is defined by a unique Γ/Δ, the time interval between the beginning of a significant increase in the CO_2 and tracer atmospheric histories, the assumed C_{dis} equal to zero, and the neglect of lateral mixing between surface water masses. The use of anthropogenic transient tracers as C_{ant} proxies assumes that these gases are exchanged at the surface of the ocean with similar processes. However, C_{ant} was released in the atmosphere around a century before the CFCs, leading to flux discrepancies generally corrected estimating tracer partial pressures in the Mixed Layer Depth (MLD) and comparing those estimates to the associated atmospheric measurements, quantifying the tracer saturations. This propagates an uncertainty on the TTD C_{ant}: based on the 24.5°N data collected in 2010, we estimate a rise of 1.0 μmol kg^{-1} (2 %) in the TTD C_{ant} after reducing the tracer saturation by 1 %. Implicitly, the TTD assumes there is no C_{ant} in water masses where no transient tracers are measurable. This assumption leads to the unrealistic conclusion that water masses older than $\sim$70 years have no C_{ant}, causing an overall underestimate of the carbon concentration. To limit the effect of this uncertainty source, different transient tracers are used in different time intervals, enlarging the period of TTD reliability. In this work, we use observations of CFC-12, between 1960 and 1990, as the associated atmospheric history linearly increases in this period (Fig 1.9). In 1989, CFC-12 was banned from production (UNEP, 2005) with a consequent decrease in the atmospheric concentration, and so an increasing unreliability in the estimate of water mass ages younger than 30 years. Since 1990, we replace CFC-12 with the SF_6 observations, as this tracer still increases in the atmosphere (Fig 1.9). CFC-11, CFC-113, and CCl_4 were also measured during our work but were not used because the first carries information analogous to CFC-12, CFC-113 is rapidly sorbed near

the surface (Roether et al., 2001), and the last degrades over time.

However, the exact definition of the limits of tracer applicability is challenging, requiring often ad-hoc analyses. To illustrate this, we discuss a study conducted at the 24.5°N transect in 2010. This analysis isolates the layer where the TTD C_{ant} estimates based on SF_6 give more reliable results from the one where the CFC-12 based counterparts are more robust. We apply the methodology defined by Tanhua et al. (2008), determining differences (ΔC_{ant}) between the CFC-12 and SF_6 based TTD C_{ant} estimates and plotting them as a neutral density (γ) function in Fig 2.5. Here, positive values indicate a higher reliability of the CFC-12 based TTD C_{ant} estimates, while negative values identify the areas where the TTD C_{ant} estimates based on the SF_6 observations are more reliable. Differences in the two tracer use are caused by their atmospheric histories, with the SF_6 being unreliable in water masses ventilated before its recent release, and CFC-12 being unreliable in water masses ventilated after the start of the inversion in its atmospheric history.

This division is statistically significant only where the ΔC_{ant} estimates are higher than the TTD analytical uncertainty (vertical dot-dashed lines in Fig 2.5). Results suggest more reliable SF_6 based TTD C_{ant} estimates in the upper MoW (uMoW, $\gamma < 26.7$ kg m^{-3}), while the CFC-12 based TTD C_{ant} estimates are more reliable below this layer. As an additional quality control, we quantify C_{ant} mean values in the uMoW (STMoW + MMoW) and SPMoW, comparing them to the estimates obtained by Guallart et al. (2015b) in Fig 2.6. Overall, all calculations agree within the TTD analytical uncertainty (± 5.0 μmol kg^{-1}), with minor differences due to the use of different saturations (see caption of Fig 2.6), statistical interpolations, and the removal of the upper 150 m in the work of Guallart et al. (2015b).

Another source of TTD uncertainty is the Γ/Δ ratio estimate necessary to define the function G. This quantifies the comparative mixing and advection influences considered in the ocean ventilation: when it is set to zero, no mixing is accounted, so resulting in a purely advective circulation (comparable to the back calculations 'weak' mixing), while greater influence of the ocean mixing is included increasing the ratio progressively. Waugh et al. (2006) compared several Γ/Δ values with the TTD C_{ant} estimates, quantifying an uncertainty of ± 10.0 μmol kg^{-1} (± 20 %) for

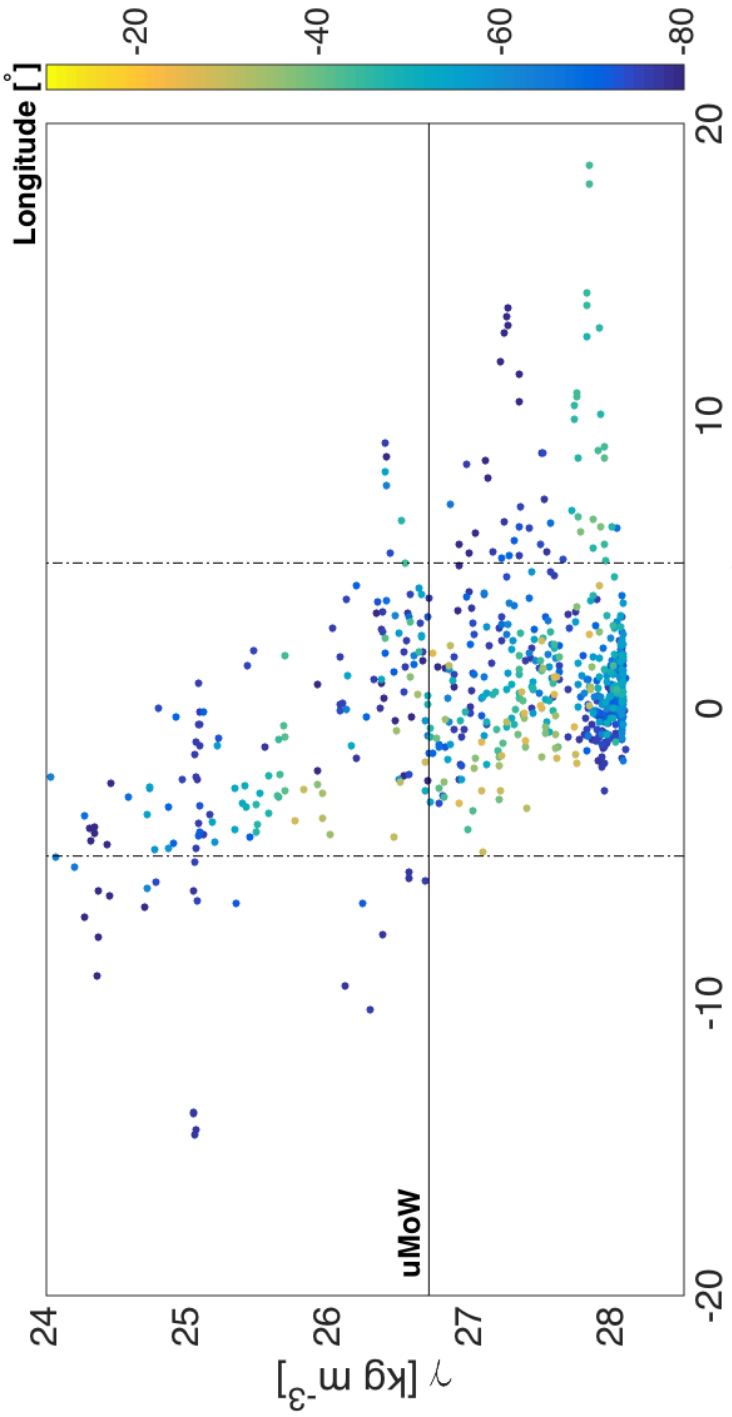

FIGURE 2.5: *Scatter plot showing anthropogenic carbon differences (ΔC_{ant}) versus neutral density (γ) at the 24.5°N Atlantic transect in 2010. Data are estimated subtracting from the CFC-12 based TTD C_{ant} the analogous based on the SF_6. The associated uncertainty (± 5 μmol kg^{-1}) is reported as vertical dot-dashed lines, with the colours indicating the transect longitude. The uMoW lower limit (26.7 kg m^{-3}) is also highlighted as a horizontal continuous line to isolate this water mass.*

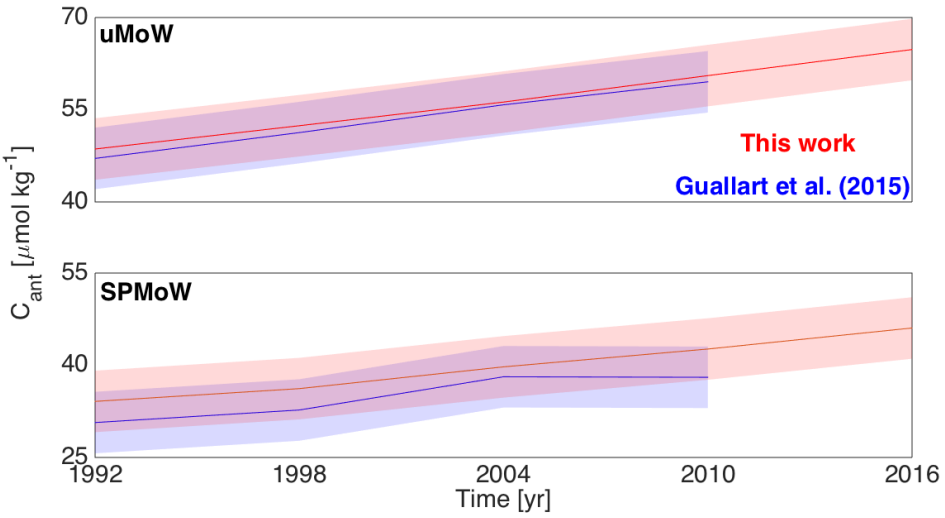

FIGURE 2.6: *Shaded error plots of TTD C_{ant} estimates versus time in the 24.5°N uMoW (STMoW + MMoW) and SPMoW. Red lines show the results obtained in this work: the CFC-12 is used in 1992, 1998, and 2004 with an increasing saturation of 80 %, 90 %, and 95 % in the uMoW and 5 % less in the SPMoW; the SF_6 is used in 2010 and 2016 with a saturation of 95 % and 100 %, respectively. Blue lines show the estimates taken from Guallart et al. (2015b) and based on the use of CFC-12 observations saturated at 100 %, with no variations over time.*

Γ/Δ variations between 0.2 and 0.8, and ± 0.5 μmol kg^{-1} (± 1 %) outside it.

Finally, the TTD C_{ant} uncertainty is influenced by ocean eddies. Changes in these seawater circular currents propagate amplified to tracer concentrations, influencing the comparison with the atmospheric history and the resulting mean age estimates. Fine et al. (2017) quantified the uncertainty due to ocean eddies comparing tracer concentrations obtained within five model simulations where the forcing are kept identical but each simulation has an independent realisation of the ocean mesoscale circulation. Those authors found an age variability of ± 4.0 yr, which translates into an uncertainty of ± 2.0 μmol kg^{-1} (± 4 %) for the TTD C_{ant} estimates.

Many of the TTD uncertainty sources can be overcome using the Maximum Entropy Method (MEM; Holzer et al. (2010)). For instance, the MEM no longer requires the tracer saturation and Γ/Δ estimates, as no oceanic surface divisions and seawater mass paths are in any way prohibited. However, we decided to avoid the MEM use in this thesis, focusing on the five most widely adopted C_{ant} techniques.

TABLE 2.4: *Table summarising the resolution and relevant outputs of the Earth system and global circulation models used in this work.*

Model	Horizontal resolution	Vertical resolution	Temporal resolution	Outputs
CM2Mc	2.5°	28 levels	1860 - 2100	DIC_i, DIC_c, DIC^{pre}, DIC_{sat}, Alk, NO_3, $Si(OH)_4$, PO_4, O_2, T, and S
GFDL-ESM2M	1°	50 levels	1860 - 2100	DIC_i, DIC_c,Alk, NO_3, $Si(OH)_4$, PO_4,CFC-11, O_2, T, and S
OCCAM	1°	66 levels	1860 - 2004	DIC, Alk, O_2, NO_3, T, S, and CFC-12
CCSM	1.4° - 3.6°	25 levels	1860 - 2012	DIC, Alk, NO_3, $Si(OH)_4$, PO_4, T, S, O_2, and CFC-12

2.4 Earth system and general circulation models

Earth System (ESM) and General Circulation (GCM) Models are useful test beds for studies over large temporal and spatial scales. Here, they are used to compare C_{ant} estimated using different methods with a reference (C_{ant}^{MOD}, Eq 2.15), which cannot be calculated from observations (sections 1.1 and 1.3.1). Additionally, they are used to enlarge the study of the DIC partitions spatial and temporal variabilities to the North Atlantic and to the industrial era (1860 - 2100). Influencing processes (e.g. changes in circulation) are studied within model pre-industrial 'control' outputs and consequences evaluated within 'control' and 'industrial' data. However, unavoidable internal drifts, components availability, spatial and temporal resolutions influence the reliability of the model outputs. So, ensembles of two or more models are used to limit the uncertainty that influences the result of each (Taylor et al., 2012).

Here, we consider four climate models: the CM2Mc, GFDL-ESM2M, OCCAM, and CCSM. Their outputs, horizontal and vertical resolutions are summarised in Tab 2.4, while their comparative reliabilities are assessed with respect to the GLODAPv2 climatology (Lauvset et al., 2016) in Figs 2.7 and 2.8.

The CM2Mc. The Climate Model 2 Model coordinate (CM2Mc) is a version of the Geophysical Fluid Dynamics Laboratory (GFDL) ESM with a lower resolution (Bernardello et al., 2014a,b). This combines the Modular Ocean Model (MOM4p1)

physics (Griffies et al., 2010), the Biology Light Iron Nutrient and Gas (BLING) biogeochemistry (Galbraith et al., 2011), the Atmospheric Model version 2 (AM2) physics (Anderson et al., 2004), the Sea Ice Simulator (SIS; Delworth et al. (2006)), and the Land Dynamics (LaD) model (Milly and Shmakin, 2002).

We use outputs of four CM2Mc configurations: 'control', 'climate', 'oceanic', and 'industrial'. In the control, atmospheric CO_2 concentration is held at pre-industrial values, guaranteeing a reference to which anthropogenic impacts may be compared. Conversely, in the other three configurations, the atmospheric CO_2 is simulated, from reanalyses, between 1860 and 2005, and modelled as for the Representative Concentration Pathway[3] 8.5 (RCP8.5; IPCC (2014); Taylor et al. (2012); van Vuuren et al. (2011)) from 2006 to 2100. In the industrial, the direct increases in ocean CO_2 uptake and indirect climate change (e.g. global warming) effects due to the atmospheric CO_2 rise are simulated, representing the most comprehensive CM2Mc simulation. In the climate run, the direct CO_2 uptake is neglected in the ocean, but indirect climate influences are maintained. The oceanic run neglects any anthropogenic CO_2 influence on the climate, but simulates the increasing oceanic carbon uptake. Each CM2Mc run includes prognostic tracers of preformed (C^{pre}) and saturated (C_{sat}) carbon fractions, preformed alkalinity (Alk^{pre}), and preformed phosphate (PO_4^{pre}). Therefore, it is possible to quantify exactly the ocean carbon partitions (Eqs 2.12 to 2.14; Bernardello et al. (2014a)), allowing for comparisons with the Williams and Follows (2011) empirical framework (section 4.2.1).

$$C_{soft}^{CM2Mc} = RR_{C:P}\,(PO_4 - PO_4^{pre}) \tag{2.12}$$

$$C_{carb}^{CM2Mc} = 0.5\,(Alk - Alk^{pre} + RR_{N:P}\,(PO_4 - PO_4^{pre})) \tag{2.13}$$

$$C_{dis}^{CM2Mc} = C^{pre} - C_{sat} \tag{2.14}$$

[3]The representative concentration pathways are four ensembles (2.6, 4.5, 6.0, and 8.5) of possible GHG emissions to the end of the 21$^{\mathrm{st}}$ century. They were use in the fifth IPCC assessment (IPCC, 2014) to constrain model projections and were named after the increase in mean radiative forcing of 2.6 W m^{-2}, 4.5 W m^{-2}, 6.0 W m^{-2}, and 8.5 W m^{-2}, respectively.

An exact C_{ant} can be also quantified as the difference between industrial (DIC_i) and climate CM2Mc DICs. However, to allow for direct comparisons with the methods described in section 2.3, we assume negligible climate change influence in the pre-industrial carbon storage. So, simulated C_{ant} estimates are calculated by subtracting the industrial and control DICs (DIC_c, Eq 2.15), as reported by Yool et al. (2010).

$$C_{ant}^{MOD} = DIC_i - DIC_c \tag{2.15}$$

A second GFDL implementation is also used in this thesis: the GFDL-ESM2M (Galbraith et al., 2011). This model differs from the CM2Mc as it has been run at a higher resolution. Furthermore, the GFDL-ESM2M does not include prognostic tracers, unlike the CM2Mc, but it simulates the CFC-11, allowing for the use of the TTD technique (section 3.5.2).

OCCAM. The Ocean Circulation and Climate Advanced Model (OCCAM) is a GCM developed from the MOM with a configuration based on four repeats of fourty-eight years each (Webb et al., 1996). Among them, the first one is used as the model spin-up, while the last three cycles are used as outputs, covering the period between 1860 and 2004 (Tab 2.4). The lack of $Si(OH)_4$ in the OCCAM outputs is compensated, in this work, by assuming a 1:1 correlation with the model NO_3. This approach is challenging in reality, as the $NO_3/Si(OH)_4$ varies with primary producer composition changes. However, a model environment is more constrained, with this ratio frequently based on fixed Redfield stoichiometric ratios. So, our approach can be applied with negligible effects. The OCCAM model has not been run under a control configuration, but it explicitly includes a pre-industrial DIC.

The CCSM. The Community Climate System Model (CCSM) was developed at the National Centre for Atmospheric Research (Graven et al., 2012). This evolves from the Los Alamos Parallel Ocean Program (POP) model (Smith et al., 2010), being forced with the Common Ocean-ice Reference Experiments Corrected Normal Year Forcing (CORE-CNYF; Large and Yeager (2004)). The CCSM is used in this work under the 'industrial' and 'control' configurations between 1860 and 2012.

Model assessment. Overall, climate models struggle to reproduce the carbonate cycle and biological carbonate precipitation, with more significant differences from observations in salinity, Alk, and DIC outputs. Also, models assume that seawater subduction occurs in a more confined and less variable ensemble of areas than it realistically happens. Depending on their resolution over space, models struggle to reproduce small-scale eddies and other physical processes, showing differences in the oceanic carbon cycle (England et al., 2015). We test the reliability of the models used in this work by comparing their Alk distributions with the GLODAPv2 climatology, at the North Atlantic surface and at the 24.5°N transect. This test is relevant for our purpose as it allows us to separate between differences in C_{ant} estimates that are due to dissimilarities between model outputs and observations and differences due to method related challenges (section 3.5).

The simulated Alk distributions at the surface of the ocean are broadly consistent with observations (Fig 2.7). In the subpolar gyre, the CM2Mc and CCSM models underestimate this variable, with the smallest differences confined to the eastern North Atlantic. The GFDL-ESM2M and OCCAM overestimate the observed Alk by roughly 50.0 μmol kg^{-1}. Nevertheless, all of the models capture consistently the Alk major patterns, such as the Labrador Sea southern edge minimum. In the subtropical gyre, the CCSM is the most consistent with the observed Alk distribution, while the other models overestimate this variable.

Comparing against the 24.5°N Atlantic transect (Fig 2.8), the CCSM model is still the most reliable: this model captures the mean Alk, but overestimates its spread. The other models overestimate the Alk mean value, with a larger spread in the water masses that originate in the Southern Ocean. Overall, all of the models capture less ventilation than it realistically happens, therefore overestimating the Alk.

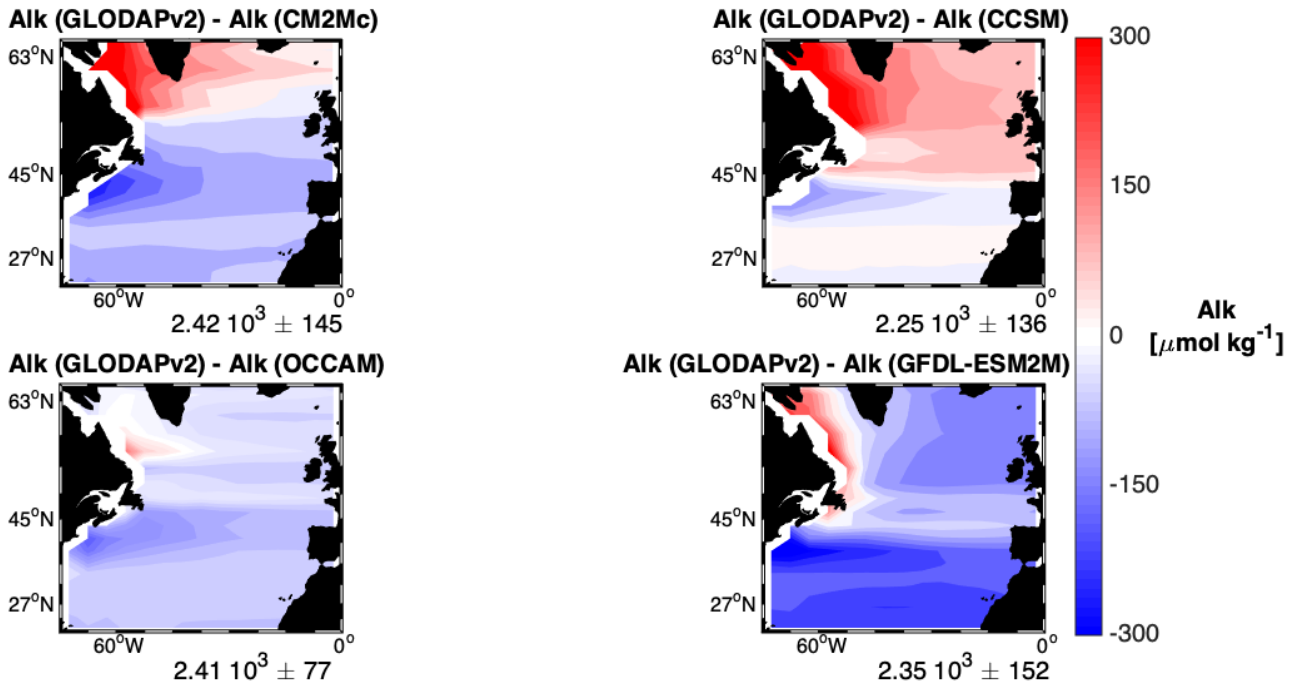

FIGURE 2.7: *Contour plots of North Atlantic surface Alkalinity (Alk) anomalies in 2002. Data taken from the Global Ocean Data Analysis Project version 2 database (GLODAPv2) climatology (Lauvset et al., 2016), CM2Mc, CCSM, OCCAM, and GFDL-ESM2M 'industrial' outputs and plotted as difference from the first for each model output. Associated Alk averages and standard deviations are reported at the lower right edge of each panel to quantify the differences.*

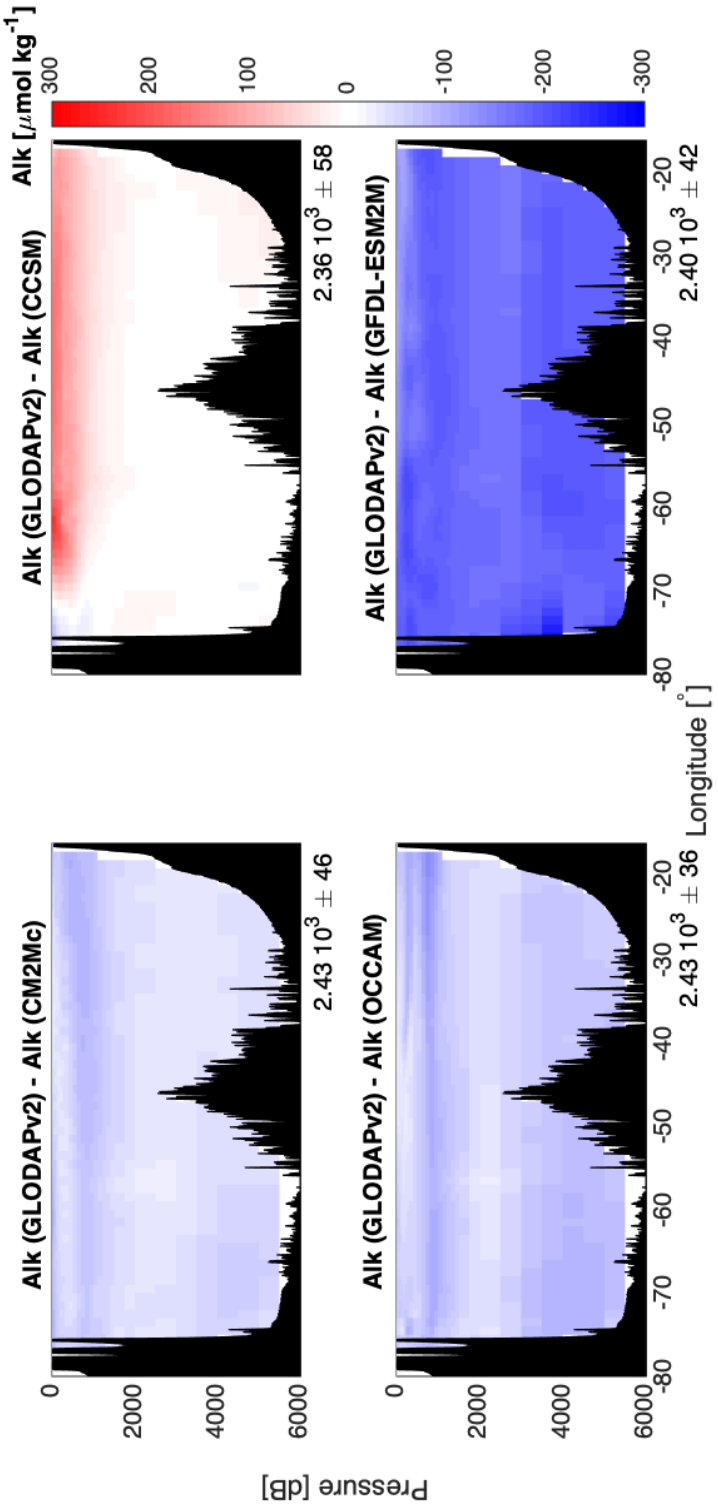

FIGURE 2.8: *Same as in Fig 2.7, but for the 24.5°N Atlantic transect.*

2.5 Sensitivity analyses

Sensitivity analysis is a well-established set of methodologies used to quantify the impacts of one or more independent or interactive factors on a variable of interest. Here, we adopt the One Factor At a Time (OFAT) and the Variance Based Sensitivity Analysis (VBSA), as described in the next paragraphs and applied in section 3.2. These approaches allow for an assessment of the comparative contributions of each factor in the analytical and methodological uncertainties of the C_{ant} estimates.

One Factor At a Time analysis (OFAT). The OFAT approach assesses the influence of independent factors when calculating a dependent variable variance (Morris, 1991). Assuming absence of interactions between factors, each of them is varied singularly by a known amount, which we term Δ, whilst keeping the others constant. Δ is then used as an estimate of the factor influence.

To better describe the OFAT approach, one can consider Eq 2.16 to be a generic equation, describing C_{ant} as a function of the input factors x_1 to x_i:

$$C_{ant} = f(x_1, x_2, x_3, ..., x_i) \tag{2.16}$$

In this equation, one factor, for instance x_1, can be varied incrementally (Δx_1), without changing x_2 to x_i, until C_{ant} varies by a given amount (e.g. ΔC_{ant}):

$$C_{ant} + \Delta C_{ant} = f(x_1 + \Delta x_1, x_2, x_3, ..., x_i) \tag{2.17}$$

We perform the OFAT approach for each factor until ΔC_{ant} exceeds ± 5.0 μmol kg^{-1} (or ± 10 %), which estimates the C_{ant} nominal uncertainty. Each factor influence (Δx_i) is then quantified by defining the Limit Value (LV_{x_i}, Eq 2.18) as the ratio of Δx_i over the measured maximum of the factor (Max_{x_i}):

$$LV_{x_i} = \frac{\Delta x_i}{Max_{x_i}} \tag{2.18}$$

We also defined the Analytical Ratio (AR_{x_i}, Eq 2.19) as the factor Precision (Pre_{x_i}) over Max_{x_i}:

$$AR_{x_i} = \frac{Pre_{x_i}}{Max_{x_i}} \tag{2.19}$$

We divided Δx_i and Pre_{x_i} by Max_{x_i} to obtain values comparable across factors: DIC observations could vary within 200 μmol kg^{-1} while T observations may vary within a maximum of 20°C. Then, we defined the Propagated Uncertainty (PrU_{x_i}) by:

$$PrU_{x_i} = \frac{a\, Pre_{x_i}}{\Delta x_i} \tag{2.20}$$

where the coefficient a depends on the analysed variation. In this study, we use 0.1 as we examine the factor influence on a 10 % change in the equation result.

Variance Based Sensitivity Analysis (VBSA). The VBSA estimates the fraction of the equation result variance due to changes in one (independent effect) or more (interactive effect) input factors (Saltelli et al., 2008; Sobol, 2001). So, the method improves on the OFAT, accounting for non-linearity and interactions.

Under the VBSA, input ensembles based on a quasi Monte Carlo approach (Kroese et al., 2014; Metropolis and Ulam, 1949) are used to quantify the ratio between the factor x and the equation result variances as an estimate of the x influence on the calculated variable. This is termed the Main Effect (ME, Eq 2.21). Similarly, one can estimate the influence of the factor x and all interactions due to it quantifying the Total Effect (TE, Eq 2.22). The fraction of variance due to Interactions (I) can be inferred as in Eq 2.24. The ME_x quantifies the equation result variance decrease when fixing the factor x, while TE_x quantifies the reduction in the same variance when fixing all factors but the studied x (Saltelli and Annoni, 2010).

In this thesis, ME and TE are calculated with the approach defined in the section 4.6 of Saltelli et al. (2008) and summarised in the next paragraphs. By doing so, we solve the VBSA equations avoiding multi dimensional integrals and reducing the computational cost from N^2 to N (k + 2), where N is the amount of quasi Monte Carlo runs ($100 < N < 100000$) and k is the number of input factors.

$$A = \begin{bmatrix} x_1^{(1)} & x_2^{(1)} & x_3^{(1)} & x_4^{(1)} & ... & x_k^{(1)} \\ x_1^{(2)} & x_2^{(2)} & x_3^{(2)} & x_4^{(2)} & ... & x_k^{(2)} \\ ... & ... & ... & ... & ... & ... \\ x_1^{(N-1)} & x_2^{(N-1)} & x_3^{(N-1)} & x_4^{(N-1)} & ... & x_k^{(N-1)} \\ x_1^{(N)} & x_2^{(N)} & x_3^{(N)} & x_4^{(N)} & ... & x_k^{(N)} \end{bmatrix}$$

As a first step, we generate a matrix M of quasi Monte Carlo random values, with dimensions 2kN. Then, we separate the matrix M into two sub-matrices A and B, each of which has dimensions kN. From A and B, we build a third matrix C_{x_k} that includes all B columns except for the A k^{th} one (e.g. k = 2).

$$B = \begin{bmatrix} x_{k+1}^{(1)} & x_{k+2}^{(1)} & x_{k+3}^{(1)} & x_{k+4}^{(1)} & ... & x_{k+k}^{(1)} \\ x_{k+1}^{(2)} & x_{k+2}^{(2)} & x_{k+3}^{(2)} & x_{k+4}^{(2)} & ... & x_{k+k}^{(2)} \\ ... & ... & ... & ... & ... & ... \\ x_{k+1}^{(N-1)} & x_{k+2}^{(N-1)} & x_{k+3}^{(N-1)} & x_{k+4}^{(N-1)} & ... & x_{k+k}^{(N-1)} \\ x_{k+1}^{(N)} & x_{k+2}^{(N)} & x_{k+3}^{(N)} & x_{k+4}^{(N)} & ... & x_{k+k}^{(N)} \end{bmatrix}$$

$$C_i = \begin{bmatrix} x_{k+1}^{(1)} & x_2^{(1)} & x_{k+3}^{(1)} & x_{k+4}^{(1)} & ... & x_{k+k}^{(1)} \\ x_{k+1}^{(2)} & x_2^{(2)} & x_{k+3}^{(2)} & x_{k+4}^{(2)} & ... & x_{k+k}^{(2)} \\ ... & ... & ... & ... & ... & ... \\ x_{k+1}^{(N-1)} & x_2^{(N-1)} & x_{k+3}^{(N-1)} & x_{k+4}^{(N-1)} & ... & x_{k+k}^{(N-1)} \\ x_{k+1}^{(N)} & x_2^{(N)} & x_{k+3}^{(N)} & x_{k+4}^{(N)} & ... & x_{k+k}^{(N)} \end{bmatrix}$$

For all of the described matrices (A, B, C_{x_k}), we determine the equation output at each row, defining three vectors of dimensions 1N, named y(A), y(B), and $y(C_{x_k})$. These vectors are used to estimate the main (ME) and total (TE) effects:

$$ME_x = \frac{\mathbf{y}_A \cdot \mathbf{y}_{C_i} - f_0^2}{\mathbf{y}_A \cdot \mathbf{y}_A - f_0^2} \tag{2.21}$$

$$TE_x = 1 - \frac{\mathbf{y}_B \cdot \mathbf{y}_{C_i} - f_0^2}{\mathbf{y}_A \cdot \mathbf{y}_A - f_0^2} \tag{2.22}$$

$$f_0 = \frac{1}{N} \sum_{i=1}^{N} y_A^{(x_i)} \tag{2.23}$$

$$I_x = TE_x - ME_x \tag{2.24}$$

where the symbol $\cdot$ indicates the scalar product between vectors.
Saltelli et al. (2008) proved the approach validity. Those authors show that if the factor resampled in the k^{th} column of C_{x_k} is influential, the equation results in y(A) or y(B) preferably multiply by it, increasing the scalar products, and so increasing the ME and TE estimates. We use the MATLAB toolbox named Sensitivity Analyses For Everybody (SAFE; Pianosi et al. (2015)) to quantify the ME and TE of the most commonly used C_{ant} techniques (section 3.2).

2.6 Synthesis and discussion

Multiple caveats limit the reliability of the C_{ant} estimates in the ocean. Within the ΔC^* and ΦC_T^0 techniques, the estimate of the ocean RRs, the regressed Alk^{pre}, the regressed C_{eq}, and the assumed C_{dis} constancy propagate an uncertainty of ±3-6 %, ±4 %, ±5 %, and ±2 %, respectively. The uncertainty of the C_{ant} estimated with the TrOCA technique is mostly influenced by the DIC, O_2, and Alk analytical precisions with respective propagated uncertainties of ±4 %, ±3 %, and ±2 %. The eMLR ΔC_{ant} uncertainty is influenced by the regression residuals (±10 %) and NO_3 precision (±1 %), while we found that the TTD C_{ant} estimates mainly depend on the transient tracer saturation reliability (±2 %), with additional influences of the Γ/Δ estimate (±20 % if $0.2 < \Gamma/\Delta < 0.8$ or ±1 % elsewhere), the assumed C_{dis} constancy (up to ±20 %), and the influence of ocean eddies on the tracer concentrations (±4 %). These method-specific uncertainties will be further assessed in chapter 3, combining them with additional sources of C_{ant} variability shared between two or more methods. We will use observations and outputs of GCMs and ESMs, carefully quantifying the associated degrees of reliability. Several statistical approaches will be used, such as the VBSA, highlighting key parameters and specific criticalities.

Chapter 3

Sensitivity analyses of anthropogenic carbon estimates

3.1 Introduction

Oceanic C_{ant} is inferred indirectly with an uncertainty assessed nominally as 10-20 %. In chapter 2, we discussed the method-specific sources of this uncertainty. Here, we analyse influences of analytical precisions and method underlying assumptions by using the repeated measurements (1992-2010) collected at the 24.5°N Atlantic transect and by applying two statistical techniques, the One Factor At a Time and the Variance Based Sensitivity Analyses (section 3.2). Factors impacting on C_{ant} are identified and associated independent and interactive influences are estimated as fractions of variances. Method assumptions are explored for the ΔC^*, TrOCA, ΦC_T^0, and TTD C_{ant} estimates. We use the measurements of the atmospheric CO_2 mole fraction collected at the Mauna Loa observatory to investigate the assumed constancy in the disequilibrium carbon partition (section 3.3). All of the results are combined in the study of section 3.4. Here, we also quantify the effects propagated on to derived variables, such as the natural and anthropogenic pH partitions. Finally, the C_{ant} estimates accuracy is evaluated with three climate models (GFDL-ESM2M, OCCAM, CCSM), where the difference between the industrial and control DICs is assumed to be the 'true' C_{ant} to which other estimates are assessed (section 3.5).

3.2 C_{ant} uncertainty from analytical precisions

The uncertainty on the C_{ant} estimates is influenced by the analytical precision of the measurements used to infer them, with values dependent on the chosen data, location, time interval, and technique, and included within ± 5.0 μmol kg^{-1} (± 10 %), as Matsumoto and Gruber (2005) and Vázquez-Rodríguez et al. (2009b) suggested. Associated assessments were done for single techniques (e.g. TTD; Waugh et al. (2006)), using synthetic data (Matsumoto and Gruber, 2005), or in confined areas of the global ocean (e.g. eastern Atlantic; Vázquez-Rodríguez et al. (2009b)).
We present a more comprehensive study, considering the nominal uncertainty due to analytical precisions of ± 5.0 μmol kg^{-1} for each technique and assessing its influence on the ΔC^*, $\Phi C_T{}^0$, TrOCA, and TTD C_{ant} estimates at the 24.5°N section in 1992, 1998, 2004, and 2010. The eMLR is not used as it quantifies C_{ant} variations in time. We isolate the water column upper 200 m (Subtropical Mode Water (STMoW)) and two additional Mode Waters (MoW), currently carrying the highest amount of North Atlantic subtropical C_{ant}: the Madeira (M) and Subpolar (SP) MoW (Fig 1.13). In the STMoW, the $\Phi C_T{}^0$ C_{ant} estimates must be taken with care, as this technique removes the upper 100 m by definition (section 2.3.1; Vázquez-Rodríguez et al. (2009a)), hence accounting for half of the water mass volume. Nevertheless, we include it in the uncertainty assessment for completeness. Then, we assess the C_{ant} analytical uncertainty using the One Factor At a Time (OFAT; Morris (1991)) and Variance Based Sensitivity Analysis (VBSA; Saltelli et al. (2008); Sobol (2001)) approaches. The first methodology estimates each factor influence and its range of variability that leads to a C_{ant} variation included within ± 5.0 μmol kg^{-1}. The VBSA approach improves on the OFAT results, estimating potential interactions between factors. We base the OFAT on 282, 855, 1911, and 1286 data points for the 1992, 1998, 2004, and 2010 datasets, respectively, as these amounts represent the greatest availability of reliable observations (Tab 1.2). The VBSA is applied on ensembles of quasi Monte Carlo (MC; Kroese et al. (2014); Metropolis and Ulam (1949)) inputs generated within the measurement ranges and, then, uncertainties (Tab 1.2).

3.2.1 C_{ant} sensitivity to analytical precisions (OFAT)

Using OFAT (section 2.5), we separately quantify the influence of each factor on the ΔC^*, $\Phi C_T{}^0$, TrOCA, and TTD C_{ant} analytical uncertainties, hence treating these influences as independent from each other. For the TTD, we explore the uncertainty due to the CFC-12 precision, but we avoid the study of the SF_6 owing to the absence of measurements before 2010.

Under the OFAT assumptions (section 2.5), we increase each factor incrementally keeping all others constant, then calculating the C_{ant} variations from the unchanged value. We stop the analysis when the C_{ant} changes exceed ± 5.0 μmol kg^{-1} (nominal uncertainty), and determine the Limit Value (LV, Eq 2.18), Analytical Ratio (AR, Eq 2.19), and Propagated Uncertainty (PrU, Eq 2.20). The results are shown in Fig 3.1 where we use a y-logarithmic scale, which aids the interpretation, after increase each percentage by one to avoid quick changes.

The back-calculations (ΔC^*, $\Phi C_T{}^0$, and TrOCA) analytical uncertainty depends on the Dissolved Inorganic Carbon (DIC) and total Alkalinity (Alk) measurement precisions, since the variations in these factor LVs and ARs are comparable (Fig 3.1). Comparing the DIC and Alk precisions (Tab 1.2) with the estimated PrUs, we quantify values of ± 5.0 μmol kg^{-1} (± 2.3 % of the background concentration) and ± 10.0 μmol kg^{-1} (± 4.3 % of the background concentration), for DIC and Alk measurements, necessary to maintain the ΔC^* C_{ant} analytical uncertainty within ± 5.0 μmol kg^{-1}. Comparative precisions are ± 5.1 μmol kg^{-1} (DIC) and ± 7.8 μmol kg^{-1} (Alk) to obtain the same result for TrOCA, and ± 7.5 μmol kg^{-1} (DIC) and ± 13.2 μmol kg^{-1} (Alk) for $\Phi C_T{}^0$. Therefore, $\Phi C_T{}^0$ is the least sensitive (lower PrUs) amongst the back-calculations due to the Optimum Multi Parameter (OMP) constraint. This OMP statistical approach requires highly reliable measurements of potential temperature (Θ) and Salinity (S), but the precisions achieved on them counterbalance the effects in the $\Phi C_T{}^0$ equation.

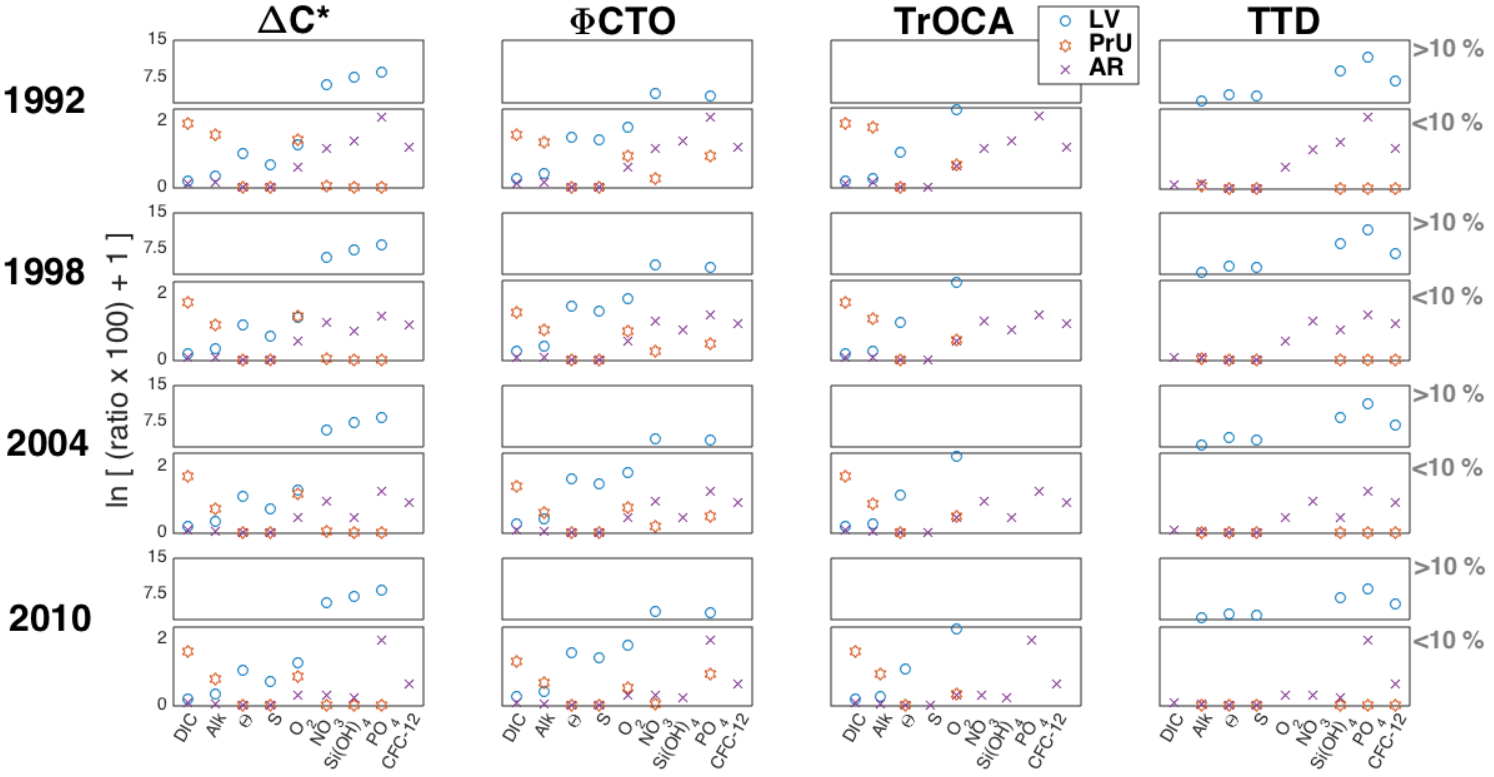

FIGURE 3.1: *Scatter plots showing the influence of the anthropogenic carbon (C_{ant}) input factors calculated with the One Factor At a Time (OFAT) approach at the 24.5°N Atlantic transect for the ΔC^*, $\Phi {C_T}^0$, TrOCA, and TTD methods in 1992, 1998, 2004, and 2010. The Analytical Ratio (AR, purple crosses) estimates the C_{ant} variation due to the factor precision by calculating the precision of the factor as a ratio to the measured maximum of the factor (Eq 2.19). The Limit Value (LV, blue circles) estimates the variation in the input factor necessary to vary C_{ant} by 10 % by calculating the ratio of the variability of the factor to the measured maximum of the factor (Eq 2.18). The Propagated Uncertainty (PrU, orange diamonds) estimates the ratio between AR and LV (Eq 2.20): the factors associated with the greatest PrU values are likely to be the most influential in the C_{ant} estimates. All values are reported in the figure using the natural logarithmic scale, after increase each by one to maintain comparable variations in the derived estimates. To better understand the final comparisons, each panel is divided between percentages higher and lower than 10 %.*

Overall, the back-calculations PrUs decrease over time, reflecting improvements in the measurement (Tab 1.2). This pattern mostly emerges for the alkalinity influence that reduces by roughly 50 %.

For the TTD method, the most influential factor is the CFC-12, with the associated AR and LV estimates resulting as the closest in the right panels of Fig 3.1. This influence propagates to the mean age and hence to the surface ocean pCO_2 estimates at the water mass origin. Within the 24.5°N data, the CFC-12 was measured in 1992 with a precision of $\pm 2.4 \times 10^{-2}$ pmol kg^{-1} (± 4.0 % of the background level), which propagates an analytical uncertainty of ± 15.8 μmol kg^{-1} (± 31.6 %) in the TTD C_{ant}. Similarly, we estimate an uncertainty of ± 14.5 μmol kg^{-1}, ± 9.9 μmol kg^{-1} and ± 6.5 μmol kg^{-1} due to CFC-12 in 1998, 2004, and 2010, respectively. All measurements used to estimate the surface C_{ant} from the pCO_2 estimate with the co2sys (section 2.3.3) have an influence in the TTD C_{ant} analytical uncertainty ten times lower than the CFC-12 precision. So, constant values can be considered for these variables with negligible influences on the TTD C_{ant} uncertainty.

In summary, our OFAT analysis identifies the DIC and CFC-12 precisions as the most influential factors respectively in the back-calculations and the TTD C_{ant} analytical uncertainties. However, the OFAT approach excludes interactions between factors, potentially underestimating or overestimating their influence on the C_{ant} uncertainty.

3.2.2 C_{ant} sensitivity to analytical precisions (VBSA)

To account for potential interactions among factors, we improve on the OFAT using the VBSA. We explore interactive effects among the factors (DIC, Alk, Θ, S, oxygen (O_2), CFC-12, nitrate (NO_3), silicate ($Si(OH)_4$), and phosphate (PO_4)) that are most influential on the C_{ant} estimated by using the ΔC^*, $\Phi C_T{}^0$, TrOCA, and TTD. Under the VBSA assumptions, we link C_{ant} variances with that associated to each independent factor and the interactions among them. Variable numbers of quasi MC runs (specified in the captions of Figs 3.2 to 3.6) are used in this analysis, as the balance between acceptable results and computational costs is different for each C_{ant}

method. The VBSA result acceptability is investigated after a thousand additional runs, leading to comparable results, and hence giving confidence to our analyses.
We use maximums and minimums of the most influential C_{ant} factors observed in the upper 1000 m of the 24.5°N Atlantic transect in 2010 to confine the quasi MC probabilistic inputs (panels a in Figs 3.2 to 3.4 and whole Figs 3.5 and 3.6, section 2.5). This approach allows us to quantify the influences of natural variabilities on the C_{ant} estimates. We also use the VBSA to estimate the uncertainty propagated by each measurement and possible interactions among them on C_{ant}. This second approach is based on the same upper-ocean factor averaged values, but it uses their measurement precisions (Tab 1.2) instead of their standard deviations as estimates of variability. This second approach is applied here to the back-calculation results in the panels b of Figs 3.2 to 3.4. We do not apply it however to the TTD calculations because the mean age estimate remains the dominant source of uncertainty.
Estimates of the Main Effect (ME) and Total Effect (TE) are shown in Figs 3.2 to 3.6 as orange and blue bars, respectively. As established in section 2.5, the ME is the ratio between each input variable and the variance of the equation result, while the TE also quantifies non-linear interactions influencing the equation output.
ME estimates identify Θ, DIC, and O_2 as the ΔC^* most influential factors when using their observed upper-ocean spreads (Fig 3.2a). They account for 52 %, 31 %, and 14 % of the ΔC^* C_{ant} variance, respectively. Turning attention to the $\Phi C_T{}^0$ method, the Θ and DIC effects remain significant, influencing 43 % and 20 % of the C_{ant} variance, while the O_2 influence drops to a negligible value (Fig 3.3a). The TrOCA C_{ant} variance is mostly influenced by Θ and DIC changes, in line with the other back-calculations, with MEs of 47 % and 37 %, respectively (Fig 3.4a).
If we use the measurement precisions instead of the factor standard deviations in the quasi MC calculations (Figs 3.2b to 3.4b), the influence of variations in Θ drops to negligible values for all of the back-calculation estimates. This is due to the high precision achieved in temperature measurements and agrees with the OFAT results of section 3.2.1. Conversely, the DIC effect approximately doubles for the same C_{ant} estimates. This suggests that DIC is not only the second most influential factor of C_{ant} observed variability, but this factor precision is the primary driver of analytical

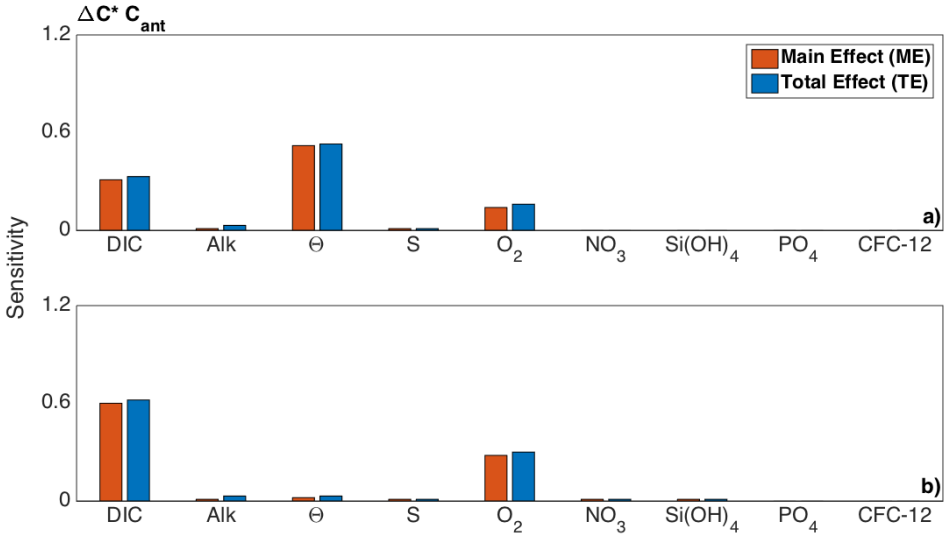

FIGURE 3.2: *Variance Based Sensitivity Analysis (VBSA) of $\Delta C^* C_{ant}$ estimates. Main (orange) and total (blue) effects are estimated using the Matlab SAFE toolbox (Pianosi et al., 2015) and measurements collected in 2010 in the upper 1000 m of the 24.5°N Atlantic transect. The approach was conducted by varying the region DIC, Alk, Θ, S, O_2, NO_3, $Si(OH)_4$, PO_4, and CFC-12 mean values within their standard deviations after 16000 runs (a) and analytical precisions (Tab 1.2) after 91000 evaluations (b). The study in panel (b) required a larger amount of runs as it reached later an acceptable stability in the Monte Carlo probabilistic results (see the text for details). The $\Delta C^* C_{ant}$ estimates variability differs between panel (a) and (b): the results reported in the figure can be compared for variables of the same panel but should not be used to infer changes across the two panel results.*

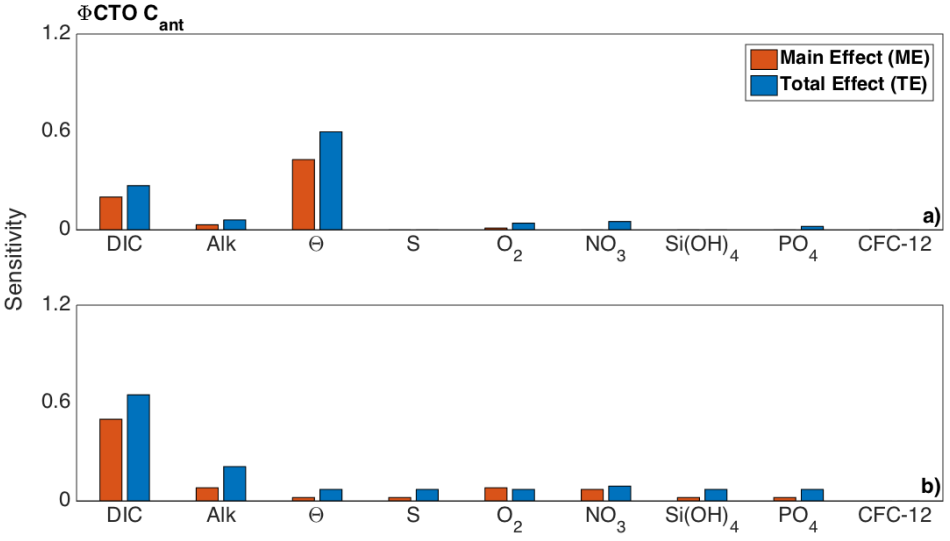

FIGURE 3.3: *Same as in Fig 3.2, but for $\Phi {C_T}^0$ C_{ant} estimates after 60000 and 106000 runs for the panels (a) and (b), respectively.*

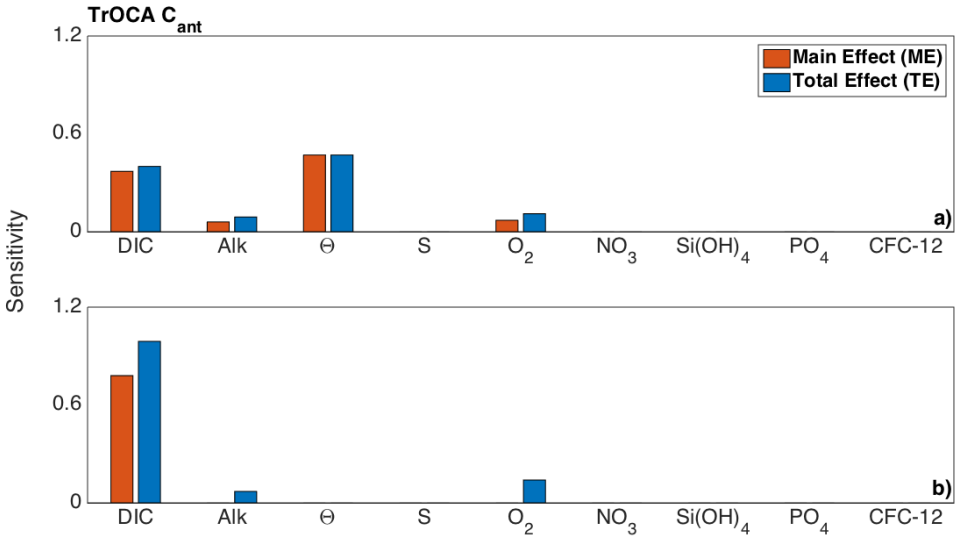

FIGURE 3.4: *Same as in Fig 3.2, but for TrOCA C_{ant} estimates after 24000 and 80000 runs for the panels (a) and (b), respectively.*

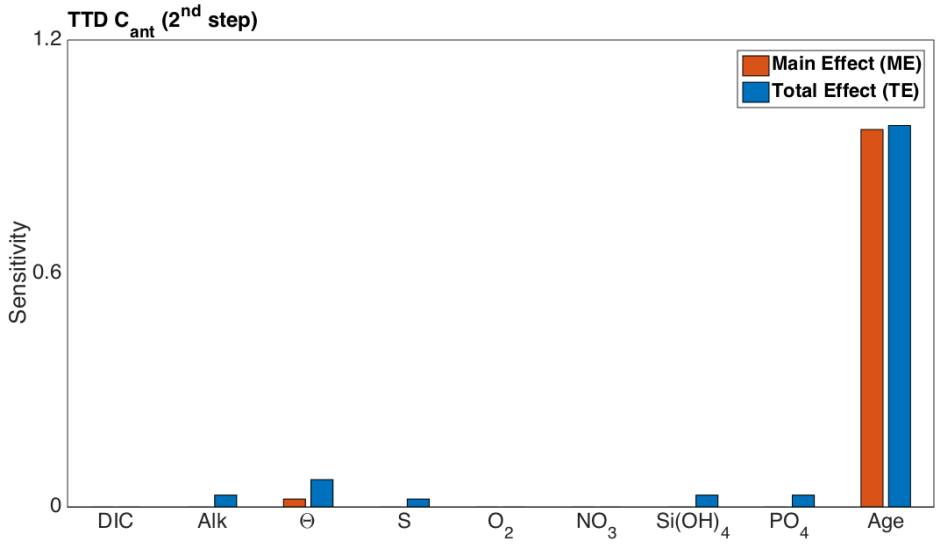

FIGURE 3.5: *Same as in Fig 3.2, but for the TTD 2^{nd} step after 54000 runs.*

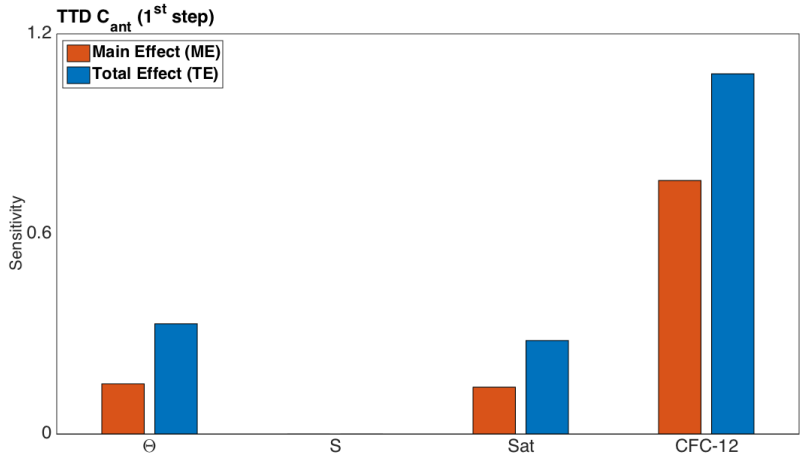

FIGURE 3.6: *Same as in Fig 3.2, but for the TTD* 1^{st} *step after 8800 runs.*

uncertainty in the back-calculations estimates. Those methods should be applied only where several and highly precise DIC observations are available.

In the TTD, we find the CFC-12 and mean age to be the most influential factors in the OFAT (Fig 3.1) and VBSA (Fig 3.5) analyses. The VBSA shows that the mean age ME accounts for the totality of the TTD C_{ant} variance in the TTD second step. TE estimates compare to the MEs for the ΔC^* technique (within an uncertainty of ± 5 %), highlighting a lack of interactions among factors. This result is consistent with the linearity of the method equations (section 2.3.1). The $\Phi {C_T}^0$ C_{ant} variance is however influenced by Interactions (I = TE - ME) due to Θ and DIC, with values of 17 % and 7 %, respectively, when using the observed factor spreads. When using the factor precisions, the values modify to 5 % (which is negligible) and 15 %, while an additional 15 % is due to Alk. The TrOCA C_{ant} variance is influenced by factor interactions only when we consider the factor precisions: an interactive effect of 21 % is visible in the DIC bars, being due partially to Alk (7 %) and partially to O_2 (14 %). The TTD second step is not influenced by interactions.

To complete our study, we assess the mean age estimate within the TTD first step (section 2.3.3), treating this assessment separately as it is not comparable with any back-calculation analysis. We consider estimates of the transient tracer Saturation (Sat) and measurements of Θ, S, and CFC-12. Independently (ME), the CFC-12 variance predominantly (76 %) influences the estimate of the TTD mean age, with

additional contributions due to Θ and Sat. TEs indicate interactive effects mostly influenced by the CFC-12 variance, but Θ and Sat also contribute. So, we suggest caution on the TTD use in regions where water mass formations, and Sat, are poorly known, such as the Southern Ocean (Stöven et al., 2016).

Our VBSA analyses show that observations of Θ, DIC, O_2, and water mass mean age estimates are of key relevance for the C_{ant} uncertainty, independently, with variable strengths that depend on chosen factors and methods. Interactively, the analysed factors influence the $\Phi C_T{}^0$, TrOCA, and TTD C_{ant} variances, suggesting caution on the use of these techniques and associated uncertainties, which are mostly calculated using the OFAT approach. Negligible interactive effects influence the variance of the ΔC^* C_{ant} estimates in agreement with the linearity of this method equations.

3.3 How constant is the CO_2 disequilibrium?

3.3.1 Approach

In addition to analytical uncertainties, C_{ant} estimates are influenced by uncertainties in method assumptions (Matsumoto and Gruber, 2005; Vázquez-Rodríguez et al., 2009b). In section 2.3, we assessed the assumption independent impacts. Here, we use the 24.5°N data to assess the methodological uncertainties in terms of a key method assumption: the assumed CO_2 disequilibrium (C_{dis}) constancy on the C_{ant} estimated using the TTD, TrOCA, $\Phi C_T{}^0$, and ΔC^* techniques. We neglect all other sources of C_{ant} uncertainty, discussing their impacts in section 3.3.2.

In order to assess the assumed C_{dis} constancy, we compare the change in seawater pCO_2 that is implied by the calculated C_{ant} in water masses on the 24.5°N section in a given interval of time, with the change in atmospheric CO_2 that occurred over that period. This gives an indication of whether the assumptions in the methods are self-consistent: if the assumptions (of steady state and constant disequilibrium between atmosphere and surface ocean) are consistent, these two changes should be equal. We use the observations collected at the 24.5°N transect between 1992 and 2010, and the CO_2 mole fraction (xCO_2) collected at the Mauna Loa observatory

between 1962 and 2010 (Dlugokencky et al., 2017) for this comparison. We do not use measurements from other observatories, assuming homogeneity over latitude in the atmospheric xCO_2 temporal increase. The assumption is unrealistic, but it propagates a negligible uncertainty of ± 0.03 ppm yr^{-1} (± 0.01 %) on average.
To calculate the change in seawater pCO_2 implied by a given increase in C_{ant}, we follow the method of Woosley et al. (2016). Using co2sys (Lewis and Wallace, 1998; Van Heuven et al., 2011) we calculate the total pCO_2 of a water sample in terms of DIC, Alk, and other measured parameters:

$$pCO_{2tot} = f(DIC, Alk, T, S, Si(OH)_4, PO_4) \tag{3.1}$$

The DIC in a given sample can be separated into a natural component C_{nat} (assumed steady state) and the C_{ant} calculated by a given method:

$$C_{nat} = DIC - C_{ant} \tag{3.2}$$

Using C_{nat} in Eq 3.1, we calculate a corresponding pCO_{2nat}, which is the pCO_2 the sample would have had pre-industrially, and is constant by assumption:

$$pCO_{2nat} = f(C_{nat}, Alk, T, S, Si(OH)_4, PO_4) \tag{3.3}$$

The difference between the pCO_{2tot} and this value gives the amount that the pCO_2 of the sample has increased (pCO_{2ant}), which should be equal to the increase in the atmospheric pCO_2 since the industrial revolution.

$$pCO_{2ant} = pCO_{2tot} - pCO_{2nat} \tag{3.4}$$

Therefore, if pCO_{2ant} is determined in a water mass at two times t_1 and t_2, the rise (expressed in μatm) should equal the xCO_2 change (in ppm) that occurred during an equivalent interval of time in the past, lagged by the water mass mean age:

$$pCO_{2ant}(t_2) - pCO_{2ant}(t_1) = xCO_2(t_2 - \tau) - xCO_2(t_1 - \tau) \tag{3.5}$$

where τ is an estimate of the time since the water was last at the surface.
When C_{dis} is not constant, the pCO_{2ant} and xCO_2 increases differ over comparable time intervals. We use mean values of this difference to estimate the C_{ant} uncertainty due to the assumed C_{dis} constancy. Results are summarised in Tab 3.1 for the water masses analysed (STMoW, MMoW, SPMoW, and AAIW), the Mode water (MoW) as a whole, and the upper 1000 m of the 24.5°N Atlantic section.
Fig 3.7 compares the changes in xCO_2, pCO_{2tot}, and pCO_{2ant} estimated as above for water masses on the 24.5°N section. We average the data for the STMoW, MMoW, SPMoW, and AAIW, documenting the change on 6 yr, 12 yr, and 18 yr intervals. For the parameter τ we use mean ages based on the TTD analysis, respectively of 0 yr, 5 yr, 10 yr, 30 yr for the four water masses (Vázquez-Rodríguez et al., 2009b).

3.3.2 Results

There is a general agreement between the pCO_{2ant} rises given by the four techniques, the pCO_{2tot} rise, and that observed in the atmosphere over the relevant time intervals (Fig 3.7). The only exception is the SPMoW, where the pCO_{2tot} rise is faster than the xCO_2 and the pCO_{2ant} increases. This suggests changes in C_{dis} over time, hence increasing the uncertainty on the steady state assumption in this water mass. The ΔC^* and TrOCA pCO_{2ant} estimates lie between the SPMoW xCO_2 and pCO_{2tot} increases, suggesting that these techniques partially capture the changes in C_{dis}.
Instead, the observed pattern is due to positive biases in both methods linked to the biogeochemical terms, being also inferable in other water masses where C_{dis} is overall constant in time (increases in xCO_2 and pCO_{2tot} are comparable). Here, the discrepancies between the implied pCO_{2ant} and atmospheric xCO_2 growth are larger, and grow with time. The ΔC^* and TrOCA methods are based on regression models generally defined in a confined time interval. So, they struggle to capture potential changes in C_{dis} over time. For the TTD and $\Phi C_T{}^0$ methods, the pCO_{2ant} and xCO_2 temporal increases compare. There are reasons however why we might expect these two methods to perform well on the test.

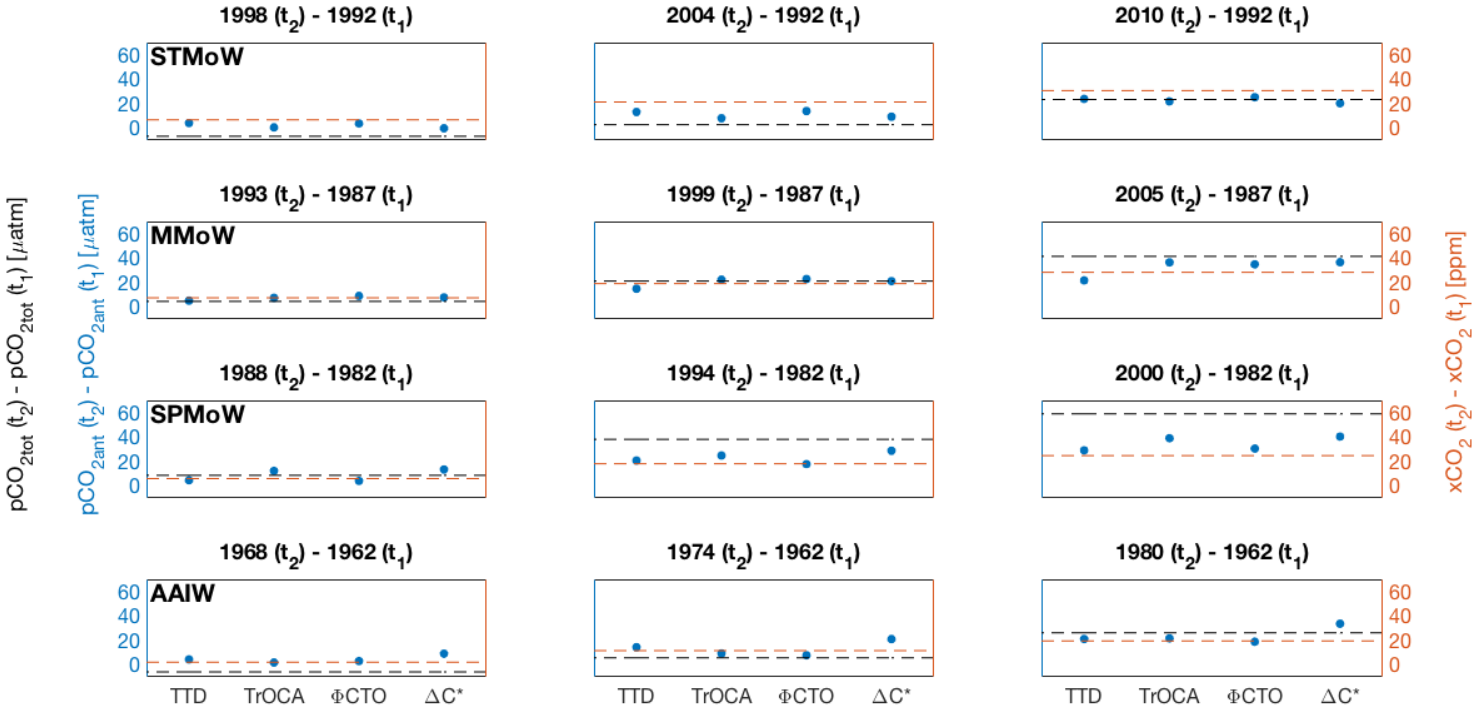

FIGURE 3.7: *Temporal increases in the atmospheric xCO_2 (orange dashed lines), oceanic total (pCO_{2tot}, black dashed lines), and anthropogenic (pCO_{2ant}, blue dots) pCO_2 of the STMoW, MMoW, SPMoW, and AAIW on the 24.5°N Atlantic transect. We study three time intervals, with the starting (t_1) and ending (t_2) years of each reported above the corresponding panel. We use the xCO_2 measurements collected at the Mauna Loa observatory (Dlugokencky et al., 2017) and four C_{ant} techniques (TTD, TrOCA, $\Phi C_T{}^0$, and ΔC^*) to estimate the pCO_{2ant}.*

TABLE 3.1: *Table summarising the uncertainties on the TTD, TrOCA, $\Phi C_T{}^0$, and ΔC^* C_{ant} due to the assumed C_{dis} constancy over time (1992-2010). These values are calculated by comparing the pCO_{2ant} estimated by each method with the atmospheric CO_2 mole fraction lagged by the TTD water mass mean age (Eq 3.5). Each uncertainty estimate is presented as concentration and percentage of the mean C_{ant} maximum (50.0 μmol kg^{-1}) in the 24.5°N STMoW, MMoW, SPMoW, AAIW, upper 1000 m, and Mode Waters (MoW). We highlight in bold the highest result for each layer.*

Location	Uncertainty units	TTD	TrOCA	$\Phi C_T{}^0$	ΔC^*
STMoW	μmol kg^{-1}	±5.9	±9.5	±5.3	**±9.8**
	%	±12	±19	±11	±20
MMoW	μmol kg^{-1}	**±4.4**	±3.8	±3.9	±3.5
	%	±9	±8	±8	±7
SPMoW	μmol kg^{-1}	±2.8	±9.2	±2.6	**±11.3**
	%	±6	±18	±5	±23
AAIW	μmol kg^{-1}	±2.2	±1.6	±1.9	**±10.2**
	%	±4	±3	±4	±20
Upper 1000 m	μmol kg^{-1}	±4.0	±6.0	±3.5	**±9.0**
	%	±8	±12	±7	±18
MoW	μmol kg^{-1}	±4.4	±7.5	±4.0	**±8.5**
	%	±9	±15	±8	±17

The $\Phi C_T{}^0$ includes a parameter Φ that is meant to account for changes in the C_{dis} term (Vázquez-Rodríguez et al., 2009a). The TTD reconstructs C_{ant} using, mostly, the atmospheric CO_2 increase and estimates of the transit-time distribution, both of which are also used in this calculation of pCO_{2ant}, which is then not a reliably independent test of the assumptions in that approach.

We have shown that there are errors associated with the assumptions particularly of the ΔC^* method. Though the errors are quantified in terms of non-constancy of C_{dis}, in reality other effects are important and contribute to them. We estimate uncertainties due to the assumed C_{dis} constancy of ±7 %, ±8 %, ±12 %, ±18 % on the $\Phi C_T{}^0$, TTD, TrOCA, and ΔC^* C_{ant} estimates in the upper 1000 m of the 24.5°N

Atlantic transect between 1992 and 2010. For the ΦC_T^0 and TTD methods, these values are within ±10 %, the uncertainty propagated by analytical precisions on C_{ant} in a more realistic view (Matsumoto and Gruber, 2005; Vázquez-Rodríguez et al., 2009b). For TrOCA and ΔC*, the estimates exceed the C_{ant} analytical uncertainty. In the next section more detailed treatment, much of the uncertainty in the ΔC* method when applied in the 24.5°N upper 1000 m will be shown to be due to other effects: the uncertainty due to the assumption of constant C_{dis} reduces to ±3 %, so comparing to the value of ±2 % estimated by Matsumoto and Gruber (2005).

3.4 Differences in C_{ant} estimates and uncertainties

3.4.1 Spatial scale dependency of C_{ant} uncertainties

Methodological assumptions and analytical precisions propagate C_{ant} uncertainties, leading to discrepancies between different technique estimates.

In this thesis section, we compare the ΔC* and TTD C_{ant}, quantifying their total uncertainties and exploring potential changes due to variations in ocean regions and data. Other method estimates are not discussed, as the ΔC* and TTD confine the probable range of C_{ant} concentrations (section 5.2; Iudicone et al. (2016)).

We synthesise the global ocean ΔC* and TTD C_{ant} total uncertainties combining our OFAT analyses presented in sections 2.3 (method assumptions influence) and 3.2.1 (analytical precisions influence) with the studies of Matsumoto and Gruber (2005), Waugh et al. (2006), and Fine et al. (2017). As analytical precisions for the global ocean measurements, we use the guidelines of the Global Ocean Ship-based Hydrographic Investigations Program (GO-SHIP; Hood et al. (2010)). Then, we compare our results with the estimates of He et al. (2018), although those authors' results were based on model studies of the TTD C_{ant} uncertainty only.

To assess potential variations due to ocean regions and data, we replicate the synthesis of the C_{ant} total uncertainties by using the 24.5°N data collected in 2010. As first step, we assess the whole transect estimates. Then, we focus on the upper 1000 m, which stores the largest C_{ant} pool in the water column. In this study, we

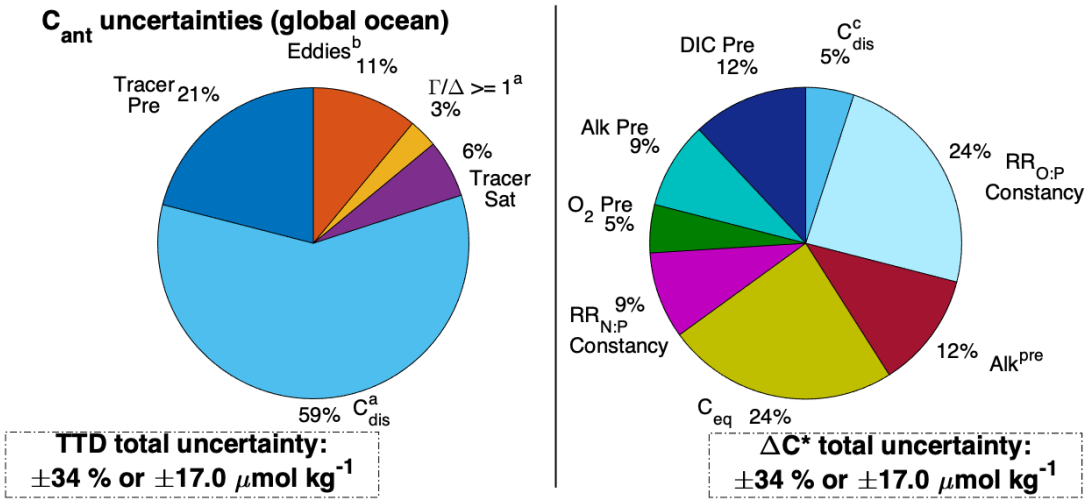

FIGURE 3.8: *Pie charts summarising the contribution of analytical precision (Pre) and underlying method assumptions to the total uncertainties of the TTD (left) and ΔC^* (right) global ocean C_{ant} estimates. 'Sat' and 'pre' indicate saturation and preformed. All values are shown as percentage of the C_{ant} total uncertainty (± 17.0 μmol kg^{-1}). Apices a, b, and c highlight estimates taken from the work of Waugh et al. (2006), Fine et al. (2017), and Matsumoto and Gruber (2005).*

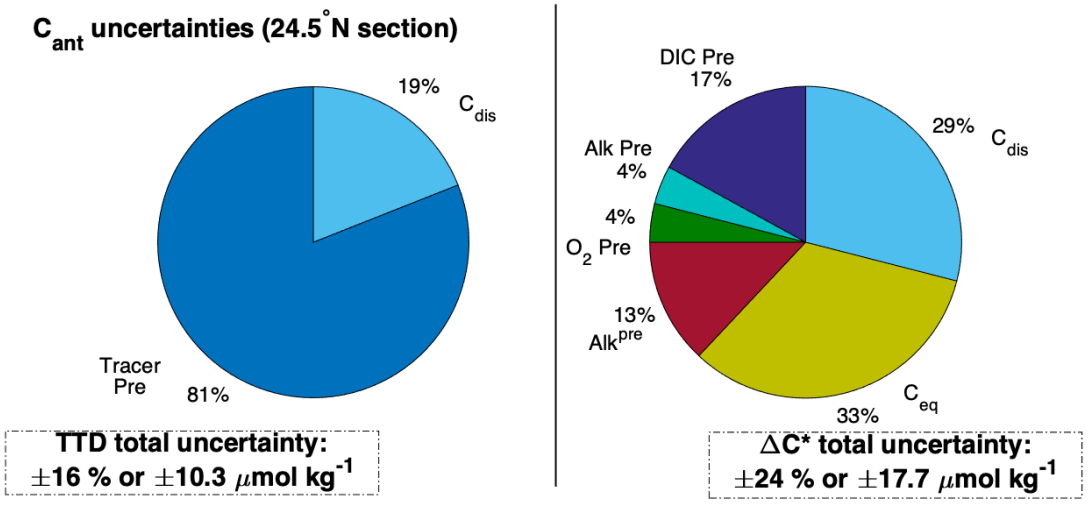

FIGURE 3.9: *Same as in Fig 3.8, but for the 24.5°N Atlantic section.*

use the analytical precisions of the hydrographic cruise report (King et al., 2012). Results are presented in Figs 3.8, 3.9, and 3.10 for the global ocean, the 24.5°N section, and the last upper 1000 m. We quantify the fraction of the uncertainty due to each source and total value as concentration and percentage to the region C_{ant} maximum. Results are shown at the bottom of each figure (see also appendix B).

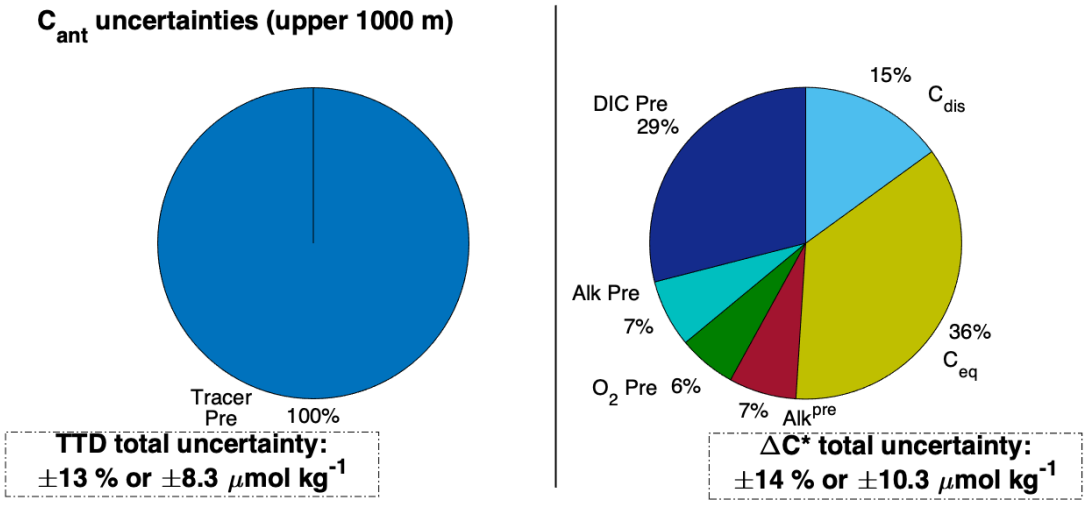

FIGURE 3.10: *Same as in Fig 3.9, but for the 24.5°N upper ocean (0-1000 m).*

In the global ocean, our TTD and ΔC* C_{ant} total uncertainty estimates agree, both resulting ±17.0 μmol kg^{-1}. So, a minimum time interval of fifteen years is necessary to reliably distinguish a change in C_{ant}, which increases by 1.4 ± 0.4 μmol kg^{-1} yr^{-1} (adapted from Khatiwala et al. (2009)). The TTD C_{ant} total uncertainty is however two times bigger than the estimate of He et al. (2018). This apparent disagreement is due to the fact that those authors studied only model outputs, where analytical uncertainties are null, and so the TTD C_{ant} total uncertainty approximately halves. The sources of C_{ant} uncertainty differ between the methods assessed. The TTD C_{ant} uncertainty mostly depends on the assumed C_{dis} constancy, the analytical precision of transient tracers, and the influence of ocean eddies. The C_{dis} constancy leads to positive biases mostly confined to the Southern Ocean (Waugh et al., 2006). Here, deep convections could change C_{dis} up to 50 %, reducing the validity of the TTD assumption. Tracer precisions depend on the analytical procedures used during the data collection. Eddies modify the water mass tracer concentrations, even assuming ventilation in steady state and known mixing in convection areas (Fine et al., 2017). This leads to more uncertain estimates of the water mass mean age and TTD C_{ant}. The ΔC* C_{ant} uncertainty depends on the assumed Redfield ratio constancy, the equilibrium Carbon (C_{eq}) estimates, and the analytical precisions of DIC and Alk. Redfield ratios are used to infer the DIC biological component. They are assumed constant, but more realistically vary within ten units (range between the estimates of

Redfield (1934) and Martiny et al. (2014)), decreasing the ΔC^* assumption validity: changes in biological cycles influence the C_{ant} estimated with this method. The C_{eq} estimates are based on regression models, which reliability varies with the depth or the time interval investigated. The DIC and the Alk analytical precisions depend on data collection procedures, as for the anthropogenic transient tracer counterparts.

At global scale, the TTD and ΔC^* C_{ant} uncertainties are equal, depending mostly on method assumptions and analytical precisions, respectively (Fig 3.8). Improved descriptions of oceanic processes will improve primarily the TTD reliability, while more precise observations will improve the back-calculation estimates.

In the subtropical North Atlantic (24.5°N), we are able to reduce some of the C_{ant} uncertainty sources (Fig 3.9). Here, the observations amount per unit area increases, and so does the knowledge of the ocean environment. For the TTD method, the mixing to advection ratio, estimated by Γ/Δ (section 2.3.3), and tracer saturations are relatively well known in the 24.5°N section. We neglect their uncertainties, as in the work of Guallart et al. (2015b). The 24.5°N transect is a region with no seawater fronts, lying in the North Atlantic subtropical gyre. So, the influence of mesoscale eddies is also negligible (Fine et al., 2017). For ΔC^*, the increased knowledge of the environment allows to neglect the uncertainty due to the assumed constancy in the Redfield ratios. The uncertainty due to the Alk precision halves, while the DIC counterpart increases by 50 %. The C_{eq} and Alk^{pre} uncertainties also increase, and so does the assumed C_{dis} constancy influence. We estimate the TTD and ΔC^* C_{ant} total uncertainties as ± 10.3 μmol kg^{-1} (± 20.6 %) and ± 17.7 μmol kg^{-1} (± 35.4 %) at the 24.5°N section. These values reduce to ± 8.3 μmol kg^{-1} and ± 10.3 μmol kg^{-1} in the upper 1000 m of the transect. Here, we neglect the influence of the assumed C_{dis} constancy in the TTD, improving also five of the six ΔC^* C_{ant} uncertainty sources owing to more accurate measurements. The only exception is the DIC analytical precision that maintains unaltered. See appendix B for additional details.

In summary, several factors influence the uncertainty of ocean C_{ant} estimates, with values varying with the spatial scale and chosen dataset. The TTD C_{ant} reliability mainly depends on method assumption validities, improving in well-known regions. The ΔC^* C_{ant} estimates are mostly influenced by analytical precisions, being more

reliable in regions with more accurate observations. This influences distributions of C_{ant} estimated by using different methods, as it is investigated in the next section.

3.4.2 Uncertainty influences on C_{ant} distributions

Methodological assumptions and analytical precisions influence not only the C_{ant} total uncertainty, investigated in the previous section, but also the distribution of this variable concentration over space, leading to discrepancies between estimates obtained using different methods. To explore them, we compare the TTD and ΔC^* C_{ant} distributions at the 24.5°N Atlantic transect using the data collected in 2010. Results are shown in Fig 3.11 for the TTD (panel a) and ΔC^* (panel b) estimates. We highlight the water masses on the 24.5°N section using the Tab 1.1 definitions. The TTD technique treats C_{ant} as a transient tracer, and so the estimates obtained with this technique highlight features of a physical nature only (e.g. changes in the deep western boundary current). The ΔC^* method includes a mixing influence on the circulation weaker than the TTD technique by assumption (section 2.3), also showing a higher variability between samples due to the influence of measurement analytical precisions. The ΔC^* method assumes constancy in the biogeochemical cycle influences on C_{ant}, while the TTD limits those effects to negligible values. All of these methodological and analytical challenges influence the final C_{ant} estimates. The TTD and ΔC^* C_{ant} estimates differ in the 24.5°N upper 1000 m in 2010 (Fig 3.11c). Both methods highlight the variable decrease with depth, although the ΔC^* estimates are higher than the TTD counterparts due to the biogeochemical influence. Below 1000 m, the TTD method better describes the deep ventilation and mixing influences on C_{ant}, but it cannot be used to reliably quantify this variable in water masses with ages equal or higher than 70 years, such as the lower North Atlantic Deep Water (lNADW) of the section eastern side (45-16°W). This water mass tracer concentrations are too low to be distinguishable from the uncertainty.

We conclude that there is agreement between the TTD and ΔC^* C_{ant} distributions in the subtropical North Atlantic. However, discrepancies emerge owing to the different inclusion of biogeochemical cycle and mixing influences.

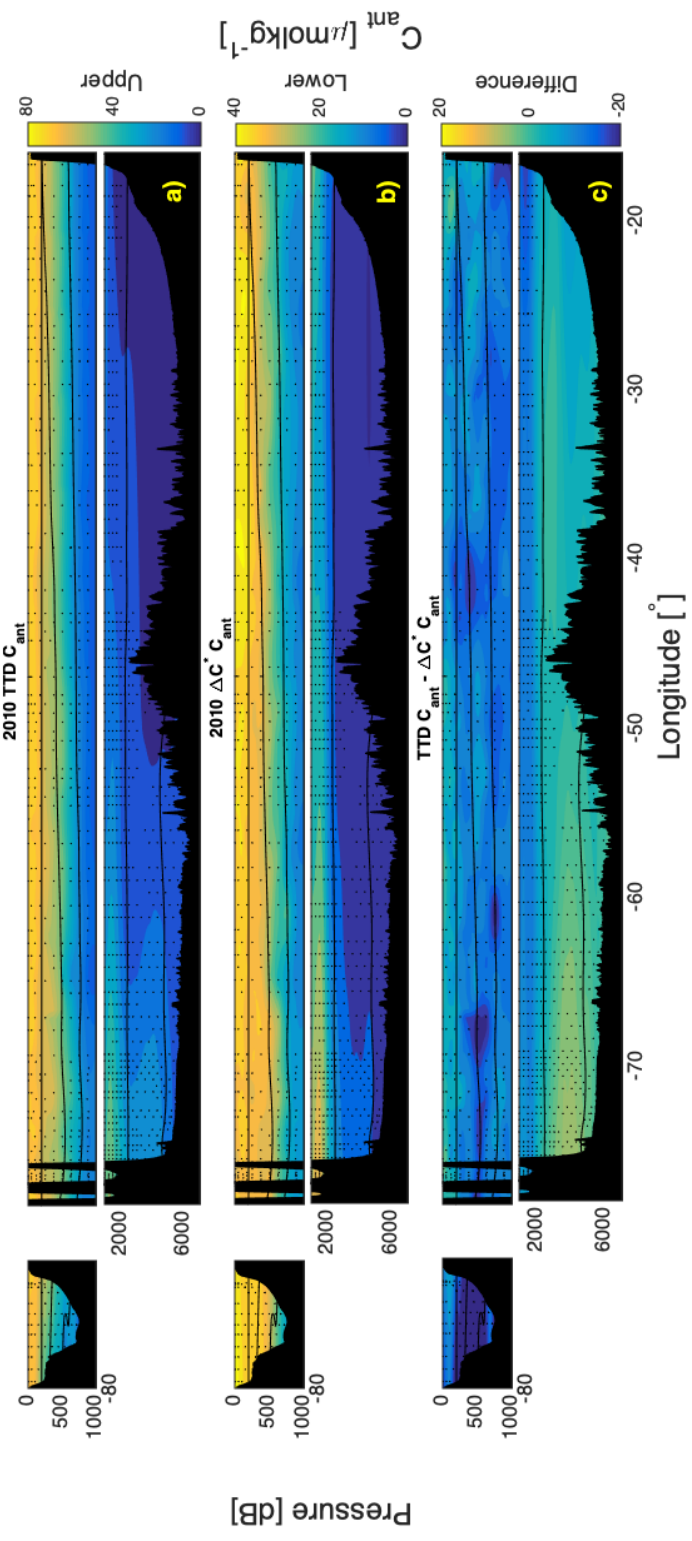

FIGURE 3.11: *(a) TTD anthropogenic Carbon (C_{ant}) estimates at the 24.5°N transect in 2010. The 200 dB isobar and five isopycnal lines isolate the seven water masses of the section (from the surface: subtropical Mode Water (MoW), Madeira MoW, Subpolar MoW, Antarctic intermediate water, upper North Atlantic Deep Water (NADW), lower NADW, and Antarctic bottom water (Tab 1.1)), while the measurement locations are plotted as black dots. The 'Upper' ocean is also separated from the 'Lower' layer at 1000 m to highlight the carbon distributions in the first. (b) ΔC^* C_{ant} estimates at 24.5°N in 2010. (c) Differences between the TTD and ΔC^* C_{ant} estimates.*

3.4.3 C_{ant} uncertainty influences on anthropogenic pH

Uncertainties in C_{ant} estimates propagate on to variables calculated from them. We assess variations in the total (pH_{tot}), natural (pH_{nat}), and anthropogenic (pH_{ant}) pH partitions, which quantify the human impact on the ocean carbon cycle referred to as acidification (Garcia-Ibánez et al., 2016; Ríos et al., 2015; Woosley et al., 2016). Again, we use the data collected at the 24.5°N section in 2010 and the C_{ant} estimated by using the TTD and ΔC^* methods for this analysis, since these span the probable range of C_{ant} concentrations (section 5.2; Iudicone et al. (2016)).

The pH_{tot} can be measured with an uncertainty of ±0.001 pH units (±0.01 %) mostly due to the in-situ T (Dickson et al., 2007). More often, the pH_{tot} is calculated from two of the inorganic carbon observations (e.g. Alk and DIC) using co2sys (Lewis and Wallace, 1998; Van Heuven et al., 2011). Under this indirect approach, the pH uncertainty increases to ±0.005 pH units, owing to the DIC and Alk precisions.

Using the second approach, we separate pH_{tot} into pH_{nat} and pH_{ant}, as also done for pCO_{2tot} in section 3.3.1. We estimate pH_{nat} by using C_{nat}, which is the difference between the measured DIC and the estimated C_{ant} (Eq 3.2). The pH_{ant} is determined by subtracting pH_{nat} from pH_{tot}. In this pH partitioning, C_{ant} propagates the highest uncertainty. To constrain its value, we use the TTD and ΔC^* estimates, and the work of Woosley et al. (2016). Those authors linked an uncertainty of ±3.0 μmol kg^{-1} in the eMLR C_{ant} to changes of ±0.005 pH units in the pH_{ant}. We adjust the value to our C_{ant} uncertainties (Fig 3.10), quantifying pH_{ant} uncertainties of ±0.014 pH units and ±0.017 pH units for the TTD and ΔC^* estimates in the 24.5°N upper 1000 m. We present the TTD and ΔC^* pH_{ant} and pH_{nat} distributions in Figs 3.12 and 3.13.

TABLE 3.2: *Table summarising mean values of natural (pH_{nat}) and anthropogenic (pH_{ant}) pH components in pH units. The estimates are quantified using the TTD and ΔC^* C_{ant} at the 24.5°N Atlantic transect in 2010 and summarised as mean values in the STMoW, MMoW, SPMoW, AAIW, upper 1000 m and MoW.*

Location	TTD pH_{nat}	TTD pH_{ant}	ΔC^* pH_{nat}	ΔC^* pH_{ant}
STMoW	8.164	-0.096	8.167	-0.098
MMoW	8.113	-0.085	8.134	-0.106
SPMoW	8.020	-0.080	8.039	-0.099
AAIW	7.918	-0.042	7.946	-0.070
Upper 1000 m	8.054	-0.076	8.071	-0.093
MoW	8.099	-0.087	8.113	-0.101

However, the discussion focuses on the upper 1000 m only. In this layer, we separate the Mode waters (STMoW, MMoW, and SPMoW) that store the highest C_{ant} pool, and the AAIW that carries the highest amount of remineralised DIC. For each, we estimate mean pH_{ant} and pH_{nat}, reporting them in Tab 3.2.

The TTD and ΔC^* estimates of pH_{ant} and pH_{nat} agree in the 24.5°N upper 1000 m, within ±0.017 pH units. This value compares with the pH_{ant} uncertainty, suggesting that the C_{ant} method choice does not influence significantly the pH partitioning.

Our results overestimate by ∼0.050 pH units the values reported by Ríos et al. (2015) and Woosley et al. (2016) in the subtropical North Atlantic. Those authors focused on latitudinal (N-S) sections, most recently sampled in 2013, while we concentrate on a longitudinal (E-W) transect sampled in 2010. Over time, Ríos et al. (2015) and Woosley et al. (2016) reported a mean rate of acidification of -0.002 pH units yr^{-1} in the North Atlantic subtropical upper ocean. According to our calculations, this trend requires 9 yr of observations to be reliably distinguishable from the uncertainty.

In summary, we partition the ocean pH into pH_{nat} and pH_{ant} at the 24.5°N transect in 2010. The approach increases the pH uncertainty from ±0.005 pH units to ±0.017 pH units regardless of the C_{ant} technique. So, we suggest caution in the acidification studies: approximately nine years of observations are necessary to reliably observed a change in pH_{ant} in the subtropical North Atlantic. We will discuss further the pH partitioning in section 5.3.4.

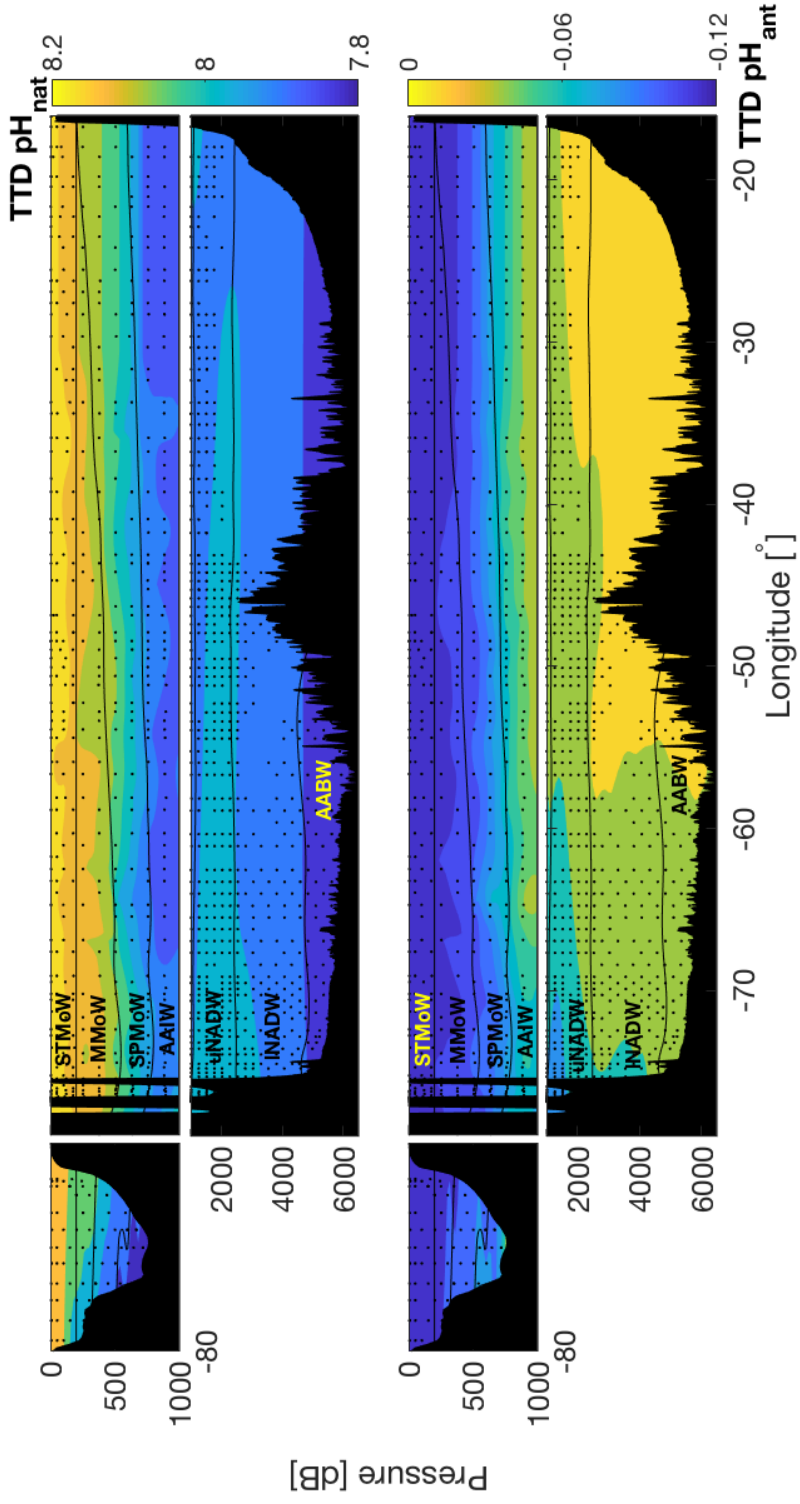

FIGURE 3.12: *Distributions of natural (pH_{nat}) and anthropogenic (pH_{ant}) pH partitions estimated by using the co2sys (Lewis and Wallace, 1998; Van Heuven et al., 2011) based on TTD C_{ant}, DIC, and Alk at 24.5°N in 2010. Refer to Fig 3.11 for details.*

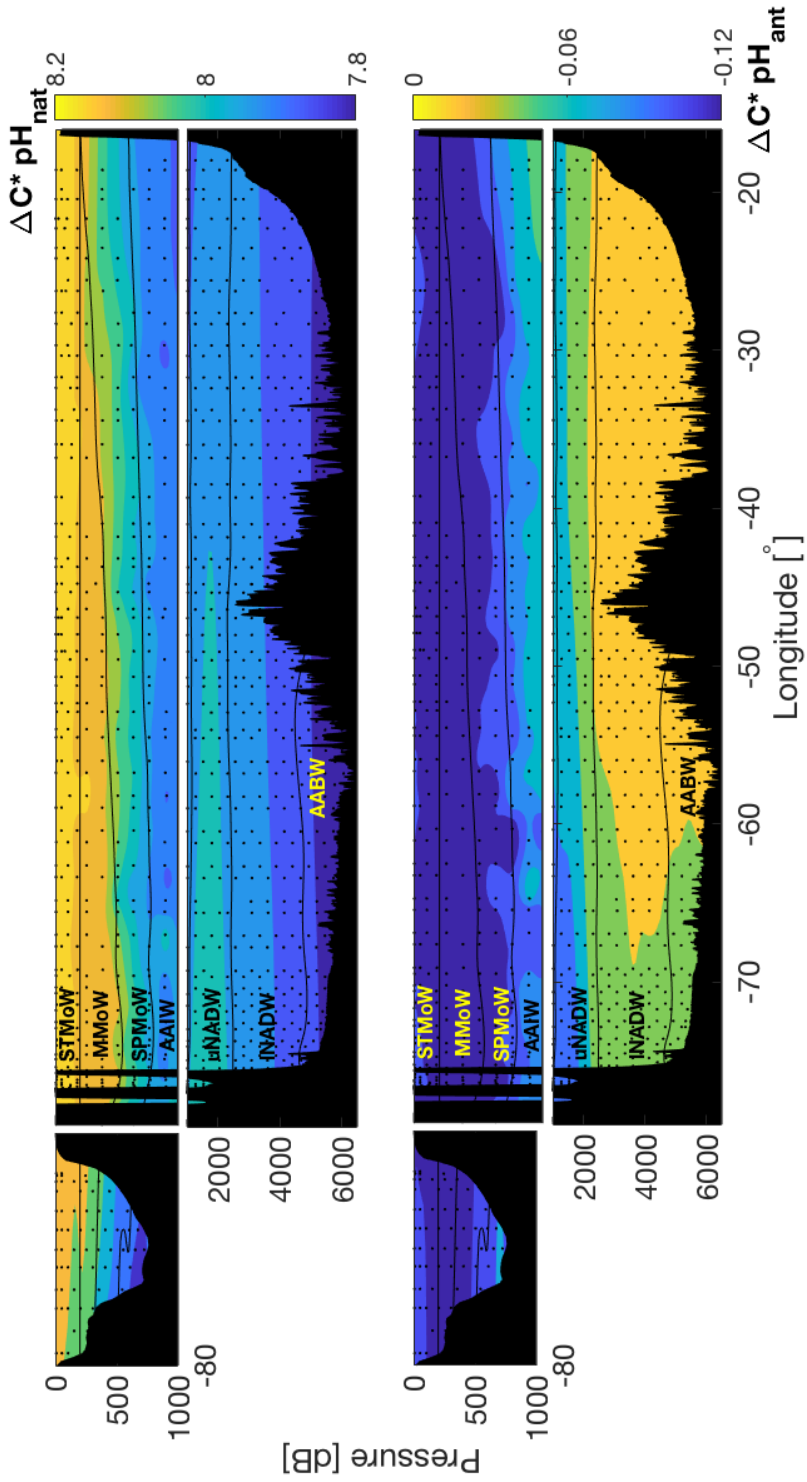

FIGURE 3.13: *Same as in Fig 3.12, but from the* ΔC^* C_{ant} *estimates.*

3.5 Model based C_{ant} comparisons

Observations limit the assessment of the accuracy of C_{ant} estimated with different methods owing to the lack of a measurable reference to compare with the indirect estimates. Ocean models overcome this challenge. Here, the 'true' Model (MOD) C_{ant} can be quantified by subtracting the control from the industrial DICs (Eq 2.15) and used as reference. The approach assumes negligible natural climate change and transferability to models of observational C_{ant} equations.

These assumptions are questionable because a fraction of the current climate change could be due to natural variability and comparisons between observations and model outputs depends on the model chosen. Notwithstanding that, the approach was used by Yool et al. (2010) to investigate the TrOCA C_{ant} estimates, by Waugh et al. (2006) for the TTD method, and by Matsumoto and Gruber (2005) for ΔC^*. We compare the MOD C_{ant} to the TTD, TrOCA, ΔC^*, and $\Phi {C_T}^0$ estimates. The assessment of those C_{ant} estimates depends on the comparability between model outputs and observations, which is evaluated in section 3.5.1. Also, we use coefficients inferred from observations for all methods (section 3.5.2) and we compare the C_{ant} results to the estimates obtained by using coefficients inferred from model outputs (section 3.5.3). By doing so, we estimate the coefficients dependency on the chosen dataset.

3.5.1 Assessment of modelled C_{ant} factors

Differences between C_{ant} estimated from model outputs are caused by differences between (1) the methods used or (2) the model outputs and observations. Separating these sources of discrepancy is necessary to assess the accuracy of the C_{ant} estimates. We investigate the similarities between model outputs and observations in the 24.5°N upper 1000 m in 1992, 1998, and 2004. We compare T, DIC, and Alk model outputs to measurements in Fig 3.14: these variables are the most influential factors in the C_{ant} estimates (section 3.2). Out of the ocean, Bronselaer et al. (2017) identified the time interval of atmospheric CO_2 increase as an additional source of disagreement between observed and simulated C_{ant} values. However, we do not explore this source, assuming it to be comparable across all of the explored model results.

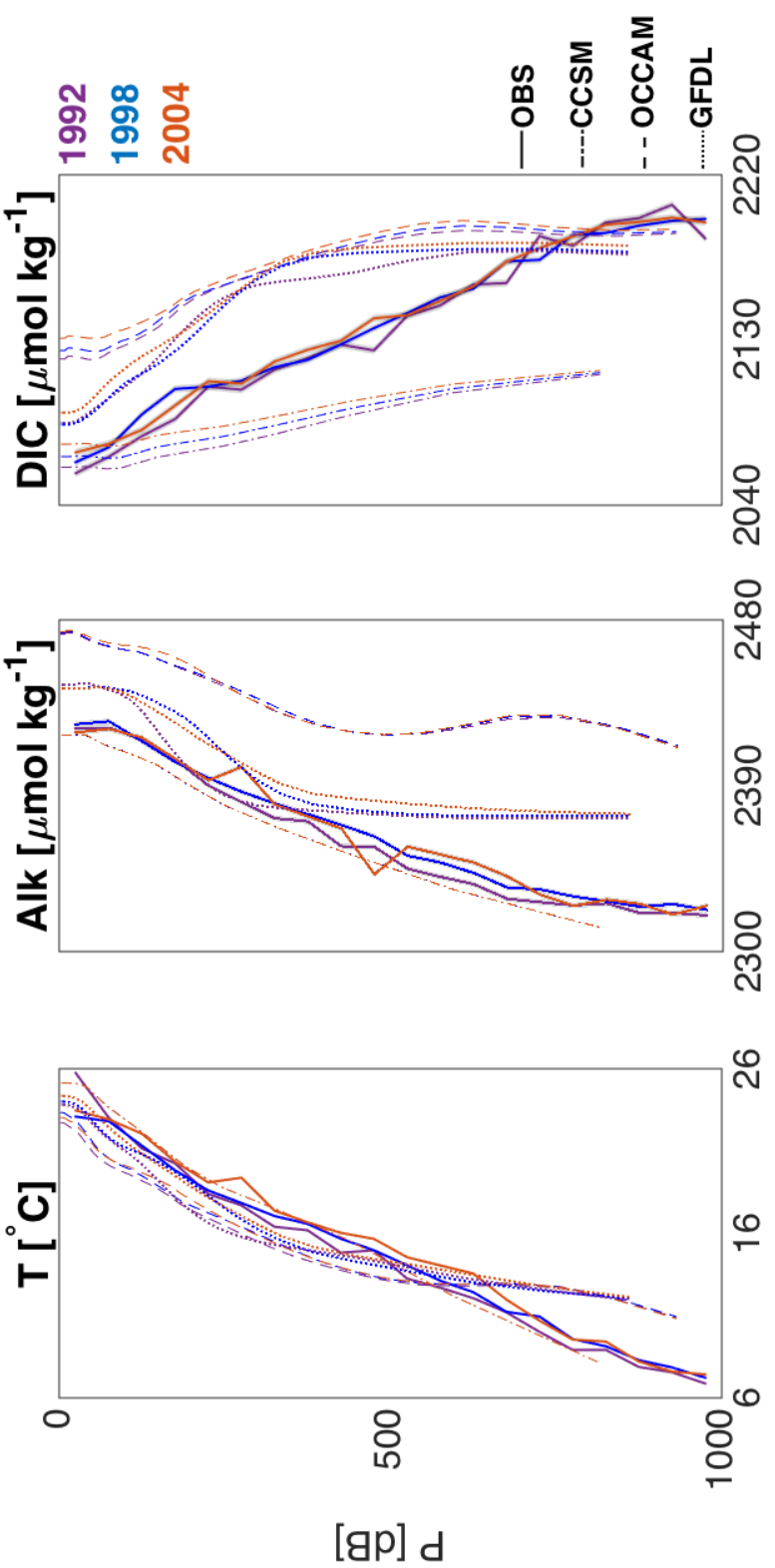

FIGURE 3.14: *Upper ocean profiles of Temperature (T), Dissolved Inorganic Carbon (DIC), and total Alkalinity (Alk) averaged at the 24.5° N Atlantic transect in 1992, 1998, and 2004. Data taken from the observations (OBS), OCCAM, CCSM, and GFDL-ESM2M models. OBS analytical uncertainties reported as shaded areas, although they are hardly discernible due to the x-axes scales.*

Temperature is the most reliably simulated variable. The outputs of the CCSM model do not significantly differ from observations (OBS), whilst the OCCAM and GFDL-ESM2M fields agree reasonably well with them above 600 m, overestimating T below this depth. All models underestimate the observed T variability over time. The DIC and Alk vertical patterns are also broadly captured by all of the models investigated. However, the OCCAM and GFDL-ESM2M overestimate the variable concentrations, whilst the CCSM underestimates the DIC below 100 m. Variations over time are comparable between the modelled and observed DIC and Alk.
In summary, the OCCAM, CCSM, and GFDL-ESM2M data of T, DIC, and Alk are comparable to observations. Among these variables, T is the most reliably modelled, suggesting the models better reproduce the oceanic ventilation, while they struggle with biogeochemistry. As a consequence, we expect the $\Phi C_T{}^0$ and TTD techniques to perform better than the ΔC^* and TrOCA methods on the model platforms.

3.5.2 Comparison of modelled C_{ant} estimates

We compare the TTD, ΔC^*, $\Phi C_T{}^0$, and TrOCA estimates with the MOD C_{ant} in the outputs of the GFDL-ESM2M, CCSM, and OCCAM models by using observations based coefficients on the C_{ant} equations. This approach highlights challenges in the C_{ant} methods, identifies the most accurate technique in the models, and it allows us to estimate the dependency of the C_{ant} method coefficients from the chosen dataset. We focus on the 24.5°N upper 1000 m in 1992, 1998, and 2004, as it was done in sections 3.2 and 3.3, but we base the analysis on model outputs conversely to those studies, which were based on observations. The TTD mean age is estimated using the CCSM and the OCCAM CFC-12, and the GFDL-ESM2M CFC-11, all of them based on a saturation of 100 %.
The OCCAM, CCSM, and GFDL-ESM2M results are presented in Figs 3.15, 3.16, and 3.17, respectively. We plot standard deviations, Root Mean Square Differences (RMSD), and Pearson's correlation coefficients relative to the MOD C_{ant} reference for the four method estimates by using Taylor diagrams (Taylor, 2001).

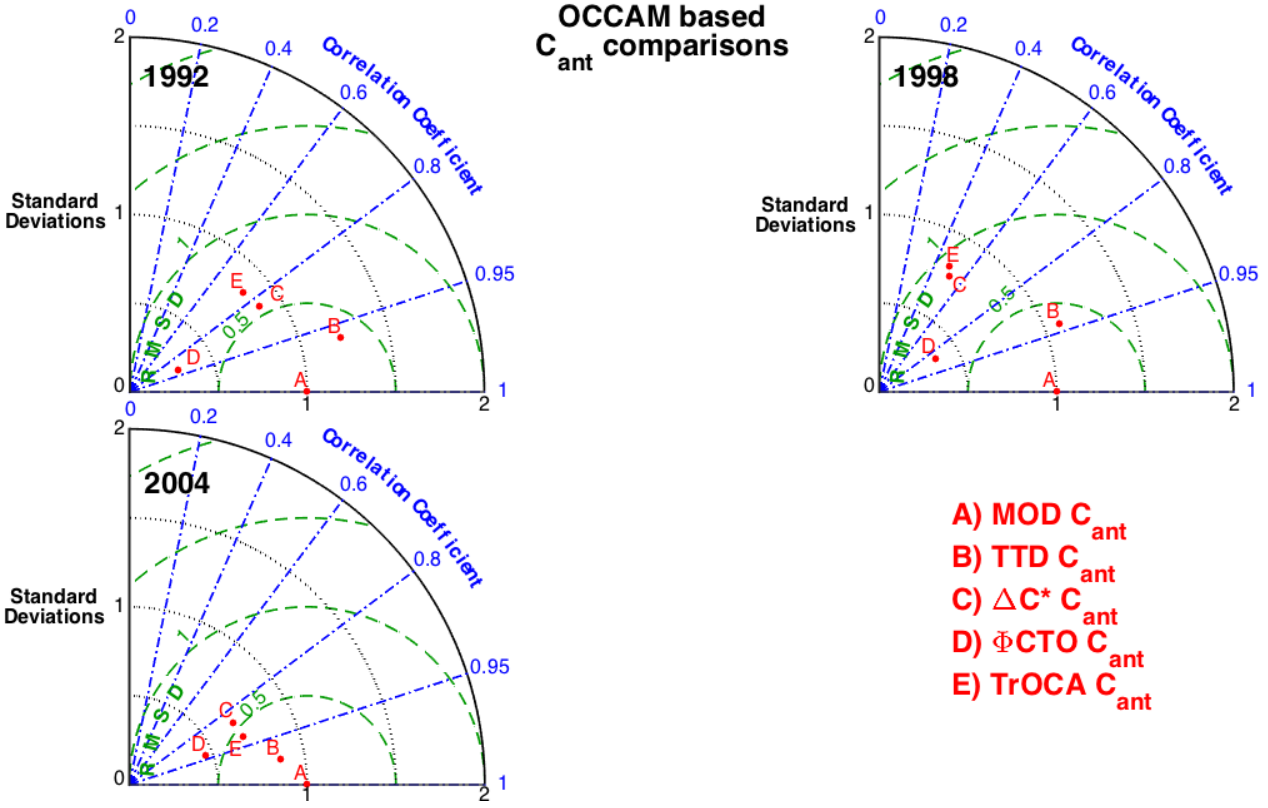

FIGURE 3.15: *Taylor diagrams showing the anthropogenic Carbon (C_{ant}) estimates based on OCCAM synthetic data. For comparisons with the observational analyses of sections 3.2 and 3.3, the study is conducted in the upper 1000 m of the 24.5°N Atlantic transect in 1992, 1998, and 2004. Standard deviations, Root Mean Square Differences (RMSD) and correlation coefficients are all quantified with respect to the reference MOD C_{ant}. The TTD C_{ant} is based on modelled CFC-12 saturated at 100 %.*

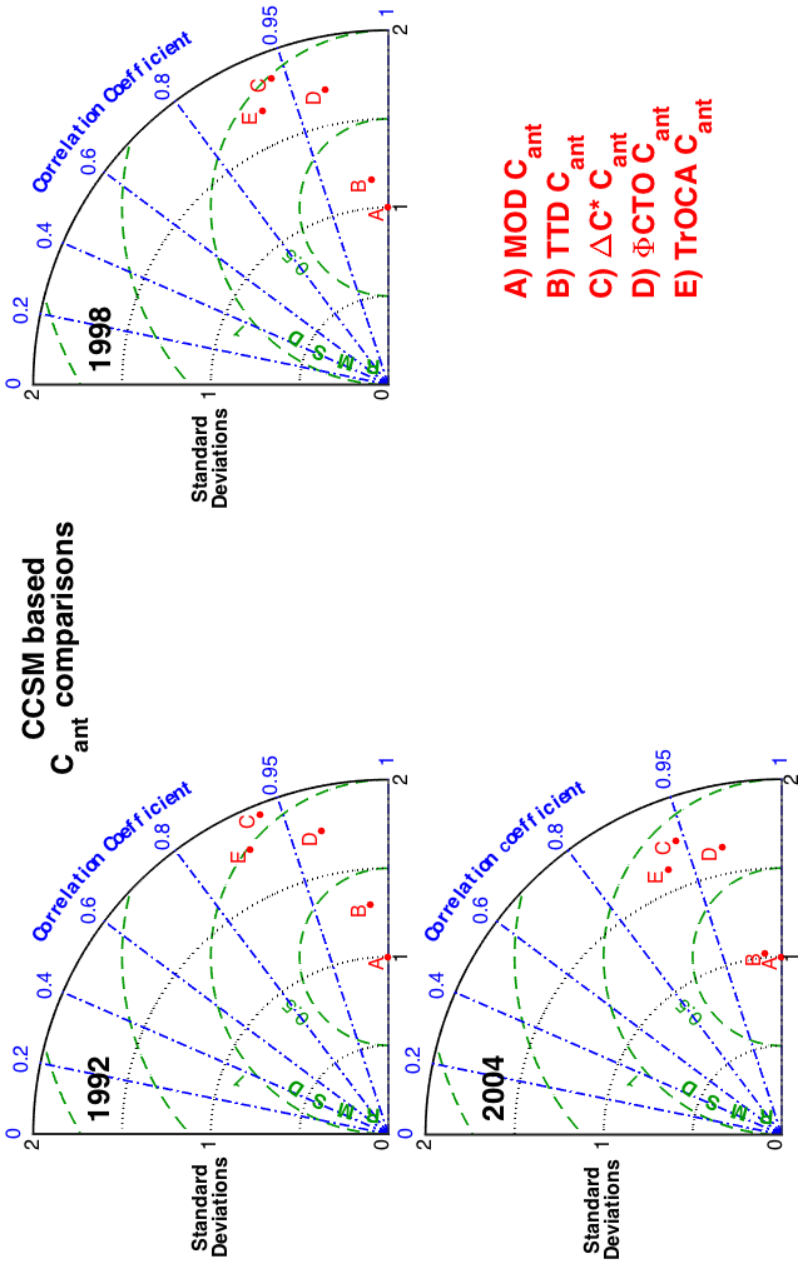

FIGURE 3.16: *Same as in Fig 3.15, but for the CCSM Earth system model outputs.*

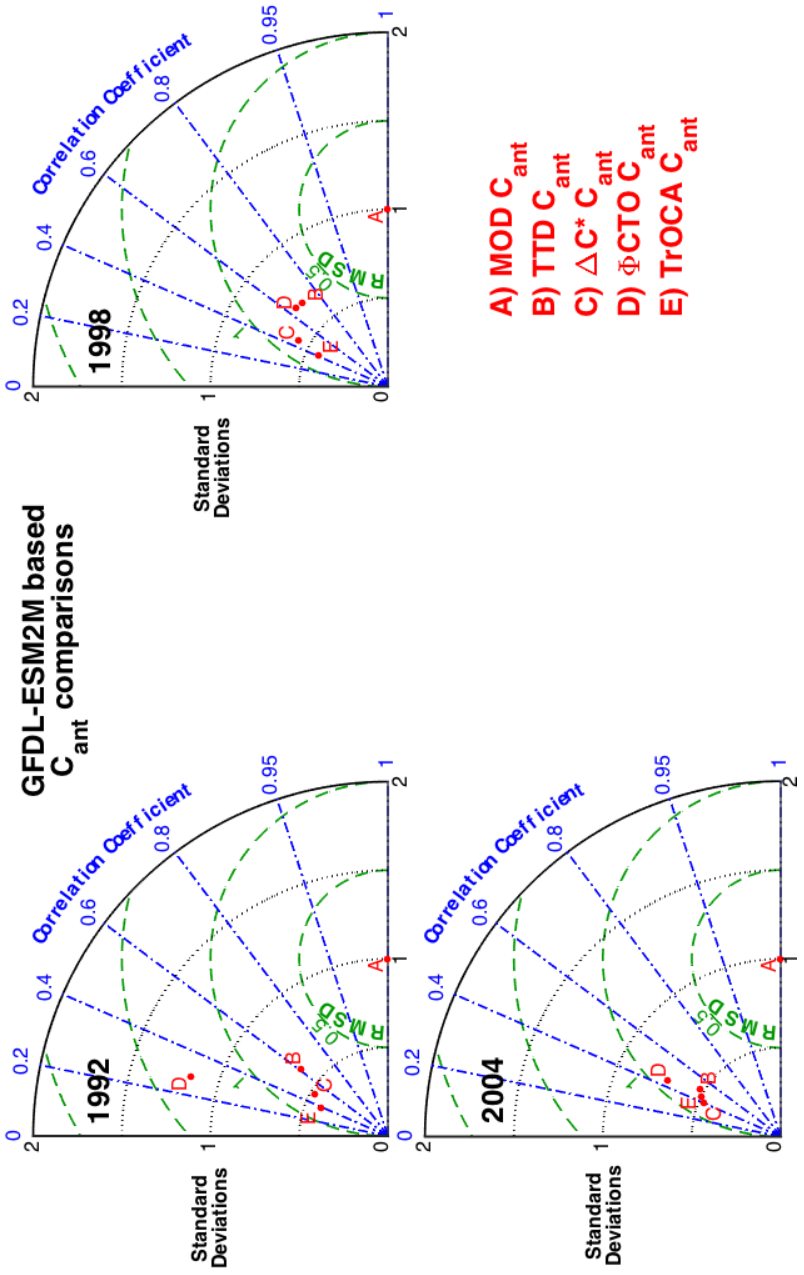

FIGURE 3.17: *Same as in Fig 3.15, but for the GFDL-ESM2M Earth system model outputs. The TTD C_{ant} estimates are based on CFC-11 simulated data saturated at 100 %.*

Within OCCAM, the TTD and MOD C_{ant} estimates are the most consistent, being the nearest in all Taylor diagrams. The ΔC^* C_{ant} is the most accurate amongst the back-calculations, followed by TrOCA. Conversely, the results obtained using $\Phi{C_T}^0$ differ from the other back-calculations potentially due to the OMP constraint in this technique. The OMP adds bias owing to its dependency on T, S, and nutrient data. Within CCSM, the TTD and MOD C_{ant} estimates are also the nearest. $\Phi{C_T}^0$ is the most accurate amongst the back-calculations, with the model outputs being the most comparable to observations. The lowest confidence is given to TrOCA and an intermediate reliability is quantified for the ΔC^* estimates.

The GFDL-ESM2M results are comparable to the OCCAM investigations. The TTD values are the closest to the MOD C_{ant}, followed by the ΔC^*, TrOCA, and $\Phi{C_T}^0$ results. As in OCCAM, the GFDL-ESM2M $\Phi{C_T}^0$ C_{ant} differs from the other back-calculation results owing to biases in the observational OMP application.

In summary, the TTD estimate is the most comparable to the MOD C_{ant} in the models investigated, followed by ΔC^*, $\Phi{C_T}^0$, and TrOCA. We confirm that the models better reproduce the ocean ventilation on which the TTD and $\Phi{C_T}^0$ are based, as it was hypothesised at the end of section 3.5.1. Conversely, they struggle with biogeochemistry, thus increasing the uncertainty in the back-calculations: the averaged C_{ant} concentration estimated with the ΔC^* method in the 24.5°N upper 1000 m is roughly two times greater than the same value estimated with the TTD.

3.5.3 Reconciling modelled and observed C_{ant} estimates

Back-calculation techniques require the calculation of the equation coefficients for each dataset on which they are applied: the use of observations based coefficients on model outputs leads to discrepancies with the MOD C_{ant} estimates (section 3.5.2). To remove this inaccuracy, we replicate the approach of Gruber et al. (1996) and redefine the ΔC^* equations using outputs of the OCCAM model. We use only this back-calculation and the OCCAM model outputs for brevity, but a similar approach can be extended to other techniques and models.

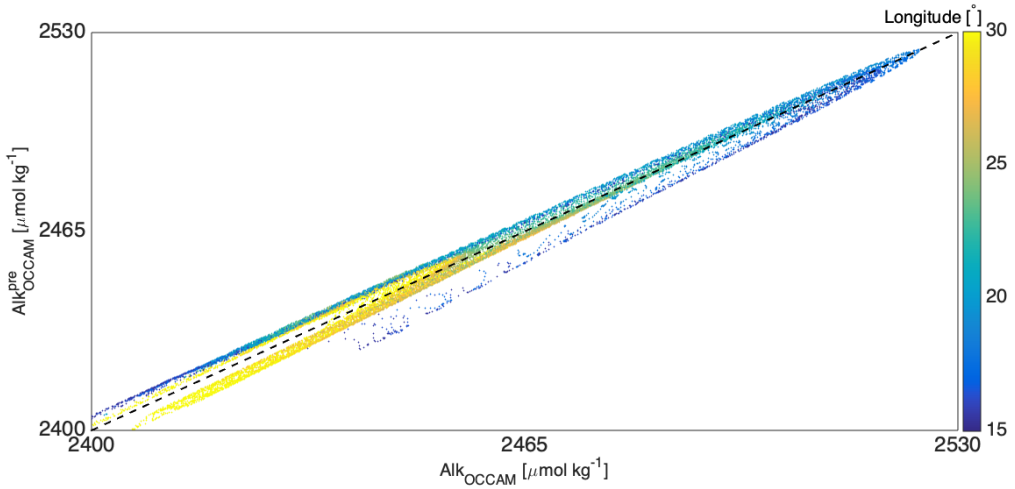

FIGURE 3.18: *Subtropical North Atlantic preformed (Alk^{pre}) versus total (Alk) Alkalinity. Data are taken from the OCCAM general circulation model between 1990 and 2004 and averaged in the subtropical North Atlantic upper 100 m between 78-16° W. Colours identify the latitude, while R^2 is 0.99 and $p < 0.01$.*

We estimate Alk^{pre} (Eq 3.6) using model outputs of salinity and preformed phosphate (PO_4^{pre}), as it was done by Gruber et al. (1996):

$$Alk^{pre}_{OCCAM} = 68.4\,S\ -\ 6.1\,10^{-2}\,PO^{pre}_4\ -\ 34.0 \tag{3.6}$$

We extract the model data in the upper 100 m of the subtropical Atlantic (15-35°N), where the C_{ant} increase does not influence Alk owing to the local super saturation of aragonite and calcite (Gruber et al., 1996; Takahashi et al., 1981). We use the data to estimate Alk^{pre} and we test the reliability of the approach in Fig 3.18.
We also quantify the C^{OCCAM}_{eq} (Eq 3.7) by using an approach similar to Eq 3.6, but relying on data of Θ, S, and the newly calculated Alk^{pre}_{OCCAM}. As C^{OCCAM}_{eq} reference, we use the model pre-industrial DIC. This approach differs from the study of Gruber et al. (1996), where the authors used an atmospheric pCO_2 of 280 ppm, but it allows to estimate the oceanic DIC before the beginning of the industrial era. The C^{OCCAM}_{eq} estimate is assessed in Fig 3.19.

$$C^{OCCAM}_{eq} = 439.3\ -\ 8.5\,\Theta\ +\ 27.9\,S\ +\ Alk^{pre}_{OCCAM} \tag{3.7}$$

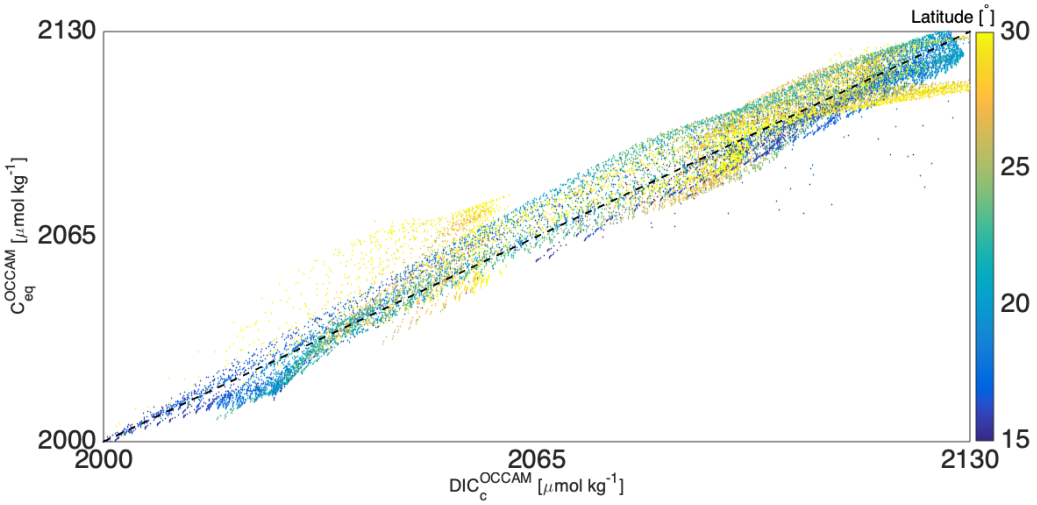

FIGURE 3.19: *Same as in Fig 3.18, but for the equilibrium Carbon (C_{eq}) estimate. R^2 and p are estimated as 0.96 and lower than 0.01 respectively.*

Applying our recalculated Alk_{OCCAM}^{pre} and C_{eq}^{OCCAM} to the model ΔC^* C_{ant}, we reduce its value in the 24.5°N upper 1000 m from 84.6 μmol kg^{-1} to 54.5 μmol kg^{-1}. The last is consistent with the C_{ant}^{MOD} (49.9 μmol kg^{-1}) and C_{ant}^{TTD} (52.3 μmol kg^{-1}) within the method uncertainty: as anticipated at the beginning of this section, the use of back-calculation techniques requires the recalculation of the equation coefficients for every change in the dataset used. This result agrees with the implicit assumptions of Yool et al. (2010), Waugh et al. (2006), and Matsumoto and Gruber (2005).
In summary, we reconcile the TTD and ΔC^* C_{ant} estimates in the assessment of the method accuracies within the OCCAM outputs. This allows us to further explore the C_{ant} uncertainty by focusing only on those methodologies (chapters 4 and 5).

3.6 Synthesis and discussion

We analyse the C_{ant} sensitivity to observed factor variabilities, analytical precisions and method assumptions by using the One Factor At a Time and Variance Based Sensitivity Analysis approaches. Under OFAT, the ΔC^* requires a precision in the DIC, Alk, and O_2 measurements of ± 4.0 μmol kg^{-1}, ± 10.0 μmol kg^{-1}, and ± 1.5 μmol kg^{-1} to keep the C_{ant} analytical uncertainty to ± 5.0 μmol kg^{-1}. The TTD necessitates precisions in the CFC-12 and SF_6 measurements of ± 0.01 pmol kg^{-1}

and ±0.03 fmol kg^{-1} to reach the same goal. Under VBSA, variances in the DIC, Θ, and O_2 measurement influence the ΔC* estimates, while the TTD C_{ant} depends on the tracer measurements, saturations, temperature, and the interactions among those factors. Merging our and other authors' results, we increase the global ocean C_{ant} total uncertainty from a previously suggested ±20 % to ±34 % for the TTD and ΔC* estimates. However, in confined and well-sampled regions of the ocean (e.g. subtropical (24.5°N) North Atlantic upper 1000 m), this value decreases to ±13 % and ±14 % for the same C_{ant} estimates, respectively. These uncertainties propagate to the variables that are calculated using C_{ant} (e.g. anthropogenic pH). Overall, the TTD C_{ant} estimates are influenced by the lowest uncertainty, but those values do not account for the export from the MLD of biologically fixed CO_2. Conversely, the ΔC* C_{ant} values are affected by a greater uncertainty potentially due to changes in ocean steady state, biogenic influences on C_{ant}, and correlations between predictive and predicted factors used by the linear regressions included in the technique equations. These uncertainty sources enhance the C_{ant} disagreements in model outputs, requiring a redefinition of the regression coefficients based on the synthetic dataset. Furthermore they cannot be investigated focusing only on C_{ant} estimates, but necessitates the study of every dissolved inorganic carbon partition (Williams and Follows, 2011), as it will be done in the next chapter.

Chapter 4

Measured and simulated carbon pools, trends, and variabilities

4.1 Introduction

In chapter 3, we found that the TTD and ΔC^* C_{ant} estimates differ, being influenced by different sources of uncertainty. The first isolates the ocean physical CO_2 uptake by using transient tracers, while the second removes a biogenic influence estimate from the measured Dissolved Inorganic Carbon (DIC). To better assess C_{ant} trends and variabilities in the North Atlantic, we investigate this variable in conjunction with the other components of the DIC cycle by using the Williams and Follows (2011) partitioning (section 4.2). Carbon trends are studied by fitting least square linear fits to mean concentrations, and they are quantified by using a quasi Monte Carlo (MC) approach (Kroese et al., 2014; Metropolis and Ulam, 1949), as done by Guallart et al. (2015b) for C_{ant}. Residuals of the fitted values indicate carbon variabilities, while we quantify the carbon partition uncertainties by randomly perturbing each estimate under a second quasi MC analysis. We investigate the repeated time series (1992-2010) at the 24.5°N Atlantic section, where we separate thirty-seven subareas to capture regional and water mass specific carbon trends and variabilities. Then, we extend the study to the North Atlantic basin (0-65°N) by using the climatology of the Global Ocean Data Analysis Project version 2 (GLODAPv2; Lauvset et al. (2016))

and Climate Model two Model coordinate (CM2Mc) Earth System Model (ESM) outputs (section 4.3). Using simulated data, we also enlarge the analysis over time to the past (1880-1900), present (1980-2000), and future (2080-2100) projected under the Representative Concentration Pathway 8.5 (RCP8.5; IPCC (2014); Taylor et al. (2012); van Vuuren et al. (2011)). We use an 'industrial', 'climate', and pre-industrial 'control' simulations to investigate the interplay between the DIC components.

4.2 Carbon trends and variabilities at 24.5°N

4.2.1 Dissolved inorganic carbon partitioning

We use the carbon partitioning of Williams and Follows (2011) to study the influence of surface fluxes, hard tissue, soft tissue, and solubility carbon pumps on the C_{ant} estimates (Fig 4.1). Under this approach, six DIC (or total inorganic Carbon (C_{tot})) partitions are identifiable as proxies for the mentioned processes. These are used to partition the DIC throughout three complimentary approaches (Eqs 4.1-4.3), which differ for the separation of the saturated Carbon (C_{sat}) between a pre-industrial and an anthropogenic components or the inclusion of the last with the disequilibrium Carbon (C_{dis}) in the residual value (Goodwin et al., 2008; MacGilchrist et al., 2014).

$$C_{tot} = C_{sat} + C_{dis} + C_{soft} + C_{carb} \tag{4.1}$$

$$C_{tot} = C^{0}_{sat} + C^{ant}_{sat} + C_{dis} + C_{soft} + C_{carb} \tag{4.2}$$

$$C_{tot} = C^{0}_{sat} + C_{res} + C_{soft} + C_{carb} \tag{4.3}$$

- **Saturated carbon (C_{sat}).** C_{sat} accounts for the DIC the ocean would have when in CO_2 equilibrium with the atmosphere. C_{sat} includes a preindustrial (C^{0}_{sat}) and an anthropogenic (C^{ant}_{sat}) components, which are due to the natural CO_2 background and human-caused contributions to its atmospheric increase since 1860. C^{0}_{sat} is estimated with measurements of Temperature (T), Salinity (S), dissolved oxygen (O_2), preformed inorganic nutrients (nitrate ($NO_3{}^{pre}$), silicate ($Si(OH)_4{}^{pre}$), and phosphate ($PO_4{}^{pre}$), Eqs 4.4-4.6), a preformed

Alkalinity (Alk^{pre}) estimate (Eq 4.7) and pre-industrial CO_2 partial pressure (pCO_2^0) of 278 ppm. From them, we infer C_{sat}^0 (Eq 4.8) using co2sys (section 2.2; Lewis and Wallace (1998); Van Heuven et al. (2011)).
C_{sat}^{ant} approximates the anthropogenic carbon component, being based on the atmospheric pCO_2 (Dlugokencky et al., 2017) measured when the water mass was last in contact with the atmosphere by using TTD mean ages.

$$PO_4^{pre} = PO_4 - (-RR_{O:P}\,(O_2^{sat} - O_2)) \tag{4.4}$$

$$NO_3^{pre} = NO_3 - \left(-\frac{RR_{O:P}}{RR_{N:P}}(O_2^{sat} - O_2)\right) \tag{4.5}$$

$$Si(OH)_4^{pre} = Si(OH)_4 - \left(-\frac{RR_{O:P}}{RR_{S:P}}\,(O_2^{sat} - O_2)\right) \tag{4.6}$$

$$\begin{aligned} Alk^{pre} = {} & 0.008\,(\Theta - 20)^2 + 0.464\,(S - 35)^2 - 0.282 \\ & \Theta + 55.592\,S + 0.019\,NO_3^{pre} + 0.001\,PO_4^{pre} + 350.54 \end{aligned} \tag{4.7}$$

$$C_{sat}^0 = f(pCO_2^0, Alk^{pre}, T, S, {Si(OH)_4}^{pre}, {PO_4}^{pre}) \tag{4.8}$$

where RR are the Redfield Ratios between phosphate and (1) O_2 ($RR_{O:P}$), (2) nitrate ($RR_{N:P}$), and (3) silicate ($RR_{S:P}$; Redfield (1934)). The preformed Alkalinity (Eq 4.7) is regressed on potential temperature (Θ), salinity, and preformed nutrients obtained from the GLODAPv2 data for the North Atlantic upper 100 m, in line with the work of Gruber et al. (1996) and section 3.5.3.

- **Soft-tissue carbon (C_{soft}).** C_{soft} quantifies the DIC that originates from the remineralisation of the sinking soft tissue (Fig 1.6; Brewer (1978)). This partition is approximated (Eq 4.9) by using the Apparent Oxygen Utilisation (AOU, Eq.4.10; Pytkowicz (1971)) and the Redfield ratio between DIC and O_2

($RR_{C:O}$). We test this approximation in section 5.4 by using CM2Mc outputs.

$$C_{soft} = -\frac{RR_{C:P}}{RR_{O:P}} AOU \tag{4.9}$$

$$AOU = O_2^{sat} - O_2 \tag{4.10}$$

where O_2^{sat} is the saturated O_2 and is estimated from T and S measurements.

- **Carbonate carbon (C_{carb}).** C_{carb} measures the DIC due to the dissolution of the sinking carbonate hard tissue (e.g. shells). This partition is estimated as in Eq 4.11 (Brewer, 1978).

$$C_{carb} = 0.5 \left(Alk - Alk^{pre} - \frac{RR_{N:P}}{RR_{O:P}} AOU \right) \tag{4.11}$$

- **Residual carbon (C_{res}).** C_{res} includes the surface disequilibrium DIC (C_{dis}), C_{sat}^{ant}, and the uncertainty in the carbon partitioning (Eq 4.12). In the literature, C_{res} is generally used as a proxy for the C_{sat}^{ant} signal owing to the difficulty in the separation between C_{sat}^{ant} and C_{dis} (MacGilchrist et al., 2014; Williams and Follows, 2011). However, we overcome this challenge, as it will be summarised later in this section and detailed in section 4.2.3.

$$C_{res} = C_{sat}^{ant} + C_{dis} \tag{4.12}$$

- **Anthropogenic carbon (C_{ant}).** C_{ant} (Eq 4.13) is inferred removing C_{sat}^{0} from the C_{sat} determined at the time when seawater was last in contact with the atmosphere (McNeil et al., 2003; Thomas and Ittekkot, 2001). This C_{ant} is equal to C_{sat}^{ant} and it allows to directly quantify the most recent changes in atmospheric CO_2 and the ocean uptake caused by the anthropogenic activities. In this thesis, we name the C_{ant} estimated by using Eq 4.13 as Decomposition (DEC) C_{ant} (C_{ant}^{DEC}) to differentiate its value from the estimates obtained with

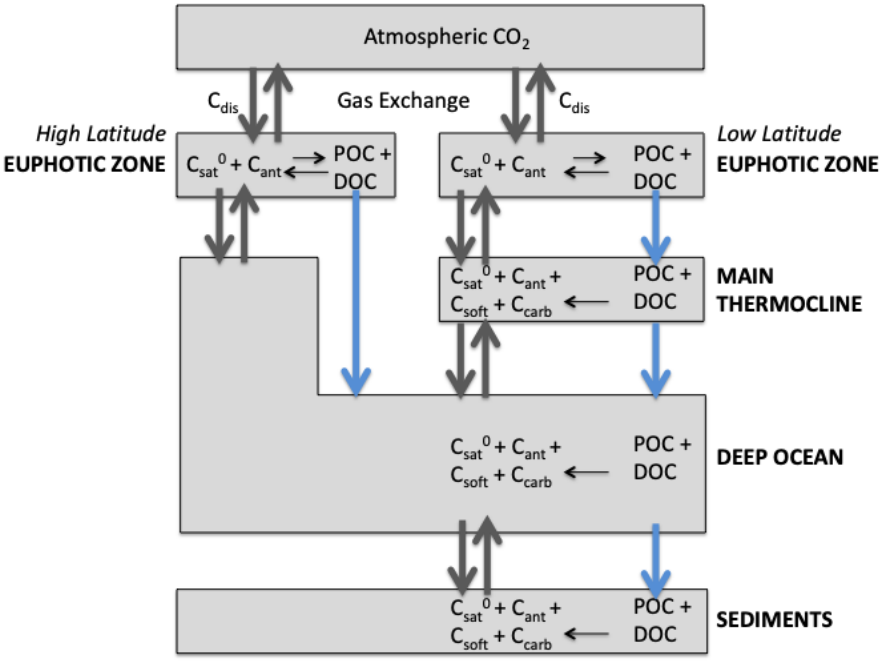

FIGURE 4.1: *Summary of dissolved inorganic carbon partitions and influencing processes in the lower atmosphere and global ocean (Williams and Follows, 2011). In addition to the Carbon dioxide (CO_2), listed partitions are disequilibrium carbon (C_{dis}), pre-industrial saturated carbon (C^0_{sat}), anthropogenic carbon (C_{ant}), soft-tissue carbon (C_{soft}), and carbonate carbon (C_{carb}). Two grey arrows schematise physical processes and identify 'gas exchanges' where shown and 'circulation and mixing' elsewhere. The blue line isolates processes of CO_2 export. The POC and DOC identify the Particulate and Dissolved Organic Carbon respectively (Fig 1.6).*

the methods described in Chapter 2.

$$C_{ant}^{DEC} = C_{sat} - C_{sat}^0 \tag{4.13}$$

- **Disequilibrium carbon (C_{dis}).** C_{dis} estimates the difference between the upper-ocean ocean and low-atmosphere CO_2 partial pressures, and therefore approximates the surface carbon fluxes (Eq 1.1). This carbon partition is estimated by removing C_{sat}^{ant} from C_{res}, being of the same order of magnitude of them. As a result, C_{dis} includes the uncertainty of the partitioning approach.

$$C_{dis} = C_{res} - C_{sat}^{ant} \tag{4.14}$$

4.2.2 Data and approach

The repeated observations collected at 24.5°N in the Atlantic are valuable to assess DIC partition trends and variabilities. Guallart et al. (2015b) used those datasets to study C_{ant} from 1992 to 2011, and found that it increases everywhere over time, with the upper-ocean (0-1000 m) range of C_{ant} trend estimates included between 0.6 $\pm$ 0.2 μmol kg^{-1} yr^{-1} (TTD) and 0.9 $\pm$ 0.2 μmol kg^{-1} yr^{-1} (ΔC*).

We enlarge the Guallart et al. (2015b) study by investigating all of the Williams and Follows (2011) carbon partitions. These are detailed in section 4.2.1 and are used to explore physical and biological carbon pump effects, separating atmospheric CO_2, primary productivity, residence time, and sea surface temperature variations. These processes were discussed in chapter 3 for C_{ant} and they are further investigated here for each of the DIC partitions at the 24.5°N Atlantic transect.

In the 24.5°N hydrographic section, we isolate seven water masses in six longitudinal areas, as shown in Fig 4.2. These water masses were introduced in Tab 1.1 and are: water column upper 200 m, referred to as subtropical Mode Water (MoW); Madeira MoW, subpolar MoW, Antarctic Intermediate Water (AAIW), upper North Atlantic Deep Water (NADW), lower NADW, and Antarctic bottom water.

Longitudinally, we divide the section at 80°W, 78°W, 70°W, 60°W, 45°W, 30°W, and 16°W. We show the resulting thirty-seven subareas in Fig 4.2 for completeness, but we focus the discussion on the MoW, which contains the highest amount of C_{ant}, and the AAIW, which includes the highest remineralised carbon pool (mostly C_{soft}) in the North Atlantic subtropical upper-ocean (0-1000 m) layer.

Over longitude, we summarise the study by focusing on three regions: (1) the Florida Strait (FS) with high remineralisation, (2) the highly ventilated Western (W) basin in comparison with (3) the Eastern (E) basin, which is influenced by a northwards return circulation of older seawater and a region of upwelling near the African coast. In these regions, we investigate C_{ant} trends and variabilities over time in conjunction with the other DIC pools. We separate four C_{tot} partitions: C^0_{sat}, C_{soft}, C_{carb}, C_{res}. We further divide C_{res} into C_{ant} and C_{dis}, as Williams and Follows (2011) suggested, but not yet applied due to the difficulty in this approach (MacGilchrist et al., 2014).

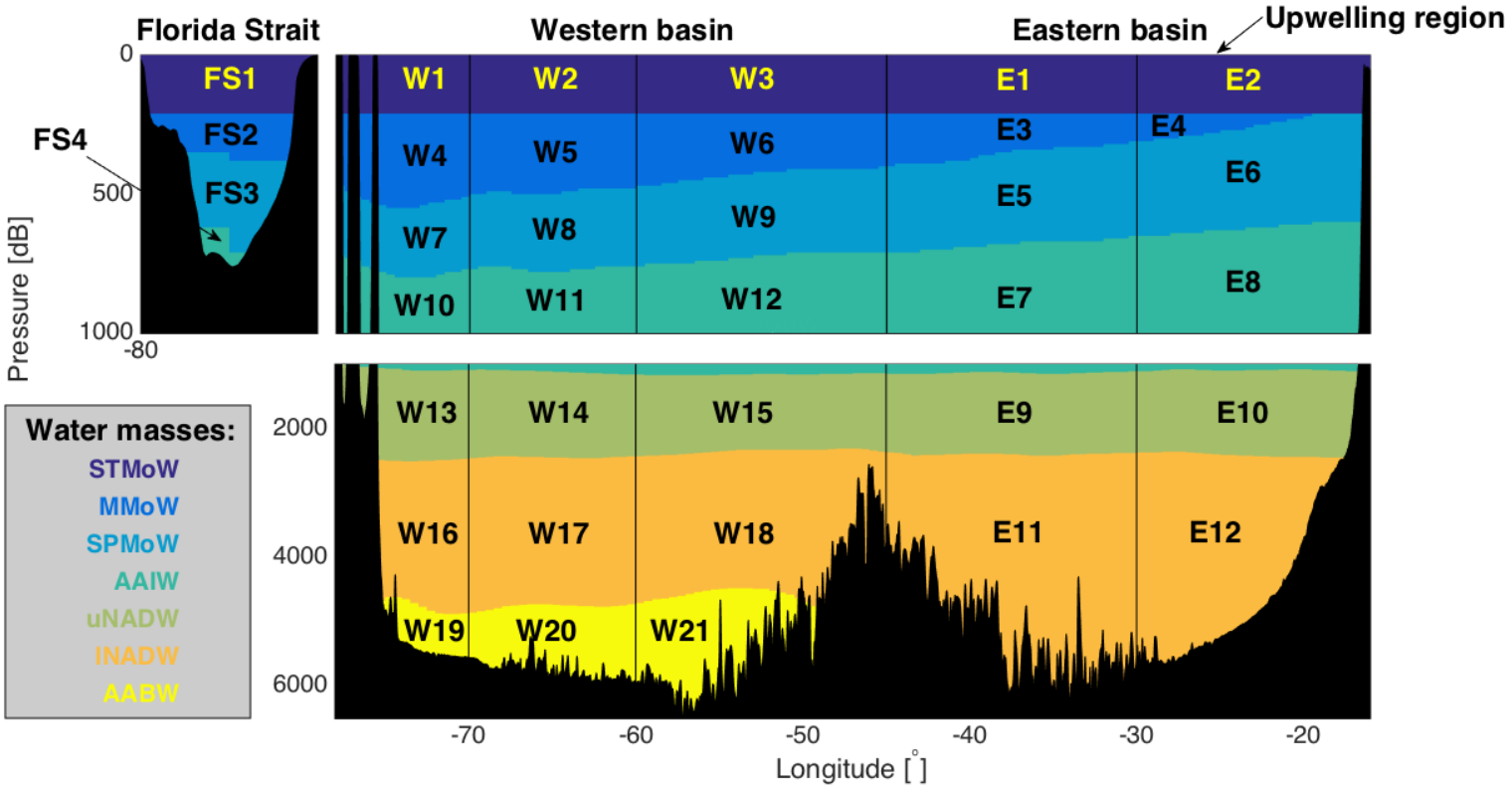

FIGURE 4.2: *Division of the 24.5°N Atlantic transect with the main water masses (Subtropical Mode water (STMoW), Madeira MoW (MMoW), subpolar MoW (SPMoW), Antarctic intermediate water (AAIW), upper North Atlantic deep water (uNADW), lower NADW (lNADW), and Antarctic bottom water (AABW)) reported in colour. The section subareas are identified by using one isobar (200 dB), six longitudinal divisions, and the water mass isopycnal definitions described in Tab 1.1. FS, W, and E respectively identify the Florida Strait, Western basin, and Eastern basin of the studied transect. The last includes the upwelling region towards the African coast. Here, the subarea E4 includes only a fraction of the MMoW, as it can be noticed by comparing its limits and the density distribution (not shown for simplicity). This is due to the use of an isobar to separate the upper 200 m.*

We overcome this challenge by quantifying each partition uncertainty, improving the C_{ant} one specifically (chapter 3), and applying a quasi MC approach on those values.

4.2.3 Carbon partition uncertainties and mean ranges

The Williams and Follows (2011) partitioning carries a set of uncertainties, different for each partition and summarised here. We analyse these uncertainties in the upper 1000 m of the 24.5°N transect and compare them to the global ocean values. We use the measurement precisions suggested in the Global Ocean Ship-based Hydrographic Investigations Program (GO-SHIP) guidelines (Hood et al., 2010), which apply to the global ocean, and the ones measured and reported in the 24.5°N cruise reports (Cunningham et al., 2005; King et al., 2012; Millero et al., 2000; Peltola et al., 2001), which apply to the subtropical North Atlantic. Results are shown in Tab 4.1.

Total carbon (C_{tot}). C_{tot} represents the ocean DIC (section 4.2.1). This partition and associated uncertainty are directly quantifiable. The last is due to the accuracy in the DIC measurements and increase from the global scale to the upper 1000 m of the 24.5°N transect. This rise is however negligible within the quasi MC estimates.

Pre-industrial saturated carbon (C^0_{sat}). C^0_{sat} quantifies the DIC fraction that the ocean would have when in carbon dioxide (CO_2) equilibrium with the overlying pre-industrial atmosphere. C^0_{sat} is the largest DIC component and is estimated using the co2sys set of calculations (Lewis and Wallace, 1998; Van Heuven et al., 2011). Then, influential sources of uncertainty are the Alk, pCO^0_2, T, and nutrient (used for the Alk^{pre} estimates) accuracies, which lead to uncertainties comparable between the global ocean and local scales.

Soft-tissue carbon (C_{soft}). C_{soft} quantifies the DIC due to the remineralisation of the sinking soft tissue in the ocean. This partition is inferred from AOU and it is influenced by T, S, and O_2 measurement precisions. Among them, the O_2 accuracy is the most influential, but we sum it with the others, obtaining a C_{soft} uncertainty comparable between the two investigated scales (global ocean and subtropics).

Carbonate carbon (C_{carb}). C_{carb} quantifies the DIC due to the remineralisation of the sinking hard tissue in the ocean. This partition is calculated from AOU, Alk,

TABLE 4.1: *Table summarising inorganic carbon partition mean ranges and uncertainties in the global ocean (Global; Hood et al. (2010)) and 24.5°N upper 1000 m. Listed partitions are total (C_{tot}), pre-industrial saturated (C^0_{sat}), soft-tissue (C_{soft}), carbonate (C_{carb}), anthropogenic (C_{ant}), and disequilibrium (C_{dis}). C_{ant} and C_{dis} are estimated by using the TTD as in the GLODAPv2 climatology (Lauvset et al., 2016). MC indicates the results of the quasi Monte Carlo analyses (Kroese et al., 2014; Metropolis and Ulam, 1949), while DT identifies the Decadal Trend uncertainty, also based on a MC analysis.*

	Range		Uncertainty			
	Global	24.5°N	Global	24.5°N	MC	DT
Units	μmol^{-1} kg^{-1}					μmol^{-1} kg^{-1} yr^{-1}
C_{tot}	1019 to 2403	2032 to 2225	2.0	3.0	1.3	0.1
C^0_{sat}	1129 to 2288	1997 to 2119	4.0	3.0	2.0	0.1
C_{soft}	0 to 196	0 to 100	2.0	2.0	1.3	0.1
C_{carb}	0 to 180	0 to 10	5.0	2.3	1.5	0.1
C_{ant}	0 to 73	9 to 65	17.0	10.0	5.2	0.2
C_{dis}	-334 to 23	-64 to 17	18.4	11.3	6.2	0.3

and Alk^{pre}. So, we sum these variable influences, obtaining a C_{carb} uncertainty in the global ocean that is two times greater than the one applicable in the 24.5°N upper 1000 m, where Alk and O_2 measurements are more precise (Tab 1.2).

Anthropogenic carbon (C_{ant}). C_{ant} concentrations are estimated with the TTD method, as explicitly reported in the GLODAPv2 climatology, and would change using other methods. Despite this source of variability, the C_{ant} uncertainty depends on locations, data, and intervals of time (section 3.4). Our 24.5°N range maximum compares to the highest limit of the interval suggested by Matsumoto and Gruber (2005), Vázquez-Rodríguez et al. (2009b), and Waugh et al. (2006): we use ±10.0 μmol kg^{-1} and ±17.0 μmol kg^{-1} as 24.5°N and global uncertainties (section 3.4.1).

Disequilibrium carbon (C_{dis}). C_{dis} quantifies the ocean DIC due to the surface CO_2 disequilibrium with the atmospheric CO_2 mole fraction. Here, this component is inferred removing C_{ant} from C_{res}: C_{dis} carries the uncertainty of all carbon partitions. These uncertainty estimates are randomly distributed and cannot be added linearly. Instead, we estimate the C_{dis} uncertainty by quantifying the square root of the sum

of the other partitions uncertainty squares and obtaining values comparable to the C_{ant} estimates (Tab 4.1). This calculation of the C_{dis} uncertainty is approximately two times greater than the one obtained by applying the same approach to C_{res} (± 7.0 μmol kg^{-1}). Therefore, changes in C_{res} are often used to approximate variations in the anthropogenic and disequilibrium pools (MacGilchrist et al., 2014; Williams and Follows, 2011). We use only the TTD method for the estimate of the C_{dis} uncertainty.

Uncertainties. We apply a quasi MC analysis (Kroese et al., 2014; Metropolis and Ulam, 1949) on the partition uncertainties, as comparably done by Guallart et al. (2015b) for C_{ant}. This approach allows us to remove effects of analytical precisions and underlying method assumptions from each carbon partition uncertainty. Thus, the MC approach isolates the observed variability, which includes influences on the CO_2 uptake and storage of variations in circulation, wind stress, buoyancy fluxes, and biological cycles (Henson et al., 2010; McKinley et al., 2017).

Decadal Trends (DTs). Figs 4.3-4.6 and Tabs 4.2-4.5 show estimates of the DTs and mean values for each of the explored carbon partitions across the 24.5°N section. We estimate the partition DTs by replicating the quasi MC analysis on cruise-mean concentrations, as also done by Guallart et al. (2015b) for C_{ant}. We determine 1000 random alterations for each concentration and method within the carbon partition nominal uncertainties, and then estimate as many linear regressions over time and slope coefficients. The average of the resulting slope values is used as partition DT. The associated uncertainty is quantified with an additional quasi MC analysis, once more in agreement with the work of Guallart et al. (2015b).

Variabilities. We determine the DT residuals by removing the trend from the mean estimates, and use them to estimate carbon variabilities. These values are inferable indirectly in Figs 4.3 to 4.6 by looking at the difference between dots, which quantify variations between cruise means from 1992, and lines, which estimate DTs.

In summary, we show an improvement in the partition uncertainties from the global to the 24.5°N upper 1000 m scales. However, this links to increases in the uncertainty influences at local scale due to a reduction in the concentration ranges. C_{tot} is the only exception, showing a greater uncertainty at local scale. Even so, the Hood et al. (2010) values, which are used here as global uncertainties, are only recommendations

to which operational oceanographers should aim. Also, the 24.5°N C_{tot} uncertainty is the only directly calculated value in Tab 4.1, while all of the others are estimates.

4.2.4 Anthropogenic carbon (C_{ant}) pool

C_{ant} carries an uncertainty due to analytical precision and method assumptions, which causes discrepancies among different method estimates. Here, we focus on the TTD and ΔC^* techniques, as those methods quantify the extremes of the probable range of C_{ant} concentrations (section 3.4). We investigate TTD and ΔC^* C_{ant} trends and variabilities in each of the 24.5°N subareas, as anticipated in section 4.2.2 and shown in Fig 4.3. C_{ant} DTs and 1992 mean values are summarised in Tab 4.2. The same approach is used for an extended time interval (1992-2016) in appendix A and for the other DIC partitions in sections 4.2.5 to 4.2.7.

C_{ant} increases over time everywhere in the section, as expected from the atmospheric CO_2 rise (Fig 1.9). We write this increase as $\delta_t C_{ant}$ and estimate its greatest values in the MoW and the ocean interior most recently ventilated western basin.

In the STMoW, the ΔC^* C_{ant} DTs are stronger than the TTD counterparts in the Florida Strait and not statistically different from them in the western and eastern basins. The only exception is subarea E2, where the TTD DT is stronger.

C_{ant} variabilities (differences between estimated and expected (from DT) increases) are not significant for both the STMoW TTD and ΔC^* C_{ant}, lying within the MC uncertainty. This result is confirmed in all of the other subareas investigated.

In the MMoW, the mean $\delta_t C_{ant}$ decreases with respect to the STMoW estimate, as expected for this older water mass. The ΔC^* and TTD C_{ant} DTs are comparable in the Florida Strait, but in the western and eastern basins the former exceeds the latter (Tab 4.2), leading to divergences over time.

In the SPMoW, the ΔC^* C_{ant} DTs are stronger than the TTD counterparts, with differences up to 0.4 $\pm$0.2 μmol kg^{-1} yr^{-1}, highlighting a C_{ant} divergence over time weaker than in the comparative MMoW.

In the AAIW, the estimates of the TTD and ΔC^* techniques are more comparable than in the MoW. Discrepancies are measurable, but the values lie within the MC

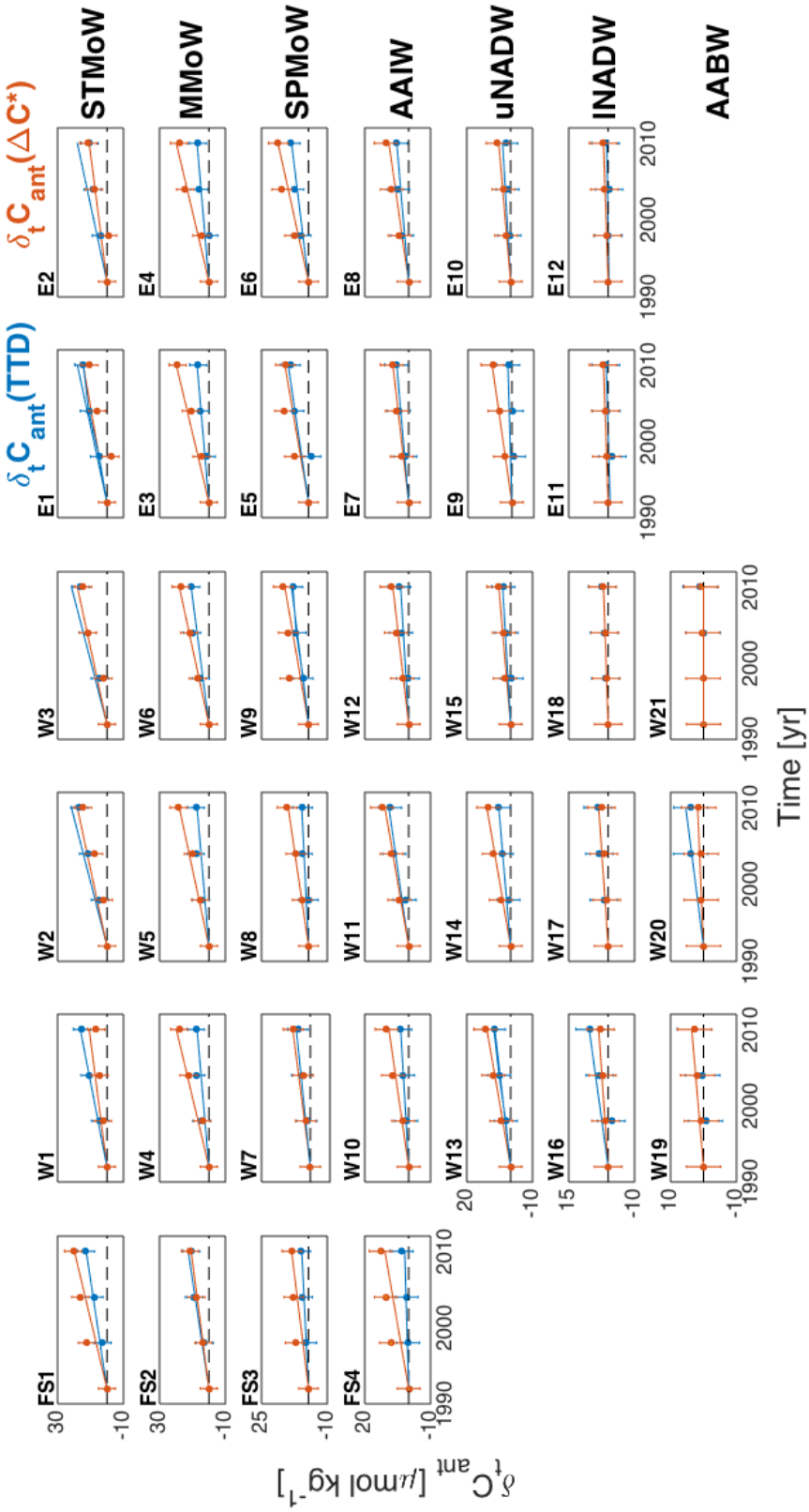

FIGURE 4.3: *Anthropogenic carbon (C_{ant}) temporal changes for each of the 24.5°N subareas (Fig 4.2). Dots identify the difference (δ_t) between the 1992 and subsequent cruise-mean estimates. C_{ant} is estimated by using the ΔC^* (orange) and TTD (blue) techniques, while error bars show the quasi Monte Carlo uncertainty of ± 5.2 µmol kg^{-1}. Decadal Trends added as least squares fitted linear regressions and forced to start at zero in 1992.*

TABLE 4.2: *Table summarising the Decadal Trends (DTs) and 1992 mean values (μ) of the TTD and ΔC^** **anthropogenic carbon** *($\mathbf{C_{ant}}$) estimated for each 24.5°N subarea (Fig 4.2). The respective uncertainties (± 0.2 $\mu mol\ kg^{-1}\ yr^{-1}$ and ± 5.2 $\mu mol\ kg^{-1}$) are approximated by randomly perturbing mean carbon concentrations and determining sets of linear regressions for each subarea within a quasi Monte Carlo approach. 'Section' refers to the averaged DT along the whole transect, and '1000 m' to the mean values in the column upper 1000 m. We highlight in bold the highest absolute trend and significant method discrepancy for each of the seven water masses investigated (subtropical Mode water (STMoW), Madeira MoW (MMoW), subpolar MoW (SPMoW), Antarctic intermediate water (AAIW), upper North Atlantic deep water (uNADW), lower NADW (lNADW), and Antarctic bottom water (AABW)). We also highlight in red the average values in the upper 1000 m that will be used in section 5.2.2.*

STMoW	FS1(DT)	FS1(μ)	W1(DT)	W1(μ)	W2(DT)	W2(μ)	W3(DT)	W3(μ)	E1(DT)	E1(μ)	E2(DT)	E2(μ)	Section
TTD	**0.7**	48.6	0.9	47.7	**1.2**	47.9	**1.2**	48.0	1.0	49.2	**1.0**	48.8	1.0
ΔC*	**1.1**	38.5	0.6	49.8	1.0	43.4	1.0	50.5	0.8	59.5	**0.6**	62.3	0.9
MMoW	FS2(DT)	FS2(μ)	W4(DT)	W4(μ)	W5(DT)	W5(μ)	W6(DT)	W6(μ)	E3(DT)	E3(μ)	E4(DT)	E4(μ)	Section
TTD	**0.7**	41.5	**0.4**	40.2	0.4	40.2	0.6	38.8	**0.4**	41.6	**0.4**	42.1	0.5
ΔC*	0.6	28.4	**1.1**	40.5	1.0	38.7	1.0	43.7	**1.1**	46.1	**1.1**	46.7	1.0
SPMoW	FS3(DT)	FS3(μ)	W7(DT)	W7(μ)	W8(DT)	W8(μ)	W9(DT)	W9(μ)	E5(DT)	E5(μ)	E6(DT)	E6(μ)	Section
TTD	0.2	24.0	0.4	25.3	0.2	27.6	0.5	29.6	**0.6**	35.5	**0.5**	31.0	0.4
ΔC*	0.5	26.2	0.5	32.4	0.6	29.8	0.7	32.6	0.7	36.1	**0.9**	38.3	0.7
AAIW	FS4(DT)	FS4(μ)	W10(DT)	W10(μ)	W11(DT)	W11(μ)	W12(DT)	W12(μ)	E7(DT)	E7(μ)	E8(DT)	E8(μ)	Section
TTD	0.1	9.9	0.1	11.4	**0.5**	12.8	0.1	10.0	0.3	9.2	0.3	8.5	0.2
ΔC*	**0.6**	12.9	0.5	19.5	**0.6**	17.3	0.4	16.1	0.4	15.1	0.5	17.5	0.5
1000 m	DT	μ	DT	μ	DT	μ	DT	μ	DT	μ	DT	μ	Section
TTD	0.4	31.0	0.5	31.2	0.6	32.1	0.6	31.6	0.6	33.9	0.6	32.6	0.5
ΔC*	0.7	26.5	0.7	35.5	0.8	32.3	0.8	35.7	0.8	39.2	0.8	41.2	0.8
UNADW			W13(DT)	W13(μ)	W14(DT)	W14(μ)	W15(DT)	W15(μ)	E9(DT)	E9(μ)	E10(DT)	E10(μ)	Section
TTD			**0.4**	15.2	**0.3**	16.1	0.2	9.2	0.1	5.2	0.2	3.6	0.2
ΔC*			**0.6**	17.1	**0.6**	18.8	0.3	18.7	0.5	13.2	0.3	11.5	0.5
lNADW			W16(DT)	W16(μ)	W17(DT)	W17(μ)	W18(DT)	W18(μ)	E11(DT)	E11(μ)	E12(DT)	E12(μ)	Section
TTD			**0.4**	6.2	0.2	13.5	0.1	5.9	0.1	4.6	0.1	2.7	0.2
ΔC*			0.2	7.7	0.2	7.1	0.1	5.8	0.1	3.6	0.1	3.9	0.1
AABW			W19(DT)	W19(μ)	W20(DT)	W20(μ)	W21(DT)	W21(μ)					Section
TTD			0.2	5.4	**0.3**	6.5	0.0	4.9					0.2
ΔC*			0.2	2.7	0.1	4.4	0.0	3.8					0.1

uncertainty. The AAIW C_{ant} pool is lower than the MoW counterpart, and so the influence of the analytical uncertainty on the AAIW $\delta_t C_{ant}$ is stronger than above. We avoid the discussion of the uNADW, lNADW, and AABW C_{ant} estimates, as anticipated in section 4.2.2. However, the ocean interior water mass estimates are reported in Fig 4.3 and Tab 4.2 for completeness. The same approach will be used in appendix A and for the other DIC partitions in sections 4.2.5 to 4.2.7.

Our estimates of the TTD and ΔC^* $\delta_t C_{ant}$ differ in the 24.5°N upper 1000 m from 1992 to 2010, as shown by Guallart et al. (2015b). Several reasons could explain these discrepancies. (1) The TTD assumes equilibrium between atmospheric and oceanic CO_2 ($C_{dis} = 0$ and $\delta_t C_{tot} = \delta_t C^0_{sat} + \delta_t C_{ant}$, section 4.2.7), correcting the transient tracer concentrations for their known under saturation (section 2.3.3). If the saturation is overestimated, the TTD quantifies $\delta_t C_{ant}$ as being weaker than the ΔC^* estimates. (2) C_{dis} may vary over time, as shown in section 4.2.5. If so, the ΔC^* carries an increasing bias between the least and most recent estimates, as the method assumes C_{dis} temporal constancy. The TTD also carries a bias, as it assumes null C_{dis}, but it limits the influence on C_{ant} when correcting the transient tracer saturations over time, as done in this thesis. (3) High rates of carbon and nutrients remineralisation modify the Redfield ratios, leading to differences between the TTD C_{ant}, which is almost uninfluenced, and the ΔC^* estimate, which varies up to ± 3.0 μmol kg^{-1} (± 6.0 %), depending on the RR considered. (4) Mixing, temperature, and biological blooms may also influence the C_{ant} estimates, propagating a bias that could enhance the inter-method differences (section 4.2.6). We suggest the combined use of TTD and ΔC^* to include more sources of uncertainty, better constraining C_{ant} (Iudicone et al., 2016; Khatiwala et al., 2013).

4.2.5 Disequilibrium carbon (C_{dis}) pool

C_{dis} estimates the distance of the ocean carbon cycle from being in CO_2 equilibrium with the overlying atmosphere. This partition is quantifiable at the ocean surface and passively transported into the interior, where it may be altered by mixing (Eggleston and Galbraith, 2017). The transported C_{dis} reaches the surface again in some ocean

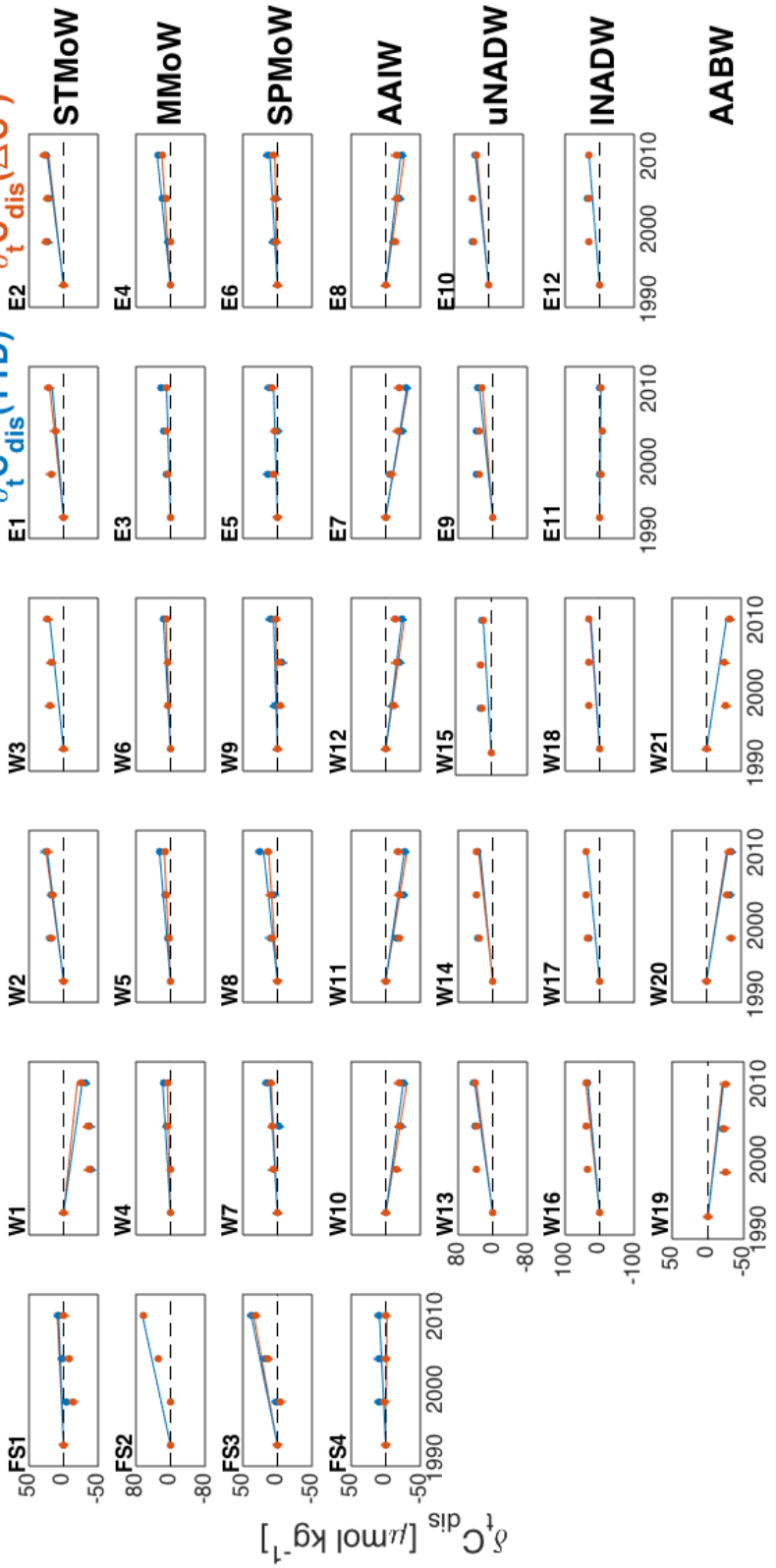

FIGURE 4.4: *Same as in Fig 4.3, but for the 24.5°N TTD and ΔC^* disequilibrium carbon partition (C_{dis}).*

TABLE 4.3: *Same as in Tab 4.2, but for the 24.5°N TTD and ΔC^** **disequilibrium carbon** *partition ($\mathbf{C_{dis}}$). Uncertainties are ± 0.3 µmol $kg^{-1}yr^{-1}$ and ± 6.2 µmol kg^{-1} for the C_{dis} Decadal Trends (DTs) and averaged concentrations (μ).*

STMoW	FS1(DT)	FS1(μ)	W1(DT)	W1(μ)	W2(DT)	W2(μ)	W3(DT)	W3(μ)	E1(DT)	E1(μ)	E2(DT)	E2(μ)	Section
TTD	0.4	-59.5	**-1.5**	-7.7	1.3	-63.7	1.1	-58.4	0.9	-51.5	1.3	-50.2	0.6
ΔC*	0.5	-49.3	**-1.1**	-9.8	**1.4**	-59.2	1.1	-60.9	1.1	-61.9	1.2	-63.7	0.7
MMoW	FS2(DT)	FS2(μ)	W4(DT)	W4(μ)	W5(DT)	W5(μ)	W6(DT)	W6(μ)	E3(DT)	E3(μ)	E4(DT)	E4(μ)	Section
TTD	**3.6**	-61.8	1.0	-13.7	1.4	-19.4	0.9	-15.3	**1.2**	-15.8	1.7	-13.3	1.6
ΔC*	**3.6**	-48.7	0.4	-14.1	0.8	-17.9	0.6	-20.1	**0.5**	-20.3	1.1	-17.9	1.2
SPMoW	FS3(DT)	FS3(μ)	W7(DT)	W7(μ)	W8(DT)	W8(μ)	W9(DT)	W9(μ)	E5(DT)	E5(μ)	E6(DT)	E6(μ)	Section
TTD	**2.1**	-37.8	0.6	-6.5	**1.1**	-8.4	0.3	-2.5	0.3	-11.0	**0.6**	-6.2	0.8
ΔC*	**1.9**	-40.0	0.5	-13.6	**0.7**	-10.6	0.1	-5.5	0.3	-11.6	**0.2**	-12.5	0.6
AAIW	FS4(DT)	FS4(μ)	W10(DT)	W10(μ)	W11(DT)	W11(μ)	W12(DT)	W12(μ)	E7(DT)	E7(μ)	E8(DT)	E8(μ)	Section
TTD	**0.5**	-19.2	-1.4	15.6	-1.5	13.5	-1.3	11.2	**-1.7**	14.3	-1.2	11.9	-1.1
ΔC*	**-0.1**	-22.2	-1.7	7.5	-1.7	9.0	-1.5	5.2	**-1.8**	8.3	-1.5	3.0	-1.4
1000 m	DT	μ	DT	μ	DT	μ	DT	μ	DT	μ	DT	μ	Section
TTD	1.7	-44.6	-0.3	-3.1	0.6	-19.5	0.3	-16.3	0.2	-16.0	0.6	-14.4	0.5
ΔC*	1.5	-40.1	-0.5	-7.5	0.3	-19.7	0.1	-20.4	0.0	-21.4	0.3	-22.8	0.3
uNADW			W13(DT)	W13(μ)	W14(DT)	W14(μ)	W15(DT)	W15(μ)	E9(DT)	E9(μ)	E10(DT)	E10(μ)	Section
TTD			**2.3**	-42.2	1.8	-39.6	1.0	-25.0	**1.7**	-37.9	1.7	-38.1	1.7
ΔC*			**2.1**	-44.2	1.6	-42.3	1.0	-34.5	**1.3**	-45.9	1.5	-46.1	1.5
lNADW			W16(DT)	W16(μ)	W17(DT)	W17(μ)	W18(DT)	W18(μ)	E11(DT)	E11(μ)	E12(DT)	E12(μ)	Section
TTD			**1.9**	-32.4	**2.0**	-42.2	1.4	-36.3	-0.2	-6.1	1.7	-43.8	1.4
ΔC*			**2.2**	-33.9	**2.0**	-35.8	1.5	-36.1	-0.2	-5.1	1.7	-45.0	1.4
AABW			W19(DT)	W19(μ)	W20(DT)	W20(μ)	W21(DT)	W21(μ)					Section
TTD			**-1.1**	3.8	**-1.6**	3.9	**-1.6**	-2.0					-1.5
ΔC*			**-1.2**	6.5	**-1.7**	6.0	-1.6	-1.0					-1.4

regions (e.g. Southern Ocean), influencing other components of the CO_2 cycle, such as C_{soft} (Ito and Follows, 2013). This may alter the carbon storage in water masses that originate in the Southern Ocean, such as the AAIW.

C_{dis} is treated as the imbalance between C_{tot} and the other partitions corrected by C_{ant} ($C_{dis} = C_{tot}$ - C^0_{sat} - C_{soft} - C_{carb} - C_{ant}, section 4.2.1). Consequently, we estimate C_{dis} trends and variabilities using the TTD and ΔC^*, so highlighting discrepancies between these two methods. The C_{dis} DTs and cruise averages are shown in Fig 4.4 and summarised in Tab 4.3. Comparisons with previous estimates are impossible, as we present the first 24.5°N C_{dis} calculation between 1992 and 2010.

In the STMoW, we identify no temporal changes or variabilities in the subarea FS1 C_{dis} by using the TTD and ΔC^* methods. Moving eastwards, the C_{dis} DTs become more negative over time in subarea W1. Elsewhere in the STMoW, $\delta_t C_{dis}$ weakens, hence decreasing the potential for additional CO_2 uptake. Excluding subareas FS1 and W1, the TTD and ΔC^* $\delta_t C_{dis}$ values are higher than the concentrations expected from the DTs in 1998 on average. In the same year, the $\delta_t C_{dis}$ values are lower than the DT estimates in subarea W1 by 44.2 ± 6.2 μmol kg^{-1}. Unrecognised problems in the 1992 measurements could explain the discrepancies: without this year data, the $\delta_t C_{dis}$ variabilities would lie in the MC uncertainty, with statistically insignificant differences from the DT estimates.

Hereafter, we use caution in the analysis of the data when including the 1992 values. When these are excluded, some partition DTs change significantly (outside the MC uncertainty). However, our analyses do not support the removal of these data.

In the subsurface (MMoW and SPMoW), the C_{dis} weakening trends increases with respect to the STMoW estimates. This pattern emerges particularly in the Florida Strait, which exhibits C_{dis} weakening trends of 3.6 ± 0.3 μmol kg^{-1} yr^{-1} (MMoW) and 2.0 ± 0.3 μmol kg^{-1} yr^{-1} (SPMoW) on average. In the main section, we see a divergence between the C_{dis} DTs estimated by using the two techniques: the TTD method quantifying the strongest C_{dis} weakening DTs in the western and eastern basins. We estimate discrepancies up to 0.7 ± 0.3 μmol kg^{-1} yr^{-1} in the subarea E3. This value is equal to the difference in C_{ant}, because C_{ant} and C_{dis} are dependent on each other, with their sum being equal to C_{res}. The values are also comparable to the

discrepancy of 0.8 ± 0.2 μatm yr^{-1} quantified between the ΔC* and TTD estimates of the MMoW pCO_{2ant} in Fig 3.7, which corresponds to an estimated difference of 0.5 ± 0.3 μmol kg^{-1} yr^{-1} between the methods $\delta_t C_{dis}$. So, differences in the $\delta_t C_{dis}$ term may be the most influential source of the observed discrepancy between the TTD and ΔC* C_{ant} estimates (section 5.2). Variabilities in the MMoW and SPMoW C_{dis} are significant in the Florida Strait only, where the $\delta_t C_{dis}$ estimates are lower than the DT values in 1998 and 2004.

In the AAIW, the TTD C_{dis} values become less negative in the Florida Strait and less positive in the main section over time. The ΔC* C_{dis} trends are also negative in the western and eastern basins, while they are insignificant in the Florida Strait. To summarise, C_{dis} estimates tend towards the CO_2 saturation (C_{dis} = 0) in the 24.5°N upper 1000 m between 1992 and 2010. However, the TTD and ΔC* estimates differ, with the strongest divergences quantifiable in the STMoW and Florida Strait. These techniques include differently changes in the disequilibrium, saturated, and remineralised DIC partitions, as discussed in sections 3.4 and 5.2.

4.2.6 Soft-tissue (C_{soft}) and carbonate (C_{carb}) carbon pools

In addition to the physical uptake (C_{ant} + C_{dis} + C^0_{sat}), the ocean sequesters atmospheric CO_2 through the biological pump. C_{carb} and C_{soft} depend on this biogenic influence, accounting for the remineralisation of sinking hard and soft tissues, respectively (Williams and Follows, 2011). Their 24.5°N DTs and 1992 mean concentrations are summarised in Fig 4.5 and Tab 4.4. We discuss their influence on the carbon cycle comparing our results with the estimates obtained by Williams and Follows (2011) in the area, which were based on data from the 1990s. C_{carb} does not influence the subtropical North Atlantic upper-ocean carbon cycle. DTs and variabilities of this partition are overall insignificant in the 24.5°N upper 1000 m. In this layer, we estimate a 2010 C_{carb} concentration of 2.3 ± 1.5 μmol kg^{-1}, which is thus almost indistinguishable to zero, but also compared to the estimate of 3.0 ± 1.5 μmol kg^{-1} reported by Williams and Follows (2011).

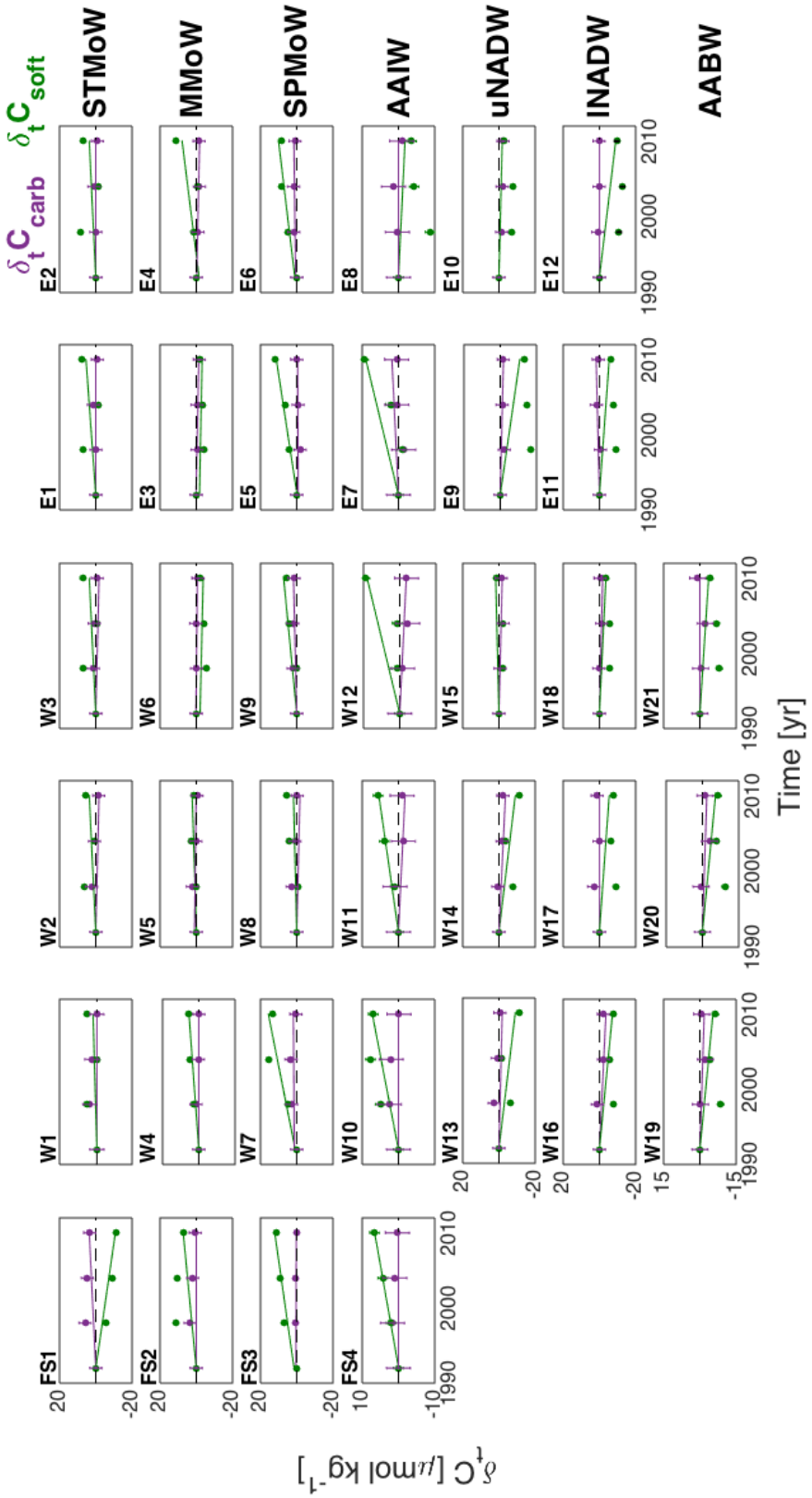

FIGURE 4.5: *Same as in Fig 4.3, but for the 24.5°N carbonate (C_{carb}) and soft-tissue (C_{soft}) carbon partitions.*

TABLE 4.4: *Same as in Tab 4.2, but for the 24.5°N* **carbonate (C_{carb})** *and* **soft-tissue (C_{soft}) carbon** *partitions. Uncertainties are ±0.1 µmol kg^{-1} yr^{-1} and ±1.5 µmol kg^{-1} for the C_{carb} Decadal Trends (DT) and averaged estimates (µ), respectively. Comparative values are ±0.1 µmol kg^{-1} yr^{-1} and ±1.3 µmol kg^{-1} for the C_{soft} DT and µ estimates, respectively. Mean estimates may result negative owing to the AOU approximation (Eqs 4.9 and 4.11), but these values are unreliable and need to be treated as zeros.*

STMoW	FS1(DT)	FS1(µ)	W1(DT)	W1(µ)	W2(DT)	W2(µ)	W3(DT)	W3(µ)	E1(DT)	E1(µ)	E2(DT)	E2(µ)	Section
C_{carb}	**0.2**	-3.3	0.0	-3.7	-0.1	-1.4	-0.1	-0.6	0.0	0.1	0.0	0.0	0.0
C_{soft}	**-0.6**	24.4	0.1	-0.4	0.2	-0.9	0.2	-2.4	0.3	-3.0	0.2	-0.5	0.1
MMoW	FS2(DT)	FS2(µ)	W4(DT)	W4(µ)	W5(DT)	W5(µ)	W6(DT)	W6 (µ)	E3(DT)	E3(µ)	E4(DT)	E4(µ)	Section
C_{carb}	0.0	-1.4	0.0	-2.2	-0.1	-1.9	0.0	-0.8	-0.1	-1.0	-0.1	-0.2	-0.1
C_{soft}	0.4	39.9	0.3	20.8	0.1	24.6	-0.1	29.7	-0.1	29.5	**0.5**	31.1	0.2
SPMoW	FS3(DT)	FS3(µ)	W7(DT)	W7(µ)	W8(DT)	W8(µ)	W9(DT)	W9(µ)	E5(DT)	E5(µ)	E6(DT)	E6(µ)	Section
C_{carb}	0.0	4.0	0.0	-0.3	0.0	-0.3	0.1	-1.6	0.0	-0.4	0.1	-2.0	0.0
C_{soft}	0.6	84.7	**0.8**	52.9	0.3	56.5	0.4	50.8	0.6	42.3	0.5	48.6	0.5
AAIW	FS4(DT)	FS4(µ)	W10(DT)	W10(µ)	W11(DT)	W11(µ)	W12(DT)	W12(µ)	E7(DT)	E7(µ)	E8(DT)	E8(µ)	Section
C_{carb}	0.0	7.9	0.0	3.6	-0.1	5.6	-0.1	7.0	0.1	4.6	0.0	5.4	0.0
C_{soft}	0.4	93.8	0.4	73.7	0.3	80.5	**0.5**	80.3	**0.5**	81.1	-0.1	99.7	0.3
1000 m	DT	µ	DT	µ	DT	µ	DT	µ	DT	µ	DT	µ	Section
C_{carb}	0.1	1.8	0.0	-0.7	-0.1	0.5	0.0	1.0	0.0	0.8	0.0	0.8	0.0
C_{soft}	0.3	60.7	0.4	36.8	0.2	40.2	0.3	39.6	0.3	37.5	0.3	44.7	0.3
uNADW			W13(DT)	W13(µ)	W14(DT)	W14(µ)	W15(DT)	W15(µ)	E9(DT)	E9(µ)	E10(DT)	E10(µ)	Section
C_{carb}			-0.1	1.3	**-0.2**	3.3	-0.1	5.9	-0.1	7.2	-0.1	9.3	-0.1
C_{soft}			-0.5	56.5	-0.5	59.0	0.1	59.6	**-0.6**	80.0	-0.1	80.3	-0.4
lNADW			W16(DT)	W16(µ)	W17(DT)	W17(µ)	W18(DT)	W18(µ)	E11(DT)	E11(µ)	E12(DT)	E12(µ)	Section
C_{carb}			**-0.2**	1.6	0.0	0.4	-0.1	5.3	0.1	5.3	0.0	8.7	0.0
C_{soft}			-0.4	41.2	-0.3	45.0	-0.2	48.3	-0.3	58.0	**-0.5**	68.5	-0.3
AABW			W19(DT)	W19(µ)	W20(DT)	W20(µ)	W21(DT)	W21(µ)					Section
C_{carb}			-0.1	9.4	-0.1	14.1	0.0	15.9					-0.1
C_{soft}			**-0.3**	44.7	**-0.3**	49.7	-0.2	52.2					-0.3

Conversely, the C_{soft} influence on the North Atlantic subtropical carbon cycle is significant. In the STMoW, C_{soft} decreases over time in the Florida Strait and varies just outside the quasi MC uncertainty in the main section. These concentrations are however shown only for completeness, because C_{soft} estimates could act non-conservatively in the STMoW due to the high variability in the sources and sinks. In the MMoW, C_{soft} increases locally in subareas FS2, W4, and E4. These $\delta_t C_{soft}$ estimates suggest changes in the remineralisation, deep western boundary current, residence time, or primary productivity (section 5.3). In subarea E4, the upwelling enhances the remineralisation carrying C_{soft} from the interior to the subsurface, and also transporting inorganic nutrients towards the surface. This increases the primary productivity, carbon export and consequent remineralisation (section 5.3).
Elsewhere in the MMoW, C_{soft} varies within the quasi MC uncertainty. Variabilities are significant in subareas FS2 and E4. In FS2, the C_{soft} increases are higher than the DT values in 1998 and 2004. Here, we suggest unrecognised problems in the 1992 measurements, as also discussed for C_{dis} in section 4.2.5. In E4, the C_{soft} increases are lower and higher than the DT based values in 2004 and 2010, respectively.
In the SPMoW, C_{soft} increases everywhere, with DTs reaching 0.8 ± 0.1 μmol kg^{-1} yr^{-1}. Variability is significant in subarea W7, where the C_{soft} increase is higher than the DT estimate in 2004. A decrease in circulation in 2010 could explain this result.
In the AAIW, C_{soft} increases everywhere except in subarea E8, where it does not vary significantly. By removing the 1992 estimates, however, C_{soft} increases significantly in this subarea. Variability is significant in subarea W10, where the $\delta_t C_{soft}$ estimates are higher than the DT values in 1998 and 2004, and in subareas W12, E7, and E8, where the $\delta_t C_{soft}$ are lower than the DT values in the same years. As anticipated above, unrecognised problems in the 1992 measurements may explain the observed patterns in subareas E7 and E8: without this year, the C_{soft} increases are comparable to the DT estimates within the MC uncertainty. In W12, we suggest an influence of a circulation slow-down or a strengthening in the lateral mixing, with the last also explaining the weakening in the 2010 $\delta_t C_{soft}$ in the subarea W10.
We quantify a C_{soft} concentration of 45.7 ± 1.3 μmol kg^{-1} in the 24.5°N upper 1000 m in 2010. This estimate is greater than the value of 40.0 ± 1.3 μmol kg^{-1} reported

by Williams and Follows (2011) and based on data collected on the 1990s. So, the 24.5°N upper-ocean C_{soft} increases from 1992 to 2010 due to potential changes in organic matter oxidation or seawater transport, increasing the DIC. The strongest variations are in the Florida Strait and eastern basin, suggesting a predominant influence of changes in oxidation or in the upwelling near the African coast.

4.2.7 Total (C_{tot}) and pre-industrial saturated (C^0_{sat}) pools

To complete the study of the 24.5°N Atlantic section carbon cycle, we assess trends and variabilities of C^0_{sat} and C_{tot}. C^0_{sat} decreases in time in the section upper ocean, except for the AAIW. This trend is driven by the increase in the ocean temperature and the reduction in the estimated Alk^{pre} and may be due to a decreasing reliability of the regression model used for the scope (Eq 4.7). However, a decrease in C^0_{sat} in the subtropical North Atlantic agrees with the work of Bernardello et al. (2014a), where the authors suggested a conversion from the C_{sat} to the C_{soft} pools due to increasing stratification over time. C_{tot} increases in the MoW, being generally stable beneath this water mass (Fig 4.6, Tab 4.5).

In the STMoW, C^0_{sat} does not vary significantly in the Florida Strait and decreases in the main section. The only exception is subarea W1, but problems in the 1992 measurements may have influenced this anomaly, in line with what we discussed for C_{dis} in section 4.2.5. The STMoW C_{tot} increases everywhere.

In the MMoW and SPMoW, C^0_{sat} decreases in the Florida Strait more rapidly than increases in the main section. This is due to an increase in the temperature of 0.2 °C, which leads to a C^0_{sat} reduction of -1.4 μmol kg^{-1}. The Alk^{pre} decreases in the eastern basin, so leading to a $\delta_t C^0_{sat}$ as large, whereas the western basin C^0_{sat} varies insignificantly. C_{tot} increases everywhere in the investigated 24.5°N subsurface.

In the AAIW, C_{tot} and C^0_{sat} decrease in subarea FS4 and increase elsewhere. Variabilities are significant in subareas FS2, FS3, FS4, and E8. Here, the C^0_{sat} rises are higher than the DT values in 1998 and 2004, while $\delta_t C_{tot}$ follows this pattern in subareas FS2 and FS4 only. Problems in the 1992 measurements may explain the results, particularly in subarea FS4, but the influence of other DIC partitions could

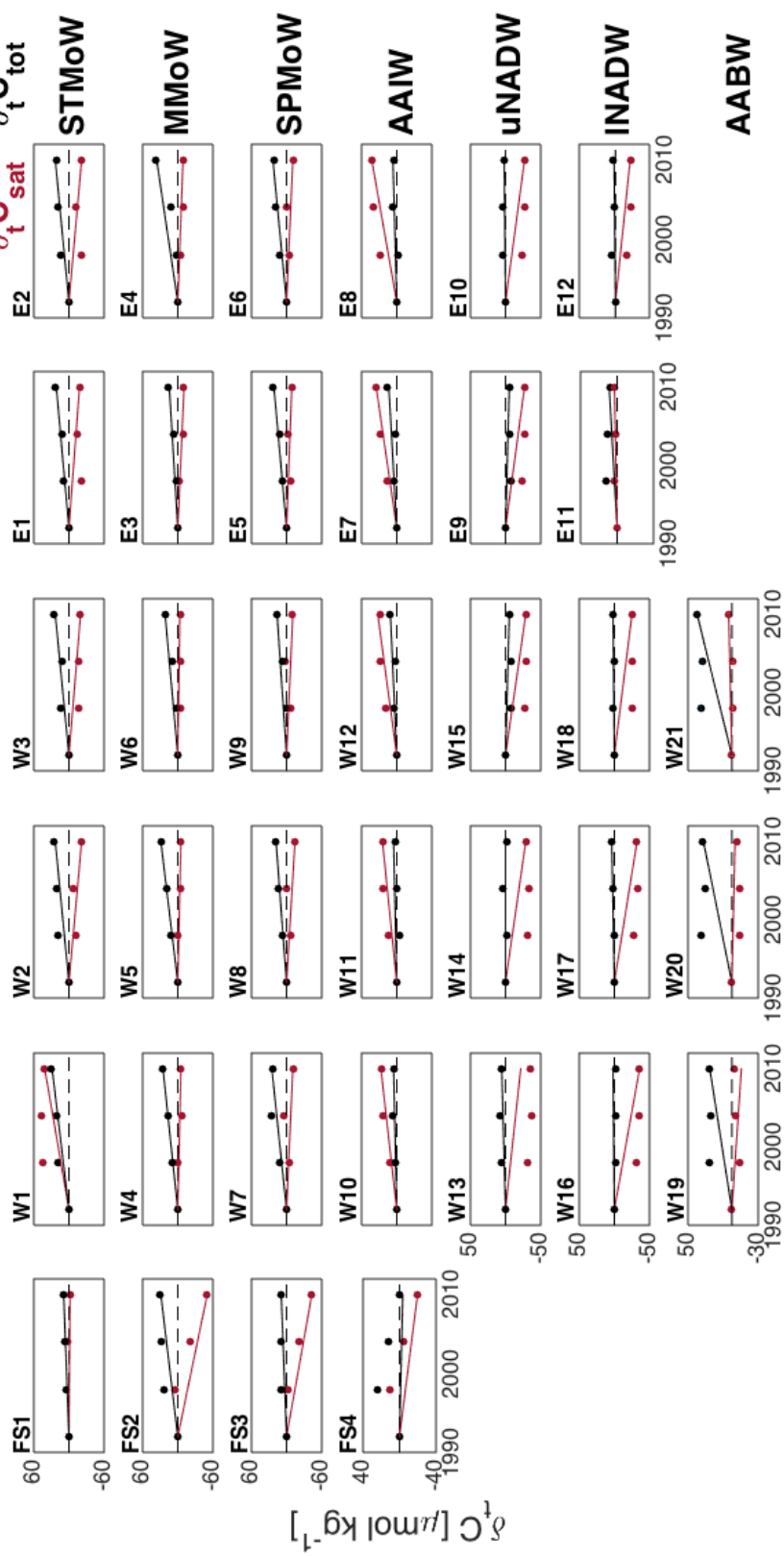

FIGURE 4.6: *Same as in Fig 4.3, but for the 24.5°N pre-industrial saturated (C^0_{sat}) and total (C_{tot}) carbon partitions.*

TABLE 4.5: *Same as in Tab 4.2, but for the 24.5°N* **pre-industrial saturated** *(*$\mathbf{C^0_{sat}}$*)* **and total** *(*$\mathbf{C_{tot}}$*)* **carbon** *partitions. Uncertainties are ±0.1 µmol kg^{-1}yr^{-1} and ±2.0 µmol kg^{-1} for the C^0_{sat} Decadal Trends (DTs) and averaged estimates (µ), respectively. Comparative values are ±0.1 µmol kg^{-1}yr^{-1} and ±1.3 µmol kg^{-1} for the C_{tot} Decadal Trends (DTs) and averaged estimates (µ), respectively.*

STMoW	FS1(DT)	FS1(μ)	W1(DT)	W1(μ)	W2(DT)	W2(μ)	W3(DT)	W3(μ)	E1(DT)	E1(μ)	E2(DT)	E2(μ)	Section
C^0_{sat}	-0.1	2043.9	**2.3**	1996.5	-1.2	2053.9	-1.1	2074.4	-1.0	2091.7	-1.2	2093.6	-0.4
C_{tot}	0.5	2054.2	**1.6**	2032.4	1.3	2035.8	1.3	2061.0	1.2	2086.5	1.3	2091.7	1.2
MMoW	FS2(DT)	FS2(μ)	W4(DT)	W4(μ)	W5(DT)	W5(μ)	W6(DT)	W6(μ)	E3(DT)	E3(μ)	E4(DT)	E4(μ)	Section
C^0_{sat}	**-2.8**	2094.8	-0.3	2048.5	-0.3	2050.9	-0.2	2053.0	-0.6	2056.8	-0.5	2059.1	-0.8
C_{tot}	1.6	2113.0	1.4	2093.5	1.6	2094.5	1.2	2105.5	0.8	2111.1	**2.0**	2118.8	1.4
SPMoW	FS3(DT)	FS3(μ)	W7(DT)	W7(μ)	W8(DT)	W8(μ)	W9(DT)	W9(μ)	E5(DT)	E5(μ)	E6(DT)	E6(μ)	Section
C^0_{sat}	**-2.4**	2111.6	-0.6	2071.3	-0.8	2072.0	-0.6	2070.7	-0.5	2070.3	-0.6	2070.3	-0.9
C_{tot}	0.5	2186.4	**1.4**	2142.6	1.0	2147.4	0.9	2146.9	1.2	2136.7	1.3	2142.7	1.1
AAIW	FS4(DT)	FS4(μ)	W10(DT)	W10(μ)	W11(DT)	W11(μ)	W12(DT)	W12(μ)	E7(DT)	E7(μ)	E8(DT)	E8(μ)	Section
C^0_{sat}	-1.1	2107.8	1.0	2081.8	0.9	2082.0	1.1	2079.5	**1.3**	2078.3	**1.3**	2076.2	0.8
C_{tot}	-0.2	2200.1	0.2	2186.2	0.2	2194.3	0.4	2188.1	**0.5**	2187.4	0.2	2201.8	0.2
1000 m	DT	μ	DT	μ	DT	μ	DT	μ	DT	μ	DT	μ	Section
C^0_{sat}	-1.6	2089.5	0.6	2049.5	-0.4	2064.7	-0.2	2069.5	-0.2	2074.3	-0.3	2074.8	-0.3
C_{tot}	0.6	2138.4	1.2	2113.7	1.0	2118.0	1.0	2125.4	0.9	2130.4	1.2	2138.8	1.0
uNADW			W13(DT)	W13(μ)	W14(DT)	W14(μ)	W15(DT)	W15(μ)	E9(DT)	E9(μ)	E10(DT)	E10(μ)	Section
C^0_{sat}			-1.2	2138.7	**-1.6**	2137.6	**-1.6**	2137.1	-1.5	2137.2	-1.5	2138.3	-1.5
C_{tot}			**0.3**	2169.4	0.0	2176.4	**-0.3**	2186.9	**-0.3**	2191.6	0.1	2193.3	0.0
lNADW			W16(DT)	W16(μ)	W17(DT)	W17(μ)	W18(DT)	W18(μ)	E11(DT)	E11(μ)	E12(DT)	E12(μ)	Section
C^0_{sat}			**-2.0**	2148.3	-1.8	2147.7	-1.4	2146.5	0.6	2111.0	-1.1	2147.0	-1.1
C_{tot}			-0.1	2164.8	**0.2**	2164.3	0.1	2169.6	**0.2**	2172.6	0.1	2183.2	0.1
AABW			W19(DT)	W19(μ)	W20(DT)	W20(μ)	W21(DT)	W21(μ)					Section
C^0_{sat}			1.4	2114.6	1.8	2115.0	**2.2**	2114.7					1.8
C_{tot}			**-0.6**	2178.0	-0.2	2189.2	0.1	2185.6					-0.2

also be relevant (section 4.2.8).

We quantify C^0_{sat} mean concentrations between 2070.4 ± 2.0 μmol kg^{-1} and 2065.2 ± 2.0 μmol kg^{-1} in the 24.5°N upper-ocean layer in 1992 and 2010. The estimates broadly match the concentration of 2060.0 ± 2.0 μmol kg^{-1} reported by Williams and Follows (2011) in the area and based on data collected on the 1990s. However, our estimates reduce in time, in line with the increasing ocean stratification due to the rising temperature, while the Williams and Follows (2011) mean estimate does not differ from our most recent C^0_{sat}, suggesting oceanic steady state instead.

In summary, C_{tot} increases over time everywhere in the 24.5°N upper 1000 m, while C^0_{sat} decreases in this region. We quantify the strongest partition DTs at the margins of the main transit (e.g. subarea W7) and in the Florida Strait. This suggests not only an influence of changes in circulation or organic matter oxidation, but also an impact of other carbon partitions, as it will be detailed in the next section.

4.2.8 Summary: carbon partition interplay at 24.5°N

C_{tot} increases everywhere in the upper 1000 m of the 24.5°N Atlantic transect from 1992 to 2010, with a mean DT of 1.0 ± 0.1 μmol kg^{-1} yr^{-1}. This corresponds to increases of 0.5 ± 0.2 μmol kg^{-1} yr^{-1} and 0.8 ± 0.2 μmol kg^{-1} yr^{-1} in the TTD and ΔC^* C_{ant} estimates, which are comparable to the values reported by Guallart et al. (2015b). The same methods quantify comparable changes in C_{dis}. C_{soft} increases by 0.3 ± 0.1 μmol kg^{-1} yr^{-1}, and we observe a decrease by the same amount in C^0_{sat}, which is the largest carbon pool. So, the increase in C_{ant} is the largest contribution to the $\delta_t C_{tot}$, as expected from the increasing atmospheric CO_2. However, the C_{soft} rise over time is unexpected. This component increases mostly in the Florida Strait, SPMoW, and upwelling region, suggesting changes in oxidation rates or circulation, which are investigated in section 5.3. The 24.5°N C_{carb} variations are insignificant.

The North Atlantic subtropical C_{tot} DTs and variabilities are influenced by climate change and increasing emissions of anthropogenic CO_2. Within the climate change, we observe a decrease in the 24.5°N upper-ocean (0-1000 m) C^0_{sat}, mostly evident in the Florida Strait and eastern basin. This pattern is due to a temperature increase

and a decrease in Alk^{pre}, which are the independent variables in the C^0_{sat} estimate (Eq 4.8) that are expected to vary the most over time. In the Florida Strait, the saturation decrease coincides with an increase in temperature, while Alk^{pre} changes are insignificant. In the eastern basin however temperature is constant, so we link the C^0_{sat} reduction to an Alk^{pre} decrease approximately as large. These patterns suggest an influence of changes in upwelling. Also, the C^0_{sat} reduction links to an aqueous CO_2 increase, which damps the idealised potential for additional carbon uptake, as confirmed by the weakening in C_{dis} (Goodwin et al., 2008). Notwithstanding that, the anthropogenic CO_2 rise in the atmosphere exceeds the increase in oceanic CO_2 partial pressure (ΔpCO_2, Eq 1.1), forcing a net carbon uptake and increasing C_{tot}. In the next sections, we will investigate where those mechanisms are more likely to happen and when they are more influential by using GLODAPv2 climatological data and outputs of three CM2Mc simulations: 'industrial', 'climate', and 'control'.

4.3 North Atlantic carbon trends and variabilities

The hydrographic section at 24.5°N in the Atlantic is of key relevance for the Atlantic Meridional Overturning Circulation (AMOC) monitoring (Bryden et al., 2014) and the study of the Mode water influence on the ocean CO_2 uptake (Bates et al., 2002). However, observations on this transect are limited in time and space. Therefore, we expand the investigation of the interplay among dissolved inorganic carbon partitions to the full North Atlantic basin (0-65°N). For this analysis, we use the spatially gap-filled GLODAPv2 climatology, referenced to the year 2002 (Lauvset et al., 2016), and the outputs of three CM2Mc ESM simulations (Bernardello et al., 2014a,b).
We use the climatological data to quantify column inventories of carbon partitions in the North Atlantic basin, hence assessing their variability over space. In appendix C, we explore these inventories in the North Atlantic upper 1000 m, where we estimate the highest C_{ant} pool, using the same approach as in sections 4.2.4 to 4.2.8. Here, we investigate the partition inventories over the entire water column, under a more comprehensive treatment, comparing GLODAPv2 and modelled estimates to assess the CM2Mc outputs. In this analysis, C_{ant} is estimated by using the TTD technique

based on CFC-12 measurements, as explicitly reported in the GLODAPv2 dataset. We do not use the ΔC^* method to simplify the carbon partitions assessment. The C_{ant}^{MOD} is quantified as difference between industrial and control DICs (Eq 2.15). However, the climatological data cannot be used to test the partition variabilities in time, being referred to a single year. Instead, we investigate outputs of a CM2Mc 'industrial' (climate change and oceanic C_{ant} uptake), 'climate' (climate change, but no oceanic C_{ant} uptake), and pre-industrial 'control' (no climate change and no oceanic C_{ant} uptake) simulations between 1860 and 2100. The anthropogenic CO_2 uptake is simulated in the CM2Mc model since 1860 and the 'control' C_{dis} at the ocean surface is modelled as in Fig 4.7. These sources of information are necessary for the evaluation of the biases in the model carbon cycle (Bronselaer et al., 2017). Also, a comparison between Fig 4.7 and Fig 4.9, which presents the CM2Mc 'industrial' outputs in 2002, shows that the anthropogenically-driven increase of CO_2 in the atmosphere has strengthened the disequilibrium with the ocean in the last 160 years: more negative C_{dis} (comparable to the difference between oceanic and atmospheric pCO_2) values are modelled at the surface of the North Atlantic in 2002, suggesting an increasing carbon uptake (section 4.2.8).

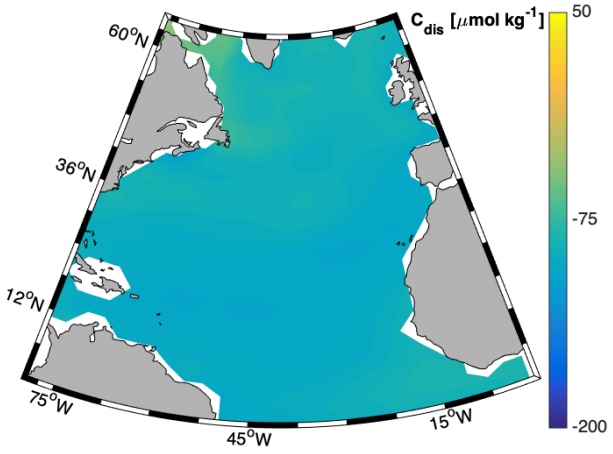

FIGURE 4.7: *Disequilibrium Carbon (C_{dis}) distribution at the North Atlantic surface in 1860. Data taken from the CM2Mc pre-industrial 'control' run and calculated as in Eq 2.14. The colour scale is the same as in Fig 4.9 for comparison.*

We examine simulated trends and variabilities over space and time for each carbon partition, exploring mean values in three intervals of twenty years each: 1880-1900 for the pre-industrial, 1980-2000 for the present, and 2080-2100 for the future oceanic states. Results are shown as anomalies of the 'background' control simulation and are compared to the 24.5°N DIC partitions interplay investigated in section 4.2.8.

4.3.1 Observational (GLODAPv2) assessment over space

The study of the full-column carbon partitions interplay based on the GLODAPv2 climatology (Fig 4.8) show a North Atlantic C_{tot} inventory of $4.2\,x\,10^3 \pm 0.9$ PgC, with the major contribution due to C^0_{sat}. Other influences are linked to C_{soft}, C_{carb}, C_{ant}, and C_{dis}. C_{soft} is the second largest carbon reservoir in the studied basin, C_{carb} is the lowest, while C_{dis} and C_{ant} are comparable and included between the other two estimates. The C_{ant} budget is also comparable to the estimates discussed by Gruber (1998) when considering this value increases by approximately 0.8 ± 0.6 PgC yr^{-1}. The relevance of C_{soft} and C_{dis} increases when considering the whole North Atlantic with respect to the basin upper 1000 m (section 4.2.8, appendix C). This is due to ocean interior water masses (e.g. AABW), which have had more time to accumulate remineralised soft tissue and less time to reach CO_2 equilibrium with the atmosphere, carrying the highest C_{soft} pool in the subtropics and the strongest C_{dis} near the Pole. Variabilities over space are masked by the North Atlantic bathymetry for the carbon partitions that have had the time to invade the whole water column, such as C^0_{sat}: at greater depths corresponds higher concentrations simply because the water mass volumes are higher. To overcome this difficulty and explore real carbon variabilities, we examine the depth-averaged value of each carbon partition (graphs not shown). This shows that the subpolar gyre stores the highest C^0_{sat} and C_{ant} pools and the strongest C_{dis}, whilst the North Atlantic subtropics store the highest C_{tot}, C_{soft}, and C_{carb} pools. Polewards, the increasing atmospheric CO_2 increases the oceanic potential carbon content (C^0_{sat}) mostly because of the water mass formation that maintains seawater away from the CO_2 saturation (section 1.3).

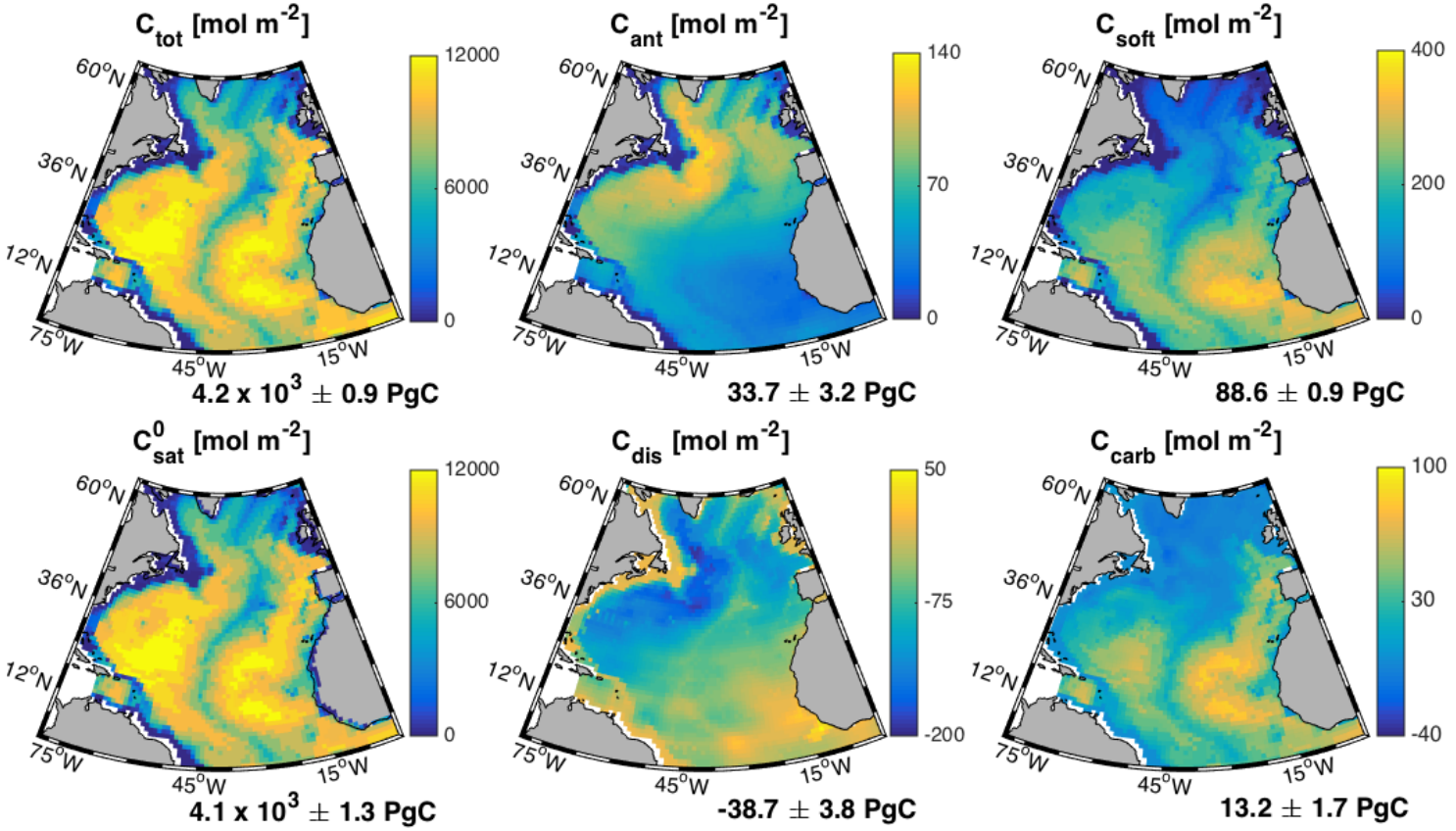

FIGURE 4.8: *North Atlantic maps showing the column inventories of inorganic carbon partitions (total (C_{tot}), anthropogenic (C_{ant}), soft-tissue (C_{soft}), pre-industrial saturated (C^0_{sat}), disequilibrium (C_{dis}), and carbonate (C_{carb}) carbon). Data taken from the GLODAPv2 climatology (2002 being the reference year; Lauvset et al. (2016)), with the budgets and uncertainties reported at the bottom right edge of each panel. C_{ant} is quantified by using the Transit-Time Distribution (TTD) method based on CFC-12 observations, as given in the GLODAPv2 climatology.*

TABLE 4.6: *Table summarising North Atlantic budgets of dissolved inorganic carbon partitions (Figs 4.8-4.9), associated differences, and uncertainties. Carbon budgets [PgC] are quantified using the GLODAPv2 climatology (Lauvset et al., 2016) and the CM2Mc "industrial" outputs in 2002. Differences are estimated as percentages of the climatological carbon budgets. Listed partitions are total (C_{tot}), pre-industrial saturated (C^0_{sat}), soft-tissue (C_{soft}), carbonate (C_{carb}), anthropogenic (C_{ant}), and disequilibrium carbon (C_{dis}).*

Partition	Observed Budget	Modelled Budget	Difference	Uncertainty
C_{tot}	4.2 x 10^3	4.8 x 10^3	+14 %	0.9
C^0_{sat}	4.1 x 10^3	4.8 x 10^3	+15 %	1.3
C_{soft}	88.6	87.6	-0.1 %	0.9
C_{carb}	13.2	55.1	+317 %	1.7
C_{ant}	33.7	33.3	-1.2 %	3.2
C_{dis}	-38.7	-49.8	-29 %	3.8

This induces a negative C_{dis} imbalance that is compensated by C_{ant} sequestrations. The subtropical gyre is characterised by higher concentrations of remineralised carbon (C_{soft} + C_{carb}) that are due to upwelling, biological cycles, and stronger stratification. These processes increase C_{tot} above the thermocline, reducing C^0_{sat}, weakening C_{dis}, and so decreasing the potential for C_{ant} uptake.

4.3.2 Modelling (CM2Mc) assessment over space and time

We assess the North Atlantic (0-65°N) inorganic carbon partition inventories in the CM2Mc outputs between 1860 and 2100 to study their trends and variabilities over space and time. As a first step, we replicate the GLODAPv2 analysis, discussed in the previous thesis section, using Eqs 2.12-2.15 and outputs of a CM2Mc industrial run in 2002, the climatological reference year. This enables us to investigate the degree to which CM2Mc replicates the observed carbon distributions. Then, we explore anomalies of North Atlantic carbon partitions, as anticipated in section 4.3. Overall, the CM2Mc ESM broadly matches the climatological data, with differences summarised in Tab 4.6. These discrepancies are however discussed only for C_{carb}, which shows the greatest disagreement due to the simulated alkalinity, comparably

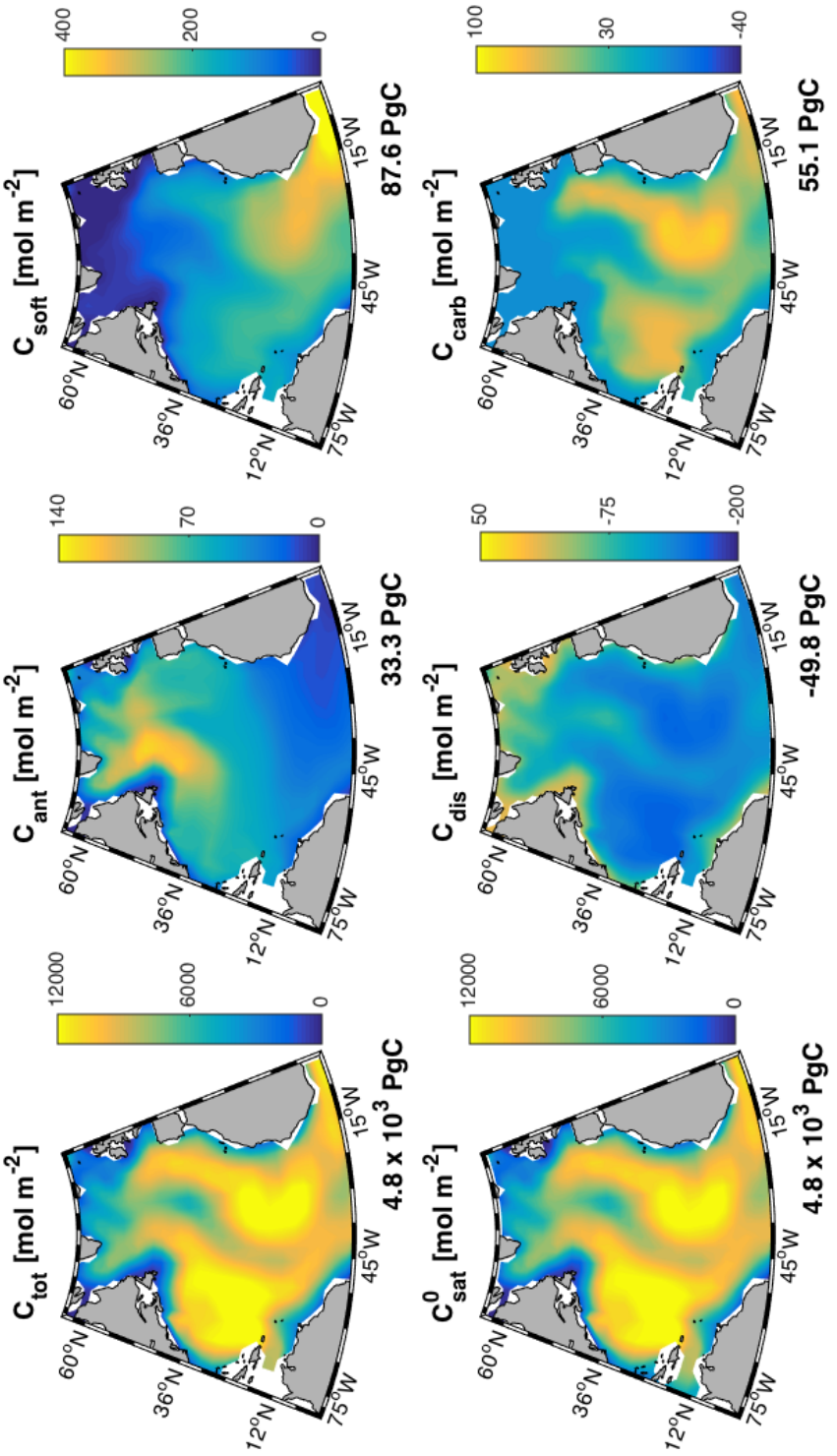

FIGURE 4.9: *Same as in Fig 4.8, but using CM2Mc industrial modelled outputs in 2002.*

higher in the model outputs and in the climatological data. Having proved that the simulated partitions track the observations (excluding C_{carb}), we use 'climate' and 'industrial' CM2Mc outputs to quantify North Atlantic full-column inventories of C_{tot}, C^0_{sat}, C_{soft}, C_{carb}, and C_{dis}. These values are averaged between 1880-1900 (past), 1980-2000 (present), and 2080-2100 (future), and shown in Figs 4.10 and 4.11. From each carbon integral, we remove the estimate obtained using pre-industrial control CM2Mc outputs, isolating the anthropogenic and climate anomalies in the total (anthropogenic and natural) carbon and natural carbon alone.

In the industrial simulation (Fig 4.10), all of the studied partitions increase from pre-industrial times, except for C^0_{sat}, also varying with space due to potential changes in circulation over time. The C_{tot} increase, on this occasion equal to C_{ant}, is 0.6 PgC yr^{-1} (value comparable to the observed 0.8 $\pm$ 0.6 PgC yr^{-1}).

The simulated C_{tot} increase is driven by increases in anthropogenic carbon dioxide in the atmosphere that force negative air-to-sea CO_2 fluxes (Fig 1.4). However, the C_{tot} increase is in opposition to the influence of the C_{dis} weakening (tendency towards air-sea CO_2 equilibrium), which drives the C_{tot} cycle towards saturation and hence decreases the potential for additional C_{ant} uptake. In pre-industrial times (1880-1900), the modelled $\delta_t C_{dis}$ matches the C_{soft} and C_{carb} anomalies, suggesting a predominance of the biological CO_2 uptake over the physical counterpart. Between 1980 and 2000, anthropogenic influences emerge, with $\delta_t C_{dis}$ being comparable to $\delta_t C_{tot}$. This comparability maintains in the following interval of time (2080-2100), when the atmospheric CO_2 increases and circulation changes further modify C_{dis}. Concurrently, the C^0_{sat} anomaly decreases throughout the simulation owing to a strengthening in the ocean stratification, in agreement with the study of Bernardello et al. (2014a) and our observational assessments of section 4.2.8.

In the climate simulation (Fig 4.11), where the direct C_{ant} uptake is not modelled, C_{soft} and C_{carb} maintain the anomalies of the CM2Mc industrial study: these runs have the same physics and, by definition, any change in the CM2Mc regenerated carbon can occur only through changes in the ocean circulation. This is potentially a major limitation of our study because a decrease in the Mixed Layer Depth (MLD) due to climate change influences the biological carbon pump (Smith and Marotzke,

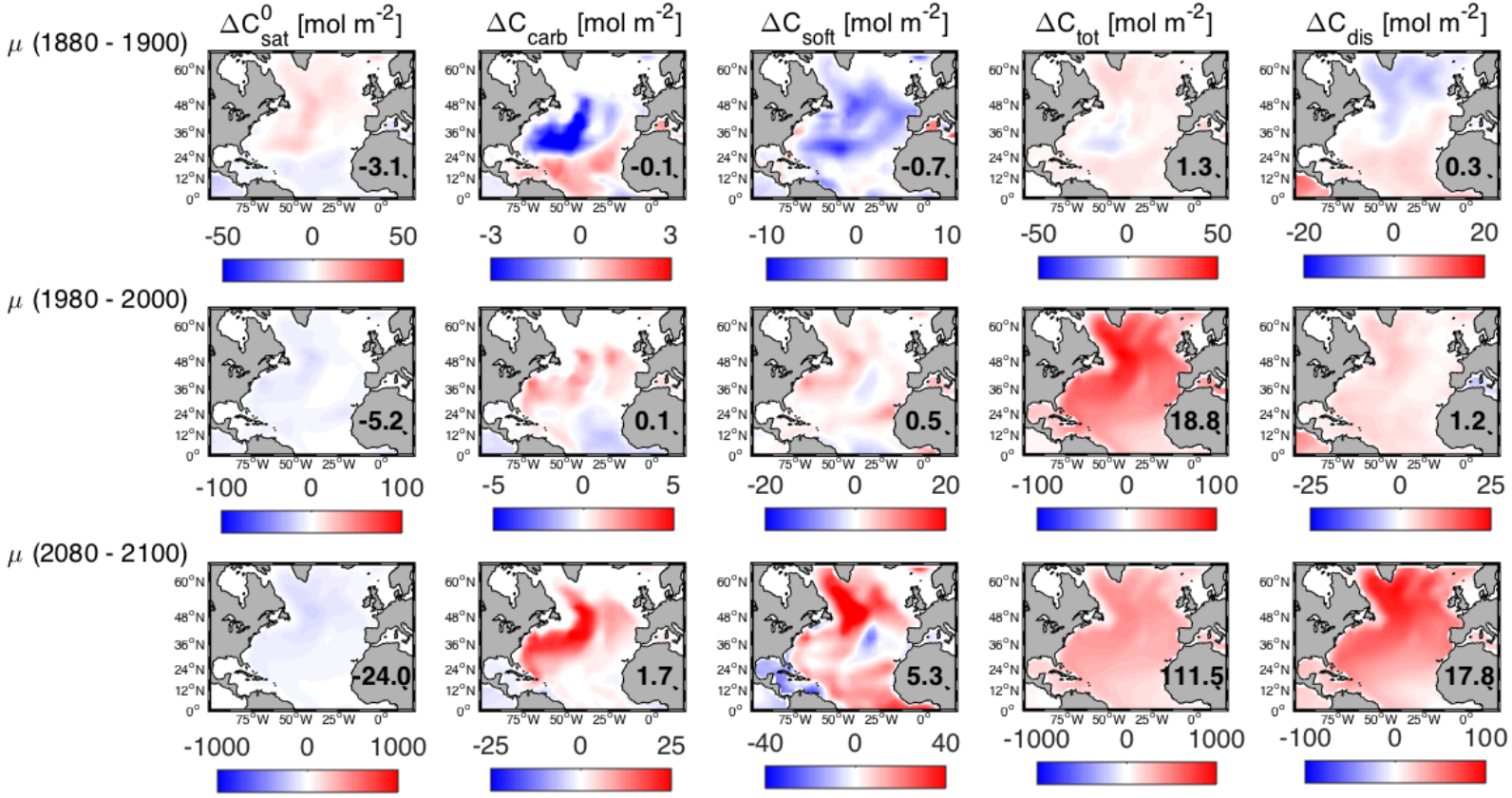

FIGURE 4.10: *Simulated anomalies of North Atlantic pre-industrial saturated (C^0_{sat}), carbonate (C_{carb}), soft-tissue (C_{soft}), total (C_{tot}) and disequilibrium (C_{dis}) carbon partitions averaged in three intervals of twenty years (1880-1900, 1980-2000, and 2080-2100). Data taken from the CM2Mc industrial outputs with the future (2006-2100) projected under the Representative Concentration Pathway 8.5 (RCP8.5; IPCC (2014); Taylor et al. (2012); van Vuuren et al. (2011)). Results in colour are column inventories corrected by removing the pre-industrial state to isolate C_{ant} and climate change influences. Associated budgets [PgC] are reported at the bottom right edge of each panel.*

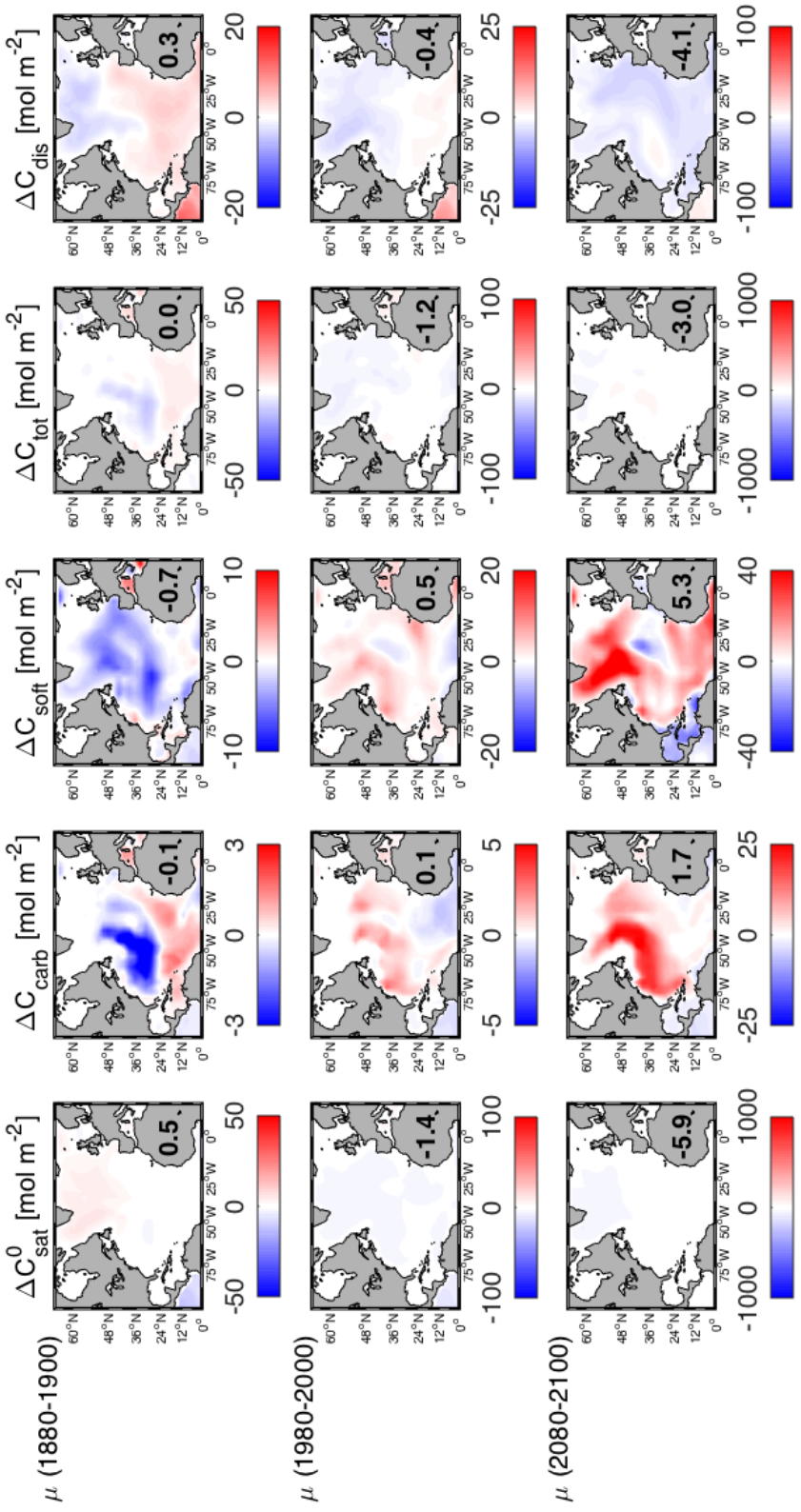

FIGURE 4.11: *Same as in Fig 4.10, but using a CM2Mc climate simulation outputs.*

2008). Such changes might be a direct response to increasing CO_2 levels for example, which would not be captured by the model. However, we will demonstrate in section 5.3 that North Atlantic subtropical C_{soft} variations are not always correlated to changes in the MLD. The simulated C^0_{sat} and C_{tot} climate anomalies decrease in time. This is due to the increase in the ocean stratification as well as reductions in CO_2 solubility not compensated for by the ΔpCO_2 increase and C_{dis} strengthening. To sum up, CM2Mc outputs allow us to investigate the carbon partitions interplay in the North Atlantic basin between 1860 and 2100. Snapshots of potential climate change and CO_2 uptake weakening, highlighted in the observations (section 4.2.8), are confirmed by the model and enhanced in the future projections. However, the CM2Mc simulates compensatory effects of increasing ΔpCO_2 at the surface and C_{soft} in the twilight zone, overall leading to a continuous CO_2 uptake and C_{tot} increase.

4.4 Synthesis and discussion

We investigate the carbon partitions interplay within the North Atlantic CO_2 uptake and storage. In the 24.5°N upper 1000 m, we quantify an averaged C_{tot} rise of 1.0 $\pm$ 0.1 μmol kg^{-1} yr^{-1} from 1992 to 2010. C_{ant} predominantly influences this C_{tot} trend, increasing by between 0.5 $\pm$ 0.2 μmol kg^{-1} yr^{-1} and 0.8 $\pm$ 0.2 μmol kg^{-1} yr^{-1} using the TTD and ΔC^* techniques, respectively. Other contributions may be due to changes in C_{dis}, C^0_{sat}, or C_{soft}. The C_{dis} trend shows a weakening in this partition barely distinguishable from the quasi Monte Carlo (MC) uncertainty. C^0_{sat} decreases over time, reducing C_{tot}. C_{soft} may be responsible for the unaccounted C_{tot} increase. We estimate the partition variability as difference between cruise-mean changes and MC trend estimates. Apart for localised changes in C_{dis}, the C_{soft} variability is the only one that is significant. Its values are positive in 2004 and negative in 2010, suggesting a change in residence time, pH, or productivity, each of which will be deepened in the next chapter.

We enlarge the study of the partitions interplay to the CM2Mc ESM between 1860 and 2100 after comparing the ESM outputs to GLODAPv2 climatological data and finding a broad match. We use the CM2Mc outputs to quantify anomalies of North

Atlantic carbon partitions from 1860 to 2100. Differences between the 'industrial' and background 'control' data show an increase in the C_{soft} and C_{carb} anomalies over the studied time interval. This result is confirmed by differences between the 'climate' and same background 'control' data, suggesting an influence of changes in the oceanic physics on the remineralised carbon partitions that will be explored in the next chapter.

Chapter 5

Time-varying influences on C_{ant} of carbon remineralisation

5.1 Introduction

We continue to investigate discrepancies of C_{ant} Decadal Trends (DTs) at 24.5°N in the Atlantic from 1992 to 2010 by comparing the TTD, DEC, ΔC^*, and eMLR estimates. In chapter 3 and section 4.2.4, the discrepancies among C_{ant} calculations were studied exploring analytical and methodological uncertainties. In this chapter, we study the influences on the divergence between C_{ant} DTs by temporal changes (noted as δ_t) in disequilibrium (C_{dis}), soft-tissue (C_{soft}), and pre-industrial saturated (C^0_{sat}) carbon partitions, and in pH, focusing on the mechanisms that control them. As an initial step, in section 5.2 we summarise the findings of section 4.2.4 plotting differences in C_{ant} cruise-means since 1992 and DTs in the upper four water masses of the 24.5°N Atlantic section (Subtropical Mode Water (STMoW), Madeira MoW (MMoW), Subpolar MoW (SPMoW), Antarctic Intermediate Water (AAIW)). We separate the carbon (ΔC^* and eMLR) and tracer (TTD and DEC) based methods, highlighting significant divergences in the estimates obtained with these techniques and exploring associated potential causes. We investigate differences in the method inclusions of C_{dis} temporal changes, as comparably done in section 3.3, and of the $\delta_t C_{soft}$ observed from 1992 to 2010 at 24.5°N in the Atlantic.

In section 5.3, we explore further the unexpected $\delta_t C_{soft}$ by investigating changes in Apparent Oxygen Utilisation (AOU), saturated (O_2^{sat}), gasex (O_2^*), and no-gasex (O_2^{ngas}) dissolved oxygen estimates. We hypothesise that increases in mean residence time, productivity, or solubility, or decreases in wind stress curl or pH could have caused them. So, we correlate the $\delta_t C_{soft}$ with variations in TTD mean ages, water volumes, and pH, which are based on observations made in the upper 1000 m of the 24.5°N hydrographic main section (78-16°W).

Following in section 5.3, we turn to a climate model in order to draw more robust conclusions. We use the outputs of a two millennia-long pre-industrial 'control' run of the Climate Model to Model coordinate (CM2Mc) Earth System Model (ESM). We investigate influences on subtropical C_{soft} of the meridional and barotropic stream functions, phosphate remineralisation rate, mixed layer depth, wind stress, water mass mean age, and pH variations over time. To avoid influences of the model drift and long-term trends on the processes investigated, we de-trend each signal removing least squares fitted regressions and approximating it by using discrete Meyer wavelet transforms. We test the C_{soft} approximation based on AOU (Eq 4.9) in section 5.4.

5.2 Partition influences on C_{ant} discrepancies

5.2.1 Overview and approach

C_{ant} increases from 1992 to 2010 in the subtropical North Atlantic upper 1000 m, but its values depend on the technique used for the estimate. In section 4.2.4, we linked the differences to analytical and methodological uncertainties, investigating subareas of the 24.5°N Atlantic transect. Here, we explore the influences of $\delta_t C^0_{sat}$, $\delta_t C_{soft}$, and $\delta_t C_{dis}$ on $\delta_t C_{ant}$, and the mechanisms that underlie these changes in the upper 1000 m of the 24.5°N main section (78-16°W).

We present four C_{ant} method estimates, dividing them into two groups: the DEC and TTD (tracer-based methods) include the CO_2 uptake carried by the physical carbon pump only using transient tracers; the ΔC^* and eMLR (carbon-based methods) separate a biogenic CO_2 uptake using AOU, Redfield ratios, and linear regressions,

therefore including more than the physical pump effect.

For each method, we estimate the C_{ant} increases since 1992 in the upper four water masses (STMoW, MMoW, SPMoW, AAIW) of the 24.5°N section, the uncertainty of C_{ant} DTs based on a quasi Monte Carlo (MC) approach (Kroese et al., 2014; Metropolis and Ulam, 1949), which uses random values in the range of determined C_{ant} (details are given in section 4.2.3), and we force the DT least-square fitted lines to start at zero in 1992 in Fig 5.1, in line with Figs 4.3-4.6.

Results are presented in Fig 5.1, where we plot the C_{ant} increases since 1992 and DTs for each of the water masses investigated. C_{ant} increases everywhere over time, as expected from the increasing atmospheric CO_2. However, we observe differences amongst the C_{ant} inferred with different methods and increases of these discrepancies over time, as it will be now briefly summarised.

In the STMoW, the carbon-based C_{ant} DTs are lower than the tracer-based trends. Elsewhere in the 24.5°N upper 1000 m, carbon-based C_{ant} DTs are higher than the tracer-based counterparts. ΔC^* and TTD confine the probable range of C_{ant} trends, as Iudicone et al. (2016) suggested. The eMLR and DEC DTs lie between the ΔC^* and TTD ones, supporting this suggestion: we explore further the discrepancies over time between the ΔC^* and TTD estimates only, in line with chapter 3 and section 4.2.4 of this thesis. We will investigate the $\delta_t C_{soft}$, $\delta_t C^0_{sat}$, and $\delta_t C_{dis}$ influences on the $\delta_t C_{ant}$ estimated by using the ΔC^* and TTD methods, analysing the underlying mechanisms and giving a new insight to the study of the divergence between C_{ant} estimates. $\delta_t C_{tot}$ is assumed to be equally captured by the C_{ant} methods (Eq 5.4), while $\delta_t C_{carb}$ is negligible in the 24.5°N upper ocean.

5.2.2 Time-varying carbon partition influences

The estimated ΔC^* and TTD C_{ant} increases diverge between 1992 and 2010 in the 24.5°N upper 1000 m, with C_{ant} DTs estimated, in this study, as 0.8 ± 0.2 μmol kg^{-1} yr^{-1} and 0.5 ± 0.2 μmol kg^{-1} yr^{-1} (Tab 4.2), and, by Guallart et al. (2015b), as 0.9 ± 0.2 μmol kg^{-1} yr^{-1} and 0.6 ± 0.2 μmol kg^{-1} yr^{-1}.

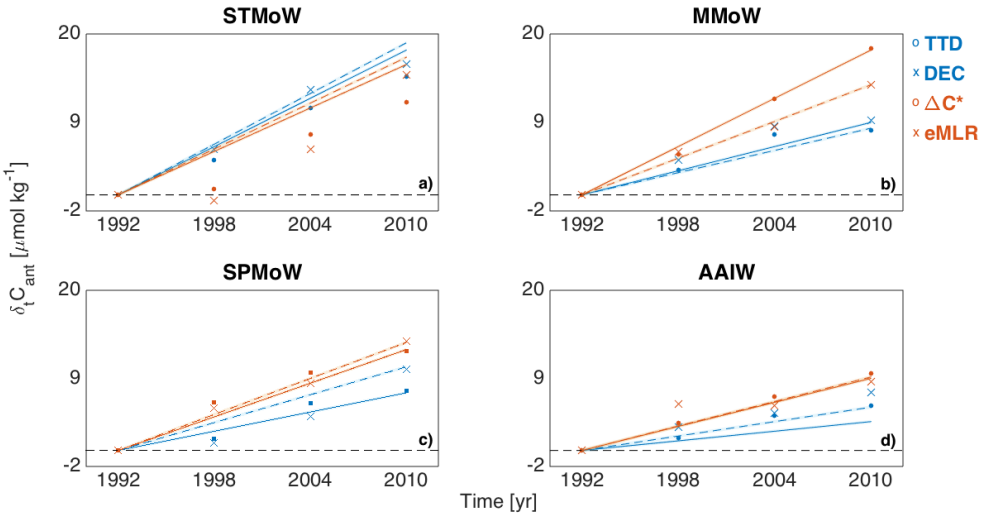

FIGURE 5.1: *Anthropogenic carbon (C_{ant}) Decadal Trends (DTs) and cruise-mean increases since 1992 ($\delta_t C_{ant}$) estimated in the upper four water masses ((a) Subtropical (STMoW), (b) Madeira (MMoW), (c) Subpolar (SPMoW) Mode Water (MoW), and (d) Antarctic Intermediate Water (AAIW)) of the 24.5°N main section (78-16° W) from 1992 to 2010. The TTD (continuous blue lines, dots), DEC (dashed blue lines, crosses), eMLR (dashed orange lines, crosses), and ΔC^* (continuous orange lines, dots) increases were determined using absolute C_{ant} values and are plotted by forcing the 1992 estimates through zero. The DTs are quantified fitting least-square linear models through C_{ant} increases over time, within the quasi Monte Carlo (MC) approach (section 4.2.3) and then forcing their starting point through zero in 1992. Uncertainties were inferred using a second MC approach and reported in the panels, but are too small to be visible.*

We hypothesise that the C_{ant} divergence may be investigated using the Williams and Follows (2011) carbon partitioning because the TTD and ΔC^* may capture carbon partition changes over time differently. We test our hypothesis comparing the ΔC^* and TTD inclusions of those partitions in Eqs 5.1 and 5.2 and then calculating the differences of their temporal changes in Eq 5.3. In those equations, the ΔC^* C^0_{sat}, C_{soft}, and C_{ant} are estimated by using Eqs 2.1-2.3. The TTD C_{ant} is estimated using Eq 2.10, the TTD C^0_{sat} is approximated using the carbon partition ($\delta_t C^0_{sat}$, Eq 4.8) estimated as by Williams and Follows (2011), and the C^{TTD}_{soft} and C^{TTD}_{carb} are zero. The TTD $\delta_t C_{dis}$ cannot be quantified directly, being indirectly based on transient tracer saturation estimates (section 2.3.3). Therefore, we avoid the ΔC^* C_{dis} (section 2.3.1) use and we estimate the difference between $\delta_t C^{\Delta C^*}_{dis}$ and $\delta_t C^{TTD}_{dis}$ using Eq 5.3. Here, we include every C_{tot} partition as potential source of C_{ant} divergence, but we investigate C^0_{sat}, C_{soft}, and C_{dis} only. C_{tot} is assumed to be equally captured by the

TTD and ΔC* techniques (Eq 5.4) and C_{carb} is negligible in the region investigated. Results are based on the 24.5°N data from 1992 to 2010, presented in Tab 5.1, and discussed hereafter.

$$C_{ant}^{\Delta C*} = C_{tot}^{\Delta C*} - (C_{sat}^{0\,\Delta C*} + C_{soft}^{\Delta C*} + C_{carb}^{\Delta C*} + C_{dis}^{\Delta C*}) \tag{5.1}$$

$$C_{ant}^{TTD} = C_{tot}^{TTD} - (C_{sat}^{0\,TTD} + C_{soft}^{TTD} + C_{carb}^{TTD} + C_{dis}^{TTD}) \tag{5.2}$$

$$\begin{aligned}(\delta_t C_{ant}^{\Delta C*} - \delta_t C_{ant}^{TTD}) = (\delta_t C_{tot}^{\Delta C*} - \delta_t C_{tot}^{TTD}) - (\delta_t C_{sat}^{0\,\Delta C*} - \delta_t C_{sat}^{0\,TTD}) - \\ (\delta_t C_{soft}^{\Delta C*} - \delta_t C_{soft}^{TTD}) - (\delta_t C_{carb}^{\Delta C*} - \delta_t C_{carb}^{TTD}) - (\delta_t C_{dis}^{\Delta C*} - \delta_t C_{dis}^{TTD})\end{aligned} \tag{5.3}$$

$$\delta_t C_{tot}^{\Delta C*} - \delta_t C_{tot}^{TTD} = 0 \tag{5.4}$$

Estimates of $\delta_t C_{sat}^{0\,\Delta C*}$ (equals to equilibrium carbon changes ($\delta_t C_{eq}$), section 2.3.1) and $\delta_t C_{sat}^{0}$ (here used as a proxy for $\delta_t C_{sat}^{0\,TTD}$) are related, both approximating the DIC differences that a layer would have when in CO_2 equilibrium with the overlying atmosphere. $\delta_t C_{sat}^{0}$ decreases by 0.3 ± 0.1 μmol kg^{-1} yr^{-1} (Tab 4.5), suggesting that $\delta_t C_{sat}^{0\,\Delta C*}$ decreases three times faster in the upper ocean (0-1000 m) taken as a whole, being the difference equals to 0.6 ± 0.1 μmol kg^{-1} yr^{-1} (Tab 5.1). The $\delta_t C_{sat}^{0}$ inclusion may be one of the main sources of C_{ant} divergence. $C_{sat}^{0\,\Delta C*}$ is based on linear regressions defined in the upper 100 m and a confined time period (Gruber et al., 1996). So, uncertainties may emerge at greater depth or different intervals. Instead, C_{sat}^{0} is calculated using co2sys (Eq 4.8; Lewis and Wallace (1998); Van Heuven et al. (2011)), thus constraining the ocean CO_2 saturation differently.

The ΔC* and TTD techniques differ also in the inclusion of $\delta_t C_{dis}$, as suggested in sections 3.3 and 4.2.5. The ΔC* includes influences from the physical and biological CO_2 uptakes, while the TTD isolates the physical carbon pump, estimating a weaker $\delta_t C_{dis}$. Additionally, the results of Tab 4.3 indicate that the TTD C_{dis} weakens over time faster than the ΔC* counterpart. However, the ΔC* and TTD methods could

TABLE 5.1: *Table summarising discrepancies in carbon partition changes over time (δ_t) between the ΔC^* and TTD estimates in the upper ocean water masses and top 1000 m of the 24.5°N main transect between 1992 and 2010. Listed carbon partitions are the anthropogenic (C_{ant}), pre-industrial saturated (C^0_{sat}), soft-tissue (C_{soft}), carbonate (C_{carb}), and disequilibrium (C_{dis}). The discrepancies in $\delta_t C_{dis}$ are inferred indirectly using Eq 5.3, and we use the C^0_{sat} estimated as by Williams and Follows (2011) to approximate $C^{0\,TTD}_{sat}$. We highlight in bold the highest difference for each carbon partition, also noting that the $\delta_t C_{ant}$ and $\delta_t C_{dis}$ differences in the top 1000 m are different from the water mass means owing to simplifications in section 4.2.4. The quasi Monte Carlo (MC) uncertainties used in this thesis for each carbon partition are summarised in Tab 4.1.*

Layers	STMoW	MMoW	SPMoW	AAIW	1000 m
Units	μmol^{-1} kg^{-1} yr^{-1}				
$\delta_t C^{\Delta C*}_{ant}$ - $\delta_t C^{TTD}_{ant}$	-0.1	**+0.5**	+0.3	+0.3	+0.3
$\delta_t C^{0\,\Delta C*}_{sat}$ - $\delta_t C^{0\,TTD}_{sat}$	0.0	+0.6	+0.6	**-1.0**	+0.6
$\delta_t C^{\Delta C*}_{soft}$ - $\delta_t C^{TTD}_{soft}$	+0.2	+0.1	**+0.6**	+0.3	+0.3
$\delta_t C^{\Delta C*}_{carb}$ - $\delta_t C^{TTD}_{carb}$	∼0.0	∼0.0	∼0.0	∼0.0	∼0.0
$\delta_t C^{\Delta C*}_{dis}$ - $\delta_t C^{TTD}_{dis}$	-0.3	-0.2	-0.9	**+1.0**	-0.6

carry an uncertainty on $\delta_t C_{dis}$ estimates due to the use of regression models and the tracer saturation estimates, respectively. We calculate the overall influence of C_{dis} discrepancies on the $\delta_t C_{ant}$ divergence indirectly using Eq 5.3.

We estimate insignificant discrepancies between $\delta_t C^{\Delta C*}_{dis}$ and $\delta_t C^{TTD}_{dis}$ in the STMoW and MMoW. Conversely, the estimates of SPMoW and AAIW $\delta_t C_{dis}$ divergences are -0.9 ± 0.3 μmol kg^{-1} yr^{-1} and 1.0 ± 0.3 μmol kg^{-1} yr^{-1} (see Tab 4.1 for details on the uncertainty). Taken as absolute values, the estimates compare to the section 3.3 results, where we estimated divergences of up to -0.7 μatm yr^{-1} between the ΔC^* and TTD $\delta_t pCO_{2ant}$ in the same water masses and interval of time, which correspond to $\delta_t C_{dis}$ differences of -0.4 ± 0.3 μmol kg^{-1} yr^{-1} under that analysis assumptions. Additional comparisons could have resulted from the study in section 4.2.5, but none of the estimated $\delta_t C_{dis}$ differences were significant in that occasion. Potential differences in the $\delta_t C_{dis}$ estimates emerge from the uncertainty only under the assumption that those values are responsible for all of the unaccountable $\delta_t C_{ant}$ divergence, which is used in sections 3.3, implicitly in the current section analysis,

but it was not adopted in section 4.2.5. So, changes in $\delta_t C^0_{sat}$ and $\delta_t C_{dis}$ significantly influence the $\delta_t C_{ant}$ divergence in the 24.5°N upper 1000 m from 1992 to 2010.
However, this influence is not exhaustive as changes in the biological carbon pump may also influence the observed divergence between the TTD and ΔC^* $\delta_t C_{ant}$. So, we investigate potential differences on the method inclusions of changes over time in the biogenic CO_2 uptake. The ΔC^* method includes a biological carbon partition (C_{bio}, section 2.3.1) that is, in this occasion, comparable to C_{soft}, with C_{carb} being negligible in the 24.5°N upper 1000 m (section 4.2.6). The TTD isolates the physical pump uptake, with negligible biogenic influences. So, the estimated positive $\delta_t C_{soft}$ (and $\delta_t C^{\Delta C*}_{soft}$) decreases the $\delta_t C^{\Delta C*}_{ant}$ but alters the $\delta_t C^{TTD}_{ant}$ insignificantly.
In summary, discrepancies in the TTD and ΔC^* inclusions of the $\delta_t C^0_{sat}$ and $\delta_t C_{dis}$ strengthen the $\delta_t C^{\Delta C*}_{ant}$ with respect to the $\delta_t C^{TTD}_{ant}$ in the upper 1000 m of the 24.5°N main transect from 1992 to 2010. These discrepancies are partially compensated by a positive $\delta_t C_{bio}$. This biological carbon variation is negligible in the TTD C_{ant} but is included by the ΔC^* technique, where decreases the estimated $\delta_t C^{\Delta C*}_{ant}$. Changes in the biogenic CO_2 pump, estimated by the $\delta_t C_{soft}$, are also unexpected, with causes, mechanisms, and consequences discussed in the next sections.

5.3 Time-increasing remineralised soft tissue

We investigate potential causes and their effects on the unexpected C_{soft} increase estimated in the 24.5°N upper 1000 m from 1992 to 2010. As causes, we explore changes in circulation, solubility, productivity, wind stress curl, and/or acidification. Effects are investigated in observations and outputs of the CM2Mc ESM. Among the last, we use only the data from a pre-industrial 'control' simulation to investigate the processes without the climate change effects (e.g. human-caused changes in surface temperature and atmospheric CO_2). Model biases were studied in section 4.3.2 and considered negligible for all carbon partitions, with the exception of C_{carb}.

5.3.1 Effects on subtropical North Atlantic C_{soft} variations

C_{soft} increases in the 24.5°N upper 1000 m from 1992 to 2010. This increase is linked to a decrease in the measured oxygen, an increase in the saturated component (O_2^{sat}), and hence a positive δ_tAOU (Eq 4.10), as Stendardo and Gruber (2012) also showed in the North Atlantic basin.

Several processes may have caused these patterns, influencing the biological carbon pump, which is a key component of the oceanic subtropical systems (Doney, 1997; Emerson et al., 1997). We investigate the most influential processes, schematising them in Fig 5.2 as circulation, productivity, acidification, and wind stress influences. These processes interact (e.g. circulation and wind stress influence the O_2 solubility) and could be all influenced by changes in ocean temperature, which is then not assessed singularly. For the present study, the variations on these four processes are reported as changes in the meridional stream function, mixed layer depth chlorophyll, upper-ocean pH, and wind velocity in the subtropical North Atlantic from 2004 to 2015 in Fig 5.3. These changes suggest increases in C_{soft}, as it will be investigated.

Circulation effect. Changes in meridional mass transport can modify the velocities across the 24.5°N transect, altering the residence time of a seawater parcel. If the region stores great concentrations of remineralised DIC, increased residence times cause the parcel to accumulate C_{soft} with respect to its mean (Parekh et al., 2006).

Productivity effect. Changes in productivity above 200 m are positively correlated to the amount of Dissolved (DOC) and Particulate (POC) Organic Carbon exported and remineralised at depth, causing variations in C_{soft} in the so-called twilight zone, which extends from 200 m to 1000 m, and potentially below (Parekh et al., 2006). In this thesis, we do not investigate changes over space and time of the North Atlantic ratio between primary production and exported organic carbon, but we use CM2Mc outputs of Phosphate Remineralisation Rate (PRR). The PRR tackles more directly the C_{soft} (Eq 2.12) accumulation in the 24.5°N twilight zone, including also potential changes in this carbon partition that happen northern than the studied section and are propagated advectively by the ocean circulation.

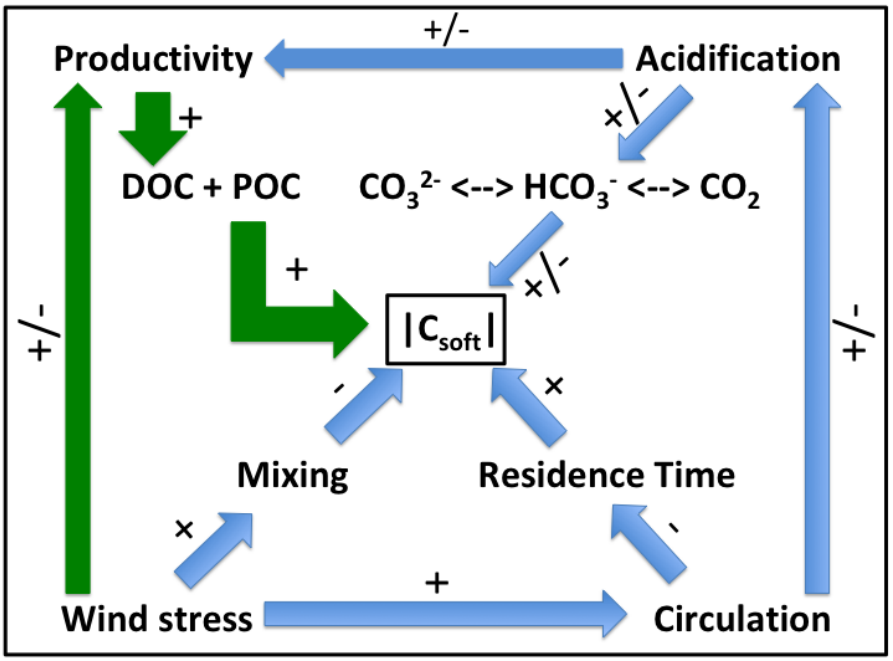

FIGURE 5.2: *Overview of the influences (+ when increases, - when decreases, and +/- when the influence depends on other variables (e.g. primary producer species)) on C_{soft} of the physical (light blue) and biological (green) carbon pumps (Godbold and Calosi, 2013; Riebesell et al., 2009). This schematic is not exhaustive, but includes processes and associated consequences discussed in this thesis chapter. Listed variables are the soft-tissue carbon (C_{soft}), carbonate ion (CO_3^{2-}), bicarbonate ion (HCO_3^-), aqueous carbon dioxide (CO_2, section 1.3), Dissolved (DOC) and Particulate (POC) Organic Carbon. The scheme corners isolate effects of changes in circulation (bottom right), wind stress (bottom left), productivity (upper left), and acidification (upper right). The arrow sizes approximate the contribution to δC_{soft} of the investigated processes.*

Acidification effect. Changes in CO_2 uptake modify pH progressively, causing potential variations in the inorganic carbon species (CO_2, HCO_3^-, and CO_3^{2-}) and shifts of the system towards an aqueous CO_2 predominance (Pedersen et al., 2013). This modifies the carbonate saturation state and amount of remineralisable carbon (Doney et al., 2009), varies the composition of the primary producers (Godbold and Calosi, 2013) and alters the efficiency of remineralisation (Kroeker et al., 2013).

Wind stress effect. Wind stress changes can modify the vertical mixing, column stratification, circulation, associated mean age and residence time, overall leading to variations in C_{soft} (Marinov et al., 2008). Changes in gyre circulation and wind driven coastal upwelling may also alter the nutrients and O_2 supplies to the euphotic zone,

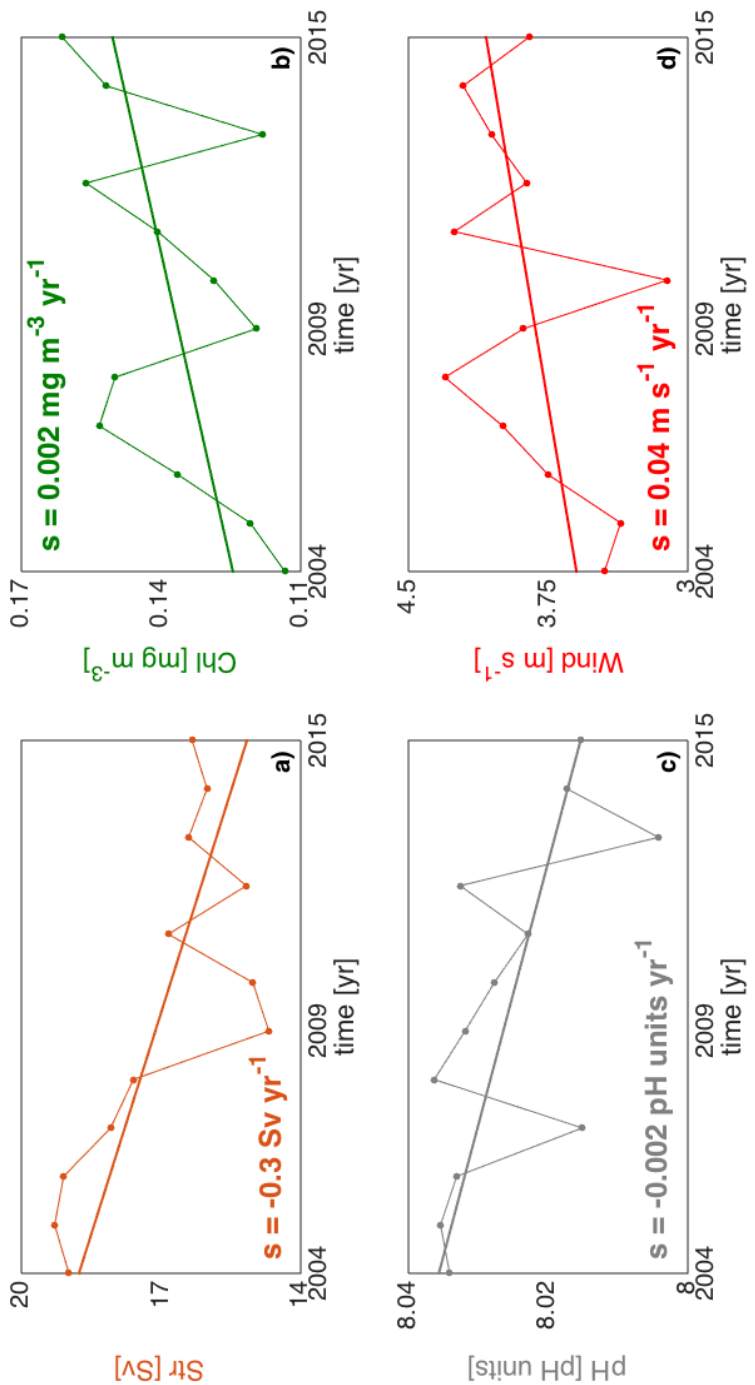

FIGURE 5.3: *Changes in meridional mass Stream function (Str, orange, panel a), mixed layer depth Chlorophyll (Chl, green, panel b), upper-ocean pH (grey, panel c), and Wind velocity (red, panel d) in the subtropical North Atlantic (24.5°N) from 2004 to 2015. The Str data are taken from the RAPID repository (Hirschi et al., 2003). The Chl data are taken from the NASA/AQUA MODIS satellite repository (NASA, 2014). The pH data are taken from the GLODAPv2 dataset (Olsen et al., 2016), with the 2011, 2014 and 2015 data replaced by the trend-line equation (pH = -0.0019 year + 11.7714) results: we considered the 2011 value an outlier, while the 2014 and 2015 values were missing. The Wind velocities are taken from the NCEP/NCAR reanalysis (Kalnay et al., 1996). For each time series we plot the least squares fitted line and report the slope (s) to highlight and quantify the trend, respectively.*

the surface productivity, and the resulting accumulation of C_{soft} at depth. Brandt et al. (2015) reported reductions of approximately a third in the subtropical North Atlantic O_2 caused by a mixing weakening in regions of coastal upwelling.

Solubility effect. The O_2 concentration (and so AOU and C_{soft}) is also influenced by changes in solubility (Stendardo and Gruber, 2012). This parameter is sensitive to changes in temperature, potentially caused by climate change, which may reduce the amount of O_2 sequestered by the ocean and potential for further uptake (O_2^{sat}). Alterations in the wind stress curl could however increase the O_2 solubility, rendering it difficult to separate the influences of those processes.

5.3.2 Circulation, solubility, and productivity effects on C_{soft}

The five processes hypothesised in the previous section are strongly interconnected. However, we consider only circulation, solubility, and productivity effects on C_{soft} in this section due to the methodology chosen. Effects of wind stress and acidification on the upper-ocean soft-tissue are discussed in sections 5.3.3 and 5.3.4, respectively. We investigate the influence of changes in meridional mass transport, O_2 solubility, and primary productivity on the δ_tAOU, which is the independent variable in the $\delta_t C_{soft}$ estimate (Eq 4.9). These can be investigated by assessing separately O_2^{sat} and O_2, from which AOU is calculated (Eq 4.10; Pytkowicz (1971)). O_2^{sat} is a function of temperature and salinity measurements, thus accounting for solubility changes, in agreement with C_{sat}^0. O_2 is also influenced by changes in solubility, but this effect can be removed by difference with the O_2^{sat} study. Doing so, we estimate the combined influence on AOU of variations in circulation and remineralisation.

Alternatively, we could investigate changes into a gas exchange (gasex) O_2 (O_2^*, Eq 5.5; Gruber et al. (2001)) and a no-gasex O_2 (O_2^{ngas}, Eq 5.6; Stendardo and Gruber (2012)). Temporal changes in O_2^* reflect O_2 gains and losses in the mixed layer depth regardless of the causal processes. $\delta_t O_2^{ngas}$ approximates changes in the ocean interior O_2, being then primarily influenced by variations in circulation and remineralisation.

$$O_2 = O_2^* + O_2^{ngas} \tag{5.5}$$

$$O_2^{ngas} = -RR_{O:P}\,(PO_4 - PO_4^{pre}) \tag{5.6}$$

where $RR_{O:P}$ is the Redfield ratio between O_2 and PO_4 (Redfield, 1934). The method can be applied in the North Atlantic, as successfully done by Gruber et al. (2001), but it may be challenging elsewhere due to the PO_4^{pre} estimate.

We show temporal changes of cruise-mean AOU, O_2^{sat}, O_2^*, and O_2^{ngas} in Tab 5.2. Here, we study the 24.5°N STMoW, MMoW, SPMoW, AAIW, and upper-ocean (0-1000 m) layer for four time intervals: 1992-1998, 1998-2004, 2004-2010, and 1992-2010. We estimate the uncertainties that are due to the observed variability by using a quasi MC approach (Kroese et al., 2014; Metropolis and Ulam, 1949).

Between 1992 and 2010, AOU increases in the 24.5°N upper 1000 m by 5.9 ± 1.3 μmol kg^{-1}. The majority of this increase is caused by an O_2^{ngas} decrease, while O_2^{sat} changes by 0.2 ± 0.002 μmol kg^{-1} and O_2^* varies insignificantly: a change in the O_2 biological consumption over time seems to be the main cause of our findings.

At a smaller spatial scale, seasonality and non-conservativeness may influence the STMoW δ_tAOU, requiring care on its analysis. Even so, we note changes over time in the STMoW $\delta_t O_2^*$, the variations of which roughly halve after 2004. This suggests an O_2 loss, but the most influential cause is not directly identifiable. The gradual strengthening in the $\delta_t O_2^{sat}$ suggests that changes in the O_2 saturation of the studied water mass are also influential on the STMoW δ_tAOU. This result agrees with the variations estimated between 1992 and 2010. Changes in $\delta_t O_2^{ngas}$ are not significant.

In the MMoW, we quantify a significant increment in time in all of the investigated O_2 from 2004 to 2010, which is a time interval characterised by a slow-down in the AMOC (Smeed et al., 2014): the observed AOU increase may have been due to a circulation weakening, which is the only causal effect that influences all of the investigated variables. The result agrees with the longer time interval analysis: between 1992 and 2010 O_2^{sat} and O_2^{ngas} changes are predominant, while O_2^* varies within the associated uncertainty.

In the SPMoW, the investigated variables vary within the uncertainty from 2004 to 2010. However, O_2^{ngas} and O_2^{sat} increase between 1998 and 2004, suggesting a shift over time with respect to the MMoW. Between 1992 and 2010, a change in O_2^{ngas}

TABLE 5.2: *Table summarising differences over time (δ_t) in Apparent Oxygen Utilisation (AOU, Eq 4.10), saturated (O_2^{sat}), gasex (O_2^*), and no-gasex (O_2^{ngas}) dissolved oxygen in the upper water masses (Subtropical Mode Water (STMoW), Madeira MoW (MMoW), Subpolar MoW (SPMoW), and Antarctic Intermediate Water (AAIW)) and top 1000 m of the 24.5° N Atlantic main section (78-16° W). Changes over time in the listed O_2 approximate the effects on AOU of solubility, gas exchanges, and ocean interior variations, respectively. All estimates are reported in μmol kg^{-1}, with the uncertainties listed in the last column. We highlight in bold the greatest variations over time that exceed the uncertainty.*

STMoW	1992-1998	1998-2004	2004-2010	1992-2010	Uncertainty
AOU	+9.5	**-10.3**	+10.0	+9.2	± 1.3
O_2^{sat}	-3.5	+4.8	**-6.1**	-4.7	± 0.002
O_2^*	+3.5	**-3.6**	+1.7	+1.7	± 1.4
O_2^{ngas}	-2.5	+1.9	-2.2	**-2.8**	± 2.7
MMoW	1992-1998	1998-2004	2004-2010	1992-2010	Uncertainty
AOU	-1.7	+1.4	**+4.6**	+4.3	± 1.3
O_2^{sat}	-2.7	-0.1	**+5.1**	+2.3	± 0.002
O_2^*	-0.5	-1.3	**+2.5**	+0.7	± 1.4
O_2^{ngas}	+3.9	-2.6	**-7.2**	-5.9	± 2.7
SPMoW	1992-1998	1998-2004	2004-2010	1992-2010	Uncertainty
AOU	+3.8	**+7.4**	+1.9	+13.1	± 1.3
O_2^{sat}	+1.1	**+5.6**	-2.1	+4.5	± 0.002
O_2^*	0.0	**+1.9**	-0.1	+1.7	± 1.4
O_2^{ngas}	-4.9	-11.1	+0.1	**-15.9**	± 2.7
AAIW	1992-1998	1998-2004	2004-2010	1992-2010	Uncertainty
AOU	**-8.4**	-1.2	+6.2	-3.4	± 1.3
O_2^{sat}	+5.0	+1.1	**-7.2**	-1.1	± 0.002
O_2^*	+1.7	+1.7	**-2.7**	+0.7	± 1.4
O_2^{ngas}	+5.1	+1.8	-1.7	**+5.2**	± 2.7
1000 m	1992-1998	1998-2004	2004-2010	1992-2010	Uncertainty
AOU	+0.8	-0.6	+5.7	**+5.9**	± 1.3
O_2^{sat}	0.0	**+2.8**	-2.6	+0.2	± 0.002
O_2^*	+1.2	-0.3	+0.4	+1.2	± 1.4
O_2^{ngas}	+0.4	-2.5	-2.7	**-4.9**	± 2.7

is the main forcing of AOU variations, suggesting that changes in remineralisation and circulation were more influential than solubility effects in that interval of time. The concurrent positive $\delta_t O_2^{sat}$ identifies the circulation variability as predominant. In the AAIW, changes in δ_tAOU are also predominantly influenced by changes in O_2 solubility. This agrees with Lauderdale et al. (2013) and Matear et al. (2000). The assessment of temporal changes in O_2^{sat}, O_2^*, and O_2^{ngas} is a powerful approach to investigate influences on δ_tAOU and $\delta_t C_{soft}$ of changes in solubility, circulation, and remineralisation. However, this approach is treated as preliminary under the circumstances used in this thesis. Any O_2 trend or variation that span for less than three decades may be affected by North Atlantic Oscillations (NAO) or other sources of long-term variability (Stendardo and Gruber, 2012), but it cannot be detected.

Changes in the TTD age. To streamline the effect of changes in circulation, we compare C_{soft} and TTD age cruise means in the STMoW, MMoW, SPMoW, and AAIW of the 24.5°N main transect between 1992 and 2010 (Fig 5.4).

In the STMoW, estimates of TTD mean ages and C_{soft} are not correlated. The last significantly varies in time, but its oscillating pattern is likely to be due to seasonality, being the data collected alternatively in late and in early spring (Cunningham et al., 2005; King et al., 2012; Millero et al., 2000; Peltola et al., 2001).

In the MMoW, the age and C_{soft} are not correlated. The squared Pearson's coefficient is 0.56 but $p = 0.25$ owing to the low amount of observations. From 1998 to 2004, we see an anomalous age increase, but the C_{soft} is not different from the 1998 mean value. From 1992 to 2010, the age and C_{soft} increase significantly, potentially owing to the mentioned circulation slow-down in 2010 (Bryden et al., 2014).

In the SPMoW, the TTD mean age and C_{soft} are correlated ($R^2 = 0.80$), although $p = 0.10$ owing to the limited number of observations. The water mass mean age and the remineralised soft tissue increase in the studied time interval.

In the AAIW, the TTD mean age and C_{soft} do not correlate, with R^2 being 0.54 and $p = 0.27$ owing to the limited number of observations.

In summary, C_{soft} increases in the 24.5°N twilight zone (200-1000 m) from 1992 to 2010, with a peak in 2004. This suggests a decrease in ventilation but we cannot

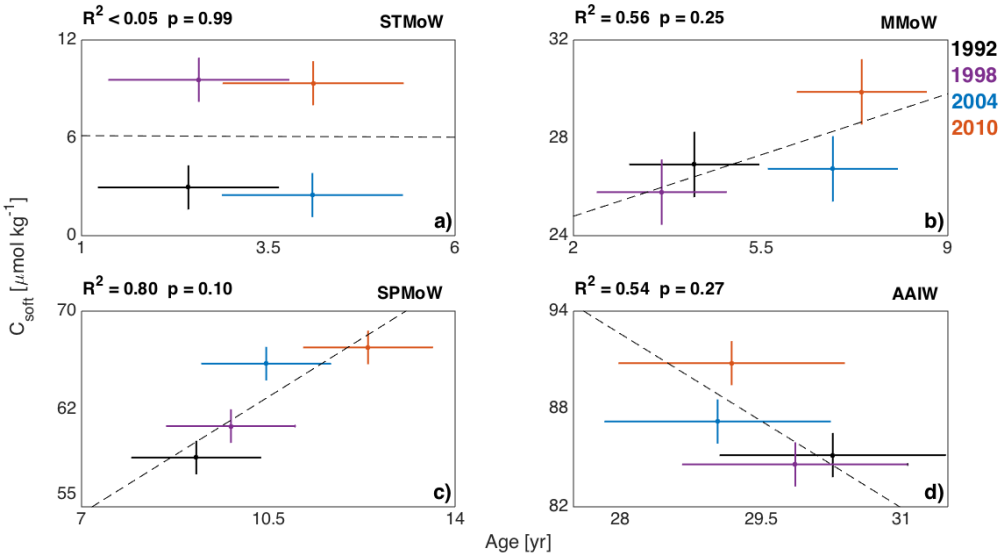

FIGURE 5.4: *Soft-tissue carbon partition (C_{soft}) versus TTD mean age in the (a) Subtropical (STMoW), (b) Madeira (MMoW), (c) Subpolar (SPMoW) Mode Water (MoW), and (d) Antarctic Intermediate Water (AAIW). Variables are quantified at the 24.5°N main section (78-16° W) and reported in 1992 (black), 1998 (purple), 2004 (blue), and 2010 (orange). Uncertainties are quantified using a quasi Monte Carlo (MC) technique (Kroese et al., 2014; Metropolis and Ulam, 1949) and result as ±1.3 μmol kg^{-1} and ±1.2 yr for the C_{soft} and TTD age, respectively. R^2 and the p values are reported to evaluate the reliability of the investigated correlations.*

quantify potential influences of primary productivity, wind stress curl, acidification, or solubility changes using the TTD mean age only.

5.3.3 Wind stress curl effect on C_{soft}

In the previous section, we explored correlations between TTD mean age and C_{soft} to assess the ventilation effect on C_{soft} in the subtropical North Atlantic.

However, TTD mean age and C_{soft} could correlate owing to an external forcing that influences both estimates. For instance, a weakening in wind stress curl would cause a decrease in mixing, which increases subsurface water mass volumes and reduces ages and C_{soft}. To account for this process, we study correlations between the cruise-mean TTD age, C_{soft}, and volume in the 24.5°N STMoW, MMoW, SPMoW, and AAIW between 1992 and 2010 (Figs 5.5 and 5.6). The STMoW (or surface layer) is defined as the seawater volume above 200 m (section 1.4.3), hence has a constant volume and no correlation with C_{soft} or TTD age (Figs 5.5a, 5.6a).

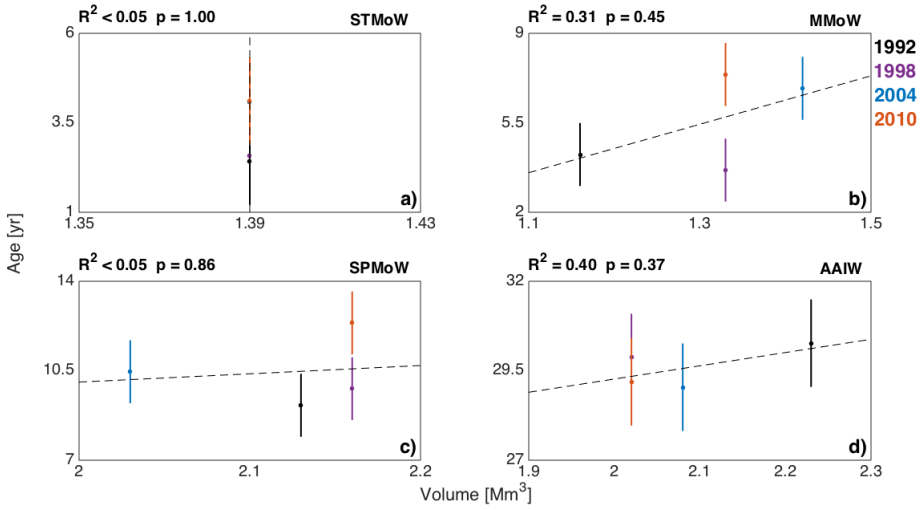

FIGURE 5.5: *Same as in Fig 5.4, but for the water mass ages and volumes. The last values are calculated by using a N-S dimension of one degree and the water mass area along the 24.5°N main transect (78-16°W). The STMoW volumes do not vary over time, with the water mass being defined on the fixed isodepth of 200 m, but they are included for completeness.*

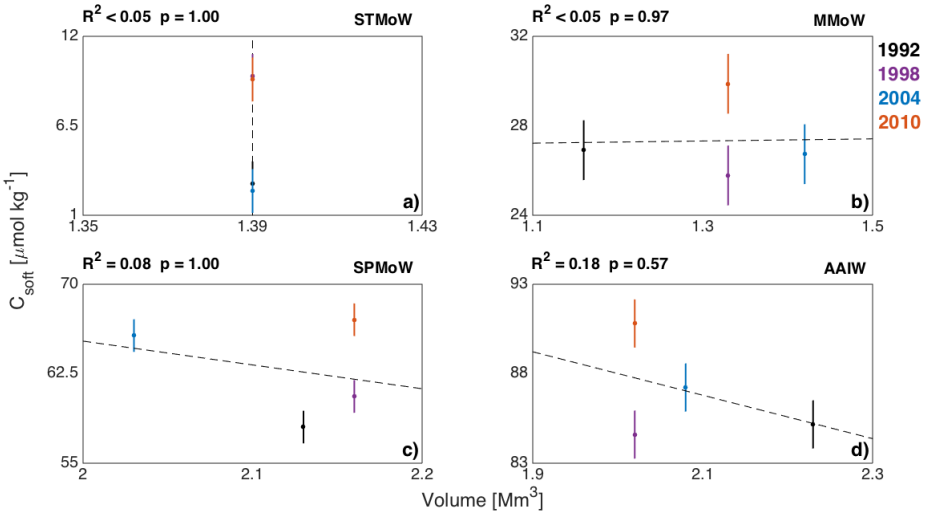

FIGURE 5.6: *Same as in Fig 5.5, but for the water mass C_{soft} and volumes.*

In the MMoW, a third of the TTD mean age rise ($R^2 = 0.31$, Fig 5.5b) seems to be influenced by the water volume increase, but the associated p value invalidates this hypothesis, whilst changes in the water mass volume do not influence C_{soft} between 1992 and 2010, being R^2 lower than 0.05 and $p = 0.97$ (Fig 5.6b).

In line with the MMoW, the increasing SPMoW volumes do not influence the water mass TTD age and C_{soft}. The AAIW analyses also agree with the MoW above it.

We evidence anomalous changes in the water mass volumes of the 24.5°N twilight zone in 2004 and 2010. However, neither the TTD mean ages nor C_{soft} estimates are affected by them, thus excluding the hypothesised wind stress curl or the consequent mixing influences on the unexpected C_{soft} increase.

5.3.4 Acidification effect on C_{soft}

In the previous thesis sections, we explored the influence of changes in circulation, solubility, wind stress curl, and remineralisation on the upper ocean C_{soft}, implicitly assuming negligible impacts of variations in pH. This assumption was necessary to isolate other mechanisms causing $\delta_t C_{soft}$, but it is unrealistic when we consider that the pH decreases by 0.002 pH units yr^{-1} from 2004 to 2015 in the subtropical North Atlantic (Fig 5.3), as also shown by Guallart et al. (2015a) between 1992 and 2011. We explore potential links between changes in pH and C_{soft} in the subtropical North Atlantic upper ocean between 1992 and 2010. In section 3.4.3, we separated the pH into an anthropogenic (pH_{ant}) and natural (pH_{nat}) components by using the method of Woosley et al. (2016) and estimated the uncertainties using a quasi MC approach (Kroese et al., 2014; Metropolis and Ulam, 1949). Here, we explore the interactions between pH_{ant}, pH_{nat} and C_{soft} estimates, focusing on the mechanisms that modify their values and on the consequences for the ocean CO_2 cycle.

We investigate correlations between cruise-mean estimates in the 24.5°N STMoW, MMoW, SPMoW, and AAIW. Here, we estimate the pH_{ant} and pH_{nat} using the ΔC^* and TTD methods as in the study of section 3.4.3. Results are presented in Fig 5.7, while the squared Pearson's coefficients (R^2) and p values associated to the panel x-y correlations of this figure are presented in Tab 5.3.

Overall, temporal changes in natural and anthropogenic pH components correlate to changes in the 24.5°N C_{soft} below the STMoW, which is expected as all of the investigated components participate in the carbon cycle. In the STMoW, however, we calculate insignificant correlations, most probably due to seasonal effects on C_{soft}. Comparing the results of the TTD and ΔC^* methods below the STMoW, changes in the latter estimates are more strongly correlated to the C_{soft} increases than the

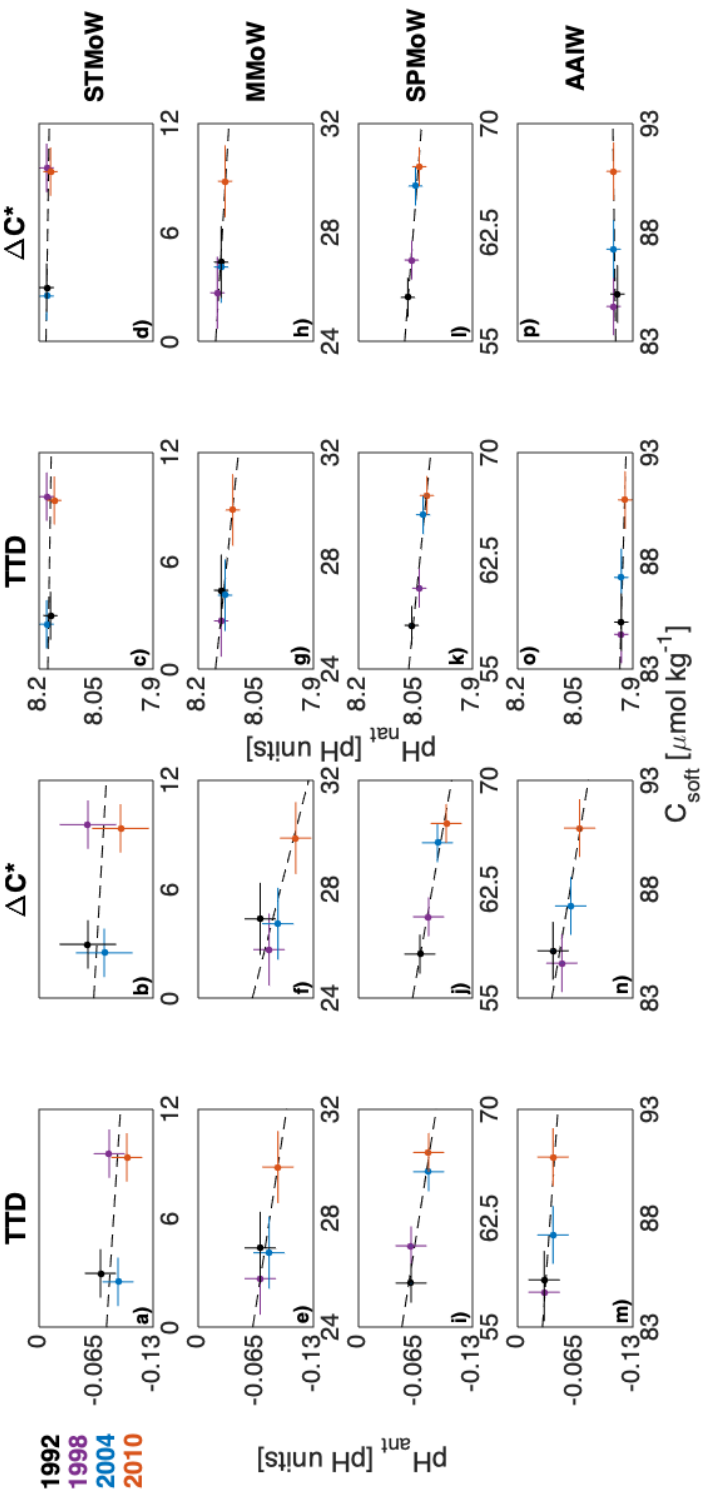

FIGURE 5.7: *Same as in Fig 5.4, but for the water mass C_{soft}, natural (pH_{nat}) and anthropogenic (pH_{ant}) pH estimates. The last two variables are quantified using the TTD and ΔC^* methods to account for differences between these approaches. We built on the quasi Monte Carlo uncertainties calculated in section 3.4.3, applying a value of ± 0.017 pH units to all pH estimates for conservativeness. Squared Pearson's correlation coefficients and associated p values are reported in Tab 5.3.*

TABLE 5.3: *Table summarising squared Pearson's coefficients (R^2) and p values of correlations among subtropical North Atlantic soft-tissue carbon (C_{soft}), natural, and anthropogenic pH estimates (see also Fig 5.7). The pH estimates are obtained by using the TTD and ΔC^* approaches, as also shown in Fig 5.7 and discussed in the main text. Data reported for the four upper ocean water masses: Subtropical (ST), Madeira (M), Subpolar (SP) Mode Water (MoW), and Antarctic Intermediate Water (AAIW).*

	Anthropogenic pH (pH_{ant})				Natural pH (pH_{nat})			
	TTD analyses		ΔC^* analyses		TTD analyses		ΔC^* analyses	
Water mass	R^2	p value	R^2	p value	R^2	p value	R^2	p value
STMoW	0.16	0.60	0.07	0.74	0.09	0.67	0.31	0.44
MMoW	0.79	0.11	0.68	0.18	0.88	0.02	0.89	0.06
SPMoW	0.92	0.04	0.96	0.02	0.92	0.04	0.96	0.02
AAIW	0.72	0.15	0.81	0.10	0.84	0.08	0.18	0.44

TTD results. This is due to the partial inclusion in the ΔC^* of O_2 changes, which are tightly linked to acidification (Guallart et al., 2015a).

In summary, differences in the inclusion of biogeochemical temporal changes lead to disagreements between pH_{ant} and pH_{nat} estimated by the TTD and ΔC^*. This discrepancy influences the study of the correlations among pH components and C_{soft}, resulting in different R^2 and p values. Notwithstanding that, the analyses done so far in this chapter are based on observations and are therefore limited in space and time. We will obtain a wider coverage using the CM2Mc ESM hereafter.

5.3.5 From observations to climate models

We investigated how circulation, productivity, wind stress curl, and acidification contribute to the observed C_{soft} accumulation in the subtropical North Atlantic (24.5°N) upper ocean (0-1000 m) from 1992 to 2010. However, we cannot assess the role of changes in these processes over spatial and temporal scales greater than the observational window. As a consequence, we turn to a climate model: the CM2Mc ESM (section 2.4). This model platform is not the real world, but represents a useful test bed, offering more variables with a better coverage over space and time.

5.3.6 Long-term assessment of C_{soft} variations

We observed a C_{soft} rise in the subtropical North Atlantic from 2004 to 2010, a time interval characterised by a suggested AMOC slow-down (Smeed et al., 2014). This decrease was attributed to natural variability (Jackson et al., 2016), although its causes are still under debate (Bryden et al., 2014; Haine, 2016; Robson et al., 2016). Whichever is the exact cause, we study C_{soft} variations over time, comparing them with changes in meridional and barotropic mass Stream functions (Str and Str_{bar}), Wind stress curl (hereafter named Wind), Mixed Layer Depth (MLD), water mass mean Age (hereafter named Age), Phosphate Remineralisation Rate (PRR[1]), and pH by using outputs from a 2000 yr-long CM2Mc pre-industrial 'control' simulation (section 2.4). The control run isolates the mass transport influence on C_{soft}, but it simplifies the real world, not including patterns that may be relevant for our study (e.g. long-term AMOC slow-down). We use the ESM outputs to test five hypotheses. (1) A weakening in the ocean circulation increases the Age, accounting also for a remineralisation accumulation in the same water parcel. (2) A Wind strengthening reduces the Age by increasing the Str_{bar} (Moat et al., 2016), so decreasing C_{soft} with respect to the mean value. (3) A weakening in Wind and surface transport decrease the mixing, MLD, and water mass volume, therefore increasing the Age and C_{soft}. (4) An increasing primary productivity leads to higher carbon export, consumption of O_2, and nutrients remineralisation, accumulating C_{soft}. (5) Decreases in pH over time alter the primary productivity rate, carbon export, and so C_{soft} accumulation. To investigate our hypotheses, we correlate simulated Wind, MLD, Age, PRR, Str, STR_{bar}, pH, and C_{soft}, assuming that R^2 values infer the independent variable (e.g. Str) influence on the dependent estimate (e.g. C_{soft}), in line with the work of Yang and Hoskins (2016). All variables are extracted or calculated at the 24.5°N transect and in an interval between 78-16°W, so excluding the Florida Strait and focusing on the southwards transport only. MLD, Wind, and Str_{bar} are averaged at the 24.5°N surface, while the other variables are calculated in the twilight zone (200-1000 m) to

[1]To assess the biological influence on the simulated C_{soft}, we use the simulated PRR: this is more directly related to the production of C_{soft} than the surface chlorophyll averaged concentration used for the overall assessment in section 5.3.1. The PRR is calculated, in the CM2Mc model, as the variation over time in the PO_4 sources integral for the layer considered.

TABLE 5.4: *Table summarising squared Pearson's coefficients (R^2) quantified by comparing Meyer approximations (Fig 5.8) of de-trended CM2Mc simulated data. We study correlations between the soft-tissue carbon (C_{soft}), meridional Stream function (Str), barotropic Str (Str_{bar}), Wind stress curl (Wind), water mass mean Age (Age), Mixed Layer Depth (MLD), Phosphate Remineralisation Rate (PRR), and pH. R^2 values greater or equal than 0.20 are highlighted in bold.*

	C_{soft}	Str	Str_{bar}	Wind	Age	MLD	PRR	pH
C_{soft}	1.00							
Str	**0.22**	1.00						
Str_{bar}	<0.05	<0.05	1.00					
Wind	0.13	<0.05	<0.05	1.00				
Age	**0.86**	**0.20**	<0.05	**0.23**	1.00			
MLD	<0.05	<0.05	<0.05	0.09	<0.05	1.00		
PRR	0.18	<0.05	<0.05	**0.29**	**0.21**	<0.05	1.00	
pH	**0.68**	0.05	<0.05	0.17	**0.59**	<0.05	**0.26**	1.00

match the investigated observational layer. C_{soft} and Str are taken as inventory and upper-ocean maximum, while PRR, pH, and Age are calculated as layer averages. All of the correlations could vary at different periodicities, being also influenced by long-term trends[2]. We remove least squares fitted linear regression from the signals (linear de-trending), and then approximate the curves using discrete Meyer wavelet transforms (Meyer, 1993; Meyers et al., 1993). For this, we use a frequency of 20 yr, periodicity comparable with the observational time frame (1992-2010) and AMOC oscillations (Dong and Sutton, 2005). We present our results in Figs 5.8 and 5.9 for the wavelet transforms and the details[3], respectively. We calculate R^2 and p values for each variable couple, reporting them on Tab 5.4.

Hypothesis (5): the simulated C_{soft} and pH are significantly correlated (Tab 5.4), following the processes summarised in section 5.3.1, and this correlation is negative, as can be deduced in Fig 5.8g. This leads to a positive feedback, which causes further changes in pH and so in C_{soft}, until the CO_2 system reaches a new equilibrium.

[2]We expect the temporal drifts to be almost negligible after 5000 years of CM2Mc spin-up.

[3]By using the wavelet transform method, the original signal is decomposed in a transform of a specific frequency and a curve generally called detail.

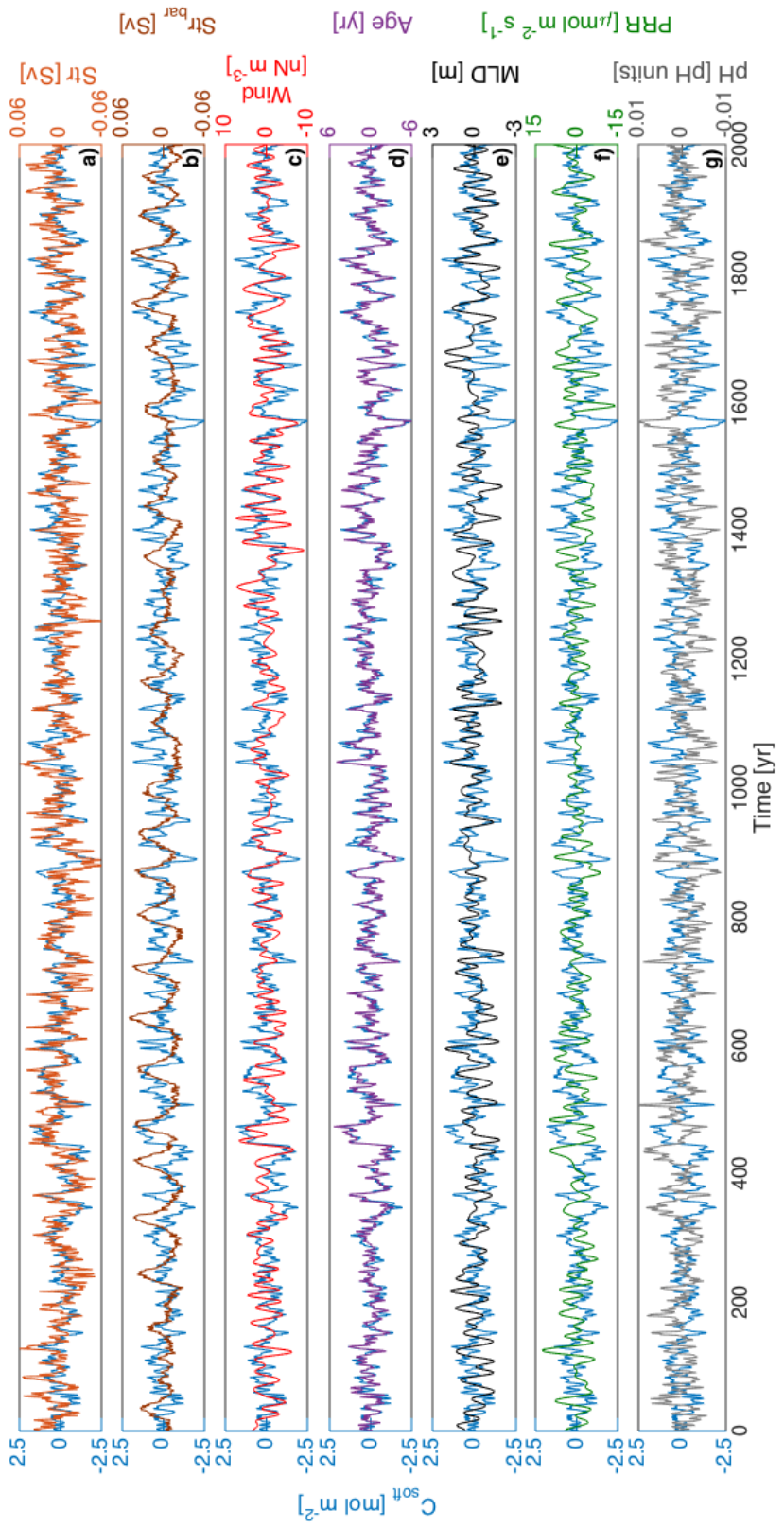

FIGURE 5.8: *Discrete Meyer approximations of de-trended simulated soft-tissue carbon inventory (C_{soft}), (a) meridional mass Stream function (Str), (b) barotropic Str (Str_{bar}), (c) Wind stress curl (Wind), (d) water mass mean Age (Age), (e) Mixed Layer Depth (MLD), (f) Phosphate Remineralisation Rate (PRR), and (g) pH. C_{soft}, Str, PRR, Age, and pH are quantified between 200-1000 m (twilight zone) at the 24.5°N section. Wind, Str_{bar} and MLD are determined at the surface of the same transect. Each signal is approximated by using a 20yr-frequency discrete Meyer wavelet transform (Meyer, 1993; Meyers et al., 1993), and compare with C_{soft}.*

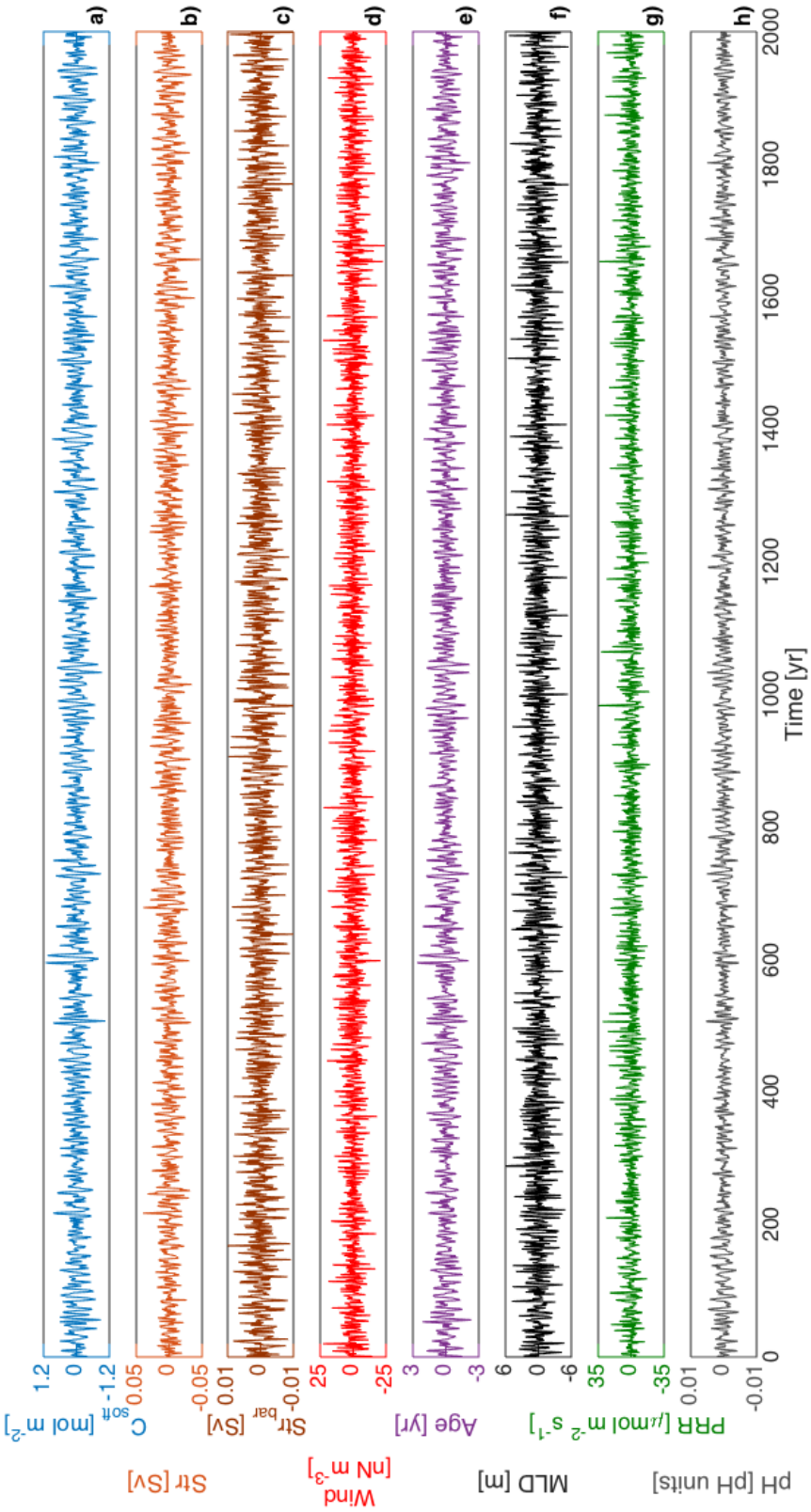

FIGURE 5.9: *Discrete Meyer details of de-trended simulated C_{soft}, Str, Str_{bar}, Wind, Age, MLD, PRR, and pH. The associated Meyer approximations are shown in Fig 5.8 for each of those variables, while the details are reported here for completeness, following the recommendations of Meyer (1993) and Meyers et al. (1993).*

So, the process could modify the North Atlantic subtropical CO_2 uptake, increasing the DIC and limiting the imminent climate change influence.
Hypothesis (4): using a twenty years frequency, the PRR accounts for approximately a fifth of the changes in the DIC from remineralised soft tissue. This pattern links to a strengthening of the productivity, carbon and oxygen exports above 200 m, and therefore a C_{soft} accumulation in the twilight zone.
Hypotheses (3) and (2): Wind, Str_{bar}, MLD, and upwelling variations influence the subtropical C_{soft} insignificantly, with the values of squared Pearson's coefficients being equal or lower than 0.10. These results agree with the study of section 5.3.3.
Hypothesis (1): changes in Str however affect significantly the twilight zone C_{soft}. This effect may be caused by increases in residence time and in remineralisation. However, C_{soft} could increase also due to a strengthening in the horizontal transport of biologically produced carbon, remineralised and exported northern than 24.5°N. By streamlining the residence time effect, we determine a R^2 of 0.86 between the simulated Age and C_{soft}, with a p value lower than 0.01 (Tab 5.4).
In summary, the observed 24.5°N C_{soft} increase could have happened as a result of an AMOC slow-down, an increase in residence time, acidification, and/or inorganic nutrients supply to the sunlit ocean. This result confirms our hypotheses 1, 4, and 5, and proves hypotheses 2 and 3 to be not valid in the CM2Mc ESM outputs. These simulated data show that an increase in the local phosphate remineralisation rate, a decrease in pH, and a slow-down in the meridional mass stream function increase the 24.5°N twilight zone C_{soft} inventory by 18 %, 68 %, and 22 %, respectively. An Age strengthening further increases the subtropical C_{soft} by 86 %. Interactions between these processes are possible, but are outside the scope of this thesis.

5.4 Comparison of C_{soft} approximations

In the previous sections we explored the C_{soft} influence on the comparison between the TTD and the ΔC^* C_{ant} estimates and the effect on C_{soft} of variations in wind stress curl, MLD, stream function, primary productivity, remineralisation, and pH using CM2Mc 'climate' outputs. This study relied on the implicit assumption that

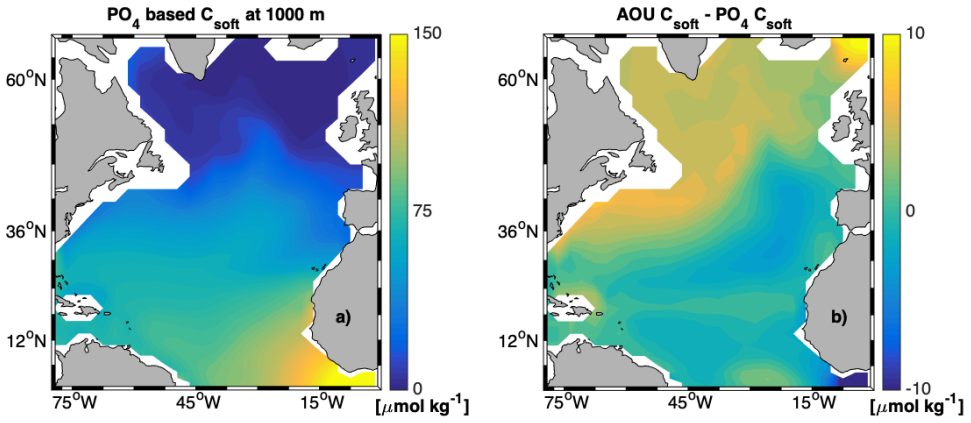

FIGURE 5.10: *Plots of North Atlantic soft-tissue Carbon (C_{soft}) estimated using Eq 4.9, which is based on Apparent Oxygen Utilisation (AOU), and Eq 2.12, which is based on total and preformed phosphate (PO_4) concentrations. We show the layer at 1000 m in the North Atlantic basin as it includes the highest C_{soft} in the upper ocean and it shows the greatest variation over latitude. Data are taken from a CM2Mc 'industrial' simulation in 2010 with the difference between the two C_{soft} estimates shown to evaluate the AOU approximation.*

C_{soft} estimates based on Eq 4.9 and observations are equivalent to the ones based on Eq 2.12 and model outputs. However, changes in O_2 and AOU, on which Eq 4.9 is based, are not necessarily correlated with PO_4 variations (Eq 2.12). Furthermore, it has been shown that water masses may leave the ocean surface without reaching the O_2 equilibrium with the atmosphere, hence leading to an under saturation in this gas and therefore an overestimation of the respiration in the ocean interior (Duteil et al., 2013; Ito et al., 2004). This causes discrepancies with the PO_4 approximation. To evaluate the assumption influence and associated differences between the C_{soft} approximations, we use the outputs of the CM2Mc 'industrial' and pre-industrial 'control' simulations already used in sections 4.3.2 and 5.3.6 respectively and calculate the saturated oxygen from the model temperature and salinity data.

We extract simulated data in the North Atlantic at a depth of 1000 m and evaluate the C_{soft} spatial distributions and approximation differences in 2010 in Fig 5.10. Then, we concentrate on the subtropical North Atlantic (24-26°N) between 78°W and 16°W, evaluating the C_{soft} temporal evolutions in the upper 1000 m of the basin within a time interval of two millennia (Fig 5.11).

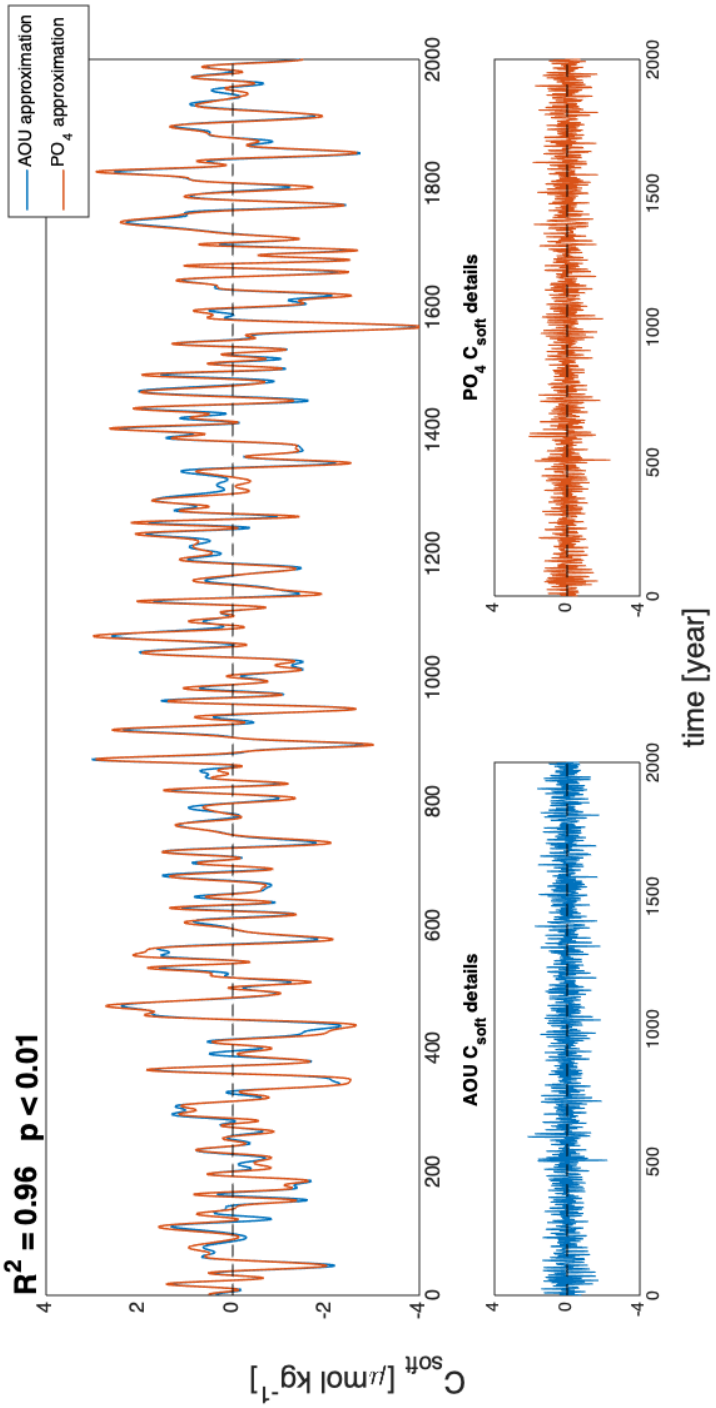

FIGURE 5.11: *De-trended approximations and details of soft-tissue carbon (C_{soft}) estimated by using Eq 4.9 (blue) and Eq 2.12 (orange). Data obtained from a CM2Mc pre-industrial 'control' run and averaged between 0-1000 m in the subtropical North Atlantic (24-26°N). R^2 and p value evaluate the similarity between the two C_{soft} approximations. See Figs 5.8 and 5.9 for additional details.*

As already discussed in section 4.3.1, C_{soft} is not homogeneous in the North Atlantic, but reaches a maximum in the eastern equatorial basin, owing to the local upwelling, and a minimum in the subpolar basin where the water masses are younger and hence less remineralised (Fig 5.10a). Overall, the AOU and PO_4 approximations capture the C_{soft} pattern, but differences exist and vary with latitude. These differences are greater in the subpolar basin (±50.0 %), where water masses are undersaturated in O_2 due to subduction, while decrease in the North Atlantic subtropics (±0.5 %). Over time, the AOU (Eq 4.9) and the PO_4 (Eq 2.12) C_{soft} approximations capture similar trends and variabilities (Fig 5.11). Limited discrepancies exist in the time interval investigated, but are likely to be caused by the model internal variability: the AOU and PO_4 approximations agree, with R^2 being 0.96 and p is less than 0.01. In summary, we tested the AOU approximation of C_{soft} in the North Atlantic upper ocean. By comparing it to model values obtained with prognostic tracers, we showed disagreements in the subpolar basin of up to 50 % but negligible differences in the subtropical North Atlantic over space (±0.05 %) and time ($R^2 = 0.98$).

5.5 Synthesis and discussion

Quantifying anthropogenic impacts on the ocean CO_2 uptake and storage depends on the reliability of the C_{ant} estimates. Between 1992 and 2010, we find significant disagreements between the TTD and ΔC^* C_{ant} decadal trends in the upper 1000 m of the 24.5°N Atlantic transect. These methods differ in the inclusion/exclusion of temporal changes in C^0_{sat}, C_{dis}, and C_{soft}, leading to the observed $\delta_t C_{ant}$ divergence. Influences of changes in C^0_{sat} and C_{dis} are expected, comparable, and opposite in sign. The subtropical North Atlantic C_{soft} increase from 1992 to 2010 is unexpected, influencing the uncertainty in the regression model used by the ΔC^* method, and impacting on the ΔC^* and TTD C_{ant} estimate disagreements. This C_{soft} increase could have resulted from an AMOC slow-down, between 2004 and 2010, or a wind stress weakening in the same period, which may have increased the residence time, the surface primary productivity, and the remineralisation. After being de-trended and approximated by using Meyer wavelet transforms, simulated oscillations of age,

meridional mass stream function, and phosphate remineralisation rate correlate with the C_{soft} modelled in the 24.5°N twilight zone (200-1000 m). We estimate respective squared Pearson's coefficients of 0.86, 0.22, and 0.18. The 68 % of the modelled C_{soft} oscillations are also influenced by acidification, with a shift towards new equilibria, and hence carbon uptakes potentially stronger than previously thought.

Chapter 6

Conclusions and future works

6.1 Conclusions

• The global ocean has sequestered around a third of the human-emitted CO_2 (anthropogenic carbon (C_{ant})), mitigating its Greenhouse effect and the increasing impacts on the Earth climate. However, direct C_{ant} estimates cannot be obtained in the ocean, requiring indirect techniques such as the tracer-based Transit-Time Distribution (TTD) or the carbon-based ΔC^*. Methodological assumptions and analytical precisions influence these C_{ant} estimates, with an uncertainty nominally estimated as ±20 % (Matsumoto and Gruber, 2005; Vázquez-Rodríguez et al., 2009b; Waugh et al., 2006). We investigate further the C_{ant} total (analytical + methodological) uncertainty using statistical approaches, such as a variance based sensitivity analysis, on repeated measurements at 24.5°N in the Atlantic between 1992 and 2010, on GFDL-ESM2M, OCCAM, CCSM outputs, and then linking our results to the studies of Fine et al. (2017), Matsumoto and Gruber (2005), and Waugh et al. (2006). We estimate the C_{ant} total uncertainty to be ±34 % in the global ocean, thus resulting higher than the previously suggested ±20 %.

• Despite this newly estimated total uncertainty of ±34 %, the reliability of the C_{ant} estimates depends on (1) definitions, (2) locations, and (3) intervals of time.
(1: definitions) In this thesis and elsewhere, C_{ant} is defined as the excess amount of

dissolved inorganic carbon present in the ocean owing to an increasing atmospheric CO_2 compared to the pre-industrial state and a physically driven uptake (Friis, 2006; Khatiwala et al., 2013; McNeil and Matear, 2013). In this instance, the uncertainty on the C_{ant} estimates is influenced by air-to-sea fluxes, circulation, and their variability, while other sources of uncertainty (e.g. changes in Redfield ratios) could be neglected. Under the C_{ant} definition of this paragraph, the TTD is the most applicable method, treating C_{ant} as a transient tracer, and hence reducing biological influences. Conversely, ΔC^* overestimates C_{ant}, as it includes effects due to the physical and biological carbon pumps.

Alternatively, C_{ant} could be defined as the disturbance in the natural carbon cycle due to human activities (Field et al., 2014), impacting the physical and biological carbon pumps and being influenced by these processes of CO_2 uptake. Potential alterations in ocean biogeochemistry, such as changes in Redfield ratios, are then relevant to the C_{ant} estimates, with the ΔC^* method being the most applicable. The TTD method struggles to capture these changes, hence underestimating C_{ant}.

(2: locations, 3: intervals) Over time and space, the C_{ant} uncertainty is influenced by the amount and accuracy of the observations. If the observational coverage is sparse or highly uncertain (e.g. Indian Ocean), all sources of C_{ant} uncertainty must be taken into account. As a result, C_{ant} variations that lie within ± 17.0 μmol kg^{-1} (± 34 %) are not significantly different from zero. Data spanning a minimum of one and a half decade are necessary for any analysis: C_{ant} increases by 1.4 ± 0.4 μmol kg^{-1} yr^{-1} (adapted from Khatiwala et al. (2009)), requiring 15 yr to emerge from the estimated uncertainty. Notwithstanding that, in the North Atlantic subtropical upper ocean (0-1000 m) observations are sufficiently accurate and dense to reliably reduce some sources of C_{ant} uncertainty. In this region, the TTD and ΔC^* C_{ant} uncertainties can be reduced to ± 8.3 μmol kg^{-1} and ± 10.3 μmol kg^{-1}.

Simply put, the reliability of the C_{ant} estimates depends on the maintenance of the observational network and its enlargement in crucial regions (e.g. Indian Ocean).

• To include both of the C_{ant} definitions discussed above in this chapter and the associated main sources of uncertainty, we suggest the combined use of the TTD

and ΔC^* techniques, which confine the C_{ant} concentrations range. However, these estimates can diverge in time, rising the uncertainty on C_{ant} studies. This is due to CO_2 disequilibrium, saturation, and/or remineralisation variations over time (δ_t) unequally captured by the ΔC^* and the TTD techniques. $\delta_t C_{dis}$ and $\delta_t C^0_{sat}$ are regressed on temperature, salinity, and total alkalinity measurements in the ΔC^*, while the TTD indirectly accounts for them using time-varying tracer saturations. $\delta_t C_{soft}$ is entirely included by the ΔC^* method only. From 1992 to 2010, we observe discrepancies in the $\delta_t C_{dis}$, $\delta_t C^0_{sat}$ and $\delta_t C_{soft}$ terms of the TTD and ΔC^* equations. Although those terms reduce each other influence, they lead to small but significant divergences between the ΔC^* and TTD C_{ant} estimates in some water masses. In the 24.5°N upper 1000 m taken as a whole, they cause a C_{ant} disagreement of 0.3 ± 0.2 μmol kg^{-1} yr^{-1}.

As a result, we note that changes in C_{ant} should not be investigated singularly, but requires the assessment of the dissolved inorganic carbon cycle taken as a whole. So, we apply the partitioning defined by Williams and Follows (2011) in this thesis.

• Analysing further the ocean carbon cycle, we investigate natural variabilities and decadal trends of anthropogenic carbon in conjunction with other inorganic carbon partitions, focusing again on the 24.5°N upper 1000 m between 1992 and 2010. As expected, C_{ant} increases over time by 0.5-0.8 ± 0.2 μmol kg^{-1} yr^{-1}, owing to rises in the atmospheric CO_2 and air-to-sea fluxes. This pattern causes two thirds of the C_{tot} increment, which disagrees with the influences of the C^0_{sat} decrease and C_{dis} tendency towards CO_2 saturation that suggest climate change. Surprisingly, C_{tot} increases also owing to a C_{soft} rise of 0.3 ± 0.1 μmol kg^{-1} yr^{-1}. This unexpected increment in the remineralised soft tissue may be due to productivity, acidification, circulation or wind stress curl changes. Similar conclusions can be drawn from the study of carbon partition anomalies in the CM2Mc ESM outputs. C_{soft} and C_{carb} increases from 1860 to 2100 when comparing the 'industrial' and pre-industrial 'control' data. These results maintain when comparing the same 'control' with the 'climate' data, suggesting a predominance of the physical effect on the oceanic C_{soft} variations.

• We investigate the unexpected increase in the 24.5°N C_{soft} exploring connections with changes in the mentioned processes. We correlate C_{soft} with the water mass volume, mean age, anthropogenic, and natural pH in the Antarctic intermediate, subpolar, and Madeira Mode water masses in 1992, 1998, 2004, and 2010. Results suggest that three quarters of the $\delta_t C_{soft}$ may be due to increments in residence time and acidification. The remainder is presumably due to a strengthening in the surface productivity (chlorophyll increases by 2 μg m^{-3} yr^{-1}), carbon export, and subsurface remineralisation, although our data do not support this hypothesis test. Decreases in the wind stress curl and mixing are not influential, being the water volume variations not correlated with the age or C_{soft} estimates. The slow-down in the Atlantic meridional overturning circulation, suggested by Smeed et al. (2014) from 2004 to 2012, could explain our findings. However, the observations are not sufficiently dense in time and space to support this hypothesis.

• We enlarge the assessment of the subtropical North Atlantic C_{soft} increase to the outputs of a 2 kyr-long CM2Mc pre-industrial control simulation. With these data, we evaluate the role of changes in the Wind stress curl (Wind), Mixed Layer Depth (MLD), local Phosphate Remineralisation Rate (PRR), meridional and barotropic Stream functions (Str and Str_{bar}), pH, and water mass mean Age (Age) within the subtropical North Atlantic twilight zone (200-1000 m). MLD and Str_{bar} changes do not influence C_{soft}, while a PRR rise, a pH reduction, and a Str decrease increase C_{soft} by 18 %, 68 %, and 22 %. Streamlining the Age effect, a strengthening in the residence time accounts for 86 % of the C_{soft} increment. The results broadly agree with our observational studies. Disagreements are likely to be due to the use of AOU and PO_4 to approximate C_{soft} in the observations and model outputs, respectively, but are confined to the subpolar basin.
We could have investigated the ratio between the surface primary productivity and associated export of organic carbon in the model, but we decided to focus on the PRR to maintain the study to the subtropical North Atlantic.

6.2 Final remarks

This thesis results improve on the on-going understanding of the human footprint on the Earth and oceanic carbon cycle. C_{ant} estimates result more uncertain than previously thought by a factor of 1.5 (uncertainty increases from ±20 % to ±34 %), but the assessment of C_{ant} variabilities and trends can be done over large time intervals and/or spatially confined ocean regions.
In the subtropical North Atlantic, our estimates agree with the previously reported C_{ant} increases, but highlight significant divergences due to the method chosen: ocean circulation and biogeochemical cycles are not in steady state, as all of the C_{ant} methods assume, propagating an uncertainty that varies with the technique used. So, we suggest the use of two or more independent estimates to capture the probable range of oceanic C_{ant} and increase the reliability of the associated studies.

6.3 Future works

Unfortunately, due to the complexity of the work done in this thesis and the short time-life of the doctoral project, we have not concluded analyses that may improve the assessment of the ocean CO_2 cycle. Here, we discuss 'snapshots' of them based on the Massachusetts Institute of Technology general circulation model (MITgcm; Marshall et al. (1997a,b)), Transport Matrix (TMM; Khatiwala (2007); Khatiwala et al. (2005)), and Maximum Entropy (MEM; Holzer et al. (2010)) Methods.

• Our sensitivity analysis of the C_{ant} total uncertainty is a step forward towards an improved estimate of the last value. However, much of the work done in this thesis is based on observations, limiting our conclusions to the 24.5°N section from 1992 to 2010. Enlargements will be essential, but possible only at sparse hydrographic sections (e.g. Labrador Sea edge) when using observations. More comprehensive results are achievable using climate models, which are useful test beds for process analyses. We run the MITgcm with a horizontal resolution of 2.8° and 15 vertical layers. The run lasts from 1980 to 2014, after thousand years of spin-up, and was

forced using ocean surface salinity, temperature, heat and fresh water fluxes from the NOAA gridded climate data. We aim to replicate the observational assessment of the C_{ant} uncertainty done in section 3.4 by altering one MITgcm input at a time and quantify its independent/interactive influence on the simulated C_{ant}.

• Concurrently, we aim to investigate the C_{ant} estimates and uncertainties by using the TMM. This method allows to estimate the independent and interactive factor (excluding temperature and salinity) influences on C_{ant} on large temporal (e.g. centuries) and spatial (global ocean) scales, limiting the necessary computational resources with respect to a GCM. The TMM relies on physical outputs from previously run models to build the implicit and explicit matrices, which describe ocean ventilation and mixing. Other variables (e.g. dissolved inorganic carbon) require initial conditions, which could be altered at each simulation, then quantifying the associated influence on C_{ant}.

• The MEM improves on the TTD estimates of mean age and C_{ant}. So, it could be used as an additional term in our analyses to which other method estimates can be compared. Also, the MEM may be used to partition a water mass of interest with respect to the locations where it was last ventilated, highlighting changes over time in ventilation and mixing (Holzer et al., 2010).

Appendix A

Extended (1992-2016) subtropical TTD C_{ant} trends and variability

In this appendix, we use observations of transient tracers and O_2 collected during the DY040 cruise (section 1.4.5) to extend for the first time to 2016 the study of the TTD C_{ant} temporal increases (δ_t), Decadal Trends (DTs), and variabilities investigated at the 24.5°N Atlantic transect between 1992 and 2010 in section 4.2.4. We avoid the use of other C_{ant} methods, as the DY040 DIC and Alk are not yet fully quality controlled. Results are presented in Fig A.1, where we show DTs and cruise-mean differences since 1992 to 1998, 2004, 2010, 2016, and summarised in Tab A.1. As for previous analyses, the DTs are estimated using a quasi Monte Carlo (MC) approach (Kroese et al., 2014; Metropolis and Ulam, 1949), which is based on random values (section 4.2.3). The same is true for the C_{ant} variabilities, but these values are not directly reported, being instead inferred as difference between points (cruise-mean differences) and lines (C_{ant} DTs) in Fig A.1.

Including the 2016 measurements in the study, the TTD C_{ant} (TTD (2016) in Tab A.1) continues to increase everywhere in the 24.5°N section, as expected from the atmospheric CO_2 increase. The DTs seem higher (by approximately 30 %) than the estimates limited to 2010 (TTD (2010) in Tab A.1), but none of these differences is statistically significant. The TTD C_{ant} observed variability is also included within the quasi MC uncertainty (± 5.2 μmol kg^{-1}).

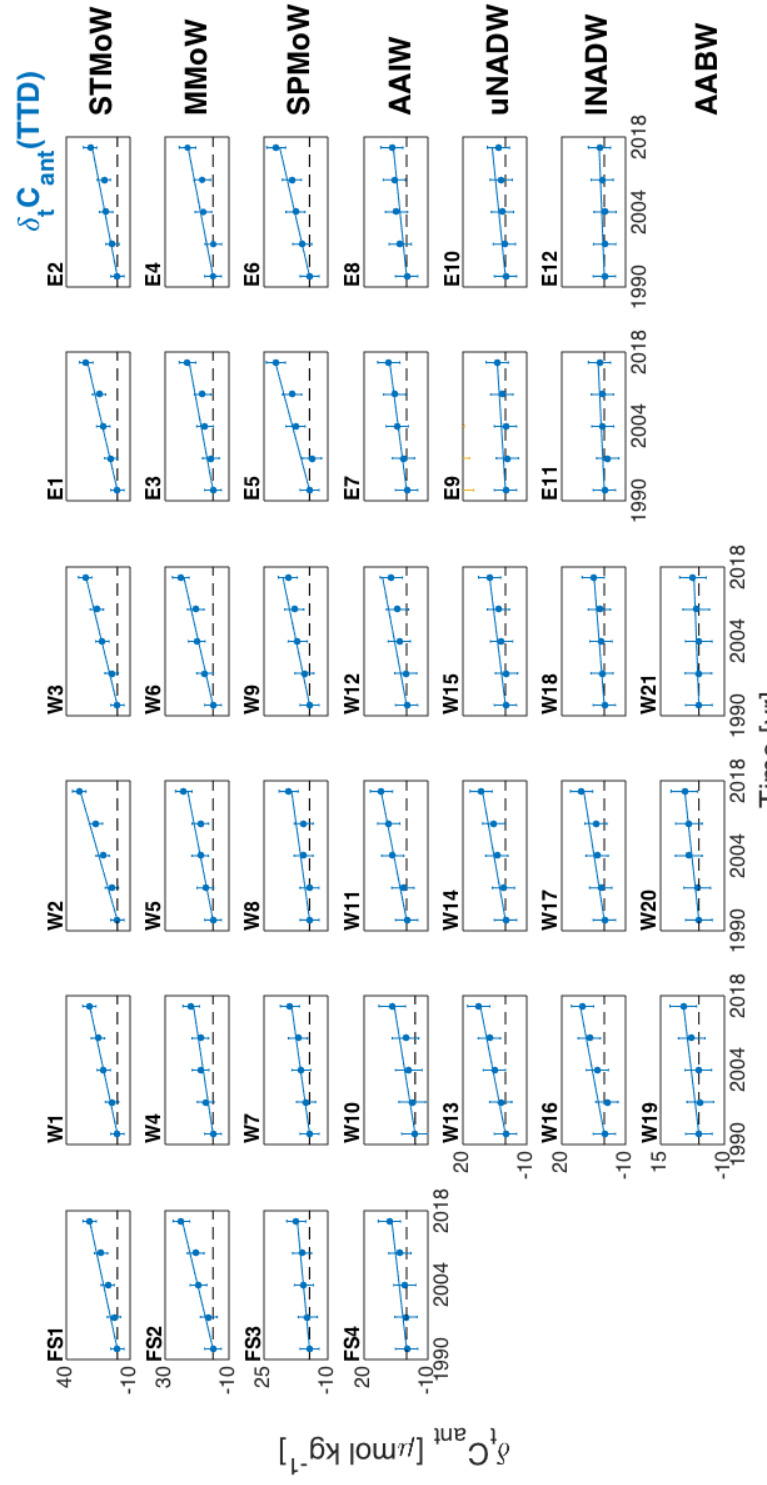

FIGURE A.1: *Anthropogenic carbon (C_{ant}) cruise-mean differences since 1992 (δ_t). Data are estimated using the TTD technique, between 1992 and 2016, in each of the 24.5°N Atlantic transect subareas defined in Fig 4.2. Uncertainties due to the observed variability are quantified by randomly perturbing 1000 times each estimate, within a quasi Monte Carlo approach, and obtaining ± 5.2 μmol kg^{-1}. Decadal trends are added as least squares fitted lines forced through zero.*

TABLE A.1: *Table summarising the Decadal Trends (DTs) from 1992 to 2016 (TTD (2016)) and 1992 cruise-mean values (μ) of the TTD* **anthropogenic carbon** *($\mathbf{C_{ant}}$) estimated for each subarea of the 24.5°N Atlantic section (Fig 4.2), with the DTs from 1992 to 2010 (TTD (2010)) also reported for comparison (Tab 4.2). The respective uncertainties (± 0.2 µmol kg^{-1} yr^{-1} and ± 5.2 µmol kg^{-1}) are approximated by randomly perturbing the mean carbon concentrations and determining sets of linear regressions for each subarea using a quasi Monte Carlo (MC) approach. 'Section' refers to the averaged DT along the whole transect, and '1000 m' to the mean values in the column upper 1000 m. We highlight in bold the highest DTs for each of the seven water masses studied (Subtropical Mode Water (STMoW), Madeira MoW (MMoW), Subpolar MoW (SPMoW), Antarctic Intermediate Water (AAIW), upper North Atlantic Deep Water (uNADW), lower NADW (lNADW), and Antarctic Bottom Water (AABW)). We also highlight in red the average values in the upper 1000 m, in line with Tab 4.2.*

STMoW	FS1(DT)	FS1(μ)	W1(DT)	W1(μ)	W2(DT)	W2(μ)	W3(DT)	W3(μ)	E1(DT)	E1(μ)	E2(DT)	E2(μ)	Section
TTD (2016)	0.9	48.6	0.9	47.7	**1.2**	47.9	1.0	48.0	1.0	49.2	0.8	48.8	1.0
TTD (2010)	0.7	48.6	0.9	47.7	**1.2**	47.9	**1.2**	48.0	1.0	49.2	1.0	48.8	1.0
MMoW	FS2(DT)	FS2(μ)	W4(DT)	W4(μ)	W5(DT)	W5(μ)	W6(DT)	W6(μ)	E3(DT)	E3(μ)	E4(DT)	E4(μ)	Section
TTD (2016)	**0.8**	41.5	0.5	40.2	0.7	40.2	**0.8**	38.8	0.6	41.6	0.7	42.1	0.7
TTD (2010)	**0.7**	41.5	0.4	40.2	0.4	40.2	0.6	38.8	0.4	41.6	0.4	42.1	0.5
SPMoW	FS3(DT)	FS3(μ)	W7(DT)	W7(μ)	W8(DT)	W8(μ)	W9(DT)	W9(μ)	E5(DT)	E5(μ)	E6(DT)	E6(μ)	Section
TTD (2016)	0.3	24.0	0.4	25.3	0.4	27.6	0.6	29.6	**0.8**	35.5	0.7	29.0	0.5
TTD (2010)	0.2	24.0	0.4	25.3	0.2	27.6	0.5	29.6	**0.6**	35.5	0.5	29.0	0.4
AAIW	FS4(DT)	FS4(μ)	W10(DT)	W10(μ)	W11(DT)	W11(μ)	W12(DT)	W12(μ)	E7(DT)	E7(μ)	E8(DT)	E8(μ)	Section
TTD (2016)	0.3	9.9	0.3	11.4	**0.5**	12.8	**0.5**	10.0	0.3	9.2	0.3	8.5	0.4
TTD (2010)	0.1	9.9	0.1	11.4	**0.5**	12.8	0.1	10.0	0.3	9.2	0.3	8.5	0.2
1000 m	DT	μ	DT	μ	DT	μ	DT	μ	DT	μ	DT	μ	Section
TTD (2010)	0.6	31.0	0.5	31.2	0.7	32.1	0.7	31.6	0.7	33.9	0.6	32.1	0.7
TTD (2016)	0.4	31.0	0.5	31.2	0.6	32.1	0.6	31.6	0.6	33.9	0.6	32.1	0.5
UNADW			W13(DT)	W13(μ)	W14(DT)	W14(μ)	W15(DT)	W15(μ)	E9(DT)	E9(μ)	E10(DT)	E10(μ)	Section
TTD (2016)			**0.5**	15.2	**0.5**	16.1	0.3	9.2	0.2	5.1	0.3	3.6	0.4
TTD (2010)			**0.4**	15.2	0.3	16.1	0.2	9.2	0.1	5.1	0.2	3.6	0.2
lNADW			W16(DT)	W16(μ)	W17(DT)	W17(μ)	W18(DT)	W18(μ)	E11(DT)	E11(μ)	E12(DT)	E12(μ)	Section
TTD (2016)			**0.5**	6.2	0.4	13.5	0.2	5.9	0.1	4.6	0.1	2.7	0.3
TTD (2010)			**0.4**	6.2	0.2	13.5	0.1	5.9	0.1	4.6	0.1	2.7	0.2
AABW			W16(DT)	W16(μ)	W17(DT)	W17(μ)	W18(DT)	W18(μ)					Section
TTD (2016)			**0.3**	5.4	0.2	6.5	0.1	4.9					0.2
TTD (2010)			0.2	5.4	**0.3**	6.5	0.0	4.9					0.2

However, we could neglect the TTD C_{ant} quasi MC uncertainty for the sake of the analysis. This approach allows investigating changes in the oceanic circulation that could have altered the TTD $\delta_t C_{ant}$ estimates, as also suggested in chapter 5. These changes are then compared, in the same water mass and time interval, to the ones in the soft-tissue carbon partition (C_{soft}), a second proxy for circulation temporal changes. The last variable is less uncertain than C_{ant} (section 4.2.3).

Overall, the TTD $\delta_t C_{ant}$ estimated between 1992 and 2010 lies below the DT, while the subsequent estimate between 1992 and 2016 exceeds this value in the MMoW, SPMoW, and in subareas E1 and E2. These results suggest a potential decrease in the oceanic circulation, and hence in the ventilation of these water masses, from 2004 to 2010 followed by a recovery in 2016, in line with our analyses in chapter 5 and the study of Jackson et al. (2016). Confirmations arise from the $\delta_t C_{soft}$ estimates (not reported for brevity), which exceed the MMoW and SPMoW DTs in 2010 and are below the DT values in 2016.

Appendix B

Detailed assessment of the TTD and ΔC* C_{ant} total uncertainties

We continue to investigate the TTD and ΔC* C_{ant} uncertainties due to the combined influences of methodological assumptions and analytical precisions. In section 3.4.1 of this thesis, we synthesised the most influential sources of C_{ant} uncertainty at the scale of the global ocean, 24.5°N Atlantic section, and upper 1000 m of this transect. Here, we deepen the study investigating each source of C_{ant} uncertainty, in the same areas, and evaluating approaches that can be used to reduce them.

We combine our studies of sections 2.3 and 3.2.1 based on the One Factor At a Time (OFAT) approach with the analyses of Fine et al. (2017), Matsumoto and Gruber (2005), and Waugh et al. (2006). We use the guidelines of the Global Ocean Ship-based Hydrographic Investigations Program (GO-SHIP; Hood et al. (2010)) to estimate the global measurement analytical precisions, whereas we use the 2010 cruise report (King et al., 2012) for the subtropical North Atlantic. We select this year occupation as it includes the greatest amount of reliable observations (Tab 1.2). Tabs B.1 and B.2 summarise the sources of the TTD and ΔC* C_{ant} uncertainties, respectively. They include Measurement (M) precision and method Assumption (A) influences, which are estimated as concentrations, percentages Relative ($\%_R$) to the area-mean C_{ant} maximum, and percentages to the Total ($\%_T$) C_{ant} uncertainty.

TABLE B.1: *Table summarising the* **TTD C_{ant} total uncertainty** *(reported as concentration ($\mu mol\ kg^{-1}$), percentage Relative to the averaged C_{ant} maximum ($\%_R$) and percentage relative to the Total C_{ant} uncertainty ($\%_T$)) due to methodological assumptions and analytical precisions. 'G' identifies the method uncertainties in the global ocean, based on the GO-SHIP guidelines for oceanographic measurements (Hood et al., 2010). 'S' isolates the method applicability at the 24.5°N Atlantic transect, where some of the uncertainty sources can be Neglected ('Neg'). 'U' identifies the method uncertainties in the upper 1000 m of the same section. 'M' and 'A' identify the influence of Measurement precisions and methodological Assumptions.*

M	U	S	G	U	S	G	U	S	G
	$\mu mol\ kg^{-1}$			$\%_R$			$\%_T$		
Θ	±5.2 x 10^{-4}	±5.2 x 10^{-4}	±2.0 x 10^{-4}	±8 x 10^{-4}	±8 x 10^{-4}	±4 x 10^{-4}	±0	±0	±0
S	±3.9 x 10^{-4}	±3.9 x 10^{-4}	±3.0 x 10^{-4}	±6 x 10^{-4}	±6 x 10^{-4}	±6 x 10^{-4}	±0	±0	±0
DIC	-	-	-	-	-	-	-	-	-
Alk	-	-	-	-	-	-	-	-	-
O_2	-	-	-	-	-	-	-	-	-
NO_3	-	-	-	-	-	-	-	-	-
$Si(OH)_4$	±2.6 x 10^{-4}	±3.9 x 10^{-4}	±2.0 x 10^{-4}	±4 x 10^{-4}	±6 x 10^{-4}	±4 x 10^{-4}	±0	±0	±0
PO_4	±5.2 x 10^{-4}	±5.2 x 10^{-4}	±2.5 x 10^{-4}	±8 x 10^{-4}	±8 x 10^{-4}	±5 x 10^{-5}	±0	±0	±0
CFC-12	±8.3	±8.4	±3.5	±13	±13	±7	±100	±81	±21
A	U	S	G	U	S	G	U	S	G
$RR_{N:P}$	-	-	-	-	-	-	-	-	-
$RR_{O:P}$	-	-	-	-	-	-	-	-	-
Alk^{pre}	-	-	-	-	-	-	-	-	-
C_{eq}	-	-	-	-	-	-	-	-	-
C_{dis}	Neg	±1.9	±10.0	Neg	±3	±20[a]	Neg	±19	±59
Sat	Neg	Neg	±1.0	Neg	Neg	±2	Neg	Neg	±6
Γ/Δ	Neg	Neg	±0.5	Neg	Neg	±1[a]	Neg	Neg	±3
Eddies	Neg	Neg	±2.0	Neg	Neg	±4[b]	Neg	Neg	±11
TOT	±8.3	±10.3	±17.0	±13	±16	±34	±100	±100	±100

[a]Uncertainty estimated by Waugh et al. (2006).
[b]Uncertainty calculated from the estimates of Fine et al. (2017).

TABLE B.2: *Same as in Tab.B.1, but for the* **ΔC* C_{ant} total uncertainty**.

M	U	S	G	U	S	G	U	S	G
	$\mu mol\ kg^{-1}$			$\%_R$			$\%_T$		
Θ	$\pm 7.3 \times 10^{-3}$	$\pm 7.3 \times 10^{-3}$	$\pm 2.5 \times 10^{-3}$	$\pm 1 \times 10^{-2}$	$\pm 1 \times 10^{-2}$	$\pm 5 \times 10^{-3}$	± 0	± 0	± 0
S	$\pm 7.3 \times 10^{-3}$	$\pm 7.3 \times 10^{-3}$	$\pm 5.0 \times 10^{-3}$	$\pm 1 \times 10^{-2}$	$\pm 1 \times 10^{-2}$	$\pm 1 \times 10^{-2}$	± 0	± 0	± 0
DIC	± 2.9	± 2.9	± 2.0	± 4	± 4	± 4	± 29	± 17	± 12
Alk	$\pm 7.3 \times 10^{-1}$	$\pm 7.3 \times 10^{-1}$	± 1.5	± 1	± 1	± 3	± 7	± 4	± 9
O_2	$\pm 6.6 \times 10^{-2}$	$\pm 7.3 \times 10^{-1}$	± 1.0	$\pm 9 \times 10^{-1}$	± 1	± 2	± 6	± 4	± 5
NO_3	$\pm 7.3 \times 10^{-3}$	$\pm 7.3 \times 10^{-3}$	$\pm 5.0 \times 10^{-3}$	$\pm 1 \times 10^{-2}$	$\pm 1 \times 10^{-2}$	$\pm 1 \times 10^{-2}$	± 0	± 0	± 0
$Si(OH)_4$	$\pm 7.3 \times 10^{-4}$	$\pm 1.4 \times 10^{-3}$	$\pm 5.0 \times 10^{-4}$	$\pm 1 \times 10^{-3}$	$\pm 2 \times 10^{-3}$	$\pm 1 \times 10^{-3}$	± 0	± 0	± 0
PO_4	$\pm 7.3 \times 10^{-3}$	$\pm 7.3 \times 10^{-3}$	$\pm 4.0 \times 10^{-4}$	$\pm 1 \times 10^{-2}$	$\pm 1 \times 10^{-2}$	$\pm 8 \times 10^{-4}$	± 0	± 0	± 0
CFC-12	-	-	-	-	-	-	-	-	-
A	U	S	G	U	S	G	U	S	G
$RR_{N:P}$	Neg	Neg	± 1.5	Neg	Neg	± 3	Neg	Neg	± 9
$RR_{O:P}$	Neg	Neg	± 4.0	Neg	Neg	± 8	Neg	Neg	± 24
Alk^{pre}	$\pm 7.3 \times 10^{-1}$	± 2.2	± 2.0	± 1	± 3	$\pm 4^a$	± 7	± 13	± 12
C_{eq}	± 3.7	± 5.8	± 4.0	± 5	± 8	$\pm 8^b$	± 36	± 33	± 24
C_{dis}	± 2.2	± 5.1	± 1.0	± 3	± 7	$\pm 2^c$	± 15	± 29	± 5
Sat	-	-	-	-	-	-	-	-	-
Γ/Δ	-	-	-	-	-	-	-	-	-
Eddies	-	-	-	-	-	-	-	-	-
TOT	± 10.3	± 17.7	± 17.0	± 14	± 24	± 34	± 100	± 100	± 100

[a]Uncertainty inferred from the combination of our OFAT approach (section 2.3.1) and the standard error determined by Gruber et al. (1996) for the Alk^{pre} regression. The last was estimated at the scale of the Atlantic Ocean, but we assume it comparable in other basins, hence using it globally.

[b]Uncertainty inferred from the combination of our OFAT approach (section 2.3.1) and the standard error determined by Gruber et al. (1996) for the C_{eq} regression. The last was estimated at the scale of the Atlantic Ocean, but we assume it comparable in other basins, hence using it globally.

[c]Uncertainty estimated by Matsumoto and Gruber (2005).

Despite their inclusion in the TTD and ΔC^* equations, potential temperature (Θ), Salinity (S), and inorganic nutrient precisions do not influence the C_{ant} uncertainty. This is due to the high accuracy in the first two measurements, which compensates their influences. The inorganic nutrient precisions are effectively not influential, as proved in section 3.2.1. On the contrary, analytical precisions of Dissolved Inorganic Carbon (DIC), total Alkalinity (Alk), and dissolved oxygen (O_2) influence the ΔC^* C_{ant} uncertainty, with percentages up to 29 %. The transient tracer (e.g. CFC-12) accuracies are the most influential on the TTD C_{ant} uncertainty, being responsible for the totality of it in the 24.5°N upper 1000 m. Overall, the tracer-based technique is influenced by an analytical precisions number lower than the carbon-based method: an improved observational accuracy would reduce more the ΔC^* C_{ant} uncertainty. Turning attention to the C_{ant} method assumptions, the assumed spatial constancy in Redfield Ratios (RRs) influences approximately a third of the ΔC^* C_{ant} total uncertainty globally. However, we neglect this uncertainty source in the subtropical North Atlantic, in agreement with the canonical approach of Redfield (1934) and the implicit assumption of Guallart et al. (2015b). Estimates of preformed Alk (Alk^{pre}) and equilibrium carbon (C_{eq}) also influence the ΔC^* C_{ant} total uncertainty. These variables are based on regression models, as detailed in section 2.3.1, and so their influence reduces from the global ocean scale to the 24.5°N upper 1000 m, in line with the rise in observational accuracy. Changes in the disequilibrium carbon component (C_{dis}) influence both the TTD and ΔC^* C_{ant} total uncertainties. These impacts have been discussed in sections 2.3.1 and 3.3. Variations over time and space in tracer saturations and Γ/Δ ratio influence the TTD C_{ant} total uncertainty, mostly where water mass formations are poorly known (e.g. Southern Ocean; Stöven et al. (2016)). However, they are relatively well known in the subtropical North Atlantic, and so their influence can be neglected. Ocean eddies also influence the TTD C_{ant} estimates (Fine et al., 2017), modifying the mixing ratio and so mean age estimate. However, this source of uncertainty is negligible in the North Atlantic subtropics, where no seawater fronts are detectable (section 3.4.1). Overall, the TTD quantifications are the most influenced by methodological uncertainties. An ocean improved knowledge would be more beneficial for them rather than for the ΔC^* estimates.

Appendix C

Inorganic carbon inventories in the North Atlantic upper 1000 m

We investigate the inorganic carbon partition inventories and spatial variabilities in the North Atlantic upper ocean. In sections 4.2.4 to 4.2.8, we applied this analysis to the same layer at the 24.5°N transect between 1992 and 2010. Here, we enlarge the study to North Atlantic upper-ocean inventories of total (C_{tot}), pre-industrial saturated (C^0_{sat}), soft-tissue (C_{soft}), carbonate (C_{carb}), disequilibrium (C_{dis}), and anthropogenic (C_{ant}) carbon partitions by using the Williams and Follows (2011) partitioning. We explore the variability of each component over space, highlighting interactions among them and suggesting causing mechanisms, as in section 4.2.8.

We use the Global Ocean Data Analysis Project version 2 (GLODAPv2; Lauvset et al. (2016)) gap-filled climatology. These data refer to the year 2002, including a C_{ant} distribution estimated using the TTD based on CFC-12 measurements. Results are presented in Fig C.1, which reports also the North Atlantic upper-ocean budget for each of the partitions investigated.

The upper ocean circulation is the main driver of North Atlantic carbon variability above 1000 m. Over latitude, we distinguish three dynamical zones: the equatorial (0-20°N), subtropical (20-40°N) and subpolar (40-65°N). A secondary effect is also evident over longitude, with the greatest remineralised carbon (C_{soft} + C_{carb}) stored in the western equatorial region (far from areas of water mass formations).

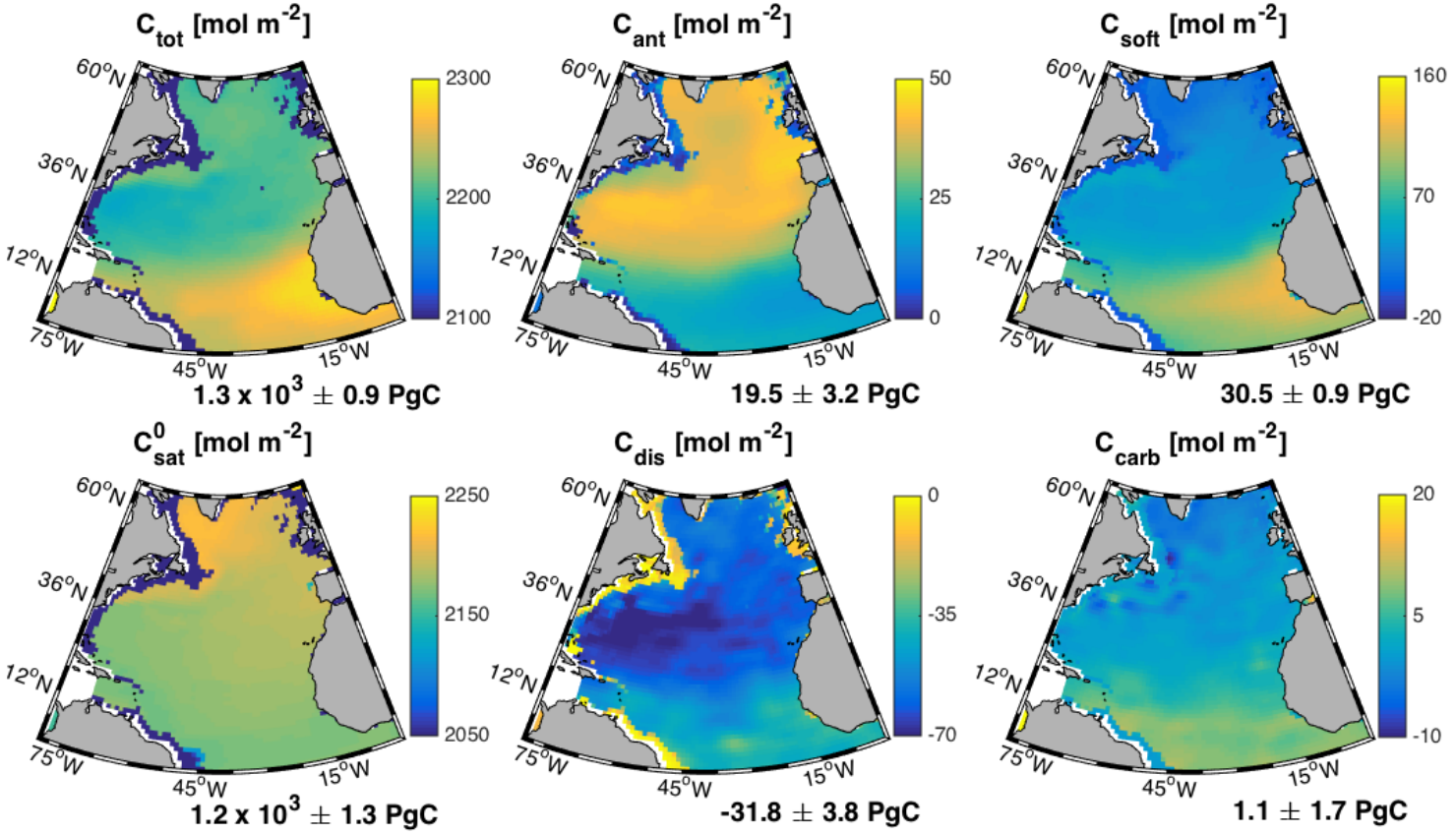

FIGURE C.1: *North Atlantic maps of the upper 1000 m column inventories of inorganic carbon partitions (total (C_{tot}), anthropogenic (C_{ant}), soft-tissue (C_{soft}), pre-industrial saturated (C^0_{sat}), disequilibrium (C_{dis}), and carbonate (C_{carb})). Results are based on the GLODAPv2 climatology (2002 being the reference year; Lauvset et al. (2016)), with budgets and uncertainties reported at the bottom right edge of each panel. C_{ant} is quantified by using the TTD method based on CFC-12 observations, as given in the GLODAPv2 climatology.*

In the subpolar zone, the atmospheric CO_2 increase due to anthropogenic activities induces the highest inventories of C^0_{sat}, which is the ocean potential equilibrium carbon. This pattern instantaneously makes C_{dis} more negative in the mixed layer depth, where biogenic effects are negligible. As a result, air-to-sea CO_2 fluxes try to compensate this imbalance, taking up the highest amount of C_{ant}.

In the subtropical zone, the carbon partition distributions are broadly comparable to the ones near the Pole. Despite this similarity, the C_{dis} inventories are more negative in this region. This is due to a reduction in CO_2 uptake, which decreases the compensation of the C_{dis} imbalance, leading also to the lowest upper-ocean C_{tot}.

In the equatorial zone, the remineralised carbon increase dominates the interplay, being influenced by the seawater upwelling, which originates nearby the African coast. This seawater motion carries high concentrations of soft-tissue and carbonates from the ocean interior to the surface. As a result, the North Atlantic upper-ocean C_{tot} increases in the region, reducing the amount of potential carbon (C^0_{sat}). This induces C_{dis} to become more positive and reduces further CO_2 uptake. However, it is also possible that these observed patterns are due to climate change, as suggested in section 4.2.8 for the 24.5°N transect. High values of sea-surface temperature induce ocean stratification, increasing C_{tot} and strengthening the conversion from C^0_{sat} to C_{soft} (Bernardello et al., 2014a).

Bibliography

C. Amante and B.W. Eakins. Etopo1 1 Arc-Minute Global Relief Model: procedures, data sources and analysis. *NOAA Technical Memorandum NES-DIS NGDC-24 National Geophysical Data Center*, 2009.

J.L. Anderson et al. The new GFDL global atmosphere and land model AM2-LM2: evaluation with prescribed SST simulations. *J. Clim.*, 17, 2004. doi: 10.1175/JCLI-3223.1.

J.M. Barnola et al. Vostok ice core provides 160,000-year record of atmospheric CO_2. *Nature*, 329, 1987. doi: 10.1038/329408a0.

N.R. Bates. Interannual variability of oceanic CO_2 and biogeochemical properties in the Western North Atlantic subtropical gyre. *Deep Sea Res., II*, 48, 2001. doi: 10.1016/S0967-0645(00)00151-X.

N.R. Bates et al. A short-term sink for atmospheric CO_2 in subtropical mode water of the North Atlantic Ocean. *Nature*, 420, 2002. doi: 10.1038/nature01253.

M. Battle et al. Atmospheric gas concentrations over the past century measured in air from firn at the South Pole. *Nature*, 383, 1996. doi: 10.1038/383231a0.

R. Bernardello et al. Response of the Ocean Natural Carbon Storage to Projected Twenty-First-Century Climate Change. *J. Clim.*, 27, 2014a. doi: 10.1175/JCLI-D-13-00343.1.

R. Bernardello et al. Impact of Weddell Sea deep convection on natural and anthropogenic carbon in a climate model. *Geophys. Res. Lett.*, 41, 2014b. doi: 10.1002/2014GL061313.

P. Brandt et al. On the role of circulation and mixing in the ventilation of oxygen minimum zones with a focus on the eastern tropical North Atlantic. *Biogeosciences*, 12, 2015. doi: 10.5194/bg-12-489-2015.

P.G. Brewer. Direct observations of oceanic CO_2 increase. *Geophys. Res. Lett.*, 5, 1978. doi: 10.1029/GL005i012p00997.

W.S. Broecker. The great ocean conveyor. *Oceanography*, 4, 1991. doi: 10.5670/oceanog.1991.07.

B. Bronselaer et al. Agreement of CMIP5 simulated and observed ocean anthropogenic CO_2 uptake. *Geophys. Res. Lett.*, 2017. doi: 10.1002/2017GL074435.

P.J. Brown. Natural and anthropogenic carbon dioxide fluxes in the subtropical North Atlantic. *Doctoral thesis*, University of East Anglia, 2008.

P.J Brown et al. Anthropogenic carbon accumulation in the subtropical North Atlantic. *J. Geophys. Res.*, 115, 2010. doi: 10.1029/2008JC005043.

H.L. Bryden et al. Impact of a 30% reduction in the Atlantic meridional overturning during 2009-2010. *Ocean Sci.*, 10, 2014. doi: 10.5194/os-10-683-2014.

J.L. Bullister and T. Tanhua. Sampling and measurement of chlorofluorocarbons and sulphur hexafluoride in seawater. *IOCCP report No. 14, ICPO*, Publication Series No. 134:Version1, 2010.

J.L. Bullister and D.P. Wisegarver. The shipboard analysis of trace levels of sulfur hexafluoride, chlorofluorocarbon-11 and chlorofluorocarbon-12 in seawater. *Deep Sea Res., I*, 55, 2008. doi: 10.1016/j.dsr.2008.03.014.

C.T. Chen and F.J. Millero. Gradual increase of oceanic CO_2. *Nature*, 277, 1979. doi: 10.1038/277205a0.

P. Ciais et al. Carbon and other biogeochemical cycles. *in: Climate Change 2013: The Physical Science Basis Contribution of Working Group I to the Fifth*

Assessment Report of the Intergovernmental Panel on Climate Change, edited by: T. Stocker, T. et al., Cambridge University Press, Cambridge, UK, 2013.

M.P. Couldrey et al. On which timescales do gas transfer velocities control North Atlantic CO_2 flux variability? *Glob. Biogeochem. Cycles*, 30, 2016. doi: 10.1002/2015GB005267.

S.A. Cunningham et al. Royal research vessel Discovery cruise D279. *National Oceanography Centre*, Cruise Report, No. 54, 2005.

T.L. Delworth et al. GFDL's CM2 global coupled climate models. Part I: Formulation and Simulation Characteristics. *J. Clim.*, 19, 2006. doi: 10.1175/JCLI3629.1.

T. DeVries et al. Recent increase in oceanic carbon uptake driven by weaker upper-ocean overturning. *Nature*, 542, 2017. doi: 10.1038/nature21068.

A. G. Dickson. Standard potential of the reaction: AgCl(s) + 1/2H2 (g) = Ag(s) + HCl(aq), and the standard acidity constant of the ion in synthetic sea water from 273.15 to 318.15 K. *J. Chem. Thermodyn.*, 22, 1990. doi: 10.1016/0021-9614(90)90074-Z.

A.G. Dickson and F.J. Millero. A comparison of the equilibrium constants for the dissociation of carbonic acid in seawater media. *Deep Sea Res., I*, 34, 1987. doi: 10.1016/0198-0149(87)90021-5.

A.G. Dickson et al. Guide to Best Practices for Ocean CO_2 Measurements. *PICES, Special Publication*, 3, 2007.

R.R. Dickson and J. Brown. The production of North Atlantic deep water: sources, rates, and pathways. *J. Geophys. Res.*, 99, 1994. doi: 10.1029/94JC00530.

E.J. Dlugokencky et al. Atmospheric carbon dioxide Dry Air Mole Fractions. *NOAA ESRL carbon cycle cooperative global air sampling network, 1968 - 2016*, version 2017 - 07 - 28, 2017.

S.C. Doney. The ocean's productive deserts. *Nature*, 389, 1997. doi: 10.1038/39993.

S.C. Doney et al. Ocean acidification: the other CO_2 problem. *Annu. Rev. Mar. Sci.*, 2009. doi: 10.1146/annurev.marine.010908.163834.

B. Dong and R.T. Sutton. Mechanisms of interdecadal thermohaline circulation variability in a coupled ocean-atmosphere GCM. *J. Clim.*, 18, 2005. doi: 10.1175/JCLI3328.1.

O. Duteil et al. A novel estimate of ocean oxygen utilisation points to a reduced rate of respiration in the ocean interior. *Biogeosci.*, 2013. doi: 10.5194/bg-10-7723-2013.

S. Eggleston and E.D. Galbraith. The devil's in the disequilibrium: sensitivity of ocean carbon storage to climate state and iron fertilization in a general circulation model. *Biogeosciences Discuss.*, 2017. doi: 10.5194/bg-2017-328.

S. Emerson et al. Experimental determination of the organic carbon flux from open-ocean surface waters. *Nature*, 1997. doi: 10.1038/40111.

W.J. Emery. Water types and water masses. *Encyclopaedia of Ocean Sciences*, 4, 2001. doi: 10.1006/rwos.2001.0108.

M.H. England et al. Robust warming projections despite the recent hiatus. *Nat. Clim. Chang.*, 5, 2015. doi: 10.1038/nclimate2575.

C.B. Field et al. IPCC, 2014: Climate Change 2014: Impacts, Adaptation, and Vulnerability. *Part A: Global and Sectoral Aspects. Contribution of Working Group II to the Fifth Assessment Report of the Intergovernmental Panel on Climate Change*, Cambridge University Press, Cambridge, NY, USA, 2014.

R.A. Fine et al. A new look at the ocean ventilation time scales and their uncertainties. *J. Geophys. Res.*, 122, 2017. doi: 10.1002/2016JC012529.

K. Friis. A review of marine anthropogenic CO_2 definitions: introducing a thermodynamic approach based on observations. *TELLUS*, 58, 2006. doi: 10.1111/j.1600-0889.2005.00173.x.

K. Friis et al. On the temporal increase of anthropogenic CO_2 in the subpolar North Atlantic. *Deep Sea Res., I*, 52, 2005. doi: 10.1016/j.dsr.2004.11.017.

E.D. Galbraith et al. Climate variability and radiocarbon in the CM2Mc Earth System Model. *J. Clim.*, 24, 2011. doi: 10.1175/2011JCLI3919.1.

M.I. Garcia-Ibánez et al. Ocean acidification in the North Atlantic: rates and mechanisms controlling pH changes. *Biogeosciences*, 13, 2016. doi: 10.5194/bg-13-3701-2016.

J.A. Godbold and P. Calosi. Ocean acidification and climate change: advances in ecology and evolution. *Philos. Trans. R. Soc. B*, 368, 2013. doi: 10.1098/rstb.2012.0448.

N.F. Goodkin et al. Impacts of temporal CO_2 and climate trends on the detection of the anthropogenic CO_2 accumulation. *Glob. Biogeochem. Cycles*, 25, 2011. doi: 10.1029/2010GB004009.

P. Goodwin et al. Analytical relationship between atmospheric carbon dioxide, carbon emissions, and ocean processes. *Glob. Biogeochem. Cycles*, 2008. doi: 10.1029/2008GB003184.

A.L. Gordon. Is there a global scale ocean circulation? *Eos, Trans. Amer. Geophys. Union*, 67, 1986. doi: 10.1029/EO067i009p00109.

H.D. Graven et al. Changing controls on oceanic radiocarbon: new insights on shallow-to-deep ocean exchange and anthropogenic CO_2 uptake. *J. Geophys. Res.*, 117, 2012. doi: 10.1029/2012JC008074.

S. Griffies et al. Elements of MOM4p1. *GFDL Ocean Group Tech*, Report 6, 2010.

N. Gruber. Anthropogenic CO_2 in the Atlantic Ocean. *Global Biogeochem. Cycles*, 12, 1998. doi: 10.1029/97GB03658.

N. Gruber et al. An improved method for detecting anthropogenic CO_2 in the oceans. *Glob. Biogeochem. Cycles*, 10, 1996. doi: 10.1029/96GB01608.

N. Gruber et al. Air-sea flux of oxygen estimated from bulk data: implications for the marine and atmospheric oxygen cycles. *Glob. Biogeochem. Cycles*, 2001. doi: 10.1029/2000GB001302.

N. Gruber et al. Interannual variability in the North Atlantic ocean carbon sink. *Science*, 298, 2002. doi: 10.1126/science.1077077.

E.F. Guallart et al. Ocean acidification along the 24.5°N section in the subtropical North Atlantic. *Geophys. Res. Lett.*, 2015a. doi: 10.1002/2014GL062971.

E.F. Guallart et al. Trends in anthropogenic CO_2 in water masses of the subtropical North Atlantic ocean. *Prog. Oceanogr.*, 131, 2015b. doi: 10.1016/j.pocean.2014.11.006.

T.W.N. Haine. Ocean sciences: vagaries of Atlantic overturning. *Nat. Geosci.*, 9, 2016. doi: 10.1038/ngeo2748.

S. Hakkinen and P.B. Rhines. Decline of Subpolar North Atlantic Circulation during the 1990s. *Science*, 304, 2004. doi: 10.1126/science.1094917.

T.M. Hall et al. Inferring the concentrations of anthropogenic carbon in the ocean from tracers. *Glob. Biogeochem. Cycles*, 16, 2002. doi: 10.1029/2001GB001835.

K. Hanawa and L.D. Talley. Mode waters. *Ocean Circulation and climate: observing and modelling the global ocean*, Siedler G, Church, Gould WJ Eds.:373 – 386, 2001.

Y.-C. He et al. A model-based evaluation of the inverse Gaussian transit-time distribution method for inferring anthropogenic carbon storage in the ocean. *J. Geophys. Res.*, 2018. doi: 10.1002/2017JC013504.

G.C. Hegerl et al. Detecting greenhouse-gas-induced climate change with an optimal fingerprint method. *J. Clim.*, 9, 1996. doi: 10.1175/1520-0442(1996)009.

C. Heinze et al. The ocean carbon sink - impacts, vulnerabilities and challenges. *Earth Syst. Dynam.*, 2015. doi: 10.5194/esd-6-327-2015.

S.A. Henson et al. Detection of anthropogenic climate change in satellite records of ocean chlorophyll and productivity. *Biogeosciences*, 2010. doi: 10.5194/bg-7-621-2010.

J. Hirschi et al. A monitoring design for the Atlantic meridional overturning circulation. *Geophys. Res. Lett.*, 30, 2003. doi: 10.1029/2002GL016776.

M. Holzer et al. Where and how long ago was water in the western North Atlantic ventilated? Maximum entropy inversions of bottle data from WOCE line A20. *J. Geophys. Res.*, 115, 2010. doi: 10.1029/2009JC005750.

E.M. Hood et al. The GO-SHIP repeat hydrography manual: a collection of expert reports and guidelines. *IOCCP Report Number 14, ICPO Publication Series Number 134*, 2010. doi: http://www.go-ship.org/HydroMan.html.

IPCC. Climate Change 2014: Synthesis Report. Contribution of Working Groups I, II and III to the Fifth Assessment Report of the Intergovernmental Panel on Climate Change. *Core Writing Team, R.K. Pacahuri and L.A. Meyer (eds.)*, IPCC, Geneva, Switzerland:151 pp, 2014.

T. Ito and M.J. Follows. Air-sea disequilibrium of carbon dioxide enhances the biological carbon sequestration in the Southern Ocean. *Glob. Biogeochem. Cycles*, 27, 2013. doi: 10.1002/2013GB004682.

T. Ito et al. Is AOU a good measure of respiration in the oceans? *Geophys. Res. Lett.*, 2004. doi: 10.1029/2004GL020900.

D. Iudicone et al. The formation of the ocean's anthropogenic carbon reservoir. *Sci. Rep.*, 6, 2016. doi: 10.1038/srep35473.

D.R. Jackett and T.J. McDougall. A neutral density variable for the World's Oceans. *J. Phys. Oceanogr.*, 27, 1997. doi: 10.1175/1520-0485(1997)027.

L.C. Jackson et al. Recent slowing of Atlantic overturning circulation as a recovery from earlier strengthening. *Nat. Geosci.*, 9, 2016. doi: 10.1038/ngeo2715.

D.C. Jones et al. Spatial and seasonal variability of the air-sea equilibration timescale of carbon dioxide. *Global Biogeochem. Cycles*, 2014. doi: 10.1002/2014GB004813.

F. Joos et al. An efficient and accurate representation of complex oceanic and biospheric models of anthropogenic carbon uptake. *TELLUS*, 48, 1996. doi: 10.1034/j.1600-0889.1996.t01-2-00006.x.

J. Jouzel et al. Vostok ice core: a continuous isotope temperature record over the last climate cycle (160,000 years). *Nature*, 329, 1987. doi: 10.1038/329403a0.

J. Jouzel et al. Climatic interpretation of the recently extended Vostok ice records. *Clim. Dyn.*, 12, 1996. doi: 10.1007/BF00207935.

T.M. Joyce et al. The relation between decadal variability of subtropical Mode water and the North Atlantic Oscillation. *J. Clim.*, 13, 2000. doi: 10.1175/1520-0442(2000)13.

E. Kalnay et al. The NCEP/NCAR 40-year reanalysis project. *Bull. Amer. Meteor. Soc.*, 1996. doi: 10.1175/1520-0477(1996)077.

R.M. Key et al. A global ocean carbon climatology: results from global data analysis project (GLODAP). *Global Biogeochem. Cycles*, 18, 2004.

S. Khatiwala. A computational framework for simulation of biogeochemical tracers in the ocean. *Glob. Biogeochem. Cycles*, 21, 2007. doi: 10.1029/2007GB002923.

S. Khatiwala. Reconstruction of the ocean sink of anthropogenic carbon. *www.ldeo.columbia.edu/∼spk/Research/AnthropogenicCarbon/anthroco2.html*, 2009.

S. Khatiwala et al. Accelerated simulation of passive tracers in ocean circulation models. *Ocean Model.*, 9, 2005. doi: 10.1016/j.ocemod.2004.04.002.

S. Khatiwala et al. Reconstruction of the history of anthropogenic CO_2 concentrations in the ocean. *Nature*, 462, 2009. doi: 10.1038/nature08526.

S. Khatiwala et al. Global ocean storage of anthropogenic carbon. *Biogeosciences*, 10, 2013. doi: 10.5194/bg-10-2169-2013.

J.T. Kiehl and E. Trenberth. Earth's annual global mean energy budget. *J. Clim.*, 78, 1997. doi: 10.1175/1520-0477(1997)078.

B.A. King et al. Royal research vessel Discovery cruise, 346, 05 Jan - 19 Feb 2010, the 2010 transatlantic hydrographic section at 24.5°N. *National Oceanography Centre*, Cruise Report, No. 16, 2012.

A.-S. Krémur et al. Impact of the subtropical mode water biogeochemical properties on primary production in the North Atlantic: new insights from an idealised study. *J. Geophys. Res.*, 114, 2009. doi: 10.1029/2008jc005161.

K.J. Kroeker et al. Impacts of ocean acidification on marine organisms: quantifying sensitivities and interaction with warming. *Glob. Chang. Biol.*, 19, 2013. doi: 10.1111/gcb.12179.

D.P. Kroese et al. Why the Monte Carlo method is so important today. *WIREs Comput Stat*, 6, 2014. doi: 10.1002/wics.1314.

P. Landschützer et al. Recent variability of the global ocean carbon sink. *Glob. Biogeochem. Cycles*, 28, 2014. doi: 10.1002/2014GB004853.

P. Landschützer et al. Decadal variations and trends of the global ocean carbon sink. *Glob. Biogeochem. Cycles*, 2016. doi: 10.1002/2015GB005359.

W. Large and S. Yeager. Diurnal to decadal global forcing for ocean and sea-ice models: the data sets and flux climatologies. *CGD Division of the National Center for Atmospheric Research, NCAR Technical note: NCAR/TN-460+STR*, 2004.

J.M. Lauderdale et al. Wind-driven changes in Southern Ocean residual circulation, ocean carbon reservoirs and atmospheric CO_2. *Clim. Dynam.*, 41, 2013. doi: 10.1007/s00382-012-1650-3.

S.K. Lauvset et al. A new global interior ocean mapped climatology: the 1° x 1° GLODAP version 2. *Earth Syst. Sci. Data*, 8, 2016. doi: 10.5194/essd-8-325-2016.

C.S. Law et al. Automated vacuum analysis of sulphur hexafluoride in seawater: derivation of the atmospheric trend (1970-1993) and potential as a transient tracer. *Mar. Chem.*, 48, 1994. doi: 10.1016/0304-4203(94)90062-0.

C. Le Quéré et al. Interannual variability of the oceanic sink of CO_2 from 1979 through 1997. *Glob. Biogeochem. Cycles*, 14, 2000. doi: 10.1029/1999GB900049.

E. Lewis and D.W.R. Wallace. Program developed for CO_2 system calculations. *ORNL/CDIAC-105. Carbon Dioxide Information Analysis Center, Oak Ridge National Laboratory, U.S. Department of Energy, Oak Ridge, Tennessee*, 1998.

D. Luthi et al. High-resolution carbon dioxide concentration record 650,000 - 800,000 years before present. *Nature*, 453:379 – 382, 2008.

G.A. MacGilchrist et al. The Arctic Ocean carbon sink. *Deep Sea Res., I*, 86, 2014. doi: 10.1016/j.dsr.2014.01.002.

A.C. Manning and R.F. Keeling. Global oceanic and land biotic carbon sinks from the scripps atmospheric oxygen flask sampling network. *TELLUS*, 2006. doi: 10.1111/j.1600-0889.2006.00175.x.

I. Marinov et al. Impact of oceanic circulation on biological carbon storage in the ocean and atmospheric pCO_2. *Glob. Biogeochem. Cycles*, 2008. doi: 10.1029/2007GB002958.

R. Marsh et al. Thermohaline circulation at three key sections of the North Atlantic over 1985 - 2002. *Geophys. Res. Lett.*, 32, 2005. doi: 10.1029/2004GL022281.

J. Marshall et al. A finite-volume, incompressible Navier Stokes model for studies of the ocean on parallel computers. *J. Geophys. Res.*, 102, 1997a. doi: 10.1029/96JC02775.

J. Marshall et al. Hydrostatic, quasi-hydrostatic, and nonhydrostatic ocean modeling. *J. Geophys. Res.*, 102, 1997b. doi: 10.1029/96JC02776.

A.C. Martiny et al. Concentrations and ratios of particulate organic carbon, nitrogen, and phosphorus in the global ocean. *Sci. Data*, 1, 2014. doi: 10.1038/sdata.2014.48.

R.J. Matear et al. Changes in dissolved oxygen in the Southern Ocean with climate change. *Geochem. Geophys.*, 2000. doi: 10.1029/2000GC000086.

K. Matsumoto and N. Gruber. How accurate is the estimation of anthropogenic carbon in the ocean? An evaluation of the $\Delta C^{\star}$ method. *Glob. Biogeochem. Cycles*, 19, 2005. doi: 10.1029/2004GB002397.

M.S. McCartney. The subtropical recirculation of Mode Water. *J. Mar. Res.*, 40, 1982.

T.J. McDougall et al. The international thermodynamic equation of seawater - 2010: calculation and use of thermodynamic properties. *Manuals and Guides 56*, Intergovernmental Oceanographic Commission, 2010.

G.A. McKinley et al. Natural variability and anthropogenic trends in the ocean carbon sink. *Annu. Rev. Mar. Sci.*, 2017. doi: 10.1146/annurev-marine-010816-060529.

B.I. McNeil and R.J. Matear. The non-steady state oceanic CO_2 signal: its importance, magnitude and novel way to detect it. *Biogeosciences*, 10, 2013. doi: 10.5194/bg-10-2219-2013.

B.I. McNeil et al. Anthropogenic CO_2 uptake by the ocean based on the global chlorofluorocarbon data set. *Science*, 10, 2003. doi: 10.1126/science.1077429.

C. Mehrbach et al. Measurements of the apparent dissociation constants of carbonic acid in seawater at atmospheric pressure. *Limnol. Oceanogr.*, 18, 1973. doi: 10.4319/Io.1973.18.6.0897.

N. Metropolis and S. Ulam. The Monte Carlo method. *J. Am. Stat. Assoc.*, 44, 1949. doi: 10.1080/01621459.1949.10483310.

Y. Meyer. Wavelets algorithms and applications. *Society for industrial and applied mathematics*, 1993.

S.D. Meyers et al. An introduction to wavelet analysis in oceanography and meteorology with application to the dispersion of Yanai Waves. *Mon. Weather Rev.*, 121, 1993. doi: 10.1175/1520-0493(1993)121.

F.J. Millero. Thermodynamics of the carbon dioxide system in the oceans. *Geochim. Cosmochim. Acta*, 59, 1995. doi: 10.1016/0016-7037(94)00354-O.

F.J. Millero et al. Carbon dioxide, hydrographic and chemical data obtained during the R/V Hespérides cruise in the Atlantic Ocean (WOCE section A5, July 14 - August 15, 1992). *Cruise Report*, www.ceos.org, 2000.

P.C.D. Milly and A.B. Shmakin. Global modeling of land water and energy balances. Part I: the land dynamics (LaD) model. *J. Hydrometeor.*, 3, 2002. doi: 10.1175/1525-7541(2002)003.

B.I. Moat et al. Major variations in subtropical North Atlantic heat transport at short timescales and their causes. *J. Geophys. Res.*, 121, 2016. doi: 10.1002/2016JC011660.

M.D. Morris. Factorial sampling plans for preliminary computational experiments. *Technometrics*, 33, 1991. doi: 10.2307/1269043.

NASA. Goddard space flight center, ocean ecology laboratory, ocean biology processing group: MODIS-AQUA ocean color data; NASA goddard space flight center. *Ocean Ecology Laboratory, Ocean Biology Processing Group*, 2014.

NOAA. Earth System Research Laboratory, Global Monitoring Division. *Global Monitoring Division, http://www.esrl.noaa.gov/gmd/ccgg/trends/*, 2016.

A. Olsen et al. The Global Ocean Data Analysis Project version 2 (GLODAPv2) - an internally consistent data product for the world ocean. *Earth Syst. Sci. Data*, 8, 2016. doi: 10.5194/essd-8-297-2016.

P. Parekh et al. Physical and biological regulation of the soft tissue carbon pump. *Paleoceanography*, 21, 2006. doi: 10.1029/2005PA001258.

O. Pedersen et al. Underwater photosynthesis of submerged plants - recent advances and methods. *Front. Plant Sci.*, 4, 2013. doi: 10.3389/fpls.2013.00140.

E. Peltola et al. Chemical and hydrographic measurements on a climate and global change cruise along 24°N in the Atlantic Ocean WOCE section A5R(epeat) during January-February 1998. *Cruise report*, pages 1 – 210, 2001.

J.R. Petit et al. Climate and atmospheric history of the past 420,000 years from the Vostok ice core, Antarctica. *Nature*, 399, 1999. doi: 10.1038/20859.

F. Pianosi et al. A Matlab toolbox for global sensitivity analysis. *Environ. Model. Softw.*, 70, 2015. doi: 10.1016/j.envsoft.2015.04.009.

A. Poisson and C.-T.A. Chen. Why is there little anthropogenic CO_2 in the Antarctic bottom waters? *Deep Sea Res., I*, 34, 1987. doi: 10.1016/0198-0149(87)90075-6.

U. Pytkowicz. On the apparent oxygen utilization and the preformed phosphate in the oceans. *Limnol. Oceanogr.*, 1971. doi: 10.4319/lo.1971.16.1.0039.

V. Racapé et al. Transport and storage of anthropogenic C in the North Atlantic Subpolar Ocean. *Biogeosci.*, 2018. doi: 10.5194/bg-15-4661-2018.

A.C. Redfield. On the proportions of organic derivations in seawater and their relation to the composition of plankton. *J.Johnstone memorial*, 1934.

M. Rhein et al. Advection of the North Atlantic Deep Water from the Labrador Sea to the southern hemisphere. *J. Geophys. Res.*, 120, 2015. doi: 10.1002/2014JC010605.

U. Riebesell et al. Sensitivities of marine carbon fluxes to ocean change. *PNAS*, 2009. doi: 10.1073/pnas.0813291106.

A.F. Ríos et al. Decadal acidification in the water masses of the Atlantic Ocean. *PNAS*, 112, 2015. doi: 10.1073/pnas.1504613112.

J. Robson et al. A reversal of climatic trends in the North Atlantic since 2005. *Nat. Geosci.*, 9, 2016. doi: 10.1038/ngeo2727.

C. Rödenbeck et al. Interannual sea-air CO_2 flux variability from an observation-driven ocean mixed-layer scheme. *Biogeosciences*, 11, 2014. doi: 10.5194/bg-11-4599-2014.

W. Roether et al. Apparent loss of CFC-113 in the upper ocean. *J. Geophys. Res.*, 2001. doi: 10.1029/1999JC000079.

C.L. Sabine et al. The oceanic sink for anthropogenic CO_2. *Science*, 305, 2004. doi: 10.1126/science.1097403.

A. Saltelli and P. Annoni. How to avoid a perfunctory sensitivity analysis. *Environ. Model. Softw.*, 25, 2010. doi: 10.1016/J.envsoft.2010.04.012.

A. Saltelli et al. Global sensitivity analyses, the primer. *WILEY Ed.*, 2008.

B.D. Santer et al. A search for human influences on the thermal structure of the atmosphere. *Nature*, 382, 1996. doi: 10.1038/382039a0.

J. Sarmiento. Global change: that sinking feeling. *Nature*, 408, 2000. doi: 10.1038/35041676.

J.L. Sarmiento and N. Gruber. Ocean biogeochemical dynamics. *Princeton university press*, 2006.

W.J. Schmitz. On the World Circulation: Volume I, some global features / North Atlantic circulation. *Woods Hole Oceanographic Institution Technical report*, WHOI-96-03:141, 1996.

W.J.Jr. Schmitz and M.S. McCartney. On the North Atlantic circulation. *Rev. Geophys.*, 31, 1993. doi: 10.1029/92RG02583.

U. Siegenthaler and F. Joos. Use of a simple model for studying oceanic tracer distributions and the global carbon cycle. *Tellus*, 1992. doi: 10.1034/j.1600-0889.1992.t01-2-00003.x.

D.A. Smeed et al. Observed decline of the Atlantic meridional overturning circulation 2004-2012. *Ocean Sci.*, 10, 2014. doi: 10.5194/os-10-29-2014.

W.M. Smethie et al. Tracing the flow of North Atlantic deep water using chlorofluorocarbons. *J. Geophys. Res.*, 105, 2000. doi: 10.1029/1999JC900274.

R. Smith et al. The parallel ocean program (POP) reference manual. *Technical report, LA-UR-10-01853*, Los Alamos National Laboratory, 2010.

R.S. Smith and J. Marotzke. Factors influencing anthropogenic carbon dioxide uptake in the North Atlantic in models of the ocean carbon uptake. *Clim. Dynam.*, 2008. doi: 10.1007/s00382-008-0365-y.

I. Sobol. Global sensitivity indices for nonlinear mathematical models and their Monte Carlo estimates. *Math. Comput. Simul.*, 55, 2001. doi: 10.1016/S0378-4754(00)00270-6.

S. Solomon et al. Climate change 2007 - The physical science basis. *Cambridge Univ. Press*, 2007.

J.D. Stanford et al. A review of the deep and surface currents around Erik drift, south of Greenland: comparison of the past with the present. *Glob. Planet. Change*, 79, 2011. doi: 10.1016/j.gloplacha.2011.02.001.

I. Stendardo and N. Gruber. Oxygen trends over five decades in the North Atlantic. *J. Geophys. Res.*, 117, 2012. doi: 10.1029/2012JC007909.

T. Stöven et al. Transient tracer distributions in the Fram Strait in 2012 and inferred anthropogenic carbon content and transport. *Ocean Sci.*, 12, 2016. doi: 10.5194/os-12-319-2016.

T. Takahashi et al. The alkalinity and the total carbon dioxide concentrations in the world's oceans. *Carbon Cycle Model.*, 16, 1981.

T. Takahashi et al. Seasonal variations of CO_2 and nutrients in the high-latitude surface oceans: a comparative study. *Glob. Biogeochem. Cycles*, 7, 1993. doi: 10.1029/93GB02263.

T. Takahashi et al. Global sea-air CO_2 flux based on climatological surface ocean pCO_2, and seasonal biological and temperature effects. *Deep Sea Res., II*, 49, 2002. doi: 10.1016/S0967-0645(02)00003-6.

T. Takahashi et al. Climatological mean and decadal change in surface ocean pCO_2, and net sea-air CO_2 flux over the global oceans. *Deep Sea Res., II*, 56, 2009. doi: 10.1016/j.dsr2.2008.12.009.

L.D. Talley. Closure of the global overturning circulation through the Indian, Pacific, and Southern Oceans: schematics and transports. *Oceanogr.*, 26, 2013. doi: 10.5670/oceanog.2013.07.

T. Tanhua et al. Use of SF_6 to estimate anthropogenic CO_2 in the upper ocean. *J. Geophys. Res.*, 113, 2008. doi: 10.1029/2007JC004416.

K.E. Taylor. Summarizing multiple aspects of model performance in a single diagram. *J. Geophys. Res.*, 106, 2001. doi: 10.1029/2000JD900719.

K.E. Taylor et al. An overview of CMIP5 and the experimental design. *J. Clim.*, 93, 2012. doi: 10.1175/BAMS-D-11-00094.1.

H. Thomas and V. Ittekkot. Determination of anthropogenic CO_2 in the North Atlantic ocean using water mass ages and CO_2 equilibrium chemistry. *J. Mar. Syst.*, 27, 2001. doi: 10.1016/S0924-7963(00)00077-4.

M. Tomczak. A multi-parameter extension of temperature/salinity diagram techniques for the analysis of non-isopycnal mixing. *Prog. Oceanogr.*, 10, 1981. doi: 10.1016/0079-6611(81)90010-0.

F. Touratier and C. Goyet. Definition, properties, and Atlantic Ocean distribution of the new tracer TrOCA. *J. Mar. Syst.*, 46, 2004. doi: 10.1016/j.jmarsys.2003.11.016.

F. Touratier et al. CFC-11, $\Delta^{14}C$ and ^3H tracers as a means to assess anthropogenic CO_2 concentrations in the ocean. *Tellus*, 2007. doi: 10.1111/j.1600-0889.2006.00247.x.

United Nations Environment Programme UNEP. Production and consumption of Ozone depleting substances under the Montreal protocol 1986 - 2004. *Ozone Secretariat*, United Nations Environment Programme, 2005.

UNFCCC. The Paris Agreement. *United Nations Framework Convention on Climate Change*, Paris, 2016.

S. Van Heuven et al. MATLAB Program Developed for CO_2 System Calculations. *ORNL/CDIAC-105b*, Carbon Dioxide Information Analysis Center, Oak Ridge National Laboratory, U.S., Department of Energy, Oak Ridge, Tennessee, 2011.

D.P. van Vuuren et al. The representative concentration pathways: An overview. *Climatic Change*, 2011. doi: 10.1007/s10584-011-0148-z.

M. Vázquez-Rodríguez et al. An upgraded carbon-based method to estimate the anthropogenic fraction of dissolved CO_2 in the Atlantic Ocean. *Biogeosciences*, 6, 2009a. doi: 10.5194/bgd-6-4527-2009.

M. Vázquez-Rodríguez et al. Anthropogenic carbon distributions in the Atlantic Ocean: data-based estimates from the Arctic to the Antarctic. *Biogeosciences*, 6, 2009b. doi: 10.5194/bg-6-439-2009.

R. Wanninkhof. Relationship between wind speed and gas exchange over the ocean. *J. Geophys. Res.*, 1992. doi: 10.1029/93JC00188.

R. Wanninkhof. Relationship between wind speed and gas exchange over the ocean revisited. *Limnol. Oceanogr.*, 12, 2014. doi: 10.4319/lom.2014.12.351.

A.J. Watson et al. Southern Ocean buoyancy forcing of ocean ventilation and glacial atmospheric CO_2. *Nat. Geosci.*, 8, 2015. doi: 10.1038/ngeo2538.

D.W. Waugh et al. Transport times and anthropogenic carbon in the subpolar North Atlantic ocean. *Deep Sea Res., I*, 51, 2004. doi: 10.1016/j.dsr.2004.06.011.

D.W. Waugh et al. Anthropogenic CO_2 in the oceans estimated using transit time distributions. *Tellus*, 58, 2006. doi: 10.1111/j.1600-0889.2006.00222.x.

D.J. Webb et al. The first main run of the OCCAM global ocean model. *James Rennell Division, Southampton Oceanography Centre*, 1996.

R.G. Williams and M.J. Follows. Ocean dynamics and the carbon cycle, principles and mechanisms. *Cambridge press*, 2011.

R.J. Woosley et al. Rapid anthropogenic changes in CO_2 and pH in the Atlantic Ocean: 2003-2014. *Glob. Biogeochem. Cycles*, 30, 2016. doi: 10.1002/2015GB005248.

G.-Y. Yang and B.J. Hoskins. ENSO-related variation of equatorial MRG and Rossby waves and forcing from higher latitudes. *Q. J. R. Meteorol. Soc.*, 142, 2016. doi: 10.1002/qj.2842.

A. Yool et al. A model-based assessment of the TrOCA approach for estimating anthropogenic carbon in the ocean. *Biogeosciences*, 7, 2010. doi: 10.5194/bg-7-723-2010.

R. E. Zeebe and D. Wolf-Gladrow. CO_2 in seawater: equilibrium, kinetics, isotopes. *First ed.*, Elsevier Science, 2000.